

## TABLE OF CONTENTS

---

<b><u>Section</u></b>	<b><u>Page</u></b>
List of Figures	xxiv
List of Tables	xxxI
List of abbreviations	xxxiv
Notation list	xxxviii
<b>CHAPTER 1: INTRODUCTION</b>	<b>1</b>
1.1 Background	1
1.2 Problem statement	4
1.3 Preliminary evaluation of water salinity and other related water contaminants in the Nandoni Dam	8
1.3.1 Physicochemical analysis	10
1.3.2 Analysis of organic compounds	17
1.3.2.1 Total organic carbon	17
1.3.2.2 Qualitative analysis of phenols and PAHs	18
1.3.2.3 Quantification of phenols	19
1.3.2.4 Quantification of PAHs	21
1.4 Aim and objectives	25
1.5 Research flow chart	26
1.6 Thesis outline	27
<b>CHAPTER 2: LITERATURE REVIEW; MEMBRANE DISTILLATION MEMBRANES FOR WATER DESALINATION</b>	<b>31</b>
2.1 Introduction	31
2.2 MD membrane synthesis methods	33
2.2.1 Phase inversion	34
2.2.2 Electrospinning techniques	36

2.3	MD membrane modification methods	38
2.3.1	Graft polymerisation	38
2.3.2	Plasma polymerisation	40
2.3.3	Interfacial polymerisation	41
2.3.4	Dip coating	41
2.4	The use of nanoparticles in membrane modification	43
2.5	Commonly used configurations in MD	48
2.5.1	Direct contact membrane distillation (DCMD)	49
2.5.2	Air gap membrane distillation (AGMD)	49
2.5.3	Sweeping gas membrane distillation (SGMD)	49
2.5.4	Vacuum membrane distillation (VMD)	50
2.6	Applications of MD processes	51
2.7	Sustainability of membrane distillation	55
2.8	Nanofibres as potential pretreatment materials in membrane distillation	60
2.9	Materials used in the synthesis of polymeric nanofibre membranes	64
2.10	Nanofibres as adsorption materials: Pretreatment role and kinetics in MD	65
2.11	Conclusion	66
<b>CHAPTER 3: ADSORPTION OF PHENOLIC COMPOUNDS BY POLYACRYLONITRILE NANOFIBRE MEMBRANES: A PRETREATMENT FOR THE REMOVAL OF COMPOUNDS BEARING HYDROPHOBIC GROUPS FROM WATER</b>		<b>68</b>
3.1	Introduction	68
3.2	Methods and materials	69
3.2.1	Reagents	69
3.2.2	Synthesis of PAN nanofibres and PEI-modified PAN nanofibres	70

3.2.3	Characterisation of PAN nanofibres and PEI-modified PAN nanofibres	70
3.2.4	Phenolic compounds analysis by solid-phase extraction (SPE)	70
3.2.5	Phenolic compounds analysis by Gas chromatography and mass spectrometry	71
3.2.6	Batch adsorption experiments	72
3.2.7	Regeneration of nanofibres and isolation of phenolic compounds	75
3.3	Results and discussion	75
3.3.1	Scanning electron microscopy analysis of nanofibres	75
3.3.2	Fourier transform infrared analysis of the nanofibres	77
3.3.3	XPS analysis of nanofibres	78
3.3.4	Zeta potential of nanofibres as a function of pH	81
3.3.5	Batch adsorption of phenols using PAN nanofibres	82
3.3.6	Comparison of adsorption to other materials	86
3.3.7	Adsorbent regeneration and isolation	86
3.3.8	Adsorption kinetic studies	88
3.3.9	Adsorption isotherms	89
3.4	Conclusion	92
<b>CHAPTER 4: ENHANCED FLUX IN DIRECT CONTACT MEMBRANE DISTILLATION USING SUPERHYDROPHOBIC PVDF NANOFIBRE MEMBRANES EMBEDDED WITH ORGANICALLY MODIFIED SiO<sub>2</sub> NANOPARTICLES</b>		<b>93</b>
4.1	Introduction	93
4.2	Materials and Methods	94
4.2.1	Reagents	94
4.2.2	Synthesis of SiO <sub>2</sub> NPs	95

4.2.3	Modification of SiO <sub>2</sub> NPs	95
4.2.4	Synthesis of PVDF nanofibre membranes	95
4.2.5	Characterisation of PVDF nanofibre membranes and organically-modified SiO <sub>2</sub> NPs	96
4.2.6	Statistical analysis of organically-modified SiO <sub>2</sub> NPs sizes	97
4.2.7	Performance of the PVDF nanofibre membranes	97
4.3	Results and discussion	98
4.3.1	Transmission Electron Microscopy (TEM) analysis of SiO <sub>2</sub> NPs	98
4.3.2	Statistical analysis of SiO <sub>2</sub> NPs sizes	100
4.3.3	Scanning Electron Microscopy (SEM) analysis of the PVDF nanofibre membranes	102
4.3.4	Atomic Force Microscopy (AFM) analysis	104
4.3.5	Contact angle and tensile strength measurements	106
4.3.6	Liquid entry pressure (LEP) measurements	108
4.3.7	Membrane pore size and porosity measurements	110
4.3.8	Salt (NaCl) rejections of the nanofibre membranes	111
4.3.9	Flux measurements	112
4.4	Conclusion	117
<b>CHAPTER 5: SYNTHESIS OF SILVER NANOPARTICLES USING ONE-POT AND MICROWAVE-ASSISTED METHODS AND THEIR SUBSEQUENT EMBEDMENT ON PVDF NANOFIBRE MEMBRANES FOR GROWTH INHIBITION OF MESOPHILIC AND THERMOPHILIC BACTERIA</b>		<b>119</b>
5.1	Introduction	119
5.2	Materials and methods	122
5.2.1	Reagents	122
5.2.2	Synthesis of AgNPs	123

5.2.3	Synthesis of PVDF nanofibre membranes	124
5.2.4	Characterisation of AgNPs and PVDF membranes	124
5.2.5	Antibacterial tests using AgNPs-embedded PVDF membranes	124
5.3	Results and discussion	126
5.3.1	One-pot and microwave-assisted reduction of Ag <sup>+</sup> ions	126
5.3.2	Kinetics of AgNPs formation: UV-Vis analysis	127
5.3.3	XRD characterisation of AgNPs and nanofibre membranes	129
5.3.4	Morphological and chemical analysis by SEM-EDS	130
5.3.5	Size, morphology, and dispersity of AgNPs: TEM analysis	131
5.3.6	Antibacterial tests	134
	5.3.6.1 Disk-diffusion agar experiments	134
	5.3.6.2 Minimum inhibitory concentration	135
5.4	Conclusion	138
<b>CHAPTER 6: SUPERHYDROPHOBIC PVDF NANOFIBRE MEMBRANES COATED WITH AN ORGANIC FOULING RESISTANT HYDROPHILIC ACTIVE LAYER FOR DIRECT CONTACT MEMBRANE DISTILLATION</b>		<b>140</b>
6.1	Introduction	140
6.2	Materials and methods	141
6.2.1	Reagents	141
6.2.2	Synthesis of silver nanoparticles (AgNPs) and silica nanoparticles (SiO <sub>2</sub> NPs)	142
6.2.3	Surface modification of SiO <sub>2</sub> NPs	142
6.2.4	Synthesis and oxidation of Multi-walled Carbon Nanotubes (MWCNTs)	143
6.2.5	Synthesis of PVDF nanofibre membranes	143
6.2.6	Characterisation of nanoparticles and PVDF nanofibre membranes	143

6.2.7	Performance of PVDF nanofibre membranes	144
6.3	Results and discussion	145
6.3.1	Structural analysis of pristine and modified PVDF nanofibre membranes, MWCNTs, and SiO <sub>2</sub> NPs by FTIR	145
6.3.2	Raman spectroscopic analysis of MWCNTs	147
6.3.3	XRD analysis of modified PVDF nanofibre membranes	149
6.3.4	XPS analysis of the SiO <sub>2</sub> NPs and MWCNTs	150
6.3.5	TEM analysis of AgNPs and SiO <sub>2</sub> NPs	153
6.3.6	Morphological analysis of pristine and modified PVDF nanofibre membranes by SEM	155
6.3.7	Contact angles, porosity and pore sizes of pristine and modified PVDF nanofibre membranes	157
6.3.8	Liquid entry pressure (LEP) measurements of modified membranes	158
6.3.9	Thermal degradation of pristine and modified PVDF nanofibre membranes	159
6.3.10	Mechanical stability of pristine and modified PVDF nanofibre membranes	161
6.3.11	Fouling experiments	163
6.3.12	AgNPs leaching experiments	165
6.4	Conclusion	166
<b>CHAPTER 7: RHYDROPHILIC THIN-LAYER COATING OF A SUPERHYDROPHOBIC PVDF NANOFIBRE MEMBRANE FOR ORGANIC, COLLOIDAL AND BIOFOULING MITIGATION IN DIRECT CONTACT MEMBRANE DISTILLATION</b>		<b>168</b>
7.1	Introduction	168
7.2	Methods and materials	169

7.2.1	Reagents	169
7.2.2	Synthesis and modification of SiO <sub>2</sub> NPs and PVDF nanofibre membranes	169
7.2.3	Characterisation of virgin and fouled nanofibre membranes	170
7.2.4	Preparation of the feed solutions	171
	7.2.4.1 Sodium alginate and colloidal silica as model organic and colloidal foulants	171
	7.2.4.2 Model biofoulants	171
7.2.5	Performance of the PVDF nanofibre membranes	171
7.2.6	Fouling of MD membranes	172
7.3	Results and discussion	174
	7.3.1 SEM-EDS analysis of the fouled membranes	174
	7.3.2 EDS analysis of fouled membranes	177
	7.3.3 Confocal laser scanning microscopy analysis of bio-fouled membranes	178
	7.3.4 AFM analysis of fouled membranes	180
	7.3.5 Contact angles of fouled membranes	181
	7.3.6 Determination of membrane-foulant interfacial free energy	183
	7.3.7 Effect of membrane fouling on water flux and salt rejection	184
7.4	Conclusion	187
<b>CHAPTER 8: HYDROPHOBIC PVDF NANOFIBRE MEMBRANES COATED WITH A FOULING-RESISTANT HYDROPHILIC LAYER FOR PURIFICATION OF ENVIRONMENTAL WATER SAMPLES IN MEMBRANE DISTILLATION</b>		<b>189</b>
8.1	Introduction	189
8.2	Methods	190
	8.2.1 Reagents	190
	8.2.2 Water samples	190

8.2.3	Synthesis of pristine and modified PVDF nanofibre membranes	191
8.2.4	Effect of the composition of brackish water samples on water fluxes and salt rejections performance of PVDF nanofibre membranes	192
8.2.5	Characterisation of PVDF nanofibre membranes	192
8.3	Results and discussion	193
8.3.1	Atomic force microscopy (AFM) analysis	193
8.3.2	Morphology of modified and fouled membranes by Scanning Electron Microscopy (SEM)	194
8.3.3	EDS analysis of fouled membranes	197
8.3.4	Contact angle measurements	198
8.3.5	Membrane and foulants interactions	201
8.3.6	Fouling studies using the water samples collected from the estuary in Belgium	203
8.3.6.1	Flux decay on modified PVDF nanofibre membranes	203
8.3.6.2	Salt rejection of modified PVDF nanofibre membranes	205
8.3.7	Fouling studies using the water samples collected at Nandoni Dam in South Africa	207
8.3.7.1	Flux decay on modified PVDF nanofibre membranes	207
8.3.7.2	Salt rejection decay of modified PVDF nanofibre membranes	208
8.3.8	Comparison of the water flux and salt rejection decay of PVDF nanofibre membranes using water samples collected from the Scheldt estuary in Belgium and Nandoni Dam in South Africa	210
8.4	Conclusion	212
<b>CHAPTER 9 GENERAL CONCLUSIONS AND RECOMMENDATIONS</b>		<b>213</b>

REFERENCES	216
<b>APPENDICES</b>	<b>267</b>
A1 Introduction	267
A2 Experimental design	267
A2.1 Materials	267
A2.2 On-Site Analysis and sampling	269
A2.3 Preparation of standard aqueous solutions	270
A2.4 Atomic absorption spectroscopy (AAS) analysis of metal ions	270
A2.5 The spectroquant analysis of anions	270
A2.6 Analysis of organic compounds	271
A2.6.1 Total organic carbon and dissolved organic carbon	271
A2.6.2 Quantification of phenols and PAHs	272
A2.6.3 Solid-phase extraction (SPE) of phenols and PAHs	273
A2.6.4 Gas chromatography-mass spectrometry analysis of phenols and PAHs	273
A.2.7 Statistical analysis	281
A3 Results and Discussion	282
A3.1 Statistical analysis results of the parameters that contribute to water salinity	282
A3.2 Qualitative analysis of phenols and PAHs	284
A3.3 Statistical analysis results of organic compounds in the Nandoni Dam	286
A3.4 Synoptic sources of phenols and PAHs in Nandoni Dam	288
<b>CURRICULUM VITAE</b>	<b>290</b>



## List of Figures

---

Figure 1.1: A picture showing public water tap with a salt deposit in Limpopo Province, South Africa. ....	6
Figure 1.2: An overview of Nandoni Dam located using Google Maps where the dam entrance is located near the bridge between the dam and Luvuvhu River in Muledane village, dam near-inlet is located 4.1 km from the dam inlet, dam near-outlet is located 2.7 km from the dam outlet and the dam outlet is 100 m away from the Thohoyandou bridge. ....	7
Figure 1.3: The average TOC and DOC of the water samples collected at four different seasons of the year between the period of August 2016 to July 2017, where D1, D2, D3, D4, WTW RW, and WTW TW were the dam-inlet, mid-dam inlet, mid-dam exit, dam exit water treatment works (WTW) raw and treated water respectively. ....	18
Figure 1.4: A flow chart summarising the roadmap of the research. ....	26
Figure 2.1: Casting of polymer films to prepare nano-TiO <sub>2</sub> surface coated membranes for membrane distillation. ....	34
Figure 2.2: Phase inversion formation of membranes. ....	35
Figure 2.3: Preparation of a hollow fibre membrane embedded with SiO <sub>2</sub> NPs. ....	36
Figure 2.4: Schematic representation of an electrospinning process of nanofibre membranes. ....	38
Figure 2.5: Schematic representation of graft polymerisation in membrane modification. ....	40
Figure 2.6: Schematic representation of interfacial polymerisation during membrane modification. ....	41
Figure 2.7: Dip coating in membrane modification. ....	42
Figure 2.8: Graphical representation of the four different configurations commonly used in MD. ....	48
Figure 2.9: The growth of publications in membrane distillation. ....	57
Figure 2.10: Current developments towards application of membrane distillation in water desalination. ....	58
Figure 2.11: Typical parameters that affect the nanofibre electrospinning method. ....	62

<b>Figure 3.1:</b> SEM micrographs of (a) PAN and (b) PAN-PEI nanofibres and their corresponding diameter distribution graphs.....	77
Figure 3.2: FTIR spectra of (a) PAN and (b) PEI-PAN modified nanofibres. ....	78
Figure 3.3: XPS analysis of iminated PAN nanofibres. (a) PAN and (b) PEI-PAN. ....	79
Figure 3. 4: Surface charge of (a) PAN and (b) PEI-PAN modified nanofibres. ...	82
Figure 3.5: Effect of (a) pH, (b) phenols initial concentration, (c) adsorbent dose, and (b) contact time on the adsorption of chlorophenol and nitrophenol on PAN and PEI-modified PAN nanofibres.....	85
Figure 3.6: Regeneration studies and their corresponding decay in adsorption efficiency.....	88
Figure 3.7: Modelling of (a) first-order and (b) second-order adsorption kinetics. ....	89
Figure 3.8: Plots of (a) Langmuir and (b) Freundlich adsorption isotherms for adsorption of phenols by PAN and PAN/PEI nanofibres.....	91
Figure 3.9: Modelling of adsorption mechanism. (a) Effect of temperature and (b) D-R model. ....	91
Figure 4.1: TEM images of SiO <sub>2</sub> NPs and their corresponding size distribution graphs: (M <sub>2SiO<sub>2</sub></sub> ): pristine SiO <sub>2</sub> NPs, (M <sub>3SiO<sub>2</sub></sub> ): ODTS-modified SiO <sub>2</sub> NPs, (M <sub>4SiO<sub>2</sub></sub> ): OTMS-modified SiO <sub>2</sub> NPs, (M <sub>5SiO<sub>2</sub></sub> ): Cl-DMOS-modified SiO <sub>2</sub> NPs. ....	100
Figure 4.2: SEM images of PVDF electrospun nanofibre membranes embedded with SiO <sub>2</sub> NPs. (M1) pristine membrane, (M2), (M3), (M4), and (M5) membranes embedded with pristine SiO <sub>2</sub> NPs, ODTS-modified SiO <sub>2</sub> NPs, OTMS-modified SiO <sub>2</sub> NPs, and Cl-DMOS-modified SiO <sub>2</sub> NPs, respectively. ....	104
Figure 4.3: AFM micrographs of nanofibre membranes decorated with organically-modified SiO <sub>2</sub> NPs.....	106
Figure 4.4: Contact angles and tensile strengths of nanofibre membranes.....	108
Figure 4.5: Liquid Entry Pressure of the PVDF nanofibre membranes.....	109
Figure 4.6: The pore size measurements of PVDF nanofibre membranes.....	111
Figure 4.7: Salt (NaCl) rejection efficiencies of PVDF nanofibre membranes. ...	112

Figure 4.8: The water flux of salty water across PVDF nanofibre membranes embedded with organically modified SiO <sub>2</sub> NPs.....	114
Figure 4.9: The effect of the long-term run of the DCMD using superhydrophobic PVDF membranes on water flux. ....	115
Figure 5.1: Schematic representation of the synthesis of AgNPs using thermally-assisted one-pot and microwave-assisted reduction methods.....	123
Figure 5.2: UV-Vis absorption spectra of AgNPs synthesised using (a) thermally assisted one-pot and (b) microwave-assisted reduction methods. ....	128
Figure 5.3: The XRD patterns of (a) AgNPs, and (b) PVDF nanofibres embedded with AgNPs. ....	129
Figure 5.4: SEM images of PVDF and AgNPs-embedded nanofibre membranes: (a) PVDF nanofibre membranes; (b) AgNPs-embedded PVDF nanofibre membranes; (c) nanofibre size distribution graphs; and (d) EDS spectra of AgNPs-embedded PVDF nanofibre membranes. ....	131
Figure 5.5: TEM images of AgNPs and AgNPs-embedded PVDF nanofibre membrane (a) AgNPs synthesised by thermally-assisted one-pot method; (b) one-pot synthesised AgNPs embedded in the PVDF nanofibre membranes; (c) AgNPs synthesised by microwave-assisted method; and (d) microwave-assisted synthesised AgNPs embedded in the PVDF nanofibre membranes.....	132
Figure 5.6: The size distribution of the AgNPs: (a) thermally-assisted one-pot and (b) microwave-assisted synthesis.....	133
Figure 5.7: The disk-diffusion method showing the growth inhibition of: (a) <i>G. stearothermophilus</i> ; (b) <i>P. aeruginosa</i> ; (c) <i>K. pneumoniae</i> ; and (d) <i>S aureus</i> using the AgNPs supported on the PVDF nanofibres where 1-4 are AgNPs on the nanofibres, 5 is the nanofibre without antibacterial AgNPs and 6 is the antibiotic (neomycin).....	137
Figure 5.8: The minimum inhibitory concentration (MIC) of AgNPs reduced at different times on <i>Geobacillus stearothermophilus</i> , <i>Staphylococcus aureus</i> , <i>Pseudomonas aeruginosa</i> , and <i>Klebsiella pneumoniae</i> . ....	138
Figure 6.1: FTIR spectra of: (a <sub>1</sub> ) MWCNTs; (a <sub>2</sub> ) f-MWCNTs; (b <sub>1</sub> ) SiO <sub>2</sub> NPs; (b <sub>2</sub> ) f-SiO <sub>2</sub> NPs; (c <sub>1</sub> ) pristine PVDF nanofibre membrane; (c <sub>2</sub> ) AgNPs/f-MWCNTs	

coated PVDF nanofibre membrane; and (c <sub>3</sub> ) f-SiO <sub>2</sub> NPs-modified PVDF nanofibre membrane.....	147
Figure 6.2: Raman spectra of: (a) MWCNTs; (b) f-MWCNTs; and (c) AgNPs/f-MWCNT-coated PVDF nanofibre membrane. ....	148
Figure 6.3: XRD spectra of: (a) AgNPs; (b) f-MWCNTs; (c) f-SiO <sub>2</sub> NPs; and (d) AgNPs/f-MWCNTs coated PVDF nanofibre membrane.....	150
Figure 6.4: XPS survey spectra of (a) SiO <sub>2</sub> NPs and (b) f-SiO <sub>2</sub> NPs.....	151
Figure 6.5: XPS spectra of SiO <sub>2</sub> NPs and f-SiO <sub>2</sub> NPs indicating the deconvoluted peaks of (a-b) C1s, (c-d) O1s, and (e-f) Si2p.....	152
Figure 6.6: TEM images of: (a) AgNPs; (b) pristine SiO <sub>2</sub> NPs; (c) f-SiO <sub>2</sub> NPs; (d) MWCNTs; and (e) f-MWCNTs.....	154
Figure 6.7: Size distributions of (a) AgNPs, (b) SiO <sub>2</sub> NPs, (c) f-SiO <sub>2</sub> NPs, and (d) f-MWCNTs.....	155
Figure 6.8: SEM micrographs of: (a) pristine PVDF nanofibre membrane; (b) cross-section of f-SiO <sub>2</sub> NPs-modified PVDF nanofibre membrane; (c) cross-section of AgNPs/f-MWCNTs coated PVDF nanofibre membrane; and (d) top surface of the AgNPs/f-MWCNTs coating layer.....	156
Figure 6.9: Contact angle measurements, porosity, and pore size of: (a) pristine PVDF nanofibre membrane; (b) f-SiO <sub>2</sub> NP-modified PVDF nanofibre membranes and (c) AgNP/f-MWCNTs coated PVDF nanofibre membrane. ....	158
Figure 6.10: The LEP measurements of the nanofibre membranes: (a) pristine PVDF nanofibre membrane; (b) f-SiO <sub>2</sub> NP-modified PVDF nanofibre membranes and (c) AgNP/f-MWCNTs coated PVDF nanofibre membrane. ....	159
Figure 6.11: Thermal degradation of: (a) pristine PVDF nanofibre membrane; (b) f-SiO <sub>2</sub> NP-modified PVDF nanofibre membrane; and (c) AgNP/f-MWCNTs coated PVDF nanofibre membrane. ....	161
Figure 6.12: Stress-strain curves for: (a) pristine PVDF nanofibre membrane; (b) f-SiO <sub>2</sub> NP-modified PVDF nanofibre membrane; and (c) AgNP/f-MWCNTs coated PVDF nanofibre membrane. ....	162
Figure 6.13: Flux of PVDF membranes as a function of time (a) and their corresponding average salt rejection (b): (a) pristine PVDF membrane; (b) f-	

SiO <sub>2</sub> NP-modified membrane; and (c) PVDF membrane coated with AgNP/f-MWCNTs. ....	165
Figure 6.14: UV-Vis absorption spectra of AgNPs tested for leaching. ....	166
Figure 7.1: SEM images of: colloidal silica fouling on (M1) pristine PVDF nanofibre, (M2) f-SiO <sub>2</sub> NPs-modified PVDF nanofibre, and (M3) thin hydrophilic layer-coated PVDF nanofibre membrane; biofouling on (M4) pristine PVDF nanofibre, (M5) f-SiO <sub>2</sub> NPs-modified PVDF nanofibre, and (M6) thin hydrophilic layer-coated PVDF nanofibre membrane; and alginate fouling on (M7) pristine PVDF nanofibre, (M8) f-SiO <sub>2</sub> NPs-modified PVDF nanofibre, and (M9) thin hydrophilic layer-coated PVDF nanofibre membrane. ....	176
Figure 7.2: Cross-sectional view of alginate-fouled membranes: (M8) f-SiO <sub>2</sub> NPs-modified PVDF and (M9) coated f-SiO <sub>2</sub> NPs-modified PVDF nanofibre membranes.....	177
Figure 7.3: EDX spectra of: (M1) colloidal silica-fouled pristine PVDF nanofibre membrane, (M6) biofouling on coated PVDF nanofibre membrane, and (M8) alginate-fouled f-SiO <sub>2</sub> NPs-modified PVDF nanofibre membrane. ...	178
Figure 7.4: Confocal laser scanning microscopy spectra of cells on: (M4) Pristine PVDF nanofibre membrane and (M6) f-MWCNTs/AgNPs-coated PVDF nanofibre membrane.....	179
Figure 7.5: AFM images of fouled membranes: colloidal silica fouling on (M1) pristine PVDF nanofibre, (M2) f-SiO <sub>2</sub> NPs-modified PVDF nanofibre, and (M3) thin hydrophilic layer-coated PVDF nanofibre membranes; biofouling on (M4) pristine PVDF nanofibre, (M5) f-SiO <sub>2</sub> NPs-modified PVDF nanofibre, and (M6) thin hydrophilic layer-coated PVDF nanofibre membrane; and alginate fouling on (M7) pristine PVDF nanofibre, (M8) f-SiO <sub>2</sub> NPs-modified PVDF nanofibre, and (M9) thin hydrophilic layer-coated PVDF nanofibre membrane. ....	181
Figure 7.6: Effect of colloidal, organic, and biofouling on MD permeate flux and salt rejection efficiency. Uncoated membranes: (M1) Pristine membrane, membrane modified with (M2) pristine SiO <sub>2</sub> NPs, (M3) ODTS-functionalised SiO <sub>2</sub> NPs, (M4) OTMS-functionalised SiO <sub>2</sub> NPs, and (M5) Cl-DMOS-functionalised SiO <sub>2</sub> NPs; coated membranes: (M6) Pristine membrane,	

membrane modified with (M7) pristine SiO<sub>2</sub>NPs, (M8) ODTs-functionalised SiO<sub>2</sub> NPs, (M9) OTMS-functionalised SiO<sub>2</sub>NPs, and (M10) Cl-DMOS-functionalised SiO<sub>2</sub>NPs..... 186

Figure 8.1: AFM micrographs of PVDF nanofibre membranes: (M1) Pristine PVDF nanofibre membrane, (M3) f-SiO<sub>2</sub>NPs-modified PVDF nanofibre membrane, (M6) coated f-SiO<sub>2</sub>NPs-modified PVDF nanofibre membrane. .... 194

Figure 8.2: SEM micrographs of uncoated PVDF membranes before and after MD treatment with low salinity (LS) and high salinity (HS) feed waters: (M1) Pristine PVDF nanofibre membrane: (M2), SiO<sub>2</sub>NPs-modified PVDF nanofibre membrane: (M3) f-SiO<sub>2</sub>NPs-modified PVDF nanofibre membrane. .... 196

Figure 8.3: SEM micrographs of coated PVDF membranes before and after MD treatment with low salinity (LS) and high salinity (HS) feed waters. (M4) Pristine PVDF nanofibre membrane, (M5), SiO<sub>2</sub>NPs-modified PVDF nanofibre membrane, (M6) f-SiO<sub>2</sub>NPs-modified PVDF nanofibre membrane. .... 197

Figure 8.4: EDX spectra of pristine PVDF membranes (M1) after MD filtration of low salinity water (M1-LS), and high salinity water (M1-HS)..... 198

Figure 8.5: Contact angles and sliding angles (HCA) of PVDF membranes before MD purification test when using low salinity (LS) and high salinity (HS) feed water. (M1) Pristine PVDF; (M2) SiO<sub>2</sub>NPs-modified PVDF (M3) f-SiO<sub>2</sub>NPs-modified PVDF; (M4) coated pristine PVDF; (5) coated SiO<sub>2</sub>NPs-modified PVDF (M6) coated f-SiO<sub>2</sub>NPs-modified PVDF nanofibre membranes..... 200

Figure 8.6: Contact angles of fouled PVDF membranes before and after MD purification test when using low salinity (LS) and high salinity (HS) feed water. (M1) Pristine PVDF; (M2) SiO<sub>2</sub>NPs-modified PVDF (M3) f-SiO<sub>2</sub>NPs-modified PVDF; (M4) coated pristine PVDF; (5) coated SiO<sub>2</sub>NPs-modified PVDF (M6) coated f-SiO<sub>2</sub>NPs-modified PVDF nanofibre membranes..... 201

Figure 8.7: Various membrane-foulant (or solute) interactions determining initial membrane fouling..... 203

Figure 8.8: Water flux of LS and HS across PVDF nanofibre membranes. Uncoated membranes: (M1) pristine, (M2) SiO<sub>2</sub>NPs-modified, (M3) f-SiO<sub>2</sub>NPs-modified; and coated membranes: (M4) coated pristine, (M5)

coated SiO <sub>2</sub> NPs-modified, and (M6) coated f-SiO <sub>2</sub> NPs-modified PVDF nanofibre membranes.....	205
Figure 8.9: Salt rejections of PVDF nanofibre membranes. Uncoated membranes: (M1) pristine, (M2) SiO <sub>2</sub> NPs-modified, (M3) f-SiO <sub>2</sub> NPs-modified; and coated membranes: (M4) coated pristine, (M5) coated SiO <sub>2</sub> NPs-modified, and (M6) coated f-SiO <sub>2</sub> NPs-modified PVDF nanofibre membranes.....	207
Figure 8.10: Water flux decay of PVDF nanofibre membranes using dam inlet (DI) and dam outlet (DO) water samples. Uncoated membranes: (M1) pristine, (M2) SiO <sub>2</sub> NPs-modified, (M3) f-SiO <sub>2</sub> NPs-modified; and coated membranes: (M4) coated pristine, (M5) coated SiO <sub>2</sub> NPs-modified, and (M6) coated f-SiO <sub>2</sub> NPs-modified PVDF nanofibre membranes.....	208
Figure 8.11: Salt rejection of PVDF nanofibre membranes using dam inlet (DI) and dam outlet (DO) water samples. Uncoated membranes: (M1) pristine, (M2) SiO <sub>2</sub> NPs-modified, (M3) f-SiO <sub>2</sub> NPs-modified; and coated membranes: (M4) coated pristine, (M5) coated SiO <sub>2</sub> NPs-modified, and (M6) coated f-SiO <sub>2</sub> NPs-modified PVDF nanofibre membranes.....	209

## List of Tables

Table 1.1: The physicochemical indicators of the water quality in the Nandoni Dam and raw and treated water of water treatment plant (conductivity, TDS, salinity, temperature, and pH) for the water samples collected in spring and summer 2016, autumn and winter 2017. ....	11
Table 1.2: The conductivity, TDS, and salinity of fresh, brackish and seawater adopted from the literature.....	13
Table 1.3: A comparison of the concentration ranges of mineral ions present in fresh and saline water.....	14
Table 1.4: The concentration of the mineral ions that contribute towards water salinity in the Nandoni Dam as well as raw and treated water from the water treatment plant for the water samples collected in spring and summer 2016, and autumn and winter 2017. ....	16
Table 1.5: The concentration of the phenols (mg/L) in the Nandoni Dam and water treatment plant raw and treated water for water samples collected in spring, summer 2016 and autumn, winter 2017 where D1, D2, D3, D4, WTP TW, and WTP RW were the dam-inlet, mid-dam inlet, mid-dam exit, dam exit, water treatment plant (WTP) treated and raw water respectively. ....	20
Table 1.6: The concentration of the PAHs ( $\mu\text{g/L}$ ) in Nandoni Dam water treatment plant raw and treated water for water samples collected in spring, summer 2016 and autumn, winter 2017 where D1, D2, D3, D4, WTP TW, and WTP RW were the dam-inlet, mid-dam inlet, mid-dam exit, dam exit, water treatment plant (WTP) treated and raw water respectively. ....	22
Table 1.7: Water services Blue Drop Performance (2010) of Thulamela Local Municipality in the Vhembe District Municipality in Limpopo, South Africa. ....	24
Table 2.1: Effect of membrane modification towards water flux and salt rejection in MD.....	42
Table 2.2: Summary of nanoparticle-embedded membranes prepared using different methods and their potential impact on MD. ....	47
Table 2.3: Advantages and disadvantages of MD configurations.....	50

Table 2.4: MD processes used for purification of different types of water. ....	52
Table 2.5: Advantages and disadvantages of flat sheet, nanofibre and hollow fibre membranes.....	53
Table 2.6: The effects of foulants on water flux in MD.....	55
Table 2.7: Estimated water production rate (WPR) and water production cost (WPC) of MD and RO applications. ....	60
Table 2.8: Adsorption of various emerging pollutants using nanofibre materials..	63
Table 3.1: Summary of atomic elements in iminated PAN nanofibres.....	80
Table 3. 2: Summary of fitted XPS of iminated PAN nanofibres.....	80
Table 3.3: Summary of concentration (%) of N-bonds and C-bonds for Iminated PAN nanofibres. ....	80
Table 3.4: Comparison of PAN and iminated PAN nanofibres to other materials on the adsorption of o-chlorophenol and p-nitrophenol. ....	86
Table 3.5: Kinetics constants.....	89
Table 3.6: Adsorption isotherm constants. ....	92
Table 4.1: Side-by-side comparison of the descriptive statistics ( $M_{2SiO_2}$ ): pristine $SiO_2$ NPs, ( $M_{3SiO_2}$ ): ODTS-modified $SiO_2$ NPs, ( $M_{4SiO_2}$ ): OTMS-modified $SiO_2$ NPs, ( $M_{5SiO_2}$ ): Cl-DMOS-modified $SiO_2$ NPs.....	101
Table 4.2: Hypothesis test results of $SiO_2$ NPs sizes; One-way ANOVA test.....	101
Table 4.3: Least Significance Difference (LSD) of the mean sizes of $SiO_2$ NPs..	101
Table 4.4: Summary of properties of the PVDF nanofibre membranes. ....	111
Table 4.5: Properties, LEP and performance comparison of PVDF-based nanofibre membranes in MD applications. ....	117
Table 6.1: $I_D/I_G$ ratios of the MWCNTs used to modify PVDF nanofibre membranes .....	148
Table 6.2: Atomic concentration of the elements in $SiO_2$ NPs.....	153
Table 6.3: Mechanical properties of: (a) pristine PVDF membrane; (b) f- $SiO_2$ NP-modified membrane; and (c) AgNP/f-MWCNTs coated PVDF membranes .....	163
Table 7. 1: The surface tension properties of the probe liquids at 20°C (486)...	173

Table 7. 2: The water contact angles of virgin and fouled membranes. ....	182
Table 7.3: Membrane-foulants interfacial free energy determining the initial membrane fouling. ....	184
Table 8.1: Physicochemical properties and microbial cell density of the low salinity (LS) and high salinity (HS) brackish water samples. ....	191
Table 8.2: Surface free energy components of clean and fouled membrane surfaces. ....	202
Table 8.3: Comparison of water flux and salt rejection decay of PVDF nanofibre membranes using the water samples collected from the estuary in Belgium and Nandoni Dam in South Africa. ....	211
Table 8.4: Comparison of flux decays when real water samples were purified in MD. ....	211
Table A1: The geographical location of the sampling points used in this study (at Nandoni Dam, Vhembe District, Limpopo Province, South Africa and the municipal water treatment plant).....	268
Table A2: MDLs and recoveries of the PAHs and phenolic compounds. ....	277
Table A3: Hypothetical test of the variation of the water parameters that contribute to water salinity and the student's t-test results. ....	282
Table A4: GC-TOF MS analysis of phenols and PAHs. ....	286
Table A5: Hypothesis test results of the mean concentration of the organic contaminants measured in four seasons of the year using the one-way ANOVA test. ....	287



## List of abbreviations

Abbreviation	Definition
AGMD	Air Gap Membrane Distillation
AgNPs	Silver nanoparticles
Al <sub>2</sub> O <sub>3</sub> NPs	Aluminium nanoparticles
ATCC	American Type Culture Collection
BOD	Biological Oxygen Demand
BSA	Bovine serum albumin
CaCO <sub>3</sub>	Calcium carbonate
Cl <sup>-</sup>	Chloride
Cl-DMOS	Chlorodimethyl-octadecyl silane
CO <sub>2</sub>	Carbon dioxide
DCM	Dichloromethane
DCMD	Direct Contact Membrane Distillation
DMAc	Dimethyl acetamide
DOC	Dissolved Organic Carbon
D-R	Dubinini-Radushkevich
EC	Electrical conductivity
EPS	Extracellular polymeric substances
F <sup>-</sup>	Fluoride
FePO <sub>4</sub>	Iron (III) phosphate
f-MWCNTs	oxidized/functionalised multiwalled carbon nanotubes
FO	Forward Osmosis
<i>G. stearothermophilus</i>	<i>Geobacillus stearothermophilus</i>
H <sub>2</sub> SO <sub>4</sub>	Sulfuric acid
H <sub>3</sub> PO <sub>4</sub>	phosphoric acid
HCA	Hysteresis of contact angle
HCO <sub>3</sub>	Hydrogen carbonate
HDMS	Hexamethyldisilazane
HNO <sub>3</sub>	Nitric acid
HS	High salinity

I <sup>-</sup>	Iodide
IEP	Isoelectric point
JCPDS	Joint Committee on Powder Diffraction Standards
<i>K. pneumoniae</i>	<i>Klebsiella pneumoniae</i>
KNO <sub>3</sub>	Potassium nitrate
La <sub>2</sub> O <sub>3</sub>	Lanthanum oxide
LEP	Liquid entry pressure
LiFePO <sub>4</sub>	Lithium iron phosphate
LMH	Litres per meter square per hour
LOD	Limit of detection
LOQ	Limit of quantification
LS	Low salinity
LSD	Least significant difference
MD	Membrane Distillation
MDL	Minimum detectable limit
MDM	Membrane Distillation membranes
MED	Multiple effect evaporation
Mg	Magnesium
MgSO <sub>4</sub>	Magnesium sulphate
MIC	Minimum inhibitory concentration
MVC	Mechanical Vapour Compression
Na	Sodium
NaBH <sub>4</sub>	Sodium borohydride
NaCl	Sodium chloride
NaF	Sodium Fluoride
NaOH	Sodium hydroxide
NF	Nanofiltration
NH <sub>4</sub> <sup>+</sup>	Ammonium cation
NOM	Natural Organic Matter
ODTS	N-Octadecyltrichlorosilane
OTMS	Octadecyltrimethoxysilane
<i>P. aeruginosa</i>	<i>Pseudomonas aeruginosa</i>
PA	Polyamide

PAHs	Polycyclic aromatic hydrocarbons
PAN	Polyacrylonitrile
PE	Polyethylene
PEI	Polyethyleneimine
PEO	Polyethylene oxide
PES	Polyethersulfone
PET	Polyethylene terephthalate
PLA	Polylactic acid
PO <sub>4</sub>	Phosphate
PP	Polypropylene
PS	Polystyrene
PS	Polystyrene
PsF	Polysulfone
PTFE	Polyfluorotetraethylene
PVC	Polyvinyl Chloride
PVDF	Polyvinylidene Fluoride
Ra	Arithmetic mean height
Rec	Recovery
RO	Reverse Osmosis
RW	Raw water
<i>S. aureus</i>	<i>Staphylococcus aureus</i>
SANS	South African National Standards
SD	standard deviation
SGMD	Sweeping Gas Membrane Distillation
SiO <sub>2</sub> NPs	Silica nanoparticles
SMP	Soluble microbial products
SO <sub>4</sub> <sup>2-</sup>	Sulphate
SP	Super phosphorus
SPE	Solid-phase extraction
SPSS	Statistical Package for the Social Sciences
Sq	Mean square height
TDS	Total dissolved solid
TEOS	Tetraethyl orthosilicate

TiO <sub>2</sub>	Titania
TOC	Total organic carbon
TW	Treated water
US EPA	United States Environmental Protection Agency
VMD	Vacuum Membrane Distillation
WHO	World Health Organization
WTP	Water treatment plant

---

## Notation list

Notation	Definition
$A$	Area
$C_f$	Feed concentration
$C_p$	Permeate concentration
$C_e$	Equilibrium concentration
$E$	Mean free energy
$J_{\text{water}}$	Water flux
$k_1$	Rate constant for pseudo-first-order kinetics
$k_2$	Rate constant for pseudo-second-order kinetics
$K_L$	Langmuir isotherm constant
$K_F$	Freundlich isotherm constant
$m/z$	Mass-to-charge ratio
$q_e$	Equilibrium adsorption capacity
$q_m$	Maximum adsorption capacity
$q_t$	Adsorption capacity at time ( $t$ )
$R_L$	Langmuir isotherm dimensionless factor
$R$	Gas constant
$R^2$	Coefficient of determination
$R(\%)$	Rejection efficiency
$T$	Absolute temperature
$t_R$	Retention time
$\sigma_l^D$	Dispersive component of the surface tension of the liquid
$\sigma_l^+$	Acid component of the surface tension of the liquid
$\sigma_l^-$	Base component of the surface tension of the liquid
$\sigma_s^D$	Dispersive component of the surface energy

	of the solid
$\sigma_s^+$	Acid component of the surface energy of the solid
$\sigma_s^-$	base component of the surface energy of the solid
$\sigma^{TOT}$	Total surface tension
$\Delta G_{swm}^D$	Interfacial free energy in the dispersive component
$\Delta G_{swm}^P$	Interfacial free energy in the polar component
$\Delta G_{swm}^{TOT}$	Interfacial free energy for interaction between the membrane ( <i>m</i> ) and the solute or foulant ( <i>s</i> ) in water ( <i>w</i> )
$\Delta m$	Change in mass
$\Delta t$	Change in time
$\Delta V$	Change in volume
$\mu$	mean value
$\rho$	density

---

# CHAPTER 1

## INTRODUCTION

---

### 1.1 Background

Water is a basic and primary resource needed by all living organisms. Without water, humans can hardly survive for more than a week (1). It is critical to socio-economic, agricultural, technological and industrial developments and an important component of the water-food-energy nexus (2). Although water is such an elixir of life, there are serious concerns that relate to its quality, availability, and accessibility for drinking and various applications (3). The rate of depletion of natural aquifers in areas where the availability is abundant is alarming (4). While its scarcity and poor quality remain the major challenges to overcome for attainment of sustainable development in affected countries, pollution of available fresh water sources is another setback that threatens the ecosystem and presents yet continuous concerns towards sustainability of the water resources (5,6).

Water security is affected by economic, social, anthropogenic and natural activities, which include agricultural activities, burning forests, industrial discharges, urban runoffs, mine drainage of discharged brines, *etc.* (7–10). These activities introduce a range of organic (*e.g.*, phenols, polycyclic aromatic hydrocarbons (PAHs), pesticides) and inorganic (*e.g.*, sodium, magnesium, calcium, chlorides, fluorides, cyanides, sulphates, carbonates) pollutants into the water bodies (11,12). These contaminants are carcinogenic and often cause illnesses when ingested (13). In addition, organic compounds further affect industrial processes by lowering the process performance and efficiency. For example, fouling of water filtration membranes in water purification processes that use this technology is known to occur in the presence of organics, a process known as organic fouling (14).

Inorganic compounds such as sodium chloride (NaCl), sodium fluoride (NaF), potassium nitrate (KNO<sub>3</sub>), magnesium sulphate (MgSO<sub>4</sub>), and ammonium phosphates (NH<sub>4</sub>)<sub>3</sub>PO<sub>4</sub> are known to increase water salinity and affect the quality of water for drinking, irrigation and industrial applications (15). Therefore, a sustainable and efficient management of water resources is the most suitable alternative to meet the water quantity and quality demands for the current and future generations (16). This starts with developing efficient and sustainable ways of purifying water.

In order to complement the supply of freshwater in stressed areas, water desalination has been employed. Desalination processes involve the use of thermal distillation or membrane-based technologies for desalination of water from various saline water sources such as seawater and brackish surface and groundwater which is available in abundance. Brackish water is mostly found in estuarine areas where the seawater mixes with freshwater. Furthermore, brackish water is observed in groundwater surrounded by highly mineralised and deep aquifers (17,18). Discharges from industrial effluents containing dissolved salts, leachates of saline soils and the runoff of salt deposits such as halite or gypsum present in the sedimentary rocks also increase the amounts of total dissolved salts and thus lead to the formation of brackish water (19–21). Primarily, the contributing source of brackish surface water (e.g., brackish dam water) is the mixing of the saline water from the open wells and the freshwater as well as the flow from the saline aquifer sourced from pumping wells to the surface water (22). Therefore, brackish water provides a secondary or alternative water source that is less costly for purification compared to seawater (23). Seawater is characterised by high levels of salts causing concentration polarization, and subsequently affects the overall desalination process. In addition to recent technological advancement in water desalination, sustainable desalination could further be achieved by the use of renewable energy.

Pilot-scale thermal distillation and membrane technologies have been used extensively for desalination of water in the first world countries (24,25). However, the use of these technologies remains a critical challenge in third world countries.

Thermal distillation technologies that involve multiple effect evaporation (MED) and mechanical vapour compression (MVC) are energy intensive and therefore very costly (26). Capital expenditure (CAPEX) is another setback in thermal processes. Furthermore, high-pressure-driven membrane processes offer the possibility of relatively high separation efficiency by rejecting almost all particulate matter from water (27). Membranes processes typically used in water desalination include reverse osmosis (RO), forward osmosis (FO), and nanofiltration (NF) (28). Although these processes use less energy (i.e. their energy demand is closer to the thermodynamic limit of separation on water and salt) compared to thermal distillation, they operate at a cost that is not economically viable in the developing countries (29). Therefore, membrane distillation (MD) has been found to counter the operational challenges of RO since it operates at comparatively lower energy requirements, making it less costly than the highly energy-driven membranes (24). A detailed comparison of water production cost between MD and RO is presented in **Table 2.5 (Chapter 2)**.

The MD process is an alternative high-purity water production technology that uses low-grade energy to provide for the separation of water and salts (30). Although MD is a promising technology currently tested at a laboratory scale (31–33), its industrial implementation has been limited due to process efficiency and operational challenges (34). Nevertheless, MD would be expected to reach a considerable and sustainable water production capacity due to the use of renewable energy (e.g. solar energy) and cost-effective waste heat (35). Briefly, during the separation process, mass and heat transfer in MD occur through a porous and hydrophobic membrane. The mass transfer is enhanced by a vapour pressure gradient (i.e., driving force) typically resulting from temperature differences between the bulk solution and membrane interfaces (36).

While MD was almost non-existent in the 1980s, research direction has demonstrated its immense potential for desalination and treatment of wastewater by the year 2000. Material developments, improvements (modifications) and process optimization have been geared towards pilot scaling and commercialization of MD (37–41). As a result, several companies focusing on the

application of MD technology in water desalination have been established. These companies include Aquastill and Aquaver in the Netherlands, Memsys in Germany and Gold Technologies Inc. in the USA. Aquaver and Memsys were recently merged to a single company (Memsys). Remarkably, New Concepts Holdings Limited (NCHL) in China has acquired all the assets and intellectual properties (IPs) of Memsys, and further plans to leverage the combination of research and development in Germany and engineering in China to support the growth of Memsys worldwide. Pilot projects using solar-driven desalination in Singapore are also emerging (24). Furthermore, various companies and research institutions investigating the upscaling of MD have been identified. These include Hyflux (Singapore), AEE INTEC Institute for Sustainable Technologies (Australia), Flemish Institute for Technological Research (Belgium), The Institute National des Sciences Appliquées de Toulouse (INSA, France), Fraunhofer Institute for Solar Energy Systems (Germany), and the Plataforma Solar de Almería (America) (42).

## 1.2 Problem statement

The quality of available water resources in rural settlements in most provinces in South Africa is poor or perceived as poor by the end users (43,44). For example, water supplied by a local water treatment plant to about 55 villages in Thulamela Local Municipality of the Vhembe District, Limpopo Province is said to be salty although no scientific information relating to water salinity has been provided (45). Fouche and co-workers (2013) have reportedly demonstrated that the levels of phosphates, nitrates and ammonium in the Nandoni Dam, a dam that supplies water to the above-mentioned municipality, are not suitable for fisheries (46), which indicates that the use of this water for drinking is also questionable. Additionally, quantification of other pollutants including PAHs, faecal contaminants, inorganic anions and cations across several areas within Vhembe district revealed that the presence of these contaminants were higher than the recommended South African National Standard (SANS241) and the World Health Organization (WHO) drinking water limits (47–49). Edokpayi *et al.* (2018) reported that some households use borehole piped water or communal tap water as their primary

water source without the knowledge of water contamination from these sources (47). Wastewater discharge was also shown to be a contributing factor towards pollution of river water sources, introducing a range of biological and chemical water contaminants (49). For some years, the residents of this municipality have been complaining about the quality of the water, which is used for irrigation and domestic purposes (45). In the years 2015-2017, the complaints turned into violent protests that resulted in burning and destroying of infrastructure and disturbances to daily community activities (50,51).

Besides poor water quality, the salts found in the water was observed to accumulate in the distribution network resulting in blockages of the pipelines. Additionally, the blockage of the pipelines was induced by the excessive growth of biofilms. High concentrations of salts and possibly other contaminants such as total dissolved solids (TDS) cause scale build-up on the surface of plumbing fixtures and appliances such as taps, which are used for the conveyance of water to the end-user. **Figure 1.1** shows salt deposits that accumulated over a period of 24 months (2015-2016) on the surface of a water tap in the Thulamela Local Municipality. Drinking water with high levels of salts is known to cause confusion and jittering in humans (52). Severe degree of intoxicification causes seizure and comma if intervention is not performed. Other related problems include thirst, weakness, nausea, and loss of appetite. Severe conditions include muscle twitching, and bleeding around the brain, causing brain swelling and death (52–54).



**Figure 1.1:** A picture showing public water tap with a salt deposit in Limpopo Province, South Africa (55,56).

Due to difficulties in producing water with a salt concentration of acceptable quality for domestic purposes, the municipality resorted to handing over the water purification project to private companies. In 2014, a task team was appointed to address all the water problems in Mopani Municipality. However, to date, the residents in this municipality still rely on a salty water supply for their daily usage. A municipal water treatment plant abstracts its raw water from the Nandoni Dam, purify it and channels it a distribution system (network of pipelines) which supplies the water to the communities in the Vhembe District Municipality (feeding approximately 800, 000 people). The Nandoni Dam is an earth-fill/concrete type of dam with a catchment area of 1380 km<sup>2</sup>. The water capacity of the dam is 1.64 x 10<sup>11</sup> litres, thus attracting some activities including fisheries, camping and lodging. The geographical view and the GPS coordinates of the dam are presented in **Figure 1.2**.

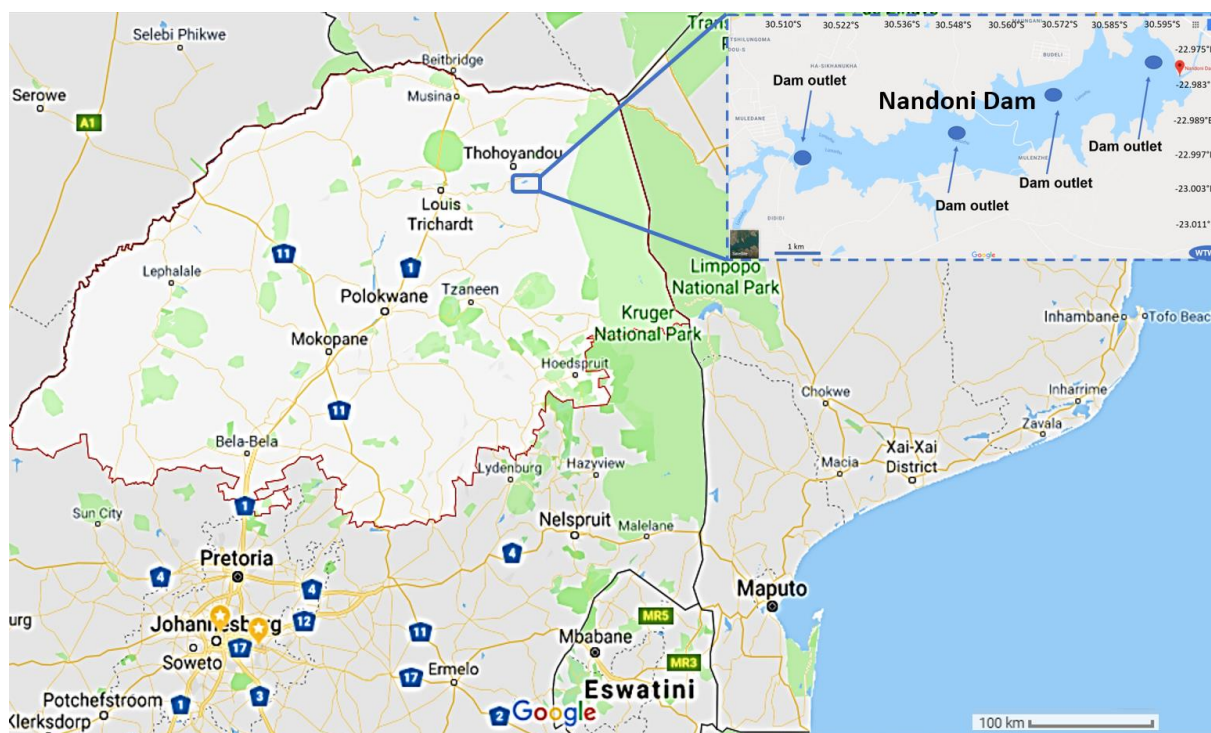


**Figure 1.2:** An overview of Nandoni Dam located using Google Maps where the dam entrance is located near the bridge between the dam and Luvuvhu River in Muledane village, dam near-inlet is located 4.1 km from the dam inlet, dam near-outlet is located 2.7 km from the dam outlet and the dam outlet is 100 m away from the Thohoyandou bridge.

Having identified the problem of water quality in the study area, another part of the problem was to develop a suitable solution for the water problem in the Nandoni dam. Due to the location of the dam in a low income and poor economy rural area, the solution needed to meet requirements of being cost-effective, robust and sustainable. Membrane technology, specifically membrane distillation (MD) membranes was identified as the most suitable technology to remove the salts from water in the area. However, design and fabrication of the MD membranes needed to be done after a thorough analysis of the water quality and current water treatment processes used in the area were assessed. Besides the many advantages of MD membrane technology over other water treatment technologies, the performance of MD membranes remains critically affected by two key factors: (i) wettability of the membranes induced by condensation of water vapour inside the pores of the membranes; and (ii) fouling due to the accumulation of biofilm,

organic, inorganic, and colloidal substances on the surface or in the internal pore structure of the membranes (24).

Wettability reduces the separation efficiency of MD membranes due to the inherent interaction of the membrane surface with water; an ideal MD membrane should be resistant to wetting. Fouling reduces the rate of water recovery due to the blockage of the MD membranes pores. These two factors limit the choice of suitable polymers and fillers for the synthesis of MD membranes. Hydrophobic polymers promote hydrophobic-hydrophobic interactions between pollutants and the membrane surface; thus potentially causing blocking of the pores of the membrane and fouling (57). In contrast, hydrophilic polymers and fouling caused by hydrophilic contaminants enhance wettability of the membranes; consequently affecting the diffusion of water vapour through the membrane or causing liquid water to pass through the pores and compromising its rejection efficiency (27).

It has been established that a superhydrophobic membrane with properties similar to that of a lotus leaf (contact angle  $\approx 180^\circ$  and hysteresis of contact angle less than  $10^\circ$ ), *i.e.*, antiwetting and self-cleaning (fouling resistant) would solve challenges associated with MD membranes. However, such a milestone has not been reached. As such, a potential solution to the problem involving an architectured antifouling MD membrane was envisaged, developed and evaluated for its capability to remove the salts from brackish/saline water.

### **1.3 Preliminary evaluation of water salinity and other related water contaminants in the Nandoni Dam**

Although there was little scientific information of water salinity in the Nandoni Dam at the inception of the study, its salty tasted suggested that the amounts of salt in it were high. Initial assumptions made were that the water could be brackish. Brackish water by definition is salty water with disagreeable taste and a higher salinity when compared with fresh water, but it is not as saline as seawater (58). Brackish water refers to water with a salinity of 500 – 30 000 mg/L (59). To put this

technical definition into perspective, seawater and salt lakes have a salt concentration of about 30,000 – 40,000 mg/L.

Besides water salinity, organic compounds such as phenols and polycyclic aromatic hydrocarbons (PAHs) have been reported as potential contaminants that could be present in the water due to activities around the dam. The use and disposal of phenols and its derivative products such as resins has resulted in the presence phenols in water bodies. The effects of phenols and PAHs on fauna and flora differ. Although phenols and PAHs are moderately persistent in water bodies (60,61), they can also be absorbed by plant roots and be translocated to other parts of the plants. Plants have mechanisms that protect them against the effects of the organic contaminants (62). Nonetheless, these phenols and PAHs can potentially bio-accumulate in fish and other animals living in water and in human beings. Depending on their concentration levels and exposure times, PAHs and phenols are known to cause tumors, affect the reproduction system and result in the development of reduced immunity. Their acute toxicity effects include irritation, vomiting, diarrhoea, confusion, and nausea (62,63) while the long-term effects are skin inflammation, liver damage, decreased immune system function, cataract and the destruction of the red blood cells (2,62,64). Other contaminants that pose a threat to the environment include mesophilic/thermophilic and drug resistant bacteria. Both organic and bacterial contaminants do not only pose threats to the humans and animals, but also affect industrial processes. In the water industry, organic, inorganic and bacterial contaminants may induce fouling of membranes technologies and negatively affect their overall performance during water treatment and recovery.

Furthermore, contamination of water sources with faecal matter and bacteria discharged from inadequately treated wastewaters remains a common problem affecting the lives of people (65). Several bacteria grow by attachment to either biotic or abiotic surfaces. The growth of bacteria on membrane surfaces results to the formation of biofilms leading to biofouling (66). Biofouling is largely attributed to the accumulation of soluble microbial products (SMP) and extracellular polymeric substances (EPS) produced by bacteria on membrane surfaces (67). Biofouling

has largely been reported in membrane separation processes and distribution systems (67,68). Fouling of membrane filters impairs filtration performance and consequently affects the overall filtration process (69,70).

Prior to developing MD membranes to address the water challenges in the Vhembe District Municipality, water quality analyses were undertaken in the Nandoni Dam in order to determine the water salinity and organic water contamination and the results are presented in the next sections. Details of the experimental procedures for the water analysis are provided in the appendices (**Appendix A2.1 – A2.7**).

### **1.3.1 Physicochemical analysis**

The physicochemical properties of the water samples such as conductivity, total dissolved solids (TDS), salinity, temperature, and pH were measured on-site where the samples were collected, and results are presented in **Table 1.1**. Three representative samples per sampling were collected in each identified sampling point within the dam and the municipal water treatment plant that sourced the water from the dam for purification.

**Table 1.1:** The physicochemical indicators of the water quality in the Nandoni Dam and raw and treated water of water treatment plant (conductivity, TDS, salinity, temperature, and pH) for the water samples collected in spring and summer 2016, autumn and winter 2017.

Sampling Point	Sampling Season	Conductivity $\mu\text{S/cm}$	TDS mg/L	Salinity mg/L	Temperature K	pH
Dam inlet	Spring	1468 $\pm$ 68	954 $\pm$ 42	712 $\pm$ 33	292 $\pm$ 6	7.95 $\pm$ 0.34
	Summer	1395 $\pm$ 45	903 $\pm$ 45	633 $\pm$ 12	298 $\pm$ 9	8.23 $\pm$ 0.45
	Autumn	1321 $\pm$ 52	833 $\pm$ 33	541 $\pm$ 36	299 $\pm$ 8	7.65 $\pm$ 0.21
	Winter	1352 $\pm$ 23	912 $\pm$ 42	625 $\pm$ 25	294 $\pm$ 5	8.02 $\pm$ 0.35
Dam Mid-Inlet	Spring	1835 $\pm$ 65	910 $\pm$ 21	751 $\pm$ 10	293 $\pm$ 5	7.61 $\pm$ 0.22
	Summer	1820 $\pm$ 12	958 $\pm$ 33	610 $\pm$ 18	298 $\pm$ 10	7.83 $\pm$ 0.32
	Autumn	1785 $\pm$ 44	821 $\pm$ 49	532 $\pm$ 34	297 $\pm$ 4	7.78 $\pm$ 0.11
Dam Mid-outlet	Winter	1798 $\pm$ 35	897 $\pm$ 22	586 $\pm$ 35	292 $\pm$ 12	7.36 $\pm$ 0.24
	Spring	1358 $\pm$ 54	864 $\pm$ 12	469 $\pm$ 17	294 $\pm$ 3	7.15 $\pm$ 0.09
	Summer	1318 $\pm$ 25	852 $\pm$ 33	417 $\pm$ 9	298 $\pm$ 10	7.90 $\pm$ 0.42
Dam Outlet	Autumn	1301 $\pm$ 56	812 $\pm$ 44	364 $\pm$ 18	299 $\pm$ 18	8.11 $\pm$ 0.23
	Winter	1311 $\pm$ 43	798 $\pm$ 43	523 $\pm$ 38	293 $\pm$ 7	7.35 $\pm$ 0.35
	Spring	1685 $\pm$ 63	985 $\pm$ 13	716 $\pm$ 14	292 $\pm$ 4	7.73 $\pm$ 0.34
WTP RW	Summer	1717 $\pm$ 32	1194 $\pm$ 32	634 $\pm$ 23	298 $\pm$ 14	7.82 $\pm$ 0.14
	Autumn	1699 $\pm$ 23	1154 $\pm$ 41	445 $\pm$ 32	298 $\pm$ 3	7.25 $\pm$ 0.41
	Winter	1765 $\pm$ 55	1245 $\pm$ 34	526 $\pm$ 22	292 $\pm$ 5	7.35 $\pm$ 0.32
WTP TW	Spring	985 $\pm$ 33	715 $\pm$ 34	408 $\pm$ 31	292 $\pm$ 10	7.89 $\pm$ 0.21
	Summer	912 $\pm$ 47	722 $\pm$ 35	361 $\pm$ 12	297 $\pm$ 8	8.19 $\pm$ 0.17
	Autumn	854 $\pm$ 69	717 $\pm$ 14	325 $\pm$ 27	296 $\pm$ 4	8.21 $\pm$ 0.31
WTP TW	Winter	978 $\pm$ 45	698 $\pm$ 36	464 $\pm$ 21	291 $\pm$ 11	7.77 $\pm$ 0.10
	Spring	772 $\pm$ 32	646 $\pm$ 29	309 $\pm$ 33	291 $\pm$ 11	7.35 $\pm$ 0.13
	Summer	565 $\pm$ 66	705 $\pm$ 36	258 $\pm$ 8	297 $\pm$ 8	7.84 $\pm$ 0.35
WTP TW	Autumn	721 $\pm$ 41	882 $\pm$ 18	221 $\pm$ 42	298 $\pm$ 4	8.13 $\pm$ 0.28
	Winter	685 $\pm$ 65	695 $\pm$ 10	336 $\pm$ 35	291 $\pm$ 5	7.68 $\pm$ 0.35

\* WTP is the water treatment plant, TW is the treated water, RW is the raw water.

The water samples in the Nandoni Dam were found to be slightly alkaline with a pH ranging from 7.19 to 8.23 (**Table 1.1**). This was expected since the water passes through various limestone rocks prior to collection into the Nandoni Dam. This meant the water contains the carbonates at concentrations that have neutralisation effect to result in the formation of slightly alkaline pH. The Nandoni

Dam is also surrounded by activities that involve discharges from a sewer network, irrigation canals, drainage network and pumped groundwater which find their way to the lake via several tributaries. These activities may also contribute to pH fluctuations depending on their hydronium and hydroxide ion dissociation potentials in water (71,72).

The temperature of the water samples was found to vary significantly with seasonal changes. In this regard, lower temperatures (291 K) were recorded during winter and the highest temperature (298 K) was recorded during summer. A significant variation in the seasonal water temperature (spring, 292 K; summer, 298 K in 2016; autumn, 295 K; and winter, 291 K in 2017) was caused by an increased cooling rate of the water bodies due to the exposure of the dam to the wind. Large open water bodies have a fast cooling rate with respect to wind direction and this results in colder water during winter and spring, and warmer water during summer and autumn (73).

The conductivity of the water is a measure of the concentration of ions that are capable of carrying electrical current (59). Water conductivity is used to estimate the TDS and salinity of the water. The conductivity, TDS and salinity classification of fresh, brackish and sea water is presented in **Table 1.2.** (58,74). The conductivity of the water sampled from the dam was found to be higher at the middle inlet and outlet of the dam. Apart from the Luvuvhu River, the Nandoni Dam has other small streams that enter the dam. These streams are most likely to deposit high amounts of total dissolved solids (TDS), which lead to an increase in the water conductivity. By all accounts, the conductivity values obtained for the water samples of the Nandoni Dam and the municipal water treatment plant indicate brackish water.

**Table 1.2:** The conductivity, TDS, and salinity of fresh, brackish and seawater adopted from the literature (58,74–76).

Water Salinity	Physicochemical Properties		
	Conductivity ( $\mu\text{S}/\text{cm}$ )	TDS (mg/L)	Salinity (mg/L)
Fresh water	150–500	<1000	<500
Brackish water	1000–80,000	1000–5000	500–30,000
Sea water	55,000	30,000–40,000	35,000–40,000
Brine	$\geq 55,000$	$\geq 100,000$	$\geq 50,000$

The total dissolved solids (TDS) are comprised of inorganic matter such as mineral, salts, metals as well as dissolved organic compounds present in the water (77). In general, the highest concentrations of TDS (1194 and 1154 mg/L) were observed during the rainy seasons (i.e., summer and autumn respectively). Such levels are associated with the runoff that carries high deposits of the dissolved compounds into the Nandoni Dam. The total dissolved solids were concentrated at the dam outlet with the highest concentration of 1245 mg/L being recorded in winter.

Salinity is defined as the total concentration of all dissolved salts in water (78). The salinity of the water in the Nandoni Dam was found to be higher during the dry seasons (i.e., winter and spring) with the highest amount (750 mg/L) being recorded for the water sampled at the middle of the dam near the inlet. This is attributable to the low dilution effect of the total dissolved salts, which were presently deposited into the dam during the dry seasons. The salinity values seem to suggest that the bulk of the water in Nandoni Dam was brackish (75,76). However, a few exceptions were observed; analyses of the water at the dam outlet and the treatment plant (the plant that sources the water from Nandoni Dam for treatment prior to distribution) indicated that this water falls within the freshwater category (i.e., salinity < 500 mg/L), although the water taste is unsatisfactory when drinking.

Fresh, brackish and seawater possess viable minerals that differ in availability and concentration. The concentrations of the common ions present in fresh, brackish and sea water are shown in **Table 1.3**. The concentration ranges of these ions serve as a guide to water management authorities for monitoring of the presence of dissolved salts in surface water. Therefore, these adopted reported concentrations were used to further determine the level of water salinity in the Nandoni Dam.

**Table 1.3:** A comparison of the concentration ranges of mineral ions present in fresh and saline water (58,79–82).

Ions	Concentration (mg/L)		
	Fresh Water	Brackish Water	Sea Water
Chloride	1–250	500–5 000	19,000
Nitrate	0–18	–	0.7
Phosphate	–	–	0.1
Sulphate	–	10–800	–
Fluoride	–	–	1.4
Iodide	–	–	0.05
Ammonium	–	–	0.05
Hydrogen carbonate	–	100–360	145
Sodium	≥ 200	5–800	10 000
Magnesium	–	5–80	1 290
Calcium	–	30 – 350	400

The concentrations of all mineral ions that constitute water salinity were determined and the results are presented in **Table 1.4**. The amounts of all ions studied were found to be significantly different throughout the seasons, with higher concentrations being observed during dry seasons (*i.e.*, winter and spring). However, the detection of individual ions such as chloride and sodium ions demonstrated that the water in the Nandoni Dam was moderately saline, with chloride and sodium ion concentrations being below those of brackish water.



Although the ion concentrations in the Nandoni Dam were lower than those of brackish water, their total chemical interactions may lead to compromised water quality with unfavourable taste (too salty for drinking) and odour. For instance, sodium is available in water bodies in several chemical compositions that include sodium chloride, sodium carbonate, sodium sulphate, sodium phosphate, sodium bicarbonate and others.

**Table 1.4:** The concentration of the mineral ions that contribute towards water salinity in the Nandoni Dam as well as raw and treated water from the water treatment plant for the water samples collected in spring and summer 2016, and autumn and winter 2017.

Sampling Point	Sampling Season	Cl <sup>-</sup> mg/L	NO <sub>3</sub> <sup>-</sup> mg/L	PO <sub>4</sub> <sup>3-</sup> mg/L	SO <sub>4</sub> <sup>2-</sup> mg/L	F <sup>-</sup> mg/L	I <sup>-</sup> mg/L	NH <sub>4</sub> <sup>+</sup> mg/L	Na <sup>+</sup> mg/L	Mg <sup>2+</sup> mg/L	Ca <sup>2+</sup> mg/L	HCO <sub>3</sub> <sup>-</sup> mg/L
Dam Inlet	Spring	59.5	8.06	1.25	0.3	0.08	1.32	0.32	34.86	6.76	25.21	44.35
	Summer	64.6	16.12	1.01	0.6	0.06	1.04	1.32	38.63	6.68	22.25	33.25
	Autumn	25.5	7.02	1.48	0.9	0.06	1.56	2.21	16.08	4.51	19.09	41.32
	Winter	35.7	5.98	1.25	0.6	0.05	1.29	2.28	15.86	4.42	29.79	45.65
Dam Mid-Inlet	Spring	110.7	19.5	1.73	0.3	0.09	1.82	3.45	55.33	4.50	19.36	38.25
	Summer	76.5	20.54	1.12	0.6	0.04	1.04	2.45	45.86	6.47	16.85	22.65
	Autumn	30.6	7.54	1.51	0.3	0.09	1.56	5.25	17.65	9.54	17.66	24.85
	Winter	37.4	5.72	1.69	0.9	0.08	1.82	4.26	17.27	17.99	20.54	35.45
Dam Mid-Outlet	Spring	114.1	20.28	1.250	0.6	0.07	1.35	4.24	34.75	7.57	15.49	19.52
	Summer	76.5	31.46	1.75	0.3	0.06	1.82	5.12	44.89	7.65	13.59	22.58
	Autumn	69.7	5.21	1.54	0.9	0.05	1.56	4.69	18.86	5.11	12.66	17.96
	Winter	37.4	5.98	1.42	0.6	0.05	1.56	4.19	18.90	5.41	14.35	24.85
Dam Outlet	Spring	54.4	3.64	1.54	0.6	0.06	1.56	5.26	34.69	5.29	13.25	27.85
	Summer	76.5	8.32	1.53	1.8	0.09	1.56	4.19	30.78	5.16	10.26	22.58
	Autumn	44.2	5.98	1.75	0.9	0.05	1.82	4.78	21.84	3.77	6.585	23.55
	Winter	35.7	5.46	1.44	0.6	0.06	1.56	4.26	19.74	10.81	12.26	26.25
TP RW	Spring	81.6	7.28	4.51	0.3	0.17	4.68	4.98	80.06	0.78	19.33	32.53
	Summer	73.1	8.06	0.25	0.6	0.21	0.26	5.96	40.07	1.09	15.25	26.54
	Autumn	25.5	8.84	1.24	0.3	0.18	1.28	3.24	14.56	0.66	14.69	21.48
	Winter	35.7	8.32	1.49	0.9	0.15	1.56	3.02	14.82	1.15	18.23	33.85
TP TW	Spring	134.7	24.96	4.08	0.3	0.07	4.16	3.02	86.16	0.16	25.25	46.85
	Summer	73.1	6.24	2.23	0.6	0.16	2.08	2.23	42.16	0.32	23.54	33.58
	Autumn	64.6	3.12	2.25	0.3	0.17	2.34	5.32	37.99	0.51	24.33	41.33
	Winter	57.8	2.86	2.15	0.9	0.18	2.08	5.12	37.84	0.22	26.33	12.25

TP TW = treatment plant treated water; TP RW treatment plant raw water

## 1.3.2 Analysis of organic compounds

### 1.3.2.1 Total organic carbon

Total organic carbon (TOC) and dissolved organic carbon (DOC) are non-specific parameters indicating the quality and purity of water (83). The TOC and DOC procedures are non-specific, simple, fast and cheap techniques that provide information about particulate and dissolved organic compounds in water. The TOC in water sources emanates from both synthetic and natural organic matter (NOM), which include detergents, pesticides, fertilisers, industrial chemicals, urea, amines, humic acids, and fulvic acids. Therefore, TOC and DOC were a good measure of organic compounds present in the water samples obtained at the Nandoni Dam as well as Nsami water treatment plant. TOC and DOC significantly varied from one season to the other as well as in sampling points (**Figure 1.3**). The highest concentration of TOC and DOC were  $5.028 \pm 0.184$  mg/L and  $3.214 \pm 0.039$  mg/L in autumn and summer respectively at the entrance of Nandoni Dam (D1) while the lowest were  $3.014 \pm 0.164$  mg/L and  $1.947 \pm 0.102$  mg/L in spring and autumn at D4 (**Figure 1.3**). This was attributed to the disposal of the organic compounds from different sources that include the tributary carrying organic compounds whose concentration accumulated at the point D1 and got diluted in the bulk of the dam water. The lower concentrations in spring and higher in autumn were associated with the moderate flow of water carrying the deposits of organics in spring and high run-offs in February (a month that begins autumn) carrying high deposits of organic matter into the dam. Ndiweni *et al.* (2019) demonstrated that NOM fractions for South African plants are mainly hydrophobic acids, aromatic proteins, biological activity, humic acid-like, and fulvic acid-like moieties (84) and these are likely to cause fouling in MD (39).

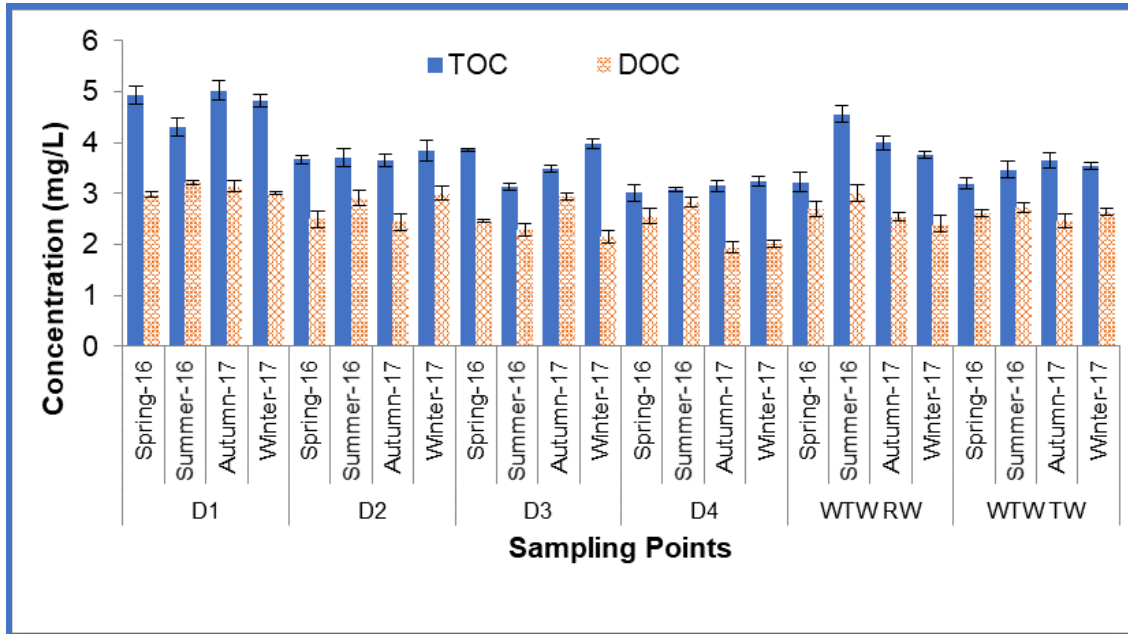


**Figure 1.3:** The average TOC and DOC of the water samples collected at four different seasons of the year between the period of August 2016 to July 2017, where D1, D2, D3, D4, WTW RW, and WTW TW were the dam-inlet, mid-dam inlet, mid-dam exit, dam exit water treatment works (WTW) raw and treated water respectively.

### 1.3.2.2 Qualitative analysis of phenols and PAHs

According to SANS 241, USEPA and WHO drinking water standards, the maximum acceptable concentrations of phenol, 2-chlorophenol, 2,6-dichlorophenol, 2,4,5-trichlorophenol, 2,4-dimethylphenol, 4-nitrophenol and p-cresol are 2.0 mg/L, 0.1 mg/L, 0.2 mg/L, 1.0 mg/L, 0.4 mg/L, 0.03 mg/L and 0.055 mg/L respectively (85). The USEPA has also classified 16 PAHs as the priority primary pollutants in water with no exception to naphthalene, pyrene, acenaphthene, benzo(a) anthracene and benzo(a) pyrene (86,87). The PAHs were reported to show cytotoxic, mutagenic and carcinogenic health effects at total PAH concentrations of 1.0  $\mu\text{g/L}$  in water and the recommended total concentration value is 0.1  $\mu\text{g/L}$  (88).

### 1.3.2.3 Quantification of phenols

The concentrations of the phenols were found to differ with seasonal changes at different sampling points and the highest being in summer and autumn at point D4. The concentrations of the some phenols were within threshold limits in drinking water with a few exceptions including 2-chlorophenol whose concentration was greater than 0.1 mg/L set by SANS 241, USEPA and WHO (*i.e.*, 0.13 mg/L, 0.23 mg/L, 0.38 mg/L, 0.24 mg/L at the dam mid-outlet (D4) and 0.15 mg/L, 0.15 mg/L, 0.13 mg/L, 0.20 mg/L in spring, summer, autumn and winter respectively) (**Table 1.5**). The other exceptions included 2,6-dichlorophenol whose concentration was greater than SANS 241 limit of 0.20 mg/L with the highest being 0.458 mg/L at the dam mid-outlet (D3) in summer and p-cresol whose concentration was higher than the acceptable drinking water standard of 0.06 mg/L at all sampling points.

**Table 1.5:** The concentration of the phenols (mg/L) in the Nandoni Dam and water treatment plant raw and treated water for water samples collected in spring, summer 2016 and autumn, winter 2017 where D1, D2, D3, D4, WTP TW, and WTP RW were the dam-inlet, mid-dam inlet, mid-dam exit, dam exit, water treatment plant (WTP) treated and raw water respectively.

Sampling point	Sampling point	P	2-CP	2,6-DCP	2,4,5-TCP	2,3-DMP	4-NP	p-MP
D1	Spring-16	0.89	0.01	0.15	0.54	0.09	0.008	0.42
	Summer-16	0.75	0.03	0.19	0.49	0.07	0.007	0.63
	Autumn-17	0.96	0.03	0.14	0.69	0.07	0.010	0.50
	Winter-17	0.68	0.04	0.13	0.66	0.03	0.006	0.33
D2	Spring-16	0.66	0.05	0.32	0.79	0.13	0.004	0.52
	Summer-16	0.35	0.07	0.39	0.69	0.10	0.010	0.46
	Autumn-17	0.79	0.08	0.42	0.89	0.15	0.006	0.69
	Winter-17	0.81	0.05	0.12	0.63	0.12	0.002	0.46
D3	Spring-16	0.99	0.13	0.25	0.49	0.10	0.004	0.13
	Summer-16	0.46	0.26	0.37	0.22	0.15	0.012	0.25
	Autumn-17	0.79	0.37	0.37	0.59	0.13	0.005	0.45
	Winter-17	0.34	0.25	0.25	0.46	0.09	0.003	0.15
D4	Spring-16	0.79	0.15	0.37	0.79	0.13	0.007	0.79
	Summer-16	0.52	0.15	0.46	0.99	0.17	0.011	0.45
	Autumn-17	0.99	0.13	0.25	1.11	0.15	0.003	0.85
	Winter-17	0.23	0.20	0.45	0.90	0.13	0.001	0.23
WTP RW	Spring-16	0.11	0.08	0.26	0.79	0.07	0.004	0.45
	Summer-16	0.35	0.05	0.25	0.66	0.05	0.006	0.33
	Autumn-17	0.22	0.09	0.20	0.80	0.08	0.003	0.25
	Winter-17	0.15	0.10	0.21	0.99	0.05	0.004	0.14
WTP TW	Spring-16	0.85	0.05	0.19	0.79	0.02	0.001	0.13
	Summer-16	0.58	0.05	0.13	0.86	0.04	0.010	0.15
	Autumn-17	0.46	0.03	0.20	0.99	0.09	0.009	0.20
	Winter-17	0.13	0.05	0.17	0.90	0.02	0.003	0.33

P = phenol, 2-CP = 2-Chlorophenol, 2,6-DCP = 2,6-Dichlorophenol, 2,4,5-TCP = 2,4,5-Trichlorophenol, 2,3-DMP = 2,3-Dimethylphenol, 4-NP = 4-Nitrophenol, p-MP = p-Cresol

The source of these phenols entering the water in Nandoni Dam was associated with a number of factors including biodegradation of the agricultural insecticides, pesticides (89) and herbicides (90) such as 2,4, 2,4,5-trichloro-phenoxy acetic

acid, dichlorophenoxyacetic acid and 4-chloro-2-methylphenoxyacetic acid which could be used in the farms upstream of the water catchments. Other sources are naturally occurring, and these comprise of chemical degradation of NOM, microbiological degradation of naturally occurring substrate, the enzymatic formation of phenols within the plants, which are stored in the plant roots and stems and released to the environment through plant exudates. The concentrations of the chlorophenols were generally found to be higher than those of the nitrophenols in the selected sampling points within the dam. This is typically associated with chlorine-containing compounds such as chlorinated detergents, chlorinated rubber swimming pool paint, and agricultural products. It is not clear why these contaminants could be present. Further studies on locating potential source of contamination are imperative.

#### 1.3.2.4 Quantification of PAHs

The concentrations of PAHs were generally higher in summer and autumn in all sampling points within the dam (**Table 1.6**). The PAHs were observed to be more concentrated in the middle part of the dam and less concentrated in the outer parts (being the entrance and the outlet of the dam). Although the bulk water that enters the dam comes from the Luvuvhu River at the sampling point labelled D1, there are other small streams that feed into the dam at the centre, and these are likely to be the main sources that discharge high amounts of the organic pollutants (PAHs, phenols, NOMs) into the dam. The following PAHs, namely fluorene, phenanthrene, fluoranthene, benzo(k) fluoranthene, indeno[1,2,3cd]pyrene and dibenzo[def,mno]chrysene were too low to be detected even at highly pre-concentrated analytes. The detected PAHs were naphthalene, acenaphthene, pyrene, benz(a) anthracene and benzo(a) pyrene. Their highest concentrations were found to be 0.058 µg/L at the mid-inlet of the dam (D2), 0.021 µg/L at the dam outlet (D4), 0.098 µg/L at the mid-inlet of the dam (D2), 0.006 µg/L at the mid-outlet of the dam (D3), 0.018 µg/L at the dam inlet (D1) and 0.019 µg/L at the mid-outlet of the dam, respectively. The concentrations of the detected PAHs were generally lower than the stipulated SANS 241, USEPA and WHO acceptable limits in drinking water in all selected sampling points. However, their total concentration

may raise a concern as they sum up to a total concentration higher than the acceptable limit in drinking water.

**Table 1.6:** The concentration of the PAHs ( $\mu\text{g/L}$ ) in Nandoni Dam water treatment plant raw and treated water for water samples collected in spring, summer 2016 and autumn, winter 2017 where D1, D2, D3, D4, WTP TW, and WTP RW were the dam-inlet, mid-dam inlet, mid-dam exit, dam exit, water treatment plant (WTP) treated and raw water respectively.

Sampling point	Sampling season	Acenaphthene	Benz(a)anthracene	Benzo(a)pyrene	Naphthalene	Pyrene
D1	Spring	0.008	0.001	0.008	0.018	0.075
	Summer	0.006	0.003	0.007	0.014	0.061
	Autumn	0.009	0.004	0.009	0.019	0.089
	Winter	0.014	0.002	0.003	0.011	0.091
D2	Spring	0.005	0.005	0.012	0.058	0.048
	Summer	0.007	0.007	0.011	0.035	0.067
	Autumn	0.008	0.006	0.018	0.046	0.098
	Winter	0.002	0.008	0.009	0.015	0.047
D3	Spring	0.011	0.006	0.019	0.025	0.071
	Summer	0.005	0.004	0.013	0.034	0.096
	Autumn	0.004	0.009	0.016	0.019	0.043
	Winter	0.001	0.007	0.015	0.048	0.055
D4	Spring	0.018	0.001	0.004	0.018	0.078
	Summer	0.013	0.001	0.012	0.046	0.066
	Autumn	0.021	0.001	0.016	0.051	0.074
	Winter	0.015	0.001	0.011	0.046	0.087
WTP RW	Spring	0.015	0.000	0.002	0.031	0.058
	Summer	0.013	0.000	0.003	0.045	0.064
	Autumn	0.019	0.001	0.002	0.018	0.083
	Winter	0.009	0.001	0.003	0.024	0.076
WTP TW	Spring	0.007	BDL	0.001	0.013	0.068
	Summer	0.009	BDL	0.001	0.011	0.029
	Autumn	0.012	BDL	0.001	0.009	0.062
	Winter	0.007	BDL	0.001	0.020	0.038

BDL = below detection limit

According to the latest Blue Drop statistics (2010) of Thulamela Local Municipality in Vhembe District, the Blue Drop scores showed that there is a need for urgent attention towards purification and supply of drinking water in the area (**Table 1.8**) (91). The Blue Drop Certification Programme is an incentive-based regulatory programme for all drinking water treatment plants in South Africa. This innovative programme was introduced by the Department of Water Affairs with the core objective of safeguarding the tap water quality management. Furthermore, this programme also regulates the wastewater treatment plants owing to the possibility of this plants discharging the water into the rivers and subsequently contaminate the potable water in Nandoni Dam which is not adequately purified for drinking purposes.

The information given in **Table 1.7** clearly indicates that, in 2010, the water treatment plants in the above-mentioned municipality were compliant with regards to microbial and chemical water quality. The major problems relate to the water safety plan, process control and maintenance, efficiency of monitoring programme, credibility of sample analysis, failure response management and publication of performance. Although, these Blue Drop statistics demonstrated that the plants complied with water quality, the residents continued complaining about the supply of salty water.

**Table 1.7:** Water services Blue Drop Performance (2010) of Thulamela Local Municipality in the Vhembe District Municipality in Limpopo, South Africa (91).

Performance area	Lwamondo, 7 small villages Thulamela LM	Makonde, 4 small villages Thulamela LM	Dzingahe Thulamela LM	Khuvvi 5 small villages Thulamela LM
Water safety plan	F	F	F	F
Process control & maintenance competency	D	D	D	D
Efficiency of Monitoring Programme	F	F	F	F
Credibility of Sample Analysis	F	F	F	F
Data Submission to DWA	A	A	A	A
Compliance with Nat. Standard	A	C	C	C
Failure Response Management	E	E	E	E
Publication of Performance	G	G	E	E
Efficacy of Asset Management	D	D	D	C
Microbial DWQ Compliance with National Standard	99.99% 12 months data	98.27%* 12 months data	98.27%* 12 months data	98.27%* 12 months data
Chemical DWQ Compliance with National Standard	99.99% 12 months data	99.00%* 12 months data	99.00%* 12 months data	99.00%* 12 months data
<b>Blue Drop Score (2010)</b>	56.00%	44.00%	44.00%	44.00%
<b>Trend</b>	↑	↑	↓	↑
<b>Blue Drop Score (2009)</b>	<i>Not assessed</i>	<i>Not assessed</i>	<i>Not assessed</i>	<i>Not assessed</i>

A = excellent situation, B = good status, C = moderate performance, D = promising performance, E = poor performance, F and G = critical state needing attention.

In summary, the Nandoni Dam which supplies water to a wide range of communities in the Limpopo Province not only requires ongoing monitoring, evaluation and advanced water purification technologies but also engineering, economic, legal, ecological and social aspects in order to manage it in a holistic way. Based on the results of the water quality assessment and the latest Blue Drop Statistics, it is recommended that the various activities happening around the

dam be monitored in order to determine and implement control measures that could prevent contamination of the water in the dam. Moreover, cost-effective water separation processes such as membrane distillation (MD) could be employed as an additional step in existing water treatment plants in order to remove all salts present in the drinking water. Membrane designs and modifications are required for a sustainable water desalination process.

#### **1.4 Aim and objectives**

The aim of this study was to develop an integrated antifouling membrane distillation (MD) membranes for desalination of brackish/saline water. This was achieved through the following objectives:

- (i) Synthesis and characterization of polyethyleneimine (PEI)-functionalised polyacrylonitrile (PAN) nanofibre materials using an electrospinning technique. The PEI-PAN nanofibres were used a pre-treatment step for the removal of potential foulants in simulated and real brackish water.
- (ii) Adsorption of model organic fouling compounds (*e.g.*, phenols) using the PEI-PAN nanofibre materials. The determination of a potential scenario for pre-treatment capability prior to purification of real brackish water samples was established.
- (iii) Synthesis and characterization of novel electrospun super-hydrophobic polyvinylidene fluoride (PVDF) nanofibre membranes modified with organically-functionalized silica nanoparticles (SiO<sub>2</sub>NPs) and a thin layer of PVDF containing silver nanoparticles (AgNPs) and multiwalled carbon nanotubes (MWCNTs). The design of these architected MD membranes was to develop membranes that possess superhydrophobic properties but with resistance to fouling and flux decay.

- (iv) Performance testing of the synthesized pre-treatment nanofibre materials and modified PDVF membranes in a direct contact membrane distillation (DCMD) setup. Real water samples collected from an estuary in Belgium and the Nandoni Dam in South Africa were used.

## 1.5 Research flow chart

**Figure 1.4** shows a flow chart summarising a layout of the research conducted and reported in this thesis.

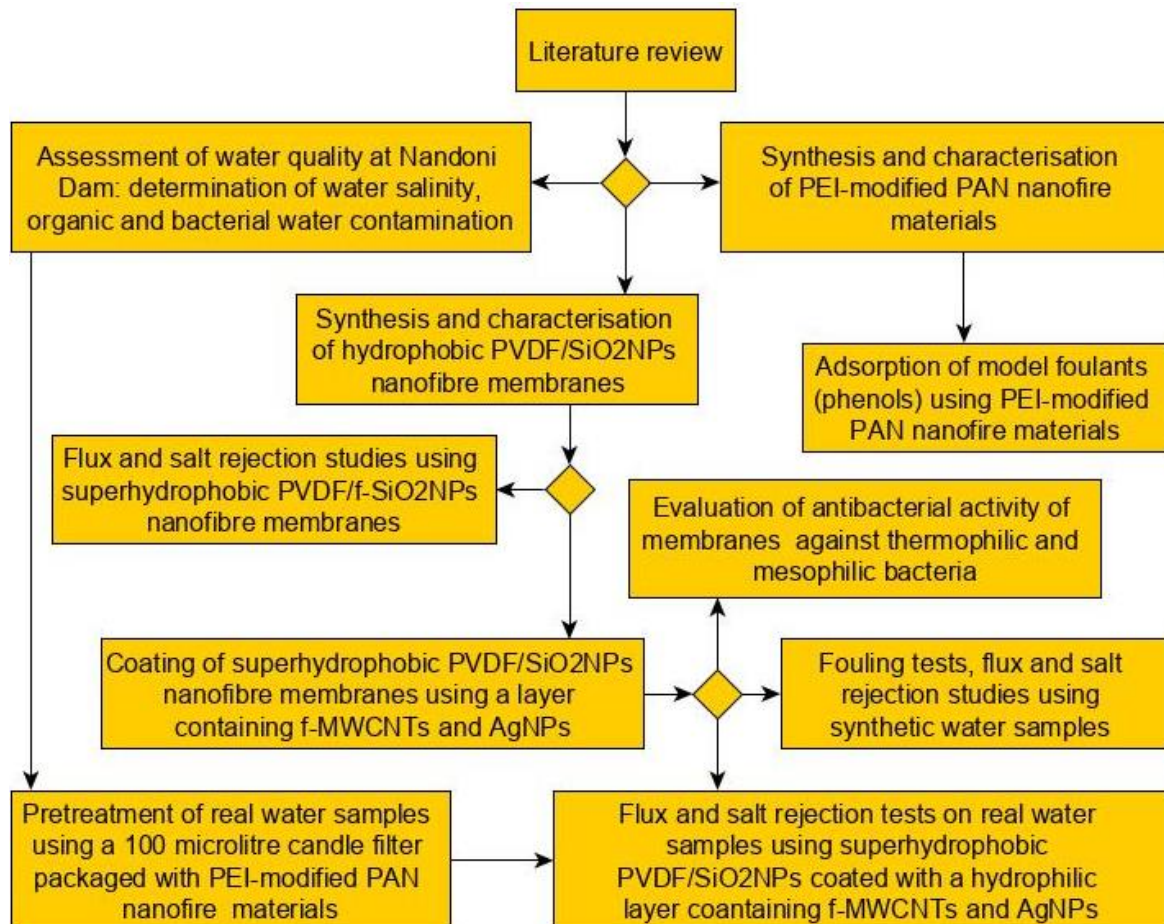


**Figure 1.4:** A flow chart summarising the roadmap of the research.

## 1.6 Thesis outline

This section provides a brief overview of the thesis with a summary of what is entailed in each chapter.

### **Chapter 1**

This chapter provides the information about the background of the study, the problems statement, results of water quality analysis, aim and objectives and a research chart outlining the organisation of the thesis. The problem statement involves a detailed description of the water challenges faced by residents in the study area and the problems associated with a proposed suitable solution i.e. MD membrane technology. The water analysis preliminary results were published in two journals, i.e. *Water* (MDPI Journal) and in the *Journal of Physics and Chemistry of the Earth*.

### **Chapter 2**

This chapter gives an extensive review of the literature relevant to this study. A detailed review of the literature on membrane distillation (MD) for water purification is presented. Methods used to synthesise the membranes including PVDF membranes are discussed. The use of nanoparticles for enhancement of membrane hydrophobicity and the use of nanofibre adsorbents for removal of organic compounds is also discussed. Finally, the various materials for pretreatment of environmental water samples prior to MD treatment are reviewed. Parts of this work have been published in a review paper in the *Journal of Chemical Technology and Biotechnology* and two book chapters in *Advanced Nanomaterials for Membrane Synthesis and its Applications* and *New Polymer Nanocomposites for Environmental Remediation*.

### **Chapter 3**

Adsorption of phenolic compounds on PEI-modified PAN nanofibres was investigated and presented in this chapter. This was done as preliminary results revealed their presence in the characterised water sources. These compounds possess hydrophobic benzene rings induced by the non-polar C-C and C-H bonds in the structure. The hydrophobic nature of this ring is believed to interact with the hydrophobic surface of the membrane while the polar end is exposed to the water, resulting in wetting. Besides their known toxicity, their removal from the water sources prior to MD purification was therefore necessary. A Manuscript forming part of this work has been published in the *Journal of Environmental Chemical Engineering*.

### **Chapter 4**

The synthesis and characterisation of the PVDF nanofibre membranes is discussed in detail in this chapter. The membranes were modified with SiO<sub>2</sub>NPs for hydrophobicity enhancement. Three silane reagents that were used to functionalise the SiO<sub>2</sub>NPs were reported for the first time in membrane distillation. Notably, silane reagents were octadecyltrimethoxysilane (OTMS), N-octadecyltrichlorosilane (ODTS), and chlorodimethyl-octadecyl silane (Cl-DMOS). These silane reagents significantly improved membrane contact angles, rendering them superhydrophobic (*i.e.*, hydrophobic with contact angles  $\geq 150^\circ$ ). PVDF nanofibre membranes not embedded with SiO<sub>2</sub>NPs were termed as M1; while PVDF nanofibre membranes modified with pristine SiO<sub>2</sub>NPs were termed as M2. Similarly, PVDF nanofibre membranes decorated with ODTS-SiO<sub>2</sub>NPs, OTMS-SiO<sub>2</sub>NPs, and Cl-DMOS-SiO<sub>2</sub>NPs were termed as M3, M4, and M5. The highest contact angle was observed on OTMS-functionalised SiO<sub>2</sub>NPs modified nanofibre membranes ( $162.6 \pm 1.8^\circ$ ). Therefore, membranes termed f-SiO<sub>2</sub>NPs-modified nanofibre membranes in the subsequent chapters refers to OTMS-functionalised SiO<sub>2</sub>NPs modified nanofibre membranes. The superhydrophobic membranes demonstrated high salt rejections and high fluxes in direct contact membrane distillation. This work been published in the *Journal Chemical Technology and Biotechnology*.

## **Chapter 5**

The antimicrobial properties of coated PVDF nanofibre membranes for mesophilic and thermophilic bacteria were determined and are discussed in detail in this chapter. The coating layer consisted of f-MWCNTs and AgNPs. Although the operation conditions of MD technology, which include high operating temperatures and saline water solutions are believed to control the growth of bacteria, biofouling in MD is still observed due to the presence of thermophilic bacteria. This chapter provides insights on the behaviour of the coated membranes towards limiting membrane biofouling in MD. This work has been published in the *New Journal of Chemistry*.

## **Chapter 6**

This chapter presents the characterisation of PVDF nanofibre membranes and their MD application in removal of salts from water. The superhydrophobic nanofibre membranes were coated with a thin layer containing f-MWCNTs and AgNPs to mitigate fouling. The superhydrophobic layer comprised of a PVDF nanofibre membrane embedded with f-SiO<sub>2</sub>NPs, for exclusively allowing the transport of water vapour. The hydrophilic layer consisted of a PVDF membrane embedded with carboxylated multi-walled carbon nanotubes (f-MWCNTs) and silver nanoparticles (AgNPs), to provide hydrophilic and biocidal (*i.e.*, biofouling control) properties, respectively. The resulting membranes were tested for their fouling resistance towards bovine serum albumin (BSA). This work has been published in *Colloids and Surfaces A; Physicochemical and Engineering Aspects*.

## **Chapter 7**

Biological, organic and colloidal fouling of the PVDF membranes were carried out in MD tests and reported in this chapter. The feed stream contained these model foulants: thermophilic bacteria present in the discharged effluent of a thermophilic bacteria bioreactor, as well as sodium alginate and colloidal silica. The effect of these model foulants towards water flux and salt was evaluated. Furthermore, the interaction between the membranes and the foulants was

investigated. A manuscript forming part of this work has been submitted to *Journal of Industrial and Engineering Chemistry* for possible publication.

### **Chapter 8**

The PEI-modified PAN nanofibre integrated MD equipped with PVDF membranes was tested on purification of environmental brackish water samples and presented in this chapter. PEI-modified PAN nanofibres were packed in a candle filter and used to filter the water samples prior to MD experiments. The water samples were collected from an estuary in Belgium and the Nandoni Dam. These water samples collected were a representative of brackish water to be tested in MD. The water samples were characterised prior to MD purification tests. Hydrophilic coating of the superhydrophobic membranes results to a resistance to flux and salt rejection decay, demonstrating a promising approach for reduction of membrane fouling in MD. The main difference between Chapter 7, 8 and 9 is that, synthetic water samples were used in chapter 7 and 8 while environmental water samples were used in chapter 9. This work has been published in *Separation and Purification Technology*.

### **Chapter 9**

This chapter sums up the conclusions made from the individual chapters. It also presents some recommendations made from the reported research.

## CHAPTER 2

# LITERATURE REVIEW: MEMBRANE DISTILLATION MEMBRANES FOR WATER DESALINATION

---

### 2.1 Introduction

Membrane technology has been extensively used as a separation technique to reduce the salinity of water from different sources. Additionally, membrane technology offers a relatively high rejection efficiency for particulate and dissolved organic matter from water (27). Membrane processes widely used in water desalination include reverse osmosis (RO) and nanofiltration (NF) (28). These pressure-driven processes operate at high energy requirements and operational/capital costs (29). Although NF is less energetically demanding relative to RO, this membrane process has low rejection efficiencies towards sodium and chloride (i.e., notwithstanding the fact that these monovalent ions are the main constituents of saline water) (24). Remarkably, Membrane Distillation (MD) process has been found to counteract the operational challenges of RO and NF membrane technologies. Also, due to its probable use of low grade or waste energy, MD would be a potential economically feasible technique comparable to pressure-driven membrane processes (92). The use of MD in water desalination and wastewater treatment has recently attracted the attention of numerous researchers (37,93–97). MD is a thermally-driven process in which water vapour molecules pass through a porous hydrophobic membrane. This process is enhanced by a vapour pressure induced by a temperature difference across the membrane (24), thus offering the possibility of solution saturation at the feed side without causing a significant flux decline (98). The heat energy required in the MD separation process can be generated by solar energy, geothermal energy, or waste-grade energy (99). In theory, the membranes used in MD processes should strictly allow the passage of vapours and retain non-volatile substances. Therefore, the filtrate would be close to 100% pure and devoid from solids or non-volatile contaminants (100). The performance of MD is however severely affected

by two key factors: (i) wettability as a result of condensation of water vapour inside the pores of the membrane; and (ii) fouling due to the accumulation of biofilm, organic, inorganic, and colloidal substances on the surface or in the internal pore structure of the membrane (24). These two limiting factors restrict the choice of suitable polymers for the synthesis of MD membranes. Briefly, hydrophobic (i.e. with contact angle  $> 90^\circ$  or water-hating) polymers promote hydrophobic-hydrophobic interactions between hydrophobic pollutants and the membrane surface; thus, causing blocking of the pores of the membranes and membrane fouling (57). On the other hand, hydrophilic polymers enhance the wettability of the membranes; consequently, affecting the diffusion of water vapour through the membrane and compromising its rejection efficiency (27). As a result, numerous membrane modification studies have been conducted to concurrently overcome the fouling and wettability challenges associated with MD membranes (70,101). Briefly, flat sheets, nanofibres, and hollow fibre membranes characterised by super-hydrophobicity (i.e. membranes with contact angles  $> 150^\circ$ ) have been synthesised and tested in MD applications (38–40,95,102). These superhydrophobic membranes were reported to be resistant towards wetting by process liquids. Additionally, the surface modification of MD membranes by the incorporation of nanoparticles (NPs) to further enhance their physicochemical properties has been extensively investigated (37,38,40,102–104). Several configurations and strategies for membrane distillation have been also developed over the past few decades. Even though, MD is a promising technology widely tested at a laboratory-scale, to date, its industrial implementation has been limited. Not only membrane wetting and fouling limited applications but also high CAPEX due to difficult fabrication of membrane modules.

This literature review provides a critical and comprehensive review of the state-of-knowledge regarding the MD process with insights toward better understanding its shortcomings and limitations. Additionally, recent advancements in membrane modification by the embedment of nanoparticles to enhance fouling resistance and address wettability are emphasized, and areas for further work are discussed. Furthermore, fabrication of ultraporous nanofibre membranes is included. Likewise, environmental sustainability of MD is also discussed to elucidate

promising approaches for a future and successful implementation of MD at an industrial scale for the desalination of brackish water/seawater at high recovery rates. Finally, adsorption of probable foulants using nanofibre adsorbents as possible pretreatment materials is also briefly discussed.

## 2.2 MD membrane synthesis methods

Membrane Distillation (MD) membranes are commonly prepared using solution-casting-phase inversion and nanofibre-electrospinning methods. In the casting process, a solution of a specific material is placed on a substrate to adopt the shape of the casting material and subsequently allowed to solidify under suitable conditions (105). **Figure 2.1** shows an illustration of a membrane casting procedure using a casting knife. In this process, the PVDF solution is cast on a non-woven fabric to adopt its flat shape. The membrane is then coagulated in a water bath and peeled off from the non-woven fabric. PVDF nanofibre membrane can be spin-coated using  $\text{TiO}_2$  nanoparticles to enhance the superhydrophobicity of the membrane (106). Other polymers such as PTFE and PP have been used for synthesis of MD membranes (107,108). However, PVDF has been extensively studied compared to PTFE and PP on synthesis of electrospun nanofibre membranes. PVDF is a semi-crystalline polymer mainly consisting of 59.4 wt.% fluorine and 3 wt.% hydrogen (109), and produced by free radical polymerisation leading to the formation of the  $-\text{CH}_2-\text{CF}_2-$  repeating units (110). The arrangements of the  $\text{CH}_2$  and  $\text{CF}_2$  bonds within the molecular chains result in the formation of a specific crystal structure leading to the formation of a polymer with unique properties. The PVDF chains can crystallise into three distinct phases ( $\alpha$ ,  $\beta$ ,  $\gamma$ ) depending on the fabrication technique (111). Owing to the high electrical dipole moment of these crystalline phases (112), PVDF dissolves in varied solvents (e.g., dimethyl formamide, dimethyl sulfoxide, N-methylpyrrolidone, or dimethylacetamide) (113); thus, making possible the versatile synthesis of flat-sheet, hollow-fibre, and nanofibre membranes.

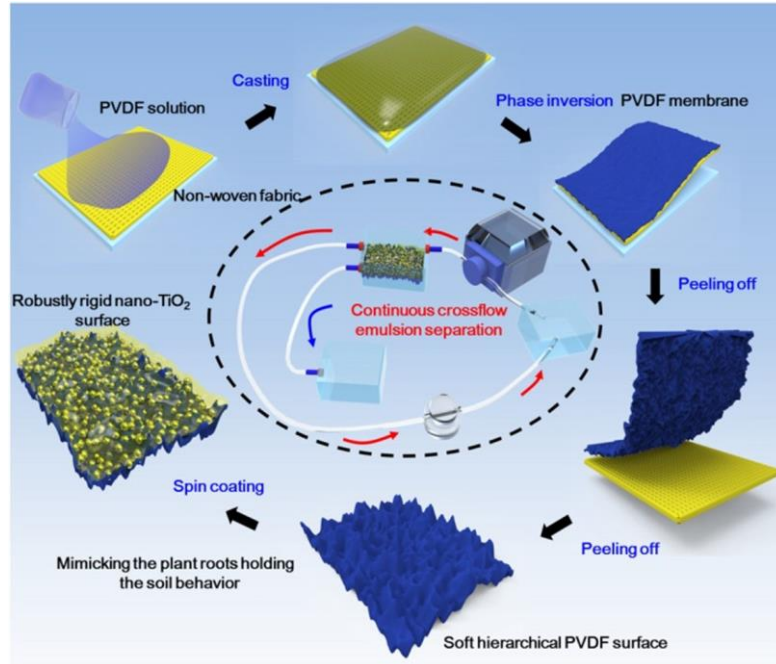


**Figure 2.1:** Casting of polymer films to prepare nano-TiO<sub>2</sub> surface coated membranes for membrane distillation (106).

The most commonly studied methods for the synthesis of MD membranes are phase inversion and electrospinning methods, involving interfacial polymerisation, graft polymerisation, and dip coating as membrane modification processes.

### 2.2.1 Phase inversion

Phase inversion is a de-mixing process whereby a homogeneous polymer solution is transformed to a solid material under controlled conditions (see **Figure 2.2**). This transformation process can be performed using the following techniques (29):

- (i) immersion precipitation, where the polymer solution is immersed in a coagulation bath to allow the exchange of solvents to occur;
- (ii) thermally induced phase separation, in which the de-mixing process occurs by subjecting the membrane to high temperatures; and



- (iii) evaporation-induced phase separation, which occurs through the evaporation of the volatile solvent used to prepare the polymer solution of interest.

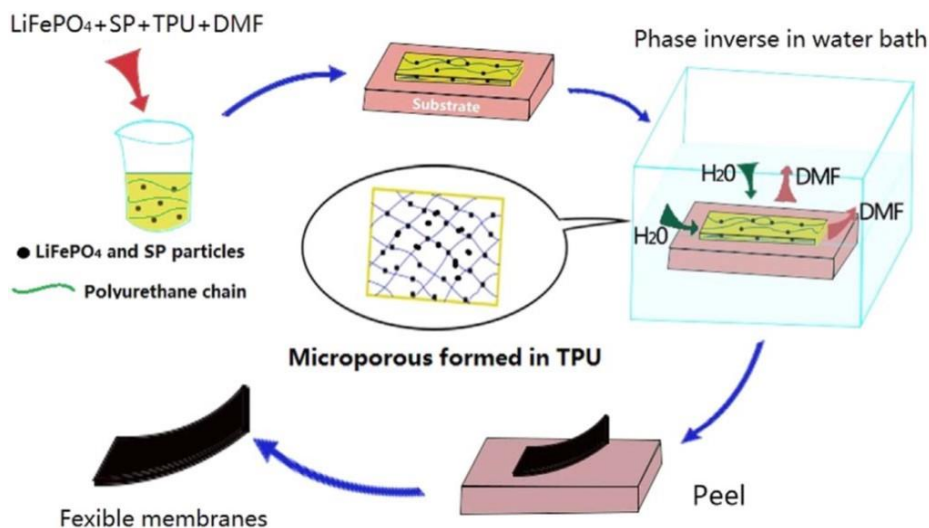


**Figure 2.2:** Phase inversion formation of membranes (114).

The phase inversion method can be applied in the synthesis of flat sheet and hollow fibre membranes. For the preparation of flat sheet membranes, the polymer solution is casted on a flat support material (e.g., glass) and subsequently immersed in a coagulating bath. The structural properties of the resulting flat sheet membrane depend on the rates of exchange of the solvent and non-solvent (115). An example of immersion precipitation phase inversion of super phosphorus (SP) and lithium iron phosphate ( $\text{LiFePO}_4$ ) nanoparticles-modified thermoplastic polyurethane (TPU) is illustrated on **Figure 2.2**. In this process, a solution of TPU and SP/ $\text{LiFePO}_4$  is casted on a flat polyfluorotetraethylene (PFTE) substrate using a casting knife. The casted solution on the substrate is placed in distilled water (coagulation bath at  $25^\circ\text{C}$ ) to remove the solvent from the liquid-solution (de-mixing process) for 4 h. The solidified membrane is peeled-off from the substrate and dried at  $100^\circ\text{C}$  for 2 h (114).

The phase inversion preparation of hollow fibre membranes involves the extrusion of the polymer solution, coagulation and sintering of the coagulated hollow fibre

(116). An illustration of the phase inversion preparation of hollow fibre membranes is provided in **Figure 2.3**. The nanocomposite membrane is prepared through a solvent transfer-induced phase separation, followed by photopolymerisation (117). Bicontinuous interfacially-jammed emulsions are used for the formation of nanoparticle-functionalised hollow fibre membranes. The ternary fluid is composed of SiO<sub>2</sub>NPs-doped monomers and the bore/sweeping fluid is water. The co-extrusion of these fluids results in the formation of hollow fibres (117). To ensure the formation of uniform hollow fibres, the nozzle of the sweeping fluid is centred, and its viscosity is adjusted by the addition of high-molecular-weight polyethylene glycol (1%). Photopolymerisation is induced by UV-light irradiation, resulting in hollow porous nanoparticle-modified membranes. The aligned hollow fibre membranes are collected in a water-filled rotating glass cylinder (117).

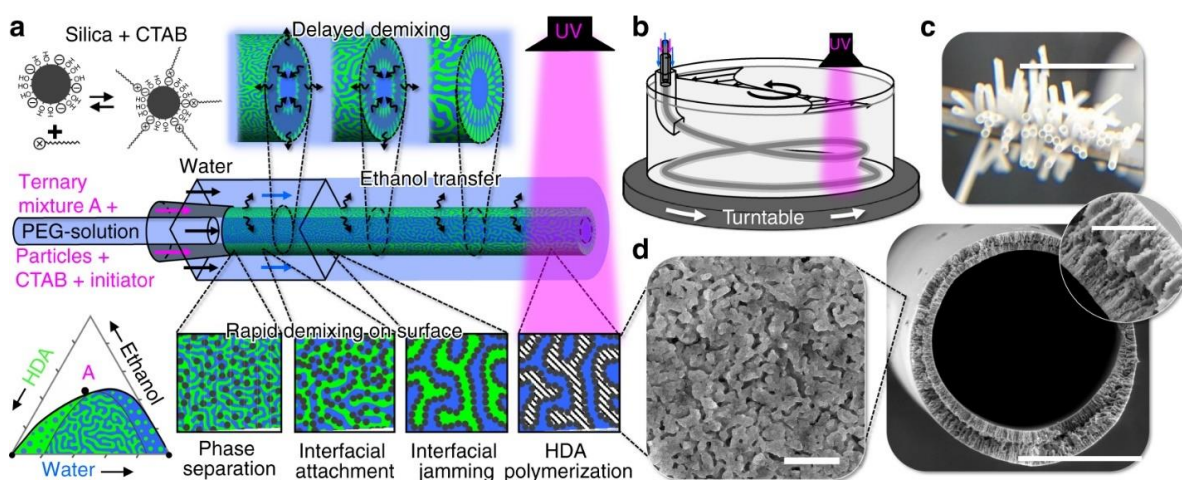


**Figure 2.3:**Preparation of a hollow fibre membrane embedded with SiO<sub>2</sub>NPs (117).

## 2.2.2 Electrospinning techniques

The electrospinning technique is a high voltage driven process in which the polymer solution becomes electrically charged and induces electrostatic repulsive forces when subjected to an electric field (see **Figure 2.4**). The polymer surface tension is broken by these forces; thus, leading to the stretching and thinning of the polymer jet (118). The electrospinning and electrospaying techniques take

place simultaneously under specific controlled conditions (119). Electrospinning occurs when entanglements and molecular cohesion of the polymer solution are not strong enough to sustain stream break-down (i.e., a process where a polymer solution is ejected from the capillary nozzle and drops as a result of jet breakage) during the ejection of the polymer solution. However, under favourable molecular cohesion conditions, the droplets form charged jets, which stretch due to electrostatic forces to synthesise uniform nanofibres (120). Simultaneous electrospinning and electrospinning can lead to the formation of beaded nanofibres as a result of stream break-down (121). Electrospinning has been successfully used for the preparation of nanofibre membranes suitable for membrane distillation. The synthesis of superhydrophobic PVDF nanofibre membranes has been achieved by the incorporation of multi-walled carbon nanotubes (MWCNTs), SiO<sub>2</sub>NPs, and TiO<sub>2</sub>NPs onto polymeric membranes (e.g., PVDF membranes) resulting in contact angles higher than 150° (37,122,123). These superhydrophobic membranes are resistant to wetting by the process liquids. Not only do these modified nanofibre membranes display high contact angles, they are also characterised by a mechanical strength high enough to sustain low pressures in MD (37,122,123). These nanofibre membranes have been successfully used in the production of potable water at fluxes between 28 – 42 L·m<sup>-2</sup>·h<sup>-1</sup> and rejection efficiencies of ~99.9%.

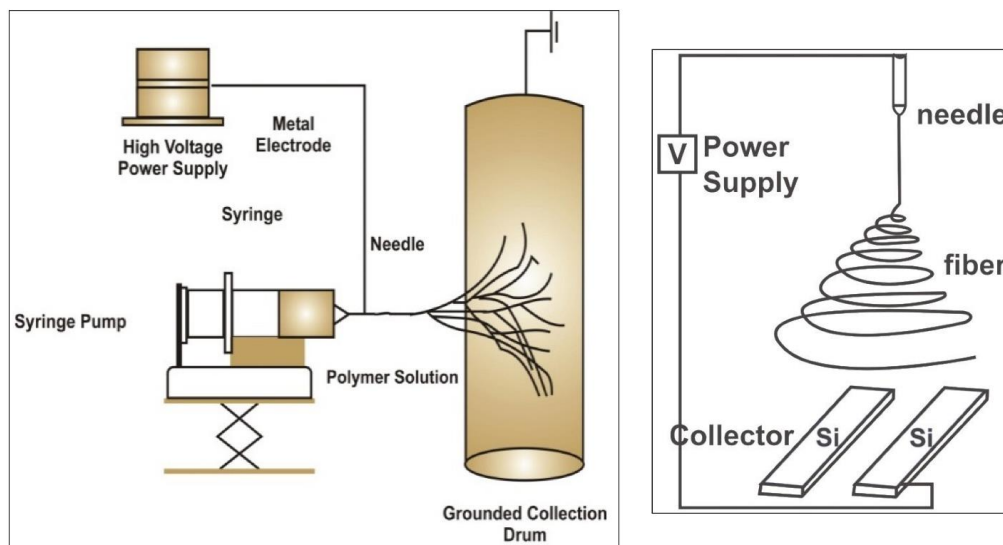


**Figure 2.4:** Schematic representation of an electrospinning process of nanofibre membranes (124).

### 2.3 MD membrane modification methods

Several methods are currently used for the modification of MD membranes. These include graft polymerisation, interfacial polymerisation, plasma polymerisation, and dip coating. Modification processes offer the possibility of synthesising membranes with the desired characteristics such as embedding of nanoparticles to enhance membrane hydrophobicity. The ultimate goals of membrane modifications are to attain wetting and fouling resistant membranes. A typical example is attainment of membrane superhydrophobicity to prevent membrane wetting. To achieve self-cleaning membrane (lotus effect), the contact angles of the membrane should be approximately  $180^\circ$  while hysteresis of contact angle (HCA) should be  $\leq 10^\circ$ . This goal has not been achieved in the current reported studies. Therefore, membrane modifications such as coating have been adopted to minimize membrane fouling. The effects of membrane modifications in MD are presented in **Table 2.1**.

#### 2.3.1 Graft polymerisation

In this method, monomers are chemically attached to the core polymer to enhance the properties and functionalities of the latter. The grafted polymer is

thermodynamically stable since the monomer is covalently bonded to the core polymer. Graft polymerisation is classified into three types: (i) grafting onto; (ii) grafting from; and (iii) grafting through. In grafting onto, the free radical active sites generated from the two polymers combine covalently to form a grafted polymer. In grafting from, the core polymer is initiated to form radicals, which subsequently react with the monomer to produce the desired graft polymer. In grafting through, the free radical active sites of the low-molecular-weight monomer reacts with the vinyl groups of the core polymer to form a graft polymer with well-defined side chains (125).

**Figure 2.5** presents a typical example of graft polymerisation process. Briefly, the polycarbonate membrane is treated with an argon plasma atmosphere and exposed to oxygen to promote the formation of hydroperoxide active radicals (126). These radicals enhance the formation of grafted membranes by initiating the graft polymerisation of the acrylic acid (126). This technique was adopted by Korolkov *et al.* (2018) (127) to synthesise triethoxyvinylsilane-grafted polyethylene terephthalate (PET) for enhancing membrane hydrophobicity. Acrylic acid (6%) is added to initiate the grafting process and the resultant membrane showed high flux with efficient salt removal from water on a direct contact membrane distillation mode (127).

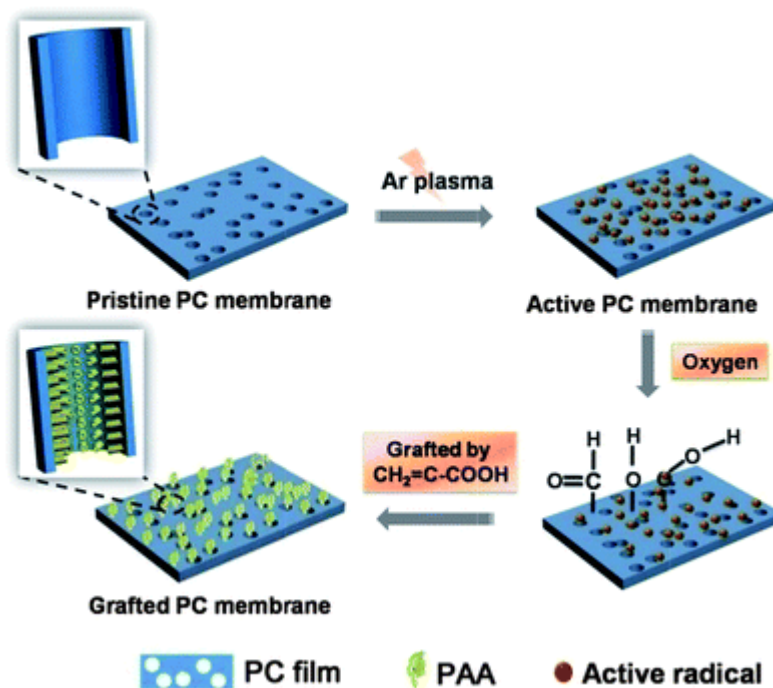


**Figure 2.5:** Schematic representation of graft polymerisation in membrane modification (126).

### 2.3.2 Plasma polymerisation

Plasma polymerisation (i.e., or Discharge polymerisation) is a modification method that activates gaseous or liquid monomers to initiate the polymerisation (128). The gas discharges that provides the activation energy are generated from the plasma source. This technique produces highly-branched and cross-linked polymers that react with solid surfaces. The formation of the branched polymers offers a great advantage by reducing several steps which are required in other modifying techniques such as grafting. Another key advantage of plasma polymerisation is its environmental friendliness (129). This technique has been used by Song and co-workers (2007) to increase the hydrophobicity of MD hollow fibre membranes (130). The coating thickness induced by plasma polymerisation is in the range of 1-2  $\mu\text{m}$ . This strongly bound modifying layer has shown a low impact on membrane porosity compared to other techniques (130,131).

### 2.3.3 Interfacial polymerisation

Interfacial polymerisation is a type of a step-growth reaction process in which polymerisation takes place at the boundary of the different polymers containing one monomer (**Figure 2.6**). Interfacial polymerisation reactions are mainly described by the reaction mechanisms proposed by Schotten-Baumann as described by Morgan (132). In this process, diacid chloride in the organic phase reacts with a monomer containing hydrogen atoms, which function as reaction centres or sites (132). This polymerisation reaction is not commonly reported on MD membranes due to difficulties it presents to get sufficient water flux (133). However, a range of interfacial polymerisation-modified polyamine membranes using a wide array of amines and acid chloride monomers were reviewed by Gohil and Ray (134). Examples of such membranes include the thin film nano-enhanced membranes for application in water purification. Interfacial polymerisation is affected by humidity, temperature, and purity of the reactants (135).

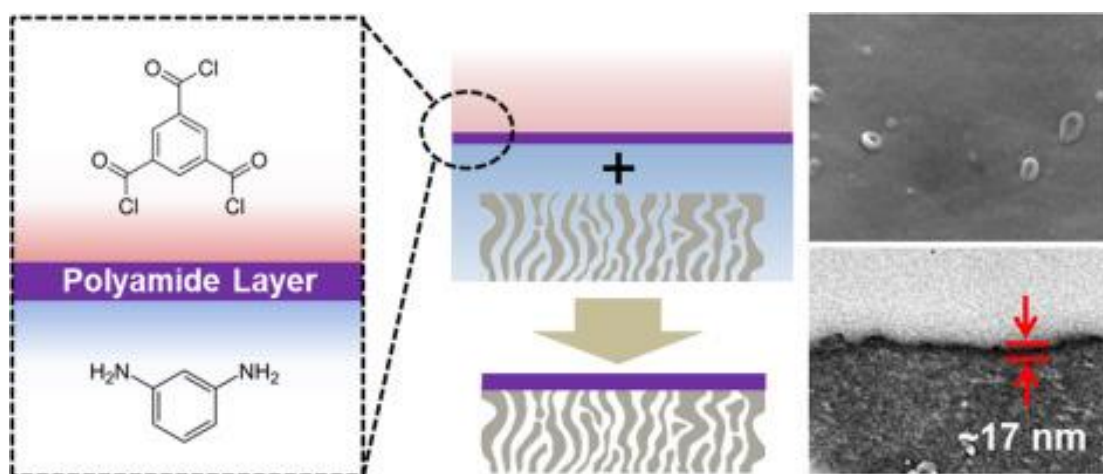


**Figure 2.6:** Schematic representation of interfacial polymerisation during membrane modification (133).

### 2.3.4 Dip coating

In dip coating, a thin film is deposited on the surface of the membrane using the polymer-solution of interest. Dip-coating processes are classified as: (i) immersion;

(ii) start-up; (iii) deposition; (vi) evaporation; and (v) drainage (**Figure 2.7**). The coating material thickness, membrane pore size, and membrane structural integrity are determined by the concentration of the dipping polymer, dipping time, and concentration of the cross-linking agent (136). Chen *et al.* (137) explored graft polymerisation of poly(N-(3-sulfopropyl)-N-(methacryloxyethyl)-N,N-dimethylammonium betaine) poly(SBMA) on a polystyrene (PS) membrane using casting and dip coating. The poly(SBMA) solution was introduced to the PS membrane through dipping as well as casting. The polymerisation reaction was subsequently exposed to UV-irradiation to ensure the formation of a covalent bond between the PS membrane and the poly(SBMA) (137).

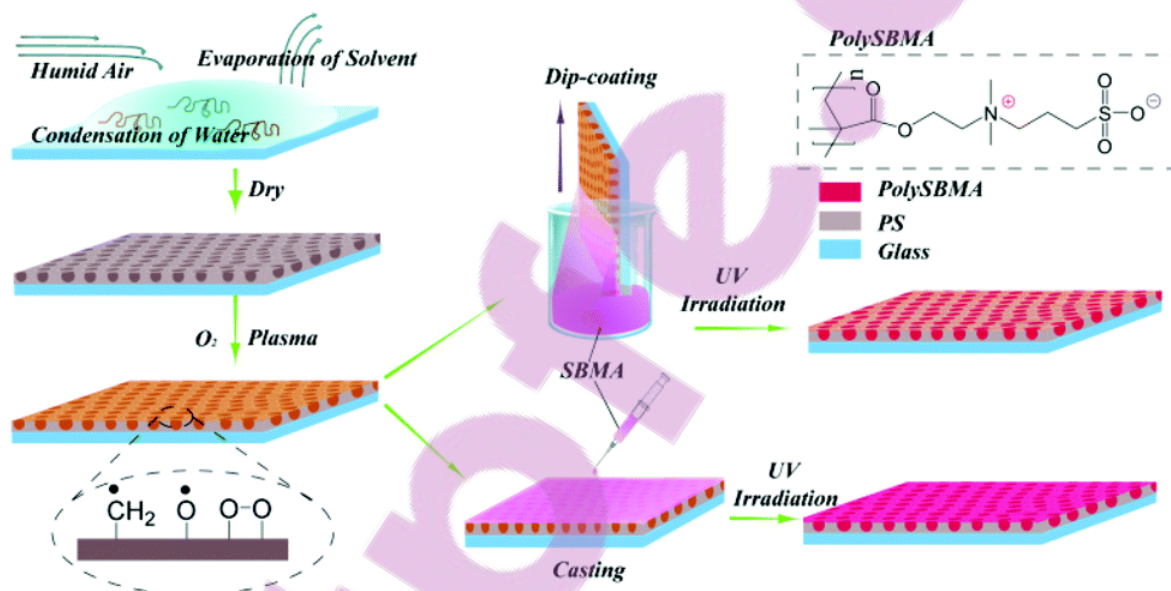


**Figure 2.7:** Dip coating in membrane modification (137).

The impact of the MD membrane modifications using different methods w

**Table 2.1:** Effect of membrane modification towards water flux and salt rejection in MD.

Membrane	Modification	Flux (LMH)		Rejection (%)	Time (h)	Ref.
		Initial	Final			
PVDF nanofibre	Plasma induced coating of PEG	6.1	5.8	99	24	(138)
SiNPs PVDF	Chitosan dip coating	Normalized flux with no decay		-	36	(94)
PTFE	-	5.2	4.8		20	(139)
zirconia supported alumina membrane	Fluoroalkylsilane grafting	Flux with no decay		99.9	-	(140)

## 2.4 The use of nanoparticles in membrane modification

Extensive research involving nanoparticle modification of MD membranes is currently being conducted to overcome the challenges associated with membrane flux, fouling, wetting, and porosity (38,39,141–143). Nanoparticles (NPs) are particulate materials with at least one dimension smaller than 100 nm but larger than atoms and molecules (144). Nanoparticles include particulate metals such as silver (Ag), silica (SiO<sub>2</sub>), and titania (TiO<sub>2</sub>). Silver nanoparticles (AgNPs) are able to penetrate through the cell walls of microorganisms, interact with their thiol groups and nucleic acids and bind their enzymes, which leads to the destruction of their cell envelopes and eventual growth inhibition (145–147). Due to their toxicity towards several microorganisms (e.g., bacteria, viruses, and fungi), AgNPs have been used in many applications including water filtration, biomedical products, clothing, and textiles (148).

In water filtration systems, AgNPs act as a preventive measure to reduce the formation of biofilms on the surface or inside the pores of the membrane, thus making the membrane less susceptible to biofouling (149,150). However, when the NPs are deposited onto the membranes at high concentrations, they block the pores of the membranes and consequently compromise the water flux (68). The MD membrane fouling studies in the literature are dominated by organic fouling and inorganic fouling (also referred to as scaling) (70,151). Although only a few studies on biofouling of MD membranes have been reported in the literature, biofilm formation has been recorded to significantly decrease the efficiency of MD systems (66). Zodrow *et al.* (2014) (66) have demonstrated that the growth of bacteria in MD is hindered by high operating temperatures ( $\geq 60^\circ$ ) and high water salinity (66). Nevertheless, thermophilic effluents (i.e., mostly discharging to water bodies) are characterised by high concentrations of thermophilic bacteria used for the removal of biological oxygen demand (BOD) (152). These thermophilic bacteria (i.e., mainly found in marine environments, hot springs, hydrothermal vents, and open surface waters) thrive in saline waters, high temperatures ( $\geq 80^\circ$ ) and could potentially induce membrane fouling in MD (153). There is no single

study reporting the use of NPs for membrane modification in MD to hinder the growth of thermophilic bacteria.

At different sizes and degree of crystallinity, TiO<sub>2</sub>NPs exhibit different affinities towards water molecules (154). Small-sized TiO<sub>2</sub>NPs have also shown high hydrophilic properties as anatase (154). Therefore, these properties can be used to render hydrophilicity to the hydrophobic surface of MD membranes for decreasing the surface adsorption of hydrophobic organic foulants. Briefly, unfavourable polar or Lewis acid-base interactions would occur between hydrophilic TiO<sub>2</sub>NPs and hydrophobic moieties on foulants. Also, a tightly-bound layer of water molecules on TiO<sub>2</sub>NPs would prevent interactions with foulants (155).

To mitigate wetting challenges associated with MD membranes, SiO<sub>2</sub>NPs have been extensively used to enhance the hydrophobicity of PVDF membranes by rendering their surfaces superhydrophobic with contact angles higher than 150° (38,103). Khumalo *et al* (2019) tested organic modification of SiO<sub>2</sub>NPs using hexamethyldisilazane (HDMS) and subsequent embedment in PVDF flat sheet membranes (107,108). The resulting membranes were characterised by hydrophobic properties (contact angle ≈115°) which enhanced MD performance for the recovery of hydrolysed urine. Silane reagents such as octadecyltrimethoxysilane (OTMS), N-octadecyltrichlorosilane (ODTS), chloro(dimethyl)-octadecylsilane (Cl-DMOS) could be used to further enhance membrane superhydrophobicity. The OTMS molecule is characterised by a long aliphatic carbon chain (CH<sub>3</sub>(CH<sub>2</sub>)<sub>17</sub>- where the anchor group is (-Si-OCH<sub>3</sub>)<sub>3</sub>. Furthermore, the anchor groups on ODTS and Cl-DMOS are (-Si-ClCH<sub>2</sub>)<sub>3</sub> and (-Si-Cl<sub>3</sub>)<sub>3</sub> respectively (156–162). The anchor groups on OTMS are more hydrophobic due to the presence of bulky nonpolar CH<sub>3</sub> groups. The presence of strong electron-withdrawing atoms such as Cl and O in Cl-DMOS and ODTS cause an uneven distribution of electrons, which could subsequently induce a minimal polarity on one end of the molecule, and slightly reduce its hydrophobicity. This differences in the hydrophobic nature of the SiO<sub>2</sub>NPs give rise to different performances (i.e. slight differences in water fluxes) in MD membranes (163,164).

Membranes prepared in alcohol as a non-solvent during the inversion phase also display intrinsic properties, which result in the formation of superhydrophobic membranes (38). These membranes are characterised by improved water fluxes as well as high separation efficiencies (38,39). Wang and co-workers (94) synthesised hydrophobic membranes using SiO<sub>2</sub>NPs, chitosan hydrogel, and fluoropolymer (i.e., the latter was added to confer amphiphilic properties to these MD membranes) for the selective separation of oil from water (94). This membrane exhibited high oil-water separation efficiencies compared to commercial hydrophobic PVDF membranes (94).

Not only do superhydrophobic characteristics improve the anti-wetting capabilities of membranes, they also enhance self-cleaning properties by a process called the lotus effect as was earlier explained (165). However, for membranes to attain this lotus effect (i.e., a property similar to that of a lotus leaf), they should be characterised by high contact angles close to 180° and significantly low sliding angle, i.e., the smallest angle that would allow an easy roll-off of water droplets and sufficient removal of dirt from materials (166,167). This lotus effect assists in the generation of a slip flow as well as in the reduction of drag forces, and thus would be useful in membrane distillation of seawater (168). Rezaei and co-workers grafted superhydrophobic SiO<sub>2</sub>NPs on the surface of PVDF membranes to mimic the effect of a lotus leaf on liquid repellent (169). The SiO<sub>2</sub>NPs were characterised by water-repellent methyl functional groups which subsequently improved the contact angles of the membranes from 139° to 154°. The water-membrane contact angle and roughness observed in this study was similar to those shown by many other previous studies reporting a decrease in membrane wetting and an improvement in membrane fouling resistance (37–39,103,169). In addition to several studies reporting the use of SiO<sub>2</sub>NPs and TiO<sub>2</sub>NPs for enhancing membrane hydrophobicity (37,40,103,169,170), graphene and carbon nanotubes (CNTs) have also been observed to render MD membranes superhydrophobic (122,171). Graphene and carbon nanotubes are characterised by benzene rings and sp<sup>2</sup> carbon atoms arranged hexagonally. This arrangement give rise to an

aromatic ring that is composed of relatively non-polar C-C and C-H bonds which are not solvated by water molecules (172). Therefore, graphene and carbon nanotubes are hydrophobic in nature unless they are functionalised with hydrophilic moieties such as carboxylic functional groups and thus enhance membrane resistance to wetting (173). Not only do graphene and carbon nanotubes considerably enhance the anti-wetting membrane properties, they also improve their mechanical strengths, which is essential in MD operations (122,171). Due to the incorporation of oxidised graphene and carbon nanotubes, the membrane hydrophobicity revert to hydrophilicity, thus, assisting in the prevention of membrane fouling (174,175). A summary of nanoparticle-enhanced membranes for MD processes is presented in **Table 2.2**.

The low rate of water production is another setback associated with membrane distillation, which could be mitigated by the use of nanofibre membranes. Notably, high fluxes have been recorded due to the high porosities of nanofibre membranes (176); which are also characterised by high surface roughness that allows air entrapment in the membrane surface roughness (171). This entrapped air promotes the repellence of water droplets, thus further improving membrane hydrophobicity (177).

**Table 2.2:** Summary of nanoparticle-embedded membranes prepared using different methods and their potential impact on MD.

Method	Polymer	Nanoparticle	$\Delta T$ (°C)	Impact	Ref.
Electrospinning	PVDF	CNTs	40	Improved flux (24-29 L·m <sup>-2</sup> ·h <sup>-1</sup> ) and salt rejection (99.9%)	(122)
Electrospinning	PVA	SiO <sub>2</sub> NPs	40	Improved amphiphilic properties leading to high fluxes (45 L·m <sup>-2</sup> ·h <sup>-1</sup> ) in the presence of surfactants in solution	(178)
Electrospinning	PVDF	TiO <sub>2</sub> NPs	40	Stabilized high water flux (40 L·m <sup>-2</sup> ·h <sup>-1</sup> )	(123)
Electrospinning	PVDF	SiO <sub>2</sub> NPs	40	High water flux in oil-water separations (24 L·m <sup>-2</sup> ·h <sup>-1</sup> )	(179)
Coating	PVDF	TiO <sub>2</sub> NPs	45	High fouling resistance	(40)
Electrospinning	PVDF	Al <sub>2</sub> O <sub>3</sub> NPs	40	High metal rejection (95%)	(180)
Electrospinning	PVDF	SiO <sub>2</sub> NPs	35	High stable flux (31 L·m <sup>-2</sup> ·h <sup>-1</sup> )	(37)
Casting and coating	PVDF	SiO <sub>2</sub> NPs	40	High oil-fouling resistance	(94)
Electrospinning	PVDF	SiO <sub>2</sub> NPs	40	High stable flux (48 L·m <sup>-2</sup> ·h <sup>-1</sup> )	(181)
Electrospinning	PVDF	TiO <sub>2</sub> NPs	40	High flux (38 L·m <sup>-2</sup> ·h <sup>-1</sup> )	(170)
Electrospinning	PVDF	CNTs	40	Flux enhancement (45 L·m <sup>-2</sup> ·h <sup>-1</sup> )	(41)
Casting	PVDF	SiO <sub>2</sub> NPs	70	High salt rejection (99.9%)	(104)
Hollowfibre	PVDF/PAN	Clay	34	High flux (55 L·m <sup>-2</sup> ·h <sup>-1</sup> ) and fouling resistance	(95)
Electrospinning	PVDF	Clay	63	Wetting resistance	(182)
Electrospinning and coating	PVDF	SiO <sub>2</sub> NPs	40	Fouling and wetting resistance	(183)
Electrospinning	PVDF-HFP	fluorosilane-coated TiO <sub>2</sub> NPs	40	Stable wetting resistance	(184)
Electrospinning	PVDF-HFP	Graphene	40	Stable flux (23 L·m <sup>-2</sup> ·h <sup>-1</sup> )	(185)
Phase inversion	PVDF	SiO <sub>2</sub> NPs	10	High salt rejection (99.8%)	(186)

## 2.5 Commonly used configurations in MD

Membrane distillation using different configurations has been evaluated for the desalination and production of high-quality water from saline water, where high rejection rates at high permeate fluxes have been achieved (37–39,41,95,164). Several configurations have also been investigated for the recovery of underground waters contaminated by heavy metals (187) and for the purification of pharmaceutical wastes and textile wastewater (i.e., commonly achieving high separation percentages) (188,189). As shown in **Figure 2.8**, MD processes are classified into four configurations: Direct contact membrane distillation (DCMD), air gap membrane distillation (AGMD), Sweeping gas membrane distillation (SGMD), and vacuum membrane distillation (VMD) (164).

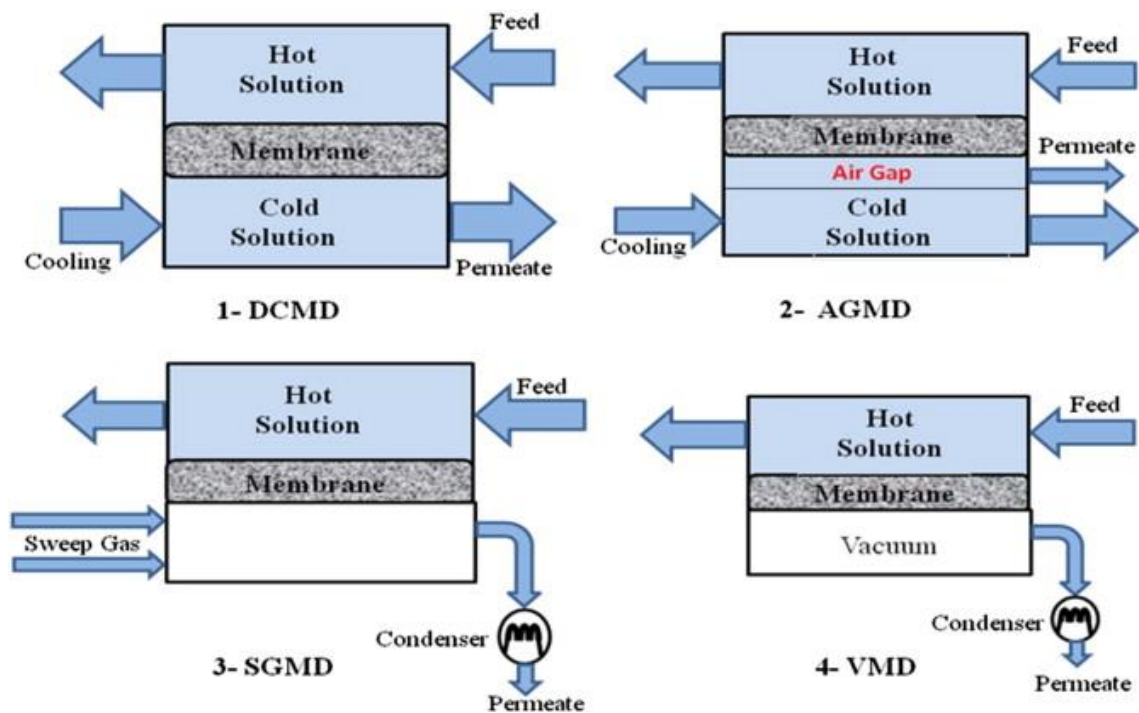


**Figure 2.8:** Graphical representation of the four different configurations commonly used in MD (190).

### 2.5.1 Direct contact membrane distillation (DCMD)

In DCMD, the hot solution (feed) is in direct contact with the surface of the hot membrane side. Water vapour is then transferred from the hot feed side to the cold permeate side where it condenses. The water vapour is transferred by the vapour gradient across the membrane as a result of the vapour pressure difference (**Figure 2.8**). Unless otherwise stated, the default MD configuration is referred to as DCMD (191). This configuration has been extensively reviewed whereby several types of NPs (*e.g.*, SiO<sub>2</sub>NPs) have been incorporated into MD membranes for its application in the purification of different types of waters (*e.g.*, oilfield and saline) as well as juice concentration and the removal of metals and ammonia (192). Although this configuration is known to be susceptible to heat loss as shown in **Table 2.3**, Lee *at al.* were able to achieve the thermal efficiency of 0.73-0.87 by a counter-current cascade which is a significant improvement in membrane distillation rendering DCMD the best configuration in MD (193).

### 2.5.2 Air gap membrane distillation (AGMD)

In this configuration, the feed solution is in direct contact with the hot side of the membrane surface. The total length of vapour diffusion is the sum of membrane thickness and air gap distance. Stagnant air is introduced between the hot surface of the membrane and the condensation side (**Figure 2.8**). The water vapour passes through the air gap to the condensation compartment of the membrane (194). This configuration has been applied in several studies including the removal of toxic metals from water using alumina-modified electrospun PVDF nanofibre membrane characterised by a contact angle close to 150° (187,195).

### 2.5.3 Sweeping gas membrane distillation (SGMD)

In the SGMD process, an unreactive gas is used to sweep the vapour from the permeate compartment of the membrane to the condensation compartment outside the membrane area (**Figure 2.8**). Also, there is a mobile gas barrier that prevents heat loss and assists in mass transfer (31). Onsekizoglu (2012) (196) has

summarised the principles, advances, and limitations of membrane configurations within SGMD, including process fundamentals, membrane characteristics, membrane materials, membrane modules, process parameters, flux enhancement, transport mechanisms, and polarisation phenomena (196).

#### 2.5.4 Vacuum membrane distillation (VMD)

In VMD configuration, vacuum is created on the permeate side of the membrane. The water vapour is driven outside the membrane and condensed (**Figure 2.8**). In this configuration, the loss of heat is significantly minimised (197). Ka *et al.* (37) have explored the use of a mechanically stable and superhydrophobic SiO<sub>2</sub>NP-modified PVDF nanofibre membrane in VMD and studies membrane wetting resistance and flux enhancement. The VMD configuration has also been used in solar energy driven systems for the recovery of water from polluted solutions (198,199).

Although MD is a promising technology for water recovery, its configurations are characterised by different advantages and disadvantages, which are highlighted in **Table 2.3**.

**Table 2.3:** Advantages and disadvantages of MD configurations.

Membrane configuration	Advantages	Disadvantages	References
DCMD	<ul style="list-style-type: none"> <li>- Simple</li> <li>- Efficient</li> </ul>	<ul style="list-style-type: none"> <li>- Susceptible to heat loss</li> </ul>	(24,200)
AGMD	<ul style="list-style-type: none"> <li>- Minimal heat loss</li> </ul>	<ul style="list-style-type: none"> <li>- Mass transfer barrier</li> <li>- Reduced permeate output</li> </ul>	(196,201)
SGMD	<ul style="list-style-type: none"> <li>- Reduction of the barrier to the mass transport</li> </ul>	<ul style="list-style-type: none"> <li>- Necessity of a higher condenser capacity</li> </ul>	(202,203)
VMD	<ul style="list-style-type: none"> <li>- Vacuum air unblocks membrane pores</li> <li>- High fluxes</li> </ul>	<ul style="list-style-type: none"> <li>- Highly complex</li> </ul>	(24,198)

## 2.6 Applications of MD processes

Several studies have reported the possible use of MD in a variety of separation processes. The MD process has been applied in the recovery and concentration of nutrients, removal of organics, bacteria, and toxic metal contaminants from water (204–206), purification of oil spills (207), and desalination of seawater, brackish water, and industrial brines (199,208). All these applications involved the use of commercial and laboratory-scale synthesised nano-enhanced membranes (37,95,104,209). For example, a TiO<sub>2</sub>-modified PVDF membrane was evaluated in terms of organic fouling resistance in a DCMD system and the results were compared to those of pristine PVDF membranes (40). Although both pristine and modified membranes showed similar fouling behaviours, the flux recovery was significantly higher in the modified membranes (40). Applications for the recovery of water from different types of solutions in MD are summarised in **Table 2.4**.

**Table 2.4:** MD processes used for purification of different types of water.

Feed solution	MD configuration	Membrane type	Thickness ( $\mu\text{m}$ )	Contact Angle ( $^{\circ}$ )	$\Delta T$ ( $^{\circ}\text{C}$ )	Flux (LMH)	Rejection efficiency (%)	Ref.
Oily water	DCMD	PVDF flat sheet	190	82.0	25	7.50	99.9	(209)
Sea water, brackish water,	DCMD	PP flat sheet	25.0	120	40	3.00	–	(200)
	DCMD	PVDF-HFP nanofibre	75	130	40	30	90	(210)
Waste water	DCMD	PVDF-Cloisite 15A hollow fibre	252	–	35	1.50	98.7	(211)
NaCl solution	DCMD	PE flat sheets	65.0	108	43	123	–	(212)
Mine water	VMD	PTFE flat sheet	–	–	25	5.00	99.9	(205)
Humic acid solution	VMD	PP hollow fibre	100	–	40	2.90	98.0	(213)
NaCl solution	DCM	PVDF-co-HFP nanofibre	80	150	40	30	98.5	(214)
Toxic metal wastewater	VMD	PTFE hollow fibre	–	101	37	5.00	–	(215)
NaCl	DCMD	PS nanofibre	–	114	63	31	99.9	(216)
Trace organic contaminants	DCMD	PTFE flat sheet	175	–	20	4.00	99.0	(217)
Lead-contaminated water	AGMD	PVDF nanofibre	100	150	40	20.0	99.3	(180)

The membranes used in MD applications include flat sheet, hollow fibre and nanofibre membranes. Remarkably, nanofibre membranes present higher water fluxes compared to flat sheet and hollow fibre membranes. Nonetheless, these membranes have pros and cons. **Table 2.5** presents the summary of advantages and disadvantages inherent to the use of these membranes (218–225).

**Table 2.5:** Advantages and disadvantages of flat sheet, nanofibre and hollow fibre membranes.

Membranes	Advantages	Disadvantages	Ref.
Flat sheet	<ul style="list-style-type: none"> <li>• Permeate can be extracted out by gravity flow</li> <li>• Cost effective for medium installations</li> <li>• Excellent chemical resistance, thermal characteristics, Surface treatments</li> <li>• Possess high surface area to volume ratio</li> <li>• Highly porous resulting in low cell resistance</li> </ul>	<ul style="list-style-type: none"> <li>• Membranes are easily damaged</li> <li>• Membrane cannot be backwashed</li> </ul>	(222,224–226)
Nanofibre		<ul style="list-style-type: none"> <li>• Required specialized equipment for material synthesis</li> <li>• Require electrically conducting polymers</li> <li>• Use organic solvents which can be toxic</li> <li>• Difficult to control their structure. Thus, nanofibre structure is not easily reproducible</li> </ul>	(218–221,227–229)
Hollow fibre	<ul style="list-style-type: none"> <li>• Membrane Space efficient for large installations</li> <li>• Cost effective for large installations</li> <li>• Compact modules with high surface area</li> <li>• Self-supporting. They do not require spacers to support them</li> </ul>	<ul style="list-style-type: none"> <li>• High packaging density</li> <li>• Cannot operate with high mixed liquor suspended solids</li> <li>• Not Cost Effective for small plants</li> <li>• Membranes damaged easily</li> </ul>	(223–225)

Remarkably, MD has a distinct transport mechanism that allows the recovery of precious minerals. This process is induced by the pre-concentration of the product to be recovered on either side of the membrane as a function of the mineral vaporisation energy. The non-volatile compounds are concentrated at the feed side of the membrane while volatile compounds are concentrated at the permeate

side (34,230). This is achieved at a temperature below the critical temperatures of the material being separated to avoid the formation of supercritical fluids in cases where the liquid and vapour state of the compounds are indistinguishable from each other (231).

The production of ammonia is mainly performed in a Haber-Bosch process. However, in a recent study (232), 1 M of free ammonia was recovered from a feed concentration of 0.2 M in a vacuum membrane distillation process. The recovered and concentrated ammonia can be precipitated for a further production of struvite. This was reported to be a cost-effective method for the production of fertiliser (233), and thus contributed to the concept of the water-food nexus. Several studies have also shown the separation and concentration of minerals such as HCl in an HCl/H<sub>2</sub>SO<sub>4</sub> mixed system, ionic liquids L-lysine-HCl syrup, extracts, and juices as well as the removal of other contaminants in the presence of organic foulants using commercial and nano-enhanced membranes in MD (97,234,235). Whereas toxic metals (e.g. boron) and organic dyes are removed from water at a 50% efficiency in MF and FO, 99% removal efficiencies have been achieved in nano-enhanced MD (236–240).

While MD remains one of the most promising processes in membrane technology, MD research has drifted towards the development of cost-effective methods for the treatment of saline water. Recent studies have generally focused on flux enhancement, fouling mitigations, optimisation of membrane properties, improvement of membrane wetting resistance using nano-enhanced membranes, optimisation of operational parameters, and configurations (142,241). It should be noted that the separation of salts from brine, seawater, and brackish water by MD is efficient at a level that allows the permeate to be used for almost any domestic application (i.e., purification efficiency >99%) (38,39). However, DCMD or VMD remain susceptible to fouling at high water recoveries due to the presence of salt precipitates (e.g., scaling). He *et al.* (2008) demonstrated the capacity of hollow fibre membranes to sustain flux decline in the presence of supersaturated precipitating salts close to the membrane surface (242). Furthermore, Song *et al.* (2008) indicated that the hollow fibre membrane surface design, module design,

and cross-flow conditions are key parameters for attaining stable water fluxes and high rejection efficiencies even when the desalination process is subjected to precipitating salts close to the membranes (131). Furthermore, the presence of organic, protein, colloidal, and oil emulsions affects the rate of water recovery in MD. **Table 2.6** presents the effects of the foulants on water flux in MD. Hydrophilic coating of the membranes resulted to flux stability, indicating their promising influence on fouling reduction in MD.

**Table 2.6:** The effects of foulants on water flux in MD.

Membrane	Foulant	Configuration	Duration (h)	Initial flux (LMH)	Final flux (LMH)	Ref.
PVDF flat sheet	Mineral oil emulsion	DCMD	24	7.5	4.1	(138)
PEG-coated PVDF flat sheet	Mineral oil emulsion	DCMD	24	6.4	6.3	(138)
PTFE flat sheet	HA	DCMD	120	35	15	(14)
PTFE flat sheet	BSA	DCMD	120	35	13	(14)
PTFE flat sheet	AA	DCMD	120	35	22	(14)
PVDF	Crude oil emulsion	DCMD	36	Normalised flux = 1.00	Normalised flux = 0.00	(94)
Chitosan-coated PVDF	Crude oil emulsion	DCMD	36	Normalised flux = 1.00	Normalised flux = 1.00	(94)
PTFE/PP	AA	DCMD	-	40	30	(243)
PTFE/PP	HA	DCMD	-	44	27	(243)
PTFE/PP	BSA	DCMD	-	40	28	(243)
PTFE/PP	Colloidal silica	DCMD	-	43	2	(243)

## 2.7 Sustainability of membrane distillation

The concept of desalination has long been investigated to mitigate the water scarcity challenges brought about by inadequate freshwater sources that fail to meet the current water demand. This involves the application of efficient processes such as reverse osmosis and nanofiltration. These processes operate under high pressures, and thus consume a lot of energy resulting in high operating costs. In order to counteract the high operating costs in pressure-driven membrane technology, membrane distillation (i.e., which is a highly efficient desalination process) has long been investigated at laboratory scale. Regardless

of the advantages in membrane distillation, piloting of this process has been relatively slow for the reasons already stated before.

The rate at which researchers have devoted their efforts to MD has exponentially increased over the years. Such efforts involved the application of synthesised nano-enhanced membranes in water desalination at laboratory-scale. An analysis of the research and development trends in the area of MD, previously documented by Thomas *et al.* (2017) (93), clearly shows the occurrence of three phases: initiation, emergence, and growth. As shown in **Figure 2.9**, an escalation in the number of publications for these three phases depicts a generally positive outlook in the development of MD.

While MD research was virtually non-existent in the 1980s, most of the research efforts were directed towards further development of the MD process during the early to mid-2000s. The current research boom being experienced in MD processes is geared towards commercialisation (93), with a specific focus on material improvements involving the use of nanomaterials (37–41). Ali *et al.* (2017) (244) conducted a study that linked publications, patents, and project pilot plants trends to MD development (**Figure 2.10**). To this end, several companies that are focusing on the application of MD technology in water desalination have been established. These companies include Aquastill and Aquaver in the Netherlands, Memsys in Germany, and Gold Technologies Inc. in the USA. Other companies involved in pilot projects in Singapore are also emerging (24). It is worth noting that Aquaver and Memsy have been recently merged to form one company (Memsys). To further expand global operation of Memsy, New Concepts Holdings Limited (NCHL), a company based in China has acquired all the assets and intellectual properties (IPs) of Memsys, and further plans to leverage the combination of research and development in Germany and engineering in China to support the growth of Memsys worldwide. Pilot projects using solar driven desalination in Singapore are also emerging [24]. Furthermore, various companies and research institutions investigating the upscaling of MD are identified. These include Hyflux (Singapore), AEE INTEC Institute for Sustainable Technologies (Australia), Flemish Institute for Technological Research (Belgium), The Institute

National des Sciences Appliquées de Toulouse (INSA, France), Fraunhofer Institute for Solar Energy Systems (Germany) and Plataforma Solar de Almería (America), [11].

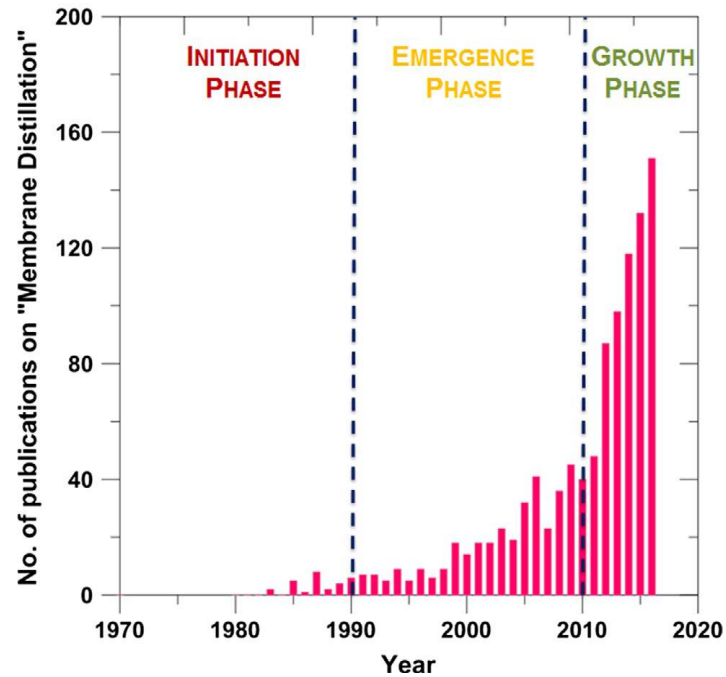


**Figure 2.9:** The growth of publications in membrane distillation (93).

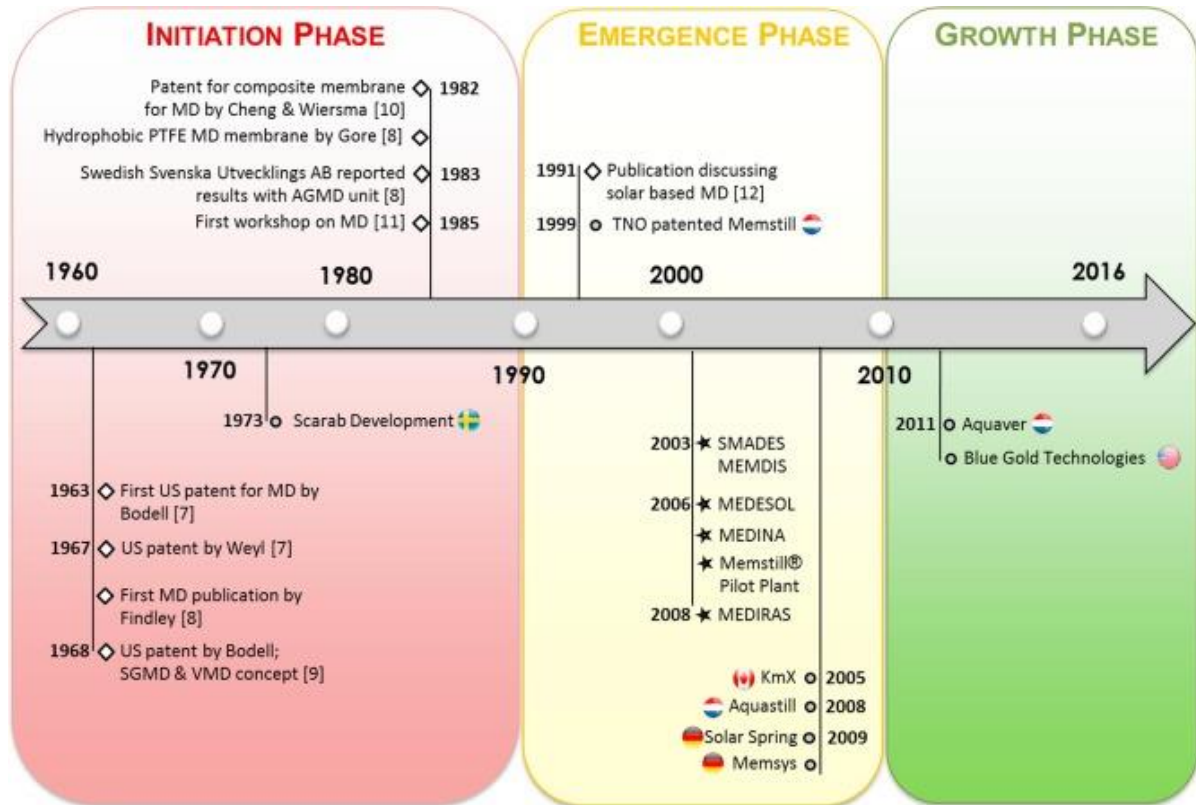


**Figure 2.10:** Current developments towards application of membrane distillation in water desalination (244).

Despite MD research work advancing to pilot-scale level, a cost-benefit analysis of the technology is rarely reported. Khayet (35) has suggested a lack of cost-benefit analysis and energy consumption studies as the main hindering parameter for the development of large-scale MD. Currently, no studies related to the cost-analysis of nanoparticle-incorporated MD membranes have been reported, although several studies have reported the use of nanoparticles in the enhancement of membrane performances (37,104). Albeit, some studies have provided general information related to the MD operational cost without necessarily considering the cost implications associated with the incorporation of nanoparticles onto MD membranes. **Table 2.7** provides a summary of cost estimations for MD and RO water purification systems. The values outlined in **Table 2.7** were calculated using information obtained from the literature. The rate of water production for some MD systems could not be determined due to a lack of information related to the estimated cost of water production.

The cost of water recovery in MD depends on a number of factors, including the cost of operational materials, the tax associated with the production of carbon dioxide from the energy required in MD processes, and many others (245–247). In the case of the low cost of heat that is free from taxes (e.g. the use of solar energy), MD becomes cheaper than highly energy demanding processes such as RO and NF (248). It was estimated that the cost of water production of 17 m<sup>3</sup>/day in MD using geothermal energy is approximately \$13/m<sup>3</sup> (249). In the case where the heat supply in MD was sourced from electricity or fuel-fired plant, Meidersma *et al.* (250) have calculated that the total cost of water was \$0.16–0.17/m<sup>3</sup>, relative to \$0.25–0.35/m<sup>3</sup> required for a RO process (250). The cost estimated at the Memtill's water recovery systems demonstrated that MD can reduce the cost of water desalination to \$0.26–0.54/m<sup>3</sup>. This considerable reduction was ascribed to the use of sustainable and cost-effective plant materials to build the operational modules as well as the use of low-cost heat supplies (250). When determining the cost implications associated with water production in MD, the general parameters that were taken into consideration include the plant availability and capacity, interest rate (%), amortization, modules and membrane assembly (\$/m<sup>2</sup>), installation (\$), supporting equipment (\$), electrical cost (\$/kWh), steam cost (\$/kg), labour cost (\$/m<sup>3</sup>), brine disposal (\$/m<sup>3</sup>), maintenance cost (%), pre-treatment cost (\$/m<sup>3</sup>), thermal energy requirement (kWh/m<sup>3</sup>), emission factor for natural gas (kg CO<sub>2</sub><sup>e</sup>/kWh), emission factor for electricity, (kg CO<sub>2</sub><sup>e</sup>/kWh), electrical energy requirement (kWh/m<sup>3</sup>), and carbon tax (\$/ton carbon) (245–247,251,252).

**Table 2.7:** Estimated water production rate (WPR) and water production cost (WPC) of MD and RO applications.

MD and RO membranes application	WPR (L/day)	WPC (\$/m <sup>3</sup> )	Year	Ref.
MD	-	1.32	1999	(253)
Small scale AGMD powered by geothermal energy	171	130	2005	(249)
RO-integrated MD with UF/MF pretreatment	-	0.54	2006	(250)
AGMD pilot plant	0.09	1.00	2007	(254)
NF/RO-integrated VMD	76.2	0.92	2007	(252)
Solar powered small scale AGMD	5.88	1.17	2008	(246)
Laboratory scale DCMD	7.50	1.72	2013	(245)
Small scale solar AGMD	21.7	5.16	2014	(247)
Laboratory scale AGMD	996	4.73	2017	(251)
Large capacity RO	40000	0.54	2013	(255)
Medium capacity RO	1200	1.33	2013	(255)
Very small capacity RO	5	12.99	2013	(255)
RO	-	1.25	1999	(253)
RO	-	8.00	2005	(249)

## 2.8 Nanofibres as potential pretreatment materials in membrane distillation

In Section 2.1, it was demonstrated that one of the limiting factors for application of MD is fouling. In MD processes, fouling originates from several factors that includes adsorption of organic compounds, deposition and growth of bacterial films on the surface of the membrane and scaling induced by the precipitation of inorganic compounds (70,256). The concentration of the foulants can therefore be reduced at the pretreatment stage using several techniques that involves ultrafiltration, microfiltration, coagulation and adsorption (257). Therefore, pretreatment step could potentially be used to remove organic foulants from MD feed solution.

In an attempt to develop new and innovative advanced, viable, economic, energy-efficient and robust water treatment processes, researchers have explored various materials for such applications. Through nanoscience and nanotechnology, it has become possible to develop materials with unique nanoscale properties that can solve many of the water quality problems, e.g. nanostructured/enhanced filtration

and adsorption materials. Amongst many nanostructured materials, nanofibres are one of the most important nanostructured materials studied for various applications including environmental applications (258). The nanofibres are produced in an optimal way to achieve a specific objective impregnated in their microscopic counterparts components. Hence, the polymeric nanofibre properties are distinctively different from those of their individual counterparts (259). The large increase in research activity in this field has been brought by their intrinsic chemical, physical, and mechanical properties embodied in their diameters which range from microns to hundreds of nanometres (260). The small (nanometer scale) dimensions of these nanofibres give rise to their large surface area-to-volume ratios which give them significant advantages to specific applications such as adsorption of water contaminants.

However, the production scale-up of polymeric nanofibres for certain applications requires further improvements. Some of these applications are influenced by the process parameters and polymer systems which include the equipment, the environment, and the solution plethora (120,261–264). Optimisation of these parameters and the polymer systems requires length milestones to optimize due to poor viscoelastic nature, poor molecular entanglements of the polymers, low solubilities in solvents of interests (263,265). Hence, according to Person and the co-workers (2013), “the main challenge related to the mass production of nanofibre materials is the implementation of methods allowing an increase of the process and product reproducibility and to extend the classes of utilizable materials” (266).

Nanofibres are synthesised using different methods depending on the nature of applications. The cost of synthesis, applications of the nanofibres and rate of production are the driving forces that determine the choice of synthesis process of the nanofibres. Production methods include electrospinning, drawing, centrifugal spinning, template synthesis, self-assembly, force-spinning, melt-blown, islands-in-the-sea spinning, force-spinning, and phase separation (195,262,267–272). The advantages of electrospinning over other nanofibre producing techniques are evidenced by an alarming increase of publications and the review reports on the

annual basis (273). The electrospinning technique was briefly explained earlier. In addition to that, the major parameters governing the electrospinning technology are given in **Figure 2.11**. More insights into different aspects of electrospinning can also be found in a mini review article on the subject appearing in *Polymer International* 56(11) 2007. Briefly, the electrospinning technique can produce micro and nanostructured fibre materials characterised by high surface areas, high mechanical properties, ease of functionalisation. These properties inherent to nanofibre membranes make them good candidates for adsorption of different compounds including organic water contaminants.

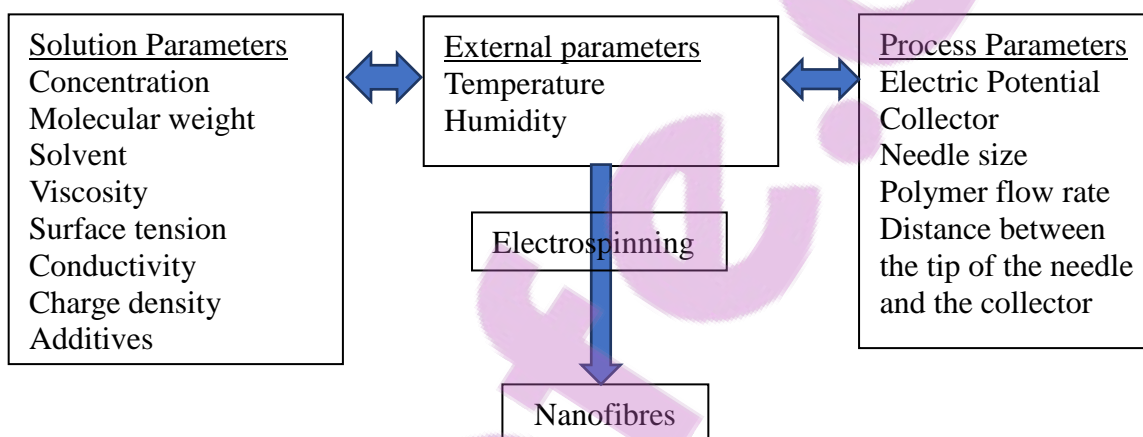


**Figure 2.11:** Typical parameters that affect the nanofibre electrospinning method (112,273–276).

Nanofibres have been employed as affinity membranes for biological (277–279) and wastewater treatment applications (280). The current literature is dominated by the application of activated carbon nanofibres for removal of phenols from water (281,282). The adsorption capacities up to 265 mg/g have been reported. The use of polymeric nanofibres for adsorption of phenols include electrospun chitosan-based nanofibres where removal efficiencies of 90% were recorded (283). However, several batch and continuous adsorption techniques have been reported for adsorption of emerging water contaminants including toxic metals, dyes and estrogens (284–288). The continuous and batch adsorption of the emerging water contaminants is presented in **Table 2.8**. In a continuous adsorption, the nanofibres were packed in a column to form a bed where the

aqueous solution containing the adsorbates (contaminants) was run through the column (284,289). Furthermore, the nanofibres were placed in a vessel containing the adsorbate solution and agitated over a specific time to undertake the batch experiments (285,288,290,291). The adsorbents used on either of the adsorption techniques can be regenerated using different methods to reduce the cost of pollutants removal as well as maintenance of waste management (284,292). The performance of nanofibres presents the potential in future to revolutionise the current water filtration technologies by providing cheaper and portable units consuming less energy.

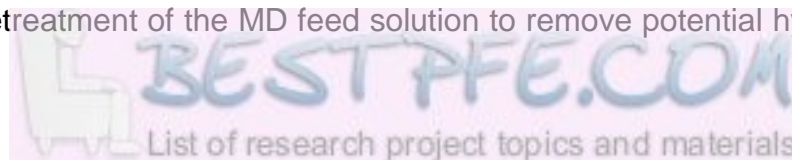
**Table 2.8:** Adsorption of various emerging pollutants using nanofibre materials.

Nanofibre adsorbent	Adsorbate	Technique	Adsorption Capacity	Ref.
PVA/zeolite nanofibres	Ni <sup>2+</sup> , Cd <sup>2+</sup>	Batch	Ni <sup>2+</sup> , 342.8 mg/g; Cd <sup>2+</sup> , 838.7mg/g	(285)
PAN/oxime nanofibres	Cu <sup>2+</sup> , Pb <sup>2+</sup>	Batch	Cu <sup>2+</sup> , 52.7 mg/g; Pb <sup>2+</sup> , 263.45 mg/g	(291)
Chitosan/PMMA nanofibres	Cr <sup>6+</sup>	Batch	Cr <sup>6+</sup> , 67.0 mg/g	(292)
PEO/chitosan nanofibres	Ni <sup>2+</sup> , Cu <sup>2+</sup> , Cd <sup>2+</sup> , Pb <sup>2+</sup>	Batch	Ni <sup>2+</sup> , 357.1 mg/g; Cu <sup>2+</sup> , 310.2 mg/g; Cd <sup>2+</sup> , 248.1 mg/g; Pb <sup>2+</sup> , 237.2 mg/g	(290)
Amidoximated PAN nanofibres	U <sup>6+</sup>	Continuous	85%	(284)
Nylon 6 nanofibres	Diethylstilbestrol, dienestrol, and hexestrol	Dynamic disk	Diethylstilbestrol, 208.95 mg/g; dienestrol, 135.21 mg/g; hexestrol, 97.71 mg/g	(286)
BTCA/PVA nanofibres	Reactive red dye	Batch	Reactive red dye, 88.3 mg/g	(288)
Chitosan/PVA nanofibres	Cr <sup>6+</sup> , Fe <sup>3+</sup> , methyl orange	Batch	Cr <sup>6+</sup> , 136 mg/g; Fe <sup>3+</sup> , 11.3 mg/g; methyl orange, 163 mg/g	(287)
Chitosan/TiO <sub>2</sub> nanofibres	Pb <sup>2+</sup> , Cu <sup>2+</sup>	Batch	Pb <sup>2+</sup> , 710.3 mg/g; Cu <sup>2+</sup> , 526.5 mg/g	(293)
hydroxyquinoline/PAN nanofibres	Cu <sup>2+</sup>	Continuous	Cu <sup>2+</sup> , μmol/g	(289)
Chitosan/PVA/zeolite nanofibres	Methyl orange	Batch	Methyl orange, 153.0 mg/g	(294)
Chitosan nanofibres	3-methyl-4-nitrophenol	Batch	3-methyl-4-nitrophenol, 90%	(295)

## 2.9 Materials used in the synthesis of polymeric nanofibre membranes

Generally, the mechanical properties of polymeric nanofibres are weaker when compared to textile fibres and films made from the same polymer. This is not only because the polymer molecules are not fully aligned during stretching at the time of electrospinning, but also due to the reduced interaction between polymer molecules in nanofibres (296). Recently, it has been reported that the mechanical properties of nanofibres are directly proportional to the fibre diameter (297). The two most commonly used aliphatic polyamide (PA) fibres are polyamide 6 and polyamide 6,6 which are made of caprolactam and hexamethylenediamine with adipic acid, respectively. The PA fibres are produced by melt-spinning and they possess moderate molecular orientation and crystallinity after post-drawing. Molecular orientation and crystallinity, along with hydrogen bonding between chains provided by the amide group ( $-\text{NH}-\text{CO}-$ ) provides them with good mechanical properties and abrasion resistance, which renders them to be one of the most widely used industrial fibres (298).

In addition to the polymers briefly discussed above, over 100 polymers have been successfully electrospun into nanofibres for use in water treatment (299,300). These are generally obtained from polymer solutions or polymer blends and they include, polysulfone (PSf), polyethersulfone (PES), nylon-6, poly(ethylene oxide) (PEO), polyvinyl chloride (PVC), polystyrene (PS), cellulose acetate (CA), poly( $\epsilon$ -caprolactone) (PCL), polylactic acid (PLA), and many more (300). Natural biopolymers such as chitosan, cellulose and cyclodextrins have also been used to prepare electrospun nanofibre membranes for water treatment and other applications (264,265,300,301). Furthermore, polyacrylonitrile (PAN) nanofibres have been widely used in adsorption studies. These include the adsorption of  $\text{CO}_2$ , toxic metals and organic pollutants (302–304). In order to enhance their adsorption capacity, PAN nanofibres were functionalised using hyperbranched polyethyleneimine (PEI) or other amine-functionalised compounds (303–306). Due to their high adsorption capacities, PEI-functionalised PAN nanofibres could be used for the pretreatment of the MD feed solution to remove potential hydrophobic foulants.



## **2.10 Nanofibres as adsorption materials: Pretreatment role and kinetics in MD**

Pretreatment of the feed water and membrane cleaning are the main techniques that are currently employed to reduce fouling. The choice of pretreatment process is based on the following: type of feed water, the level of water recovery and quality, the type of membrane to be used and its cleaning frequency. In several high purity water recovery processes such as FO, RO and NF, ultrafiltration (UF) has been employed as a pretreatment process (25). Due to poor UF removal efficiencies of the dissolved organic compounds from water, in some cases adsorption is integrated with the UF purification systems. Powdered activated carbon has been used in traditional adsorption pretreatment integrated water purification processes (307). Although activated carbon has shown excellent results in adsorption of organic compounds, it is easily saturated by adsorbates and it is difficult to separate it from the media (307). Therefore, further studies on the use of polymeric adsorbents such as nanofibres are of paramount importance. Nanofibre adsorbents are characterised by high surface area to volume ratio, rendering them highly efficient and effective for adsorption of several pollutants including organic compounds (277,308,309).

Adsorption is a process that involves the transfer of the compound to be adsorbed (adsorbate) from the bulk solution to the surface of the adsorbing material (adsorbent). The adsorbate is attached to the adsorbent or exchanged with the ions present in the cavities of the adsorbent, giving rise to physisorption, chemisorption or ion exchange (310). Physisorption is induced by weak electrostatic forces between the adsorbate and the adsorbent (311). Therefore, physisorption is reversible. Chemisorption is characterised by a strong electrostatic interaction between the adsorbate and adsorbent (310). Chemisorption is therefore irreversible.

Previous studies have suggested that chemisorption occurs when the mean free energy ( $E$ ) is 8 – 16 kJ/mol while physisorption occurs when  $E < 8$  kJ/mol (295,312). The lower the value of  $E$  which is the free energy required to transfer 1 mol of the adsorbate from the bulk of the solution to the active site of adsorption is an indication of a weak interaction between the adsorbate and the adsorbent leading to physical interaction. The inverse is therefore true for the promotion of chemisorption (313).

The adsorption process is affected by several parameters that include solution pH, initial concentration, adsorbent dose, contact time and temperature (314–317). In previous studies, it has been demonstrated that the adsorption of organic compounds increases with an increased in contact time, adsorbent, initial concentration while the inverse is true with an increase in solution pH and temperature (313,316,318–320). In order to understand the rate and mechanisms of adsorption, the kinetic and isotherms models were developed (321,322). First-order and second-order kinetic models are frequently used to determine the rate of adsorption at equilibrium (314,323–325).

## 2.11 Conclusion

The literature review has shown that research directed towards membrane distillation is an active field that is increasing at a remarkable rate. Various innovative fabrication and modification procedures for MD membranes have been reported in the literature and were summarized in this review. It has been observed that nanoparticle-modified membranes provide essential properties that can mitigate the challenges associated with MD processes, thus the role of nanoscale materials is significant. However, fouling remains a critical factor that affects the performance of MD. Although biofouling caused by thermophilic bacteria has been observed in MD processes, no study involving the use of well-known antibacterial nanoparticles such as AgNPs has been reported. The rationale behind the use of AgNPs was to incorporate them in the preparation of biofouling-resistant membranes to hinder the growth of bacterial thermophiles.

Several applications of MD processes have been tested at laboratory-scale using different configurations. A review of results from various studies involving the use of nanoparticle-modified MD membranes for the treatment of brackish and surface water provide cost implications associated with this separation process. However, sustainable development towards commercialization has been moving at a slower rate with indications of some water treatment plants based in a few developed countries. It is thus imperative to systematically develop even more cost-effective purification systems that are integrated with emerging membranes to produce high quality water at large industrial throughput. A pretreatment step involving the use nanofibre adsorbents could be integrated to MD purification process for possible reduction of membrane fouling.

# CHAPTER 3

## ADSORPTION OF PHENOLIC COMPOUNDS BY POLYACRYLONITRILE NANOFIBRE MEMBRANES: A PRETREATMENT FOR THE REMOVAL OF COMPOUNDS BEARING HYDROPHOBIC GROUPS FROM WATER

---

### 3.1 Introduction

Membrane Distillation (MD) processes are driven by a vapour pressure difference across the membrane, which is induced by a temperature difference between the two interfaces of the membrane as was earlier demonstrated. As a result, the compounds (*e.g.*, volatile organics) that pass through the membrane are those that vaporize at those operating temperatures (70,164). Depending on their chemical properties, these compounds would cause membrane fouling. Additionally, non-volatile compounds have also been observed to induce fouling at the surface or internal pore structure of membranes. These latter foulants are classified as colloidal, organic, and biological (66,70,241,326). Therefore, to significantly decrease fouling in membrane distillation processes, a pretreatment is mandatory.

The selection of a pretreatment for MD depends on the composition of water to be treated as well as the concentration of organic foulants present in that feed (327). (327). In conventional water purification systems, pretreatments involve screening, pre-chlorination, coagulation, flocculation, and adsorption (*e.g.*, using activated carbon). Certain pretreatment processes may introduce by-products into the feed water to the MD process which would change the surface characteristics of the membranes (25). In several high-purity water recovery processes such as forward osmosis (FO), reverse osmosis (RO), and nanofiltration (NF), ultrafiltration (UF) has been used as a pretreatment (25). However, due to poor UF removal efficiencies of dissolved organic compounds such as phenols, an adsorption step (*e.g.*, powdered activated carbon) has been traditionally integrated to UF (307). Although activated carbon has shown excellent results in the adsorption of organic

compounds, it becomes complicated to be separated from the purification media (307). Several pretreatment methods involving the use of polymeric adsorbents has been reported (328–330). Among other polymeric adsorbents, nanofibrous materials have been extensively used (265,302,331). Nanofibrous materials (e.g., polyacrylonitrile) are characterised by high surface-area-to-volume ratios, which highly assist in the removal of organic contaminants. Therefore, additional research on the use and modification of polymeric adsorbents (e.g. nanofibres) is required. This chapter explores the use of PAN nanofibres for the removal of phenolic organic compounds from water. The selection of phenolic compounds relies on their volatile and hydrophobic nature (332,333). Due to the use of hydrophobic membranes in MD separation, a feed solution containing hydrophobic compounds is likely to cause membrane fouling. In the current study, PAN nanofibres were chemically functionalised with polyethylene imine (PEI) to enhance their removal efficiency. Notably, the imination of PAN nanofibres synthesised by in-situ electrospinning has been rarely reported in the literature. The imination of PAN nanofibres is mainly conducted as a post-treatment for synthesised nanofibres (303–305,334); which is believed to be inefficient in the imination of all cyano groups present in PAN nanofibres. Therefore, *in-situ* electrospinning enhances imination and thus increases the active adsorption sites induced by hyperbranched PEI. To the best of our knowledge, in-situ electrospun PEI-functionalised PAN nanofibres has not been reported for the removal of phenolic compounds from water; therefore, opening new research directions as an innovative material for the pretreatment of compounds bearing hydrophobic groups in water during MD processes.

## **3.2 Methods and materials**

### **3.2.1 Reagents**

Dichloromethane (DCM, HPLC grade, 99.9%), acetonitrile (CH<sub>3</sub>CN, GC grade), methanol (CH<sub>3</sub>OH, HPLC grade, 99.9%), C18–SD SPE cartridges (4 mm/1 mL), polyacrylonitrile (PAN, MW = 150 000 g/mol), polyethyleneimine (PEI, MW = 1 200 g/mol, 50 wt. % in H<sub>2</sub>O), Dimethyl formamide (DMF, ACS reagent 99.8%), o-

chlorophenol (HPLC grade), and p-nitrophenol (GC grade) were purchased from sigma Aldrich (Germany). Deionised water was obtained by the Direct-Q® Millipore system (Merck Millipore). All reagents were used as received

### **3.2.2 Synthesis of PAN nanofibres and PEI-modified PAN nanofibres**

PAN nanofibres were synthesised using the electrospinning technique (335,336). Briefly, 8 wt% PAN solution was prepared in dimethyl formamide and electrospun at the following conditions: voltage of 14 kV, flow rate of 0.7 mL/h (i.e. 35 h to electrospun a 25 mL PAN solution), and a distance of 15 cm between the tip of the spinneret and the rotating collector. To synthesise PEI-modified PAN nanofibres, 0.5 %(v/v) PEI was added to a PAN solution (8 wt %) and electrospun using the above mentioned optimised electrospinning conditions with 2% PEI being added relative to the PAN. The imination reaction was completed by immersing the electrospun PAN/PEI nanofibres in water and autoclaving at 150°C. The iminated PAN nanofibres were washed with de-ionised water and dried in an oven at 70°C.

### **3.2.3 Characterisation of PAN nanofibres and PEI-modified PAN nanofibres**

The surface morphology of PAN and PEI-functionalised PAN nanofibres was investigated using Scanning Electron Microscopy (SEM, JEOL STM – IT300). To analyse the PEI functionalisation of PAN nanofibres, Fourier Transform Infrared (Perkin Elmer FTIR) was used. Furthermore, the zeta potential of PAN and PEI-functionalised PAN nanofibres was investigated using the Electrokinetic Analyzer for Solid Surface Analysis (SurPASS™ 3, Anton Paar, Graz, Austria).

### **3.2.4 Phenolic compounds analysis by solid-phase extraction (SPE)**

Solutions containing phenolic compounds for adsorption experiments were prepared using de-ionised water. The indicator compounds used for phenolic compounds were o-chlorophenol and p-nitrophenol. Solid-phase extraction was conducted using C<sub>18</sub> cartridges. The cartridges were pre-conditioned by passing

through 10 mL aliquots of DCM, 5 mL of methanol followed by water, and ensuring that the solid phase does not run dry (295). Water samples (100 mL) were passed through the cartridges at a rate of 1.5 mL/min. The cartridges were washed with de-ionised water and air-dried for 30 min. The analytes were eluted into the calibrated vials using 4 mL of DCM, followed by 3 mL of acetonitrile and 1 mL of methanol, thus ensuring complete elution of analytes. The eluted samples were dried under nitrogen gas. DCM (2 mL) was added to the vials and vortexed for 15 min. The SPE extracts were then injected into the Pegasus 4D GC-TOFMS equipped with an auto-sampler (337–339).

### **3.2.5 Phenolic compounds analysis by Gas chromatography and mass spectrometry**

A 7890A Agilent GC coupled to a LECO PEGASUS 4D time-of-flight (TOF) mass spectrometer equipped with an Agilent autosampler was used for the analysis of the phenolic compounds. The RXi 5SiI-MS column (24 m long, 0.25 mm internal diameter, and 0.25  $\mu\text{m}$  film thickness) was used as a primary column. This column was selected because of its high sensitivity, high thermal stability, and reduced bleeds which prevent the oxidation of the column. The temperature programming was initially set at 50°C for 5 min, then ramped to 290°C at a rate of 20°C/min, and held for 5 min. The transfer line and the ion source temperature were set at 320°C, and 250°C respectively. The electron impact ionisation energy was set to -70 eV with an offset of 300 V, making a total detector voltage of 1600 V. Helium was used as the carrier gas at a flow rate of 3 mL/min. The calibration plots were prepared using the stock solutions of the standards. Chlorophenol and nitrophenol stock solution standards were prepared in DCM. A serial dilution of the stock solutions was conducted to prepare six working standards (0.1 mg/L, 0.5 mg/L, 5 mg/L, 15 mg/L, 50 mg/L, and 100 mg/L). The coefficients of determination obtained from the linear plots of chlorophenol and nitrophenol were 0.9994 and 0.9892, respectively. These calibration plots were subsequently used for quantification of the extracted chlorophenols and nitrophenols.

### 3.2.6 Batch adsorption experiments

Batch adsorption experiments of phenols were conducted using PAN nanofibres and PEI-functionalised PAN nanofibres. 100 mL of phenolic solution at different concentrations were transferred into a conical flask containing a measured mass of nanofibres. The contents of the flask were stirred for a specific time. Furthermore, the solution containing the unabsorbed phenols was filtered from the nanofibres and prepared for SPE extraction. The effect of solution pH (5 – 11), initial phenols concentration (20 – 100 mg/L), nanofibres dose (3 – 30 mg), and contact time (0 – 180 min) were studied. Kinetic studies were performed to determine the rate of adsorption of phenols onto PAN nanofibres. Langmuir, Freundlich, and D-R model isotherms were conducted to understand the mechanism of phenol adsorption onto PAN nanofibres. The adsorption capacity of the phenols onto PAN nanofibres were calculated using the following **Equations**:

$$\text{Mass of phenols adsorbed} = (C_i - C_f) * V \quad (3.1)$$

$$\text{Adsorption capacity} = \frac{M_{\text{adsorbate}}}{M_{\text{adsorbent}}} \quad (3.2)$$

Where  $C_i$  is the initial concentration of adsorbate

$C_f$  is the final concentration of adsorbate

$V$  is the volume of the solution

$M_{\text{adsorbate}}$  is the mass of adsorbate

$M_{\text{adsorbent}}$  is the mass of the adsorbent

The linearised pseudo-first order kinetic equation proposed by Lagergren (340).

$$\log(q_e - q_t) = \log q_e - \left( \frac{k_1}{2.303} \right) t \quad (3.3)$$

Where,

$k_1$  is the rate constant of the pseudo-first-order adsorption process ( $\text{min}^{-1}$ ),

$q_e$  is the amount of material adsorbed per unit mass of adsorbent at equilibrium (mg/g),

$q_t$  is amount material adsorbed per unit mass of adsorbent at time  $t$  (mg/g),

The linearised pseudo-second order model (341).

$$\frac{t}{q_t} = \frac{1}{k_2 q_e^2} - \frac{1}{q_e} t \quad (3.4)$$

where,

$k_2$  is the rate constant of the pseudo-second order adsorption process (g/mg·min),  
 $q_e$  is the amount material adsorbed per unit mass of adsorbent at equilibrium (mg/g)

$q_t$  is the amount material adsorbed per unit mass of adsorbent at time  $t$  (mg/g).

The value of  $k_2$  was calculated from the plot of  $t/q_e$  vs  $t$  where  $(1/k_2 q_e)$  was the intercept and  $1/q_e$  was the slope of the plot.

The linearised Langmuir isotherm model is described by **Equations 3.5** and **3.6**.

$$\frac{C_e}{q_e} = \frac{1}{K_L q_m} + \frac{1}{q_m} \quad (3.5)$$

$$\frac{1}{q_e} = \frac{1}{K_L q_m C_e} + \frac{1}{q_m} \quad (3.6)$$

Where,

$q_e$  is the equilibrium uptake of the material (mg/g)

$q_m$  is the maximum adsorption capacity (mg/g)

$K_L$  is the Langmuir isotherm constant related to the adsorption energy

$C_e$  is the equilibrium (final) concentration of material in the solution (mg/L).

$K_L$  and  $q_m$  are calculated from the linear plot of  $C_e/q_e$  vs  $C_e$  when using **Equation 3.6** where  $(1/q_m)$  is the gradient of the straight line,  $1/(K_L q_m)$  is the y-intercept or from the linear plot of  $1/q_e$  vs  $1/C_e$  when using **Equation 3.5**, where  $1/(K_L q_m)$  is the gradient of the straight line and  $(1/q_m)$  is the y-intercept (316). The Langmuir isotherm constant  $K_L$  which is also known as the association constant (expressed in  $L \cdot mg^{-1}$ ), is used to determine the affinity of the adsorbate on the surface of adsorbent.

The dimensionless parameter (separation factor)  $R_L$  is calculated using **Equation 3.7**. This parameter can be used to predict the adsorption efficiency of the

adsorbent. The process is irreversible if  $R_L=0$ , favourable if  $R_L<1$ , linear if  $R_L=1$  and unfavourable if  $R_L>1$ .

$$R_L = \frac{1}{1+K_L C_i} \quad (3.7)$$

Where,

$K_L$  is the Langmuir isotherm constant determined in **Equation 3.5** or **3.6**, and  $C_i$  is the initial concentration of the adsorbate (314).

The **Equation** used for the Freundlich isotherm model is as follows:

The values of  $K_f$  and  $n$  are obtained from the y-intercept and the slope of the plot ( $\log q_e$  vs  $\log C_e$ ).

$$\log q_e = \log K_f + \frac{1}{n} \log C_e \quad (3.8)$$

Where,

$q_e$  is the equilibrium solid phase material concentration per gram of adsorbent (mg/g),

$C_e$  is the equilibrium material concentration in the bulk phase (mg/L),

$K_f$  is the Freundlich isotherm constant (mg/g), and

$n$  is the adsorption intensity.

The linearised **Equation** used to describe the D-R model isotherm is as follows:

$$\ln(q_e) = \ln(q_m) - \beta \varepsilon^2 \quad (3.9)$$

Where  $\varepsilon$  was correlated by:

$$\varepsilon = RT \ln \left( 1 + \frac{1}{C_e} \right) \quad (3.10)$$

Where  $R$  is the gas constant ( $8.314 \text{ J} \cdot \text{mol}^{-1} \cdot \text{K}^{-1}$ ) and  $T$  is the absolute temperature in Kelvin. The values of  $\varepsilon$  can be calculated using the equilibrium concentrations of organics. Furthermore, the values of  $\beta$  could be determined from the slope of the plot of  $\varepsilon^2$  vs  $\ln q_e$ . The constant  $\beta$  is related to the mean free energy ( $E$ ) of adsorption as follows:



$$E = \frac{1}{\sqrt{2\beta}} \quad (3.11)$$

### 3.2.7 Regeneration of nanofibres and isolation of phenolic compounds

The regeneration of the adsorbents and the isolation of the adsorbates is a key interest in adsorption experiments. In the current study, phenols were isolated from the PAN nanofibres with the aim of recycling the adsorbents (nanofibres) using ethanol and NaOH. Briefly, phenols dissolve in ethanol and also form stable phenolate ions at high pH values; hence, leading to weak interactions with the adsorbents. During regeneration experiments, the tested PAN and PEI-functionalised PAN nanofibres were dispersed in ethanol and stirred for 5 h. The nanofibres were filtered and re-washed with a 0.2 M NaOH solution to remove the remaining phenols. The nanofibres were further washed with de-ionised water until attaining a neutral pH, dried, and used in the next cycle. The adsorption cycles were conducted until a fifth regeneration cycle. The recovered phenols were safely disposed of.

## 3.3 Results and discussion

### 3.3.1 Scanning electron microscopy analysis of nanofibres

The surface morphology of PAN nanofibres were investigated using scanning electron microscopy (SEM). Uniform PAN nanofibres were obtained at a polymer concentration of 8 wt% and electrospinning conditions as stated in section 2.2. When the PAN solution was subjected to 14 kV, it became electrically charged; thus, inducing electrostatic repulsive forces. These forces led to the stretching and thinning of the polymer droplets, forming a conical shape (i.e., the Taylor cone) (118). The viscous solution of 8 wt% PAN stabilised the bending of the jet between the rotating collector and the tip of the needle at a 0.9 kV/cm electric field (i.e., 14 kV applied at a distance of 15 cm), leading to the formation of beaded-free nanofibres with an average diameter and variance of 219 nm and 237.4

respectively (**Figure 3.1**) (263,335,342). The diameters of uniform nanofibres followed a Gaussian distribution. The addition of PEI in the electrospinning PAN solution led to the formation of slightly beaded nanofibres with an average diameter of 160 nm and variance ( $\sigma$ ) 0.47 (**Figure 3.1**). The diameters of PEI-modified PAN nanofibres followed a lognormal distribution indicating the formation of non-uniform nanofibres. This phenomenon would be ascribed to a change in polymer viscosity. The critical polymer viscosity is a key parameter for the synthesis of uniform electrospun nanofibres (342). The beaded nanofibres are a consequence of poor molecular entanglement due to low polymer viscosity (343). Also, highly viscous polymer solutions form poor Taylor cones leading to beading during nanofibre formation. Additionally, low viscous polymers decrease the diameter of the nanofibres (344). This decrease in diameter and change in morphology during the modification of PAN nanofibres was in good agreement with findings previously reported by other studies (302,345).

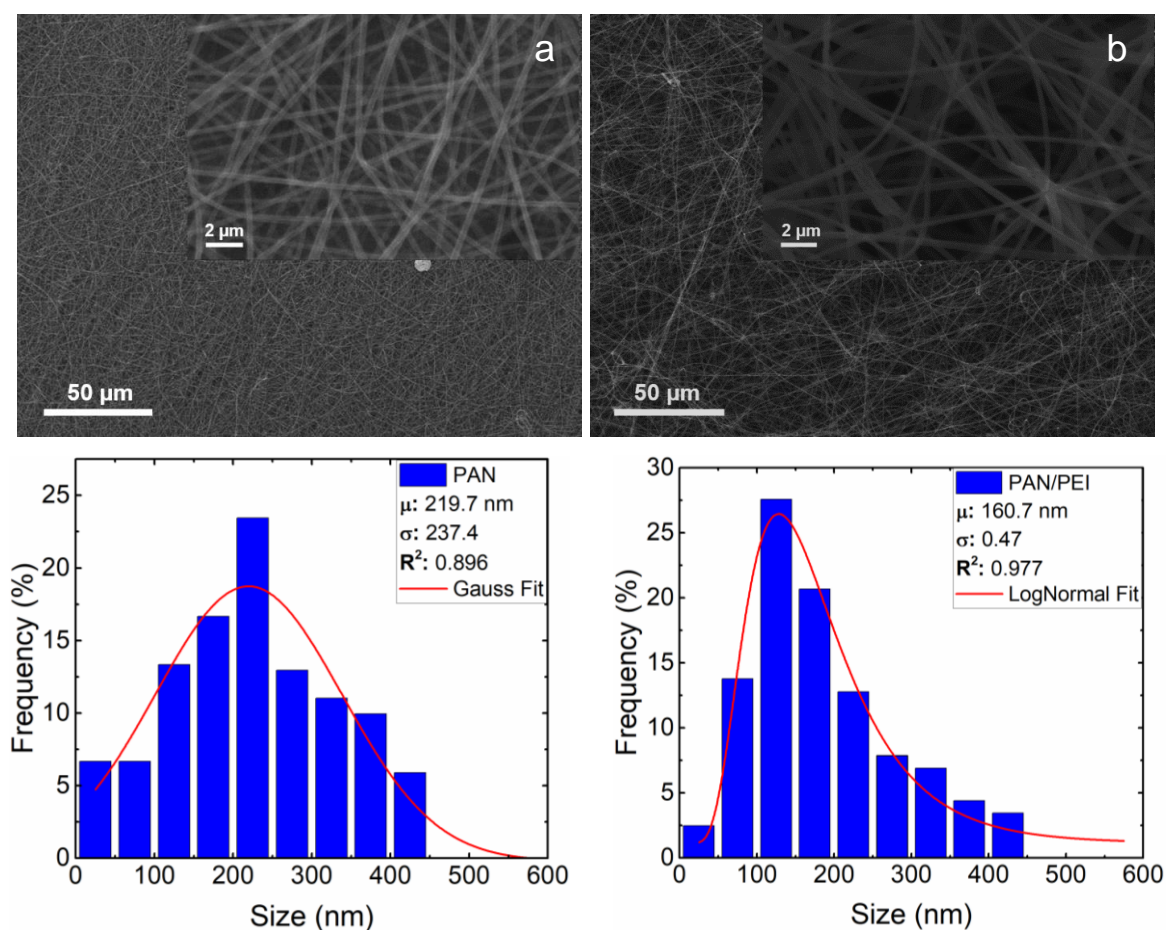


**Figure 3.1:** SEM micrographs of (a) PAN and (b) PAN-PEI nanofibres and their corresponding diameter distribution graphs.

### 3.3.2 Fourier transform infrared analysis of the nanofibres

FTIR spectroscopy was used to study the impact of imination on the chemical structure of PAN nanofibres. The FTIR spectra were obtained at a wavelength range of 4000 – 500  $\text{cm}^{-1}$  and the results are presented in **Figure 3.2**. A strong absorption peak at 2 241  $\text{cm}^{-1}$  was observed for PAN that corresponded to the stretching vibration of  $\text{C}\equiv\text{N}$ . The imination of PAN using PEI resulted in the disappearance of the intense peak of  $\text{C}\equiv\text{N}$ . The absorption peak at 3277  $\text{cm}^{-1}$  was assigned to the N-H vibration band. The additional absorption peaks at 1299, 1386, and 1656  $\text{cm}^{-1}$  (i.e., corresponding to the vibration bend of  $\text{C}=\text{N}$ ) and the peak at 1094  $\text{cm}^{-1}$  (i.e., corresponding to C-N bending) were observed on iminated PAN nanofibres. Thus, the PEI-chemically modified PAN was clearly formed as

indicated by the disappearance of the  $C\equiv N$  PAN functional group and the appearance of  $C=N$  and  $C-N$  functional groups (303–305,346).

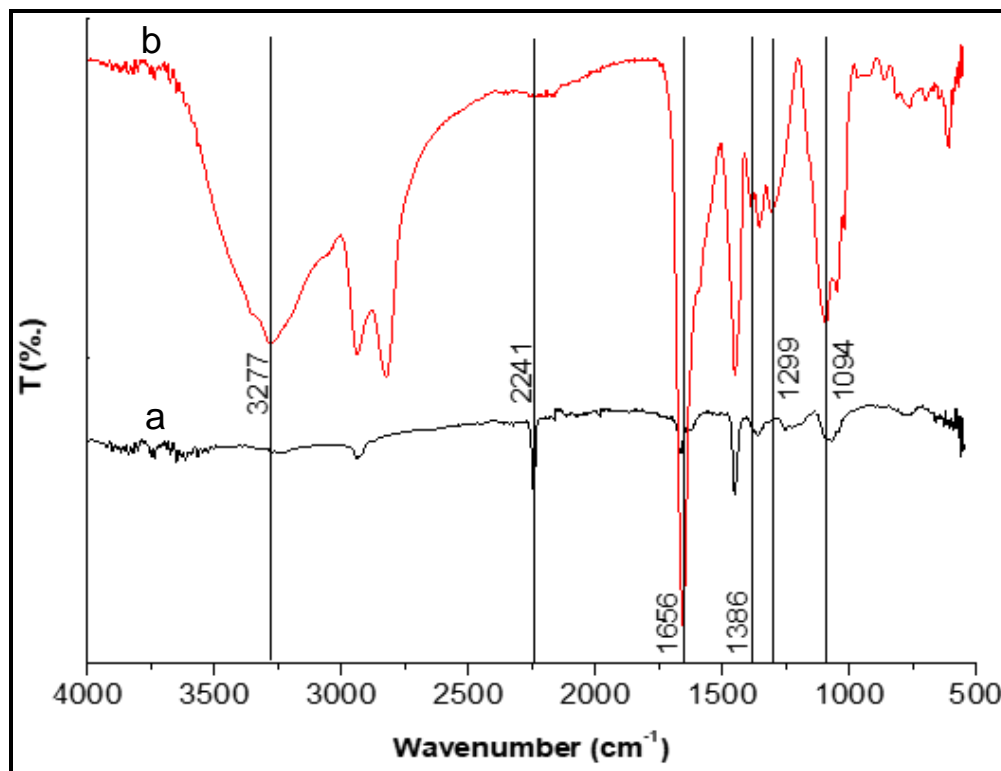


**Figure 3.2:** FTIR spectra of (a) PAN and (b) PEI-PAN modified nanofibres.

### 3.3.3 XPS analysis of nanofibres

The XPS analysis was carried out to further elucidate the imination of PAN nanofibres using hyperbranched PEI. The peak areas of survey spectra presented on **Figure 3.3a,b** were integrated to determine the percentage concentrations of C, N and O atoms. The imination of PAN nanofibres led to a decrease in C (79.2% to 76.1%) and N (20.7% to 19.1%) concentration while the O concentration increased from 0.17% to 4.80% (**Table 3.1**). The oxygen content in PAN nanofibres was due to the water molecules bound to the surface of the nanofibres. The bonding states (N-configurations) of the N atoms in the PAN nanofibres were determined by deconvolution of N1s spectra. The N1s peaks of PAN nanofibres were deconvoluted to at least five components peaks (**Table 3.2**). The

deconvoluted peaks were C-N (398.4eV), N-H (399.1eV), C-NH<sub>2</sub> (400.5eV), N-O (401.4eV) and elemental N<sub>2</sub> (402.9eV). Similarly, C-N, N-H, C-NH<sub>2</sub>, N-O and elemental N<sub>2</sub> were identified at 398.4eV, 399.7 eV, 400.6 eV, 401.5 eV and 402.7 eV respectively. C1s spectra of PAN nanofibres was also deconvoluted into at least five components including C-C, N-sp<sup>2</sup>-C, N-sp<sup>3</sup>-C/sp<sup>3</sup>-C, C-O, N-C=O/O-C=O at 283.8 eV, 285.6 eV, 286.8 eV, 287.8 eV, 288.7 eV respectively. Likewise, the similar components on IPAN were identified at 283.9 eV, 284.9 eV, 286.0 eV, 287.0 eV, 288.2 eV. The concentrations of the C-N, N-H, C-NH<sub>2</sub>, C-O, N-C=O/O-C=O generally increased on imination of PAN nanofibres (**Table 3.3**). This increase was attributed to the nitrogen-rich hyperbranched PEI and oxidation of the nanofibres. This increase in electron rich atoms suggests that iminated PAN nanofibres have strong electrostatic interactions with phenolic compounds. The XPS and FTIR results were subsequently used to estimate the imination scheme of PAN nanofibres (**Scheme 3.1**).

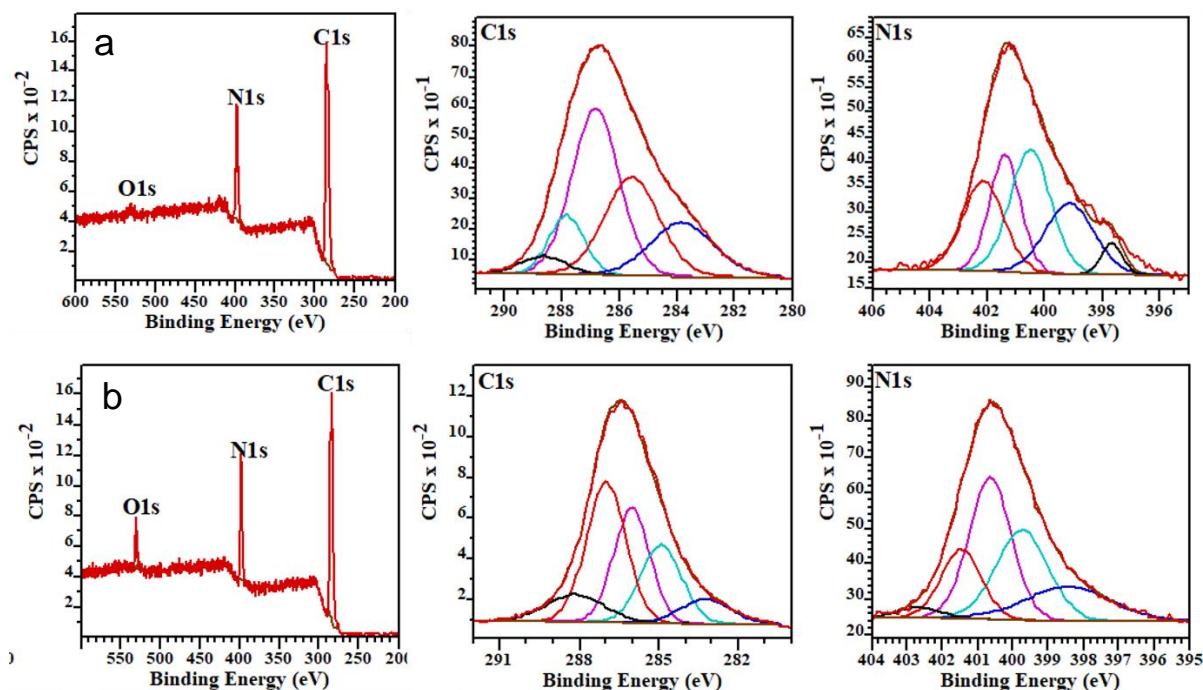


**Figure 3.3:** XPS analysis of iminated PAN nanofibres. (a) PAN and (b) PEI-PAN.

**Table 3.1:** Summary of atomic elements in iminated PAN nanofibres.

Samples	Elements				
	C (%)	N (%)	O (%)	N/C (%)	O/C (%)
PAN	79.16	20.67	0.17	0.2622	0.0021
I-PAN	76.09	19.11	4.80	0.2511	0.0562

**Table 3. 2:** Summary of fitted XPS of iminated PAN nanofibres.

Samples	Peaks				
	C-C (eV)	N-sp <sup>2</sup> -C (eV)	N-sp <sup>3</sup> -C/ sp <sup>3</sup> -C (eV)	C-O (eV)	N-C=O/O-C=O (eV)
PAN	283.84	285.57	286.83	287.84	288.65
I-PAN	283.94	284.91	286.01	286.99	288.17

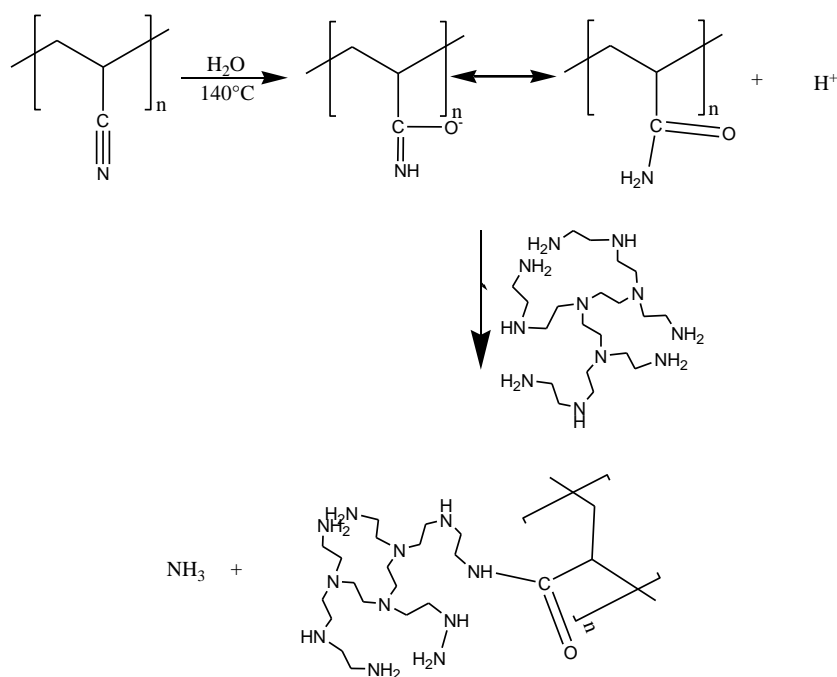
Samples	C-N (eV)	N-H (eV)	C-NH <sub>2</sub> (eV)	N-O (eV)	Elemental N2
	PAN	397.67	399.13	400.48	401.37
I-PAN	398.43	399.74	400.64	401.46	402.66

**Table 3.3:** Summary of concentration (%) of N-bonds and C-bonds for Iminated PAN nanofibres.

Peaks \ Samples	Concentration of N-bonds (%)				
	C-N (eV)	N-H (eV)	C-NH <sub>2</sub> (eV)	N-O (eV)	Elemental N2
PAN	4.18	21.19	30.42	21.88	22.32
I-PAN	17.65	27.80	35.51	16.42	2.62

Samples	Concentration of C-bonds (%)				
	C-C (eV)	N-sp <sup>2</sup> -C (eV)	N-sp <sup>3</sup> -C/ sp <sup>3</sup> -C (eV)	C-O (eV)	N-C=O (eV)/ O-C=O
PAN	17.59	27.56	39.83	10.68	4.34
I-PAN	8.33	20.53	26.16	34.69	10.29



**Scheme 3.1:** Preparation of iminated PAN nanofibres (334).

### 3.3.4 Zeta potential of nanofibres as a function of pH

The zeta potential of the PAN nanofibres was investigated to elucidate the effect of pH on the adsorption of phenols. The surface charge of the PAN nanofibres was measured at the pH range of 2.8-11 (**Figure 3.4**). The isoelectric point (IEP) of PAN nanofibres (i.e., pH of no net or neutral charge) was determined as 3.8. The surface charge of PAN nanofibres became positively and negatively charged at a solution of pH<3.8 and pH>3.8, respectively. The isoelectric point of PEI-modified PAN nanofibres was determined as 6.2, leading to a positive and negative charge at pH<6.2 and pH>6.2, respectively. For PAN nanofibres, the charge levelled-off at approximately -3.2 mV and at pH 4.3; while the negative charge of PEI-modified PAN kept increasing with increasing pH. Briefly, PEI is characterized by high electron density carrying nitrogen atoms (lone pairs on nitrogen atoms). These free lone pairs have high current density hence they highly charged. Remarkably, PEI-modified PAN nanofibres displayed a more positive and a more negative surface charge than those of PAN nanofibres at extreme acid and caustic conditions, respectively. A negatively-charged surface has a direct impact on the adsorption of phenols. Specifically, phenols form phenolate ions at pH values

higher than their pKa values (295). Repulsive forces would arise from negatively-charged phenolate ions and the adsorbent surface at a  $\text{pH} > \text{IEP}$  and would consequently reduce the adsorption capacity of the nanofibres.

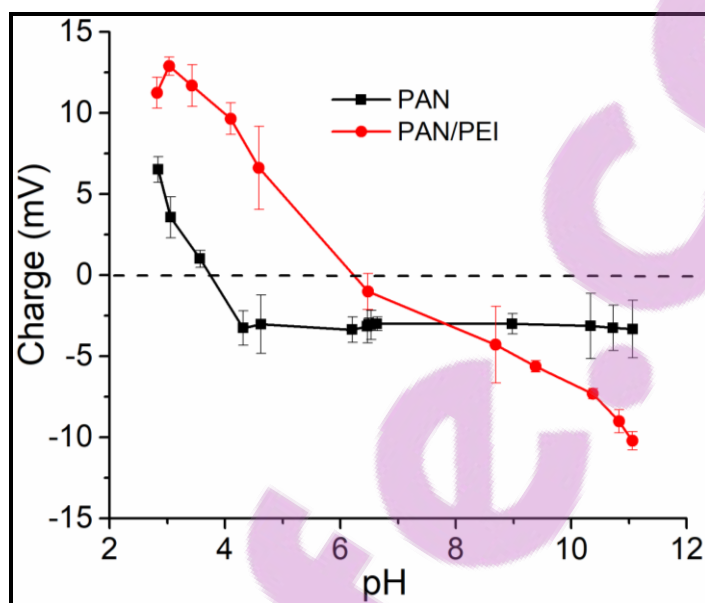


**Figure 3. 4:** Surface charge of (a) PAN and (b) PEI-PAN modified nanofibres.

### 3.3.5 Batch adsorption of phenols using PAN nanofibres

The adsorption of chlorophenol and nitrophenol using PAN and PEI-modified PAN nanofibres was studied by batch adsorption experiments. Phenolic compounds are characterised by hydrophobic aromatic functional groups which interact with the hydrophobic surface of MD membranes by a hydrophobic-hydrophobic mechanism. The adsorption rates were modelled using first-order and second-order kinetics. Langmuir, Freundlich, and Dubinin-Radushkevich (D-R) isotherms were used to elucidate the mechanism of adsorption.

The zeta potential experiments indicated that the pH of the solution impacted the electrostatic properties of adsorbents (i.e., ionic state at the surface of the adsorbents) and the adsorption potential of the phenolic compounds (302). Therefore, the adsorption experiments were conducted at the pH range 5-11. The

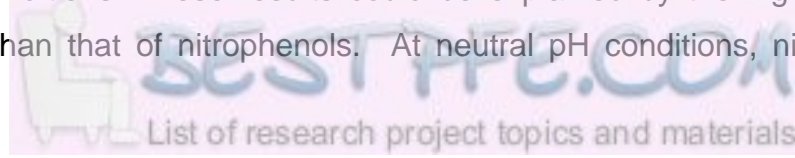
adsorption capacities were higher at acidic pH and gradually decreased towards neutral pH for all adsorbents (**Figure 3.5a**). Further increase in pH of the solution towards alkaline conditions led to rapid decrease in adsorption of phenols. At pH values higher than their pKa values, phenols form stabilised phenolate ions leading to weak interactions with the adsorbent active surface (295). Additionally, the negative phenolate ions form stronger electrostatic repulsive forces leading to weak interactions with the active surface. A faster decrease in adsorption efficiency was observed at pH>9 for chlorophenol on both PAN and PAN/PEI nanofibres (**Figure 3.5a**). The high pKa of chlorophenol (i.e., 9.1) and the isoelectric points of PAN and PAN/PEI nanofibres (i.e., 3.8 and 6.2, respectively) would induce strong electrostatic repulsive forces at caustic conditions (i.e., at pH>9 where both nanofibres and chlorophenol are negatively charged). On the other hand, due to the lower pKa of nitrophenol (i.e., 7.5), the adsorption capacity of both nanofibres experienced a faster decrease at more basic conditions. Briefly, at approximately neutral pH conditions, nitrophenols form conjugate ions which lowers their energy and consequently decreases their chemical interactions with the adsorbent (346); therefore, reducing the adsorption of phenols. Remarkably, PAN/PEI nanofibres showed a higher adsorption capacity for chlorophenol than for nitrophenol, and a higher adsorption capacity than PAN nanofibres for each phenolic species in the whole pH range tested (**Figure 3.5a**). For instance, at pH 7 the adsorption capacity of PAN/PEI and PAN nanofibres towards chlorophenol was 31.8 mg/g and 30.2 mg/g, respectively; while those of PAN/PEI and PAN nanofibres towards nitrophenols were 26.9 mg/g and 21.7 mg/g, respectively. This was ascribed to the high electron density present in PAN/PEI nanofibres compared to PAN nanofibres as shown in surface charge and XPS results.

The effect of the initial concentration of chlorophenol and nitrophenol in solution on the adsorption capacity of the nanofibres was investigated at the concentration range of 20-100 mg/L. The experiment was conducted at pH = 7 due that the nanofibres showed highest adsorption capacities from neutral to acidic conditions. The adsorption capacity of phenols rapidly increased with increasing concentration of phenolic species in solution (**Figure 3.5b**). Interestingly, these adsorption

capacities increased at a slightly slower rate beyond a phenolic concentration of 80 mg/L. The increase in adsorption capacity as a function of phenol concentration in solution could be attributed to the higher adsorbate driving force that overcomes the mass transfer resistance between the aqueous and solid phases. Furthermore, the increase in initial concentration of the adsorbate enhanced the diffusion rate to the active adsorption sites leading to an increase in adsorption capacity (347,348). However, a further increase in initial concentration would cause saturation at the active sites, resulting in a slightly slower increase in the adsorption capacity of the nanofibres towards phenolic species (324,349).

The adsorbents dose was varied from 3 mg to 30 mg to determine their effect towards their adsorption capacity. The experiments were conducted at pH 7 and 80 mg/L phenol concentrations. The adsorption capacity of PAN nanofibres towards chlorophenol and nitrophenol as a function of PAN nanofibre doses is presented in **Figure 3.5c**. The adsorption capacity increased rapidly at adsorbent doses of 3 mg to 20 mg for all nanofibres. The increase in adsorbent dose resulted in an increase in adsorption active sites (350), which facilitated a rapid uptake of phenols. The adsorption capacity of all adsorbents proceeded at a slower rate at an adsorbent dose of beyond 20 mg; thus, approaching a maximum adsorption capacity.

The adsorption kinetics of chlorophenol and nitrophenol were studied at a pH of 7 and at an initial concentration of 80 mg/L and 25 mg of adsorbent. The results presented on **Figure 3.5d** demonstrated that the adsorbent/adsorbate contact time influences the process of adsorption. The adsorption capacity of phenols increased with contact time until steady state was reached where no more phenols were adsorbed. The adsorption process was rapid in the first 30 min of contact time. The rate of adsorption slowed down beyond 30 min until reaching equilibrium at 60 min for all adsorbents. In addition to iminated PAN showing higher adsorption capacities than their counterpart PAN nanofibre membranes, the adsorption of phenols followed the trend of chlorophenols>nitrophenols at all tested batch conditions. These results could be explained by the higher pKa of chlorophenols than that of nitrophenols. At neutral pH conditions, nitrophenols



form stable phenolate ions which reduce their adsorption rate. In the case of chlorophenols, their higher pKa value (i.e., 9.1) does not promote the formation of phenolate ions; hence, inducing higher adsorption rates. The results are comparable with findings previously reported by other studies (295,313,316,317,324,349,351–353). For instance, 13.8 mg/g was reported as the maximum adsorption capacity of chitosan-modified salicylaldehyde towards p-nitrophenol (316). Furthermore, the adsorption capacity of chitosan-coated perlite beads towards o-chlorophenols was reported as 85 mg/g (313). Remarkably, adsorption of phenols on activated carbon was 5-fold greater than the adsorption capacity reported in this study. For instance, Fierro *et al.* (2008) reported an adsorption capacity of 238.10 for phenol on activated carbon (354).

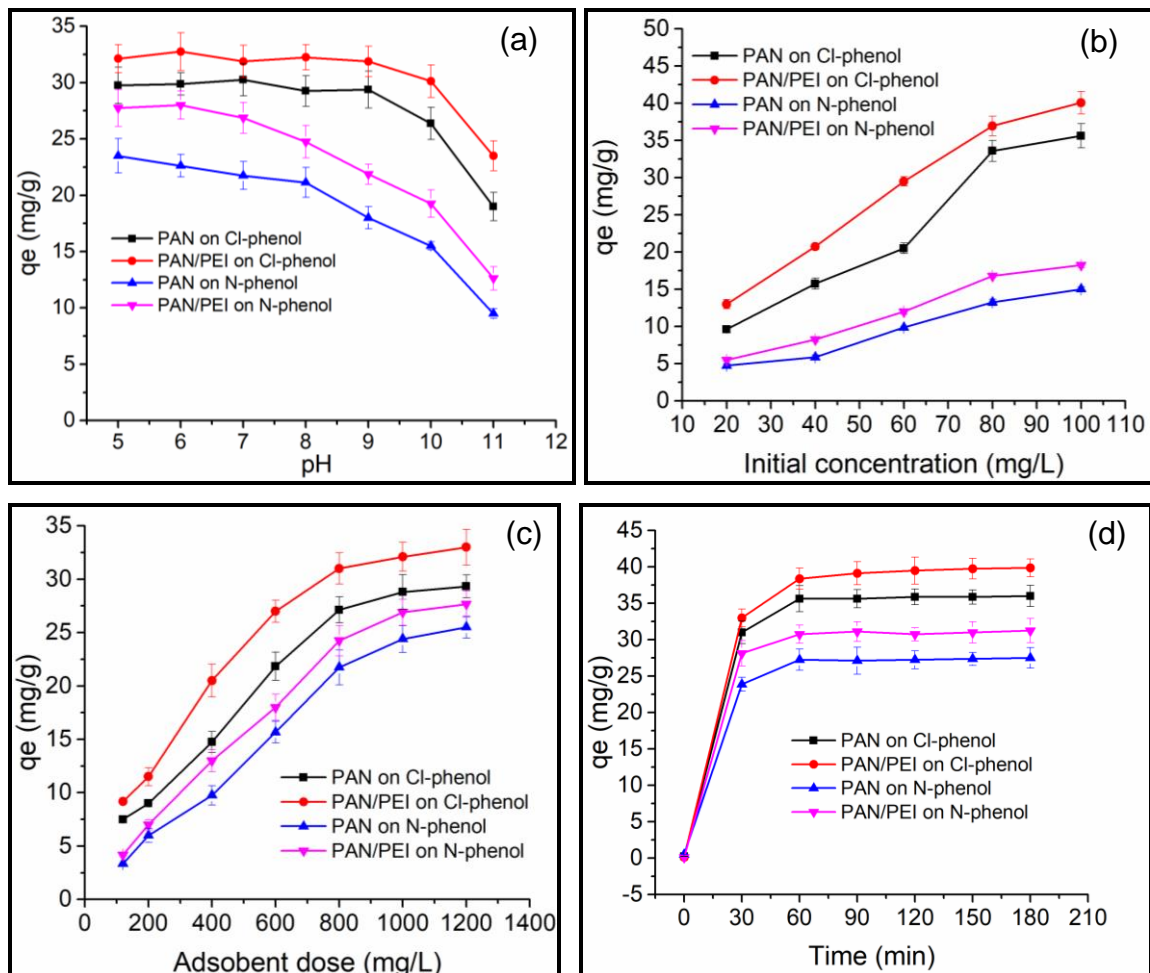


**Figure 3.5:** Effect of (a) pH, (b) phenols initial concentration, (c) adsorbent dose, and (d) contact time on the adsorption of chlorophenol and nitrophenol on PAN and PEI-modified PAN nanofibres.

### 3.3.6 Comparison of adsorption to other materials

The adsorption of chlorophenols and nitrophenols onto PAN and PEI-modified (iminated) PAN nanofibres was compared to other materials from previous studies (316,317,324,349,351,352) (**Table 3.4**). Activated carbon exhibited the highest adsorption capacities as  $380.2 \text{ mg.g}^{-1}$  and  $436 \text{ mg.g}^{-1}$  for o-chlorophenol and p-nitrophenol, respectively. Therefore, activated carbon out performs many adsorbents for the removal of phenolic compounds from water. However, other adsorbents are generally comparable to the findings of this study, demonstrating the potential of iminated PAN nanofibres for removal of phenolic compounds from water sources.

**Table 3.4:** Comparison of PAN and iminated PAN nanofibres to other materials on the adsorption of o-chlorophenol and p-nitrophenol.

Adsorbents	Adsorption capacity (mg/g)		Ref.
	o-chlorophenol	p-nitrophenol	
Chitosan	–	1.98	(316)
Chitosan-abrus blended beads	204	278	(355)
Chitosan-coated perlite beads	263	322	(313)
Cross-linked cyclodextrin	–	41.11	(316)
Olive-Stone activated carbon		436	(356)
Salicyladehyde-modified chitosan	–	44.92	(316)
Cyclodextrin-modified chitosan	–	20.56	(316)
Chitosan-calcium alginate blended beads	97	–	(357)
Activated carbon	380.2	422.1	(358)
Polyacrylonitrile nanofibres	36.1	25.5	This study
Iminated polyacrylonitrile nanofibres	39.9	31.3	This study

### 3.3.7 Adsorbent regeneration and isolation

The regeneration of adsorbents is an important and sustainable goal in adsorption processes (295,316). The ability of the adsorbent to be regenerated allows its repeated use before disposal (316). Furthermore, regeneration provides additional

space for the isolation of the adsorbent, resulting in a safe disposal. Therefore, regeneration studies were conducted at five cycles of adsorption and the results are presented in **Figure 3.6a**. The optimised conditions for adsorption used in the regeneration study were: pH of 7, initial concentration of 80 mg/L, 25 mg of adsorbent, and contact time of 60 min. Owing to their solubilities in ethanol, the phenol species were desorbed from the adsorbents using ethanol. To further ensure high isolation efficiencies of phenols from PAN and PAN/PEI nanofibres, NaOH was used to promote formation of stable phenolate ions at high pH values. The decrease in adsorption capacity was 5-10%, 14-26%, 21-41% and 35-50% for regeneration cycle 2, 3, 4, and 5, respectively, with respect to cycle 1 (**Figure 3.6b**). These decays in adsorption capacity suggest irreversible adsorption from phenolic species on the nanofibres (i.e. they form strong bonds) (359). The decay in adsorption efficiency of the adsorbents increased drastically with increasing regeneration cycles, indicating the capacity of both PAN and PAN/PEI nanofibres to be reused for at least three times. The PAN/PEI nanofibres showed the highest decrease in adsorption capacity during the 5<sup>th</sup> cycle. This was explained by the chemisorption mechanism of PAN/PEI nanofibres towards the phenols. In previously reported studies, the decay in the adsorption of nitrophenols and chlorophenols on chitosan beads was in the range of 6-20%, 18-31% for second and third regeneration cycles; further demonstrating the possibility of using these adsorbents for up to six cycles (313,316). These findings are therefore in agreement with the results of this current research.

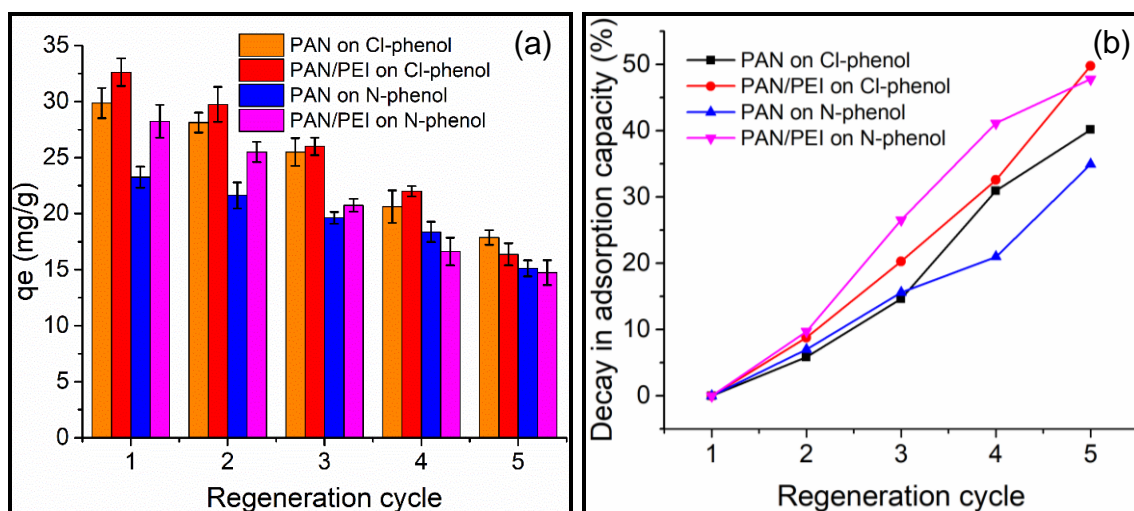


**Figure 3.6:** Regeneration studies and their corresponding decay in adsorption efficiency.

### 3.3.8 Adsorption kinetic studies

Adsorption kinetic studies of chlorophenol and nitrophenol on PAN and PAN/PEI nanofibre membranes were modelled using pseudo-first-order and pseudo-second-order kinetics. The rate constants were determined from the linearised plots presented in **Figure 3.7a,b** and were subsequently summarised and given in **Table 3.5**. The  $R^2$  values of the linearised plots were used to determine the kinetic model that best fits the adsorption of phenols onto the nanofibres. Considering the reported  $R^2$  values, the adsorption of phenols followed pseudo-second order kinetics, i.e., the coefficients of determination ( $R^2$ ) were higher ( $<0.999$ ) than those of pseudo-first-order kinetics ( $>0.966$ ). The rate constants for pseudo-first-order kinetics ( $k_1$ ) ranged from  $-0.036$  to  $-0.029 \text{ min}^{-1}$ ; while the rate constants of pseudo-second-order kinetics ( $k_2$ ) ranged from  $0.320$  to  $0.678 \text{ g/mg-min}$ , further suggesting that the adsorption of phenols onto PAN/PEI nanofibres best fits pseudo-second-order kinetics. The pseudo-second-order kinetic rate constants were found to be higher on nitrophenols and lower on chlorophenols, indicating that the adsorption of the former would rapidly reach equilibrium while adsorption of the latter would proceed for longer periods of time.

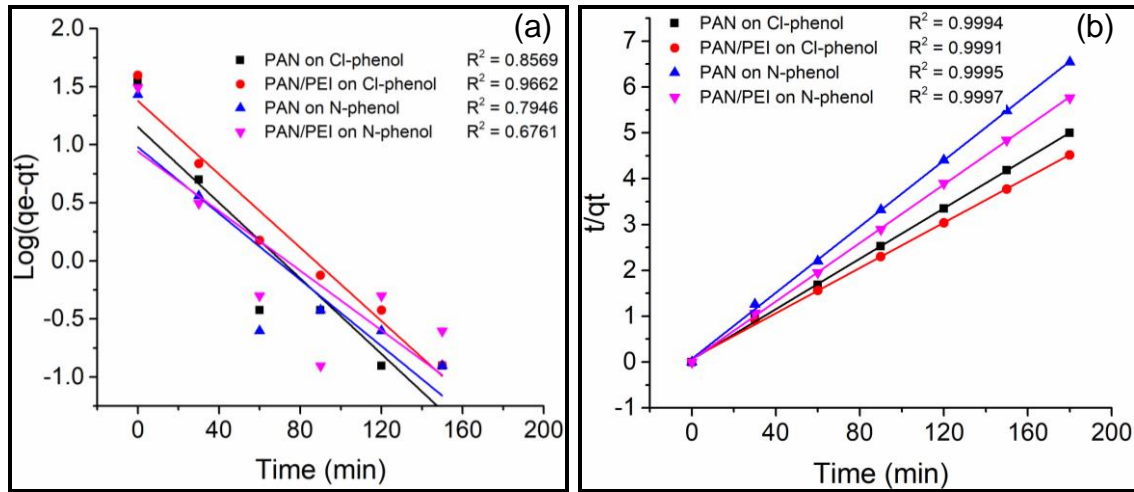


**Figure 3.7:** Modelling of (a) first-order and (b) second-order adsorption kinetics.

**Table 3.5:** Kinetics constants.

	First-order kinetics		Second-order kinetics	
	R <sup>2</sup>	k <sub>1</sub> (min <sup>-1</sup> )	R <sup>2</sup>	k <sub>1</sub> (g/mg·min)
<b>Chlorophenol</b>				
PAN	0.8569	-0.00374	0.9994	0.49505
PAN/PEI	0.9662	-0.03636	0.9991	0.32061
<b>Nitrophenol</b>				
PAN	0.7946	-0.03286	0.9995	0.51302
PAN/PEI	0.6761	-0.02952	0.9997	0.67801

### 3.3.9 Adsorption isotherms

Adsorption isotherms are key tools that assist in understanding the mechanisms of adsorption processes (312). Langmuir and Freundlich isotherms were used to determine the adsorbate layer formation on the surface of the adsorbent while the Dubinin-Radushkevich (D-R) model isotherm was used to determine the interaction (chemical or physical) of the adsorbate and the adsorbent.

The Langmuir and Freundlich isotherm plots are presented in **Figure 3.8a,b**. The Langmuir constants for adsorption of chlorophenol and nitrophenol were in the range of -0.0549 to -0.0256 mg/g while those of the Freundlich isotherm ranged between 191 and 55667 mg/g. In all cases, the values of the separation factor ( $R_L$ )

for the Langmuir isotherm were lower than 1, indicating that the adsorption of phenols onto PAN nanofibres did not follow the Langmuir isotherm (**Table 3.6**). In addition to dimensional factors, the correlation coefficients ( $R^2$ ) showed a better fit on the linear plots of the Freundlich isotherm model compared to those of the Langmuir isotherm (**Table 3.6**); suggesting that the adsorption of phenols onto PAN nanofibres followed the Freundlich isotherm. The heterogeneity factor ( $n$ ) was lower than 1 (**Table 3.6**), indicating that the adsorption of the phenols formed multiple layers on the surface of the adsorbents. This multiple layer formation would be induced by  $\pi$ - $\pi$  interactions between the benzene rings of the phenols conjugated  $\pi$  cloud (346). These findings were in good agreement with results previously reported by other studies (309,313,316).

The interaction between phenols and PAN nanofibres was evaluated using the D-R isotherm model. The linearised plots derived from the effect of temperature are presented in **Figure 3.9**. The mean absorption free energy ( $E$ ) was used to determine the adsorption mechanism. Previous studies suggested that chemisorption occurs when  $E = 8$  to  $16$  kJ/mol; while physisorption occurs when  $E < 8$  kJ/mol (295,312). The value of  $E$  is the free energy required to transfer 1 mol of the adsorbate from the bulk of the solution to the active site of adsorption and is an indication of a weak interaction between the adsorbate and the adsorbent leading to physical interaction. The inverse is therefore true for the formation of chemisorption (313). The values of  $E$  for adsorption of chlorophenol and nitrophenol on PAN nanofibres were 3.02 kJ/mol and 2.38 kJ/mol indicating the adsorption mechanism to be physical. However, imination of the PAN nanofibres led to chemisorption as the adsorption mechanism for both phenols ( $E = 8.41 - 10.92$  kJ/mol). This observation could be explained by the chemical interaction between the electron-rich imine group on PAN/PEI nanofibres and benzene groups on phenols with delocalised electrons (346,360).

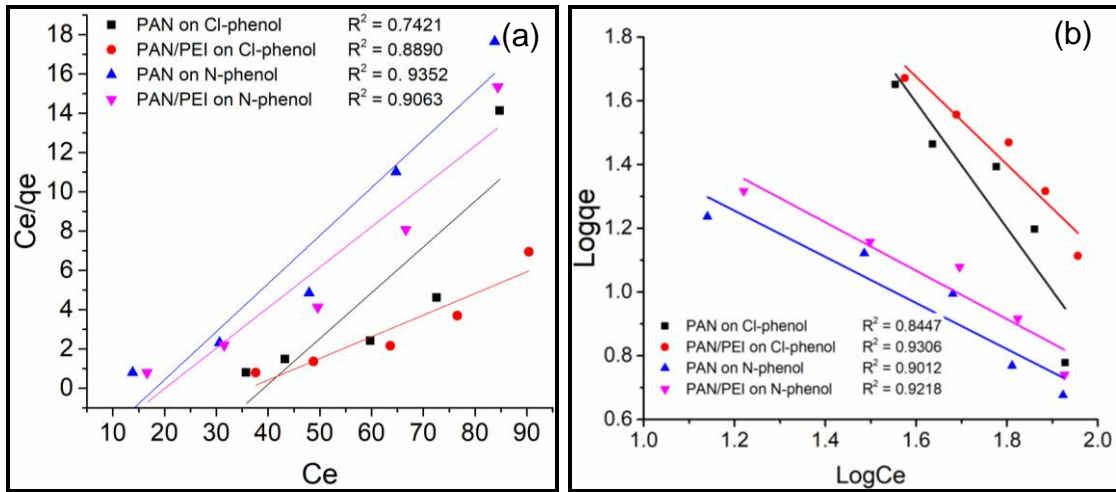


**Figure 3.8:** Plots of (a) Langmuir and (b) Freundlich adsorption isotherms for adsorption of phenols by PAN and PAN/PEI nanofibres.

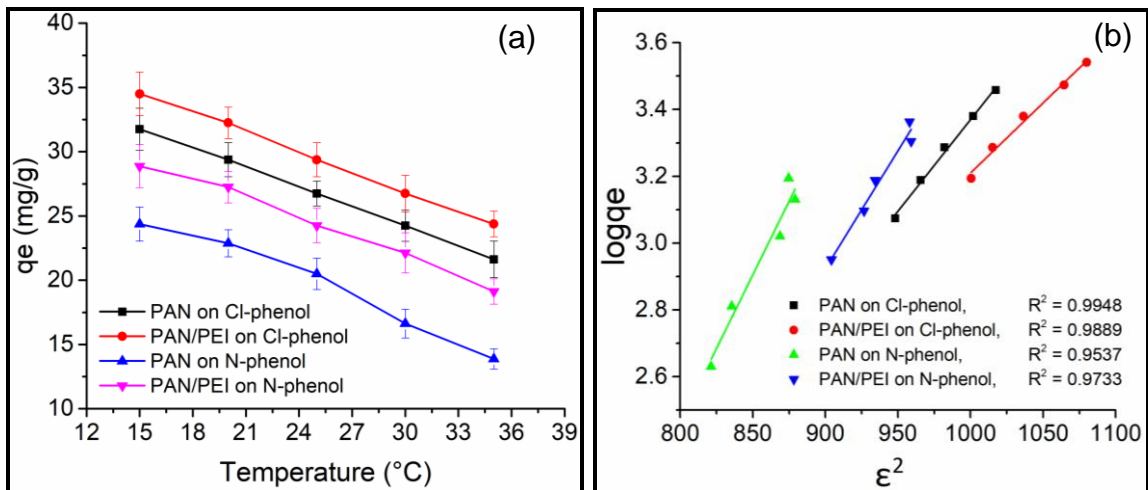


**Figure 3.9:** Modelling of adsorption mechanism. (a) Effect of temperature and (b) D-R model.

**Table 3.6:** Adsorption isotherm constants.

	Langmuir			Freundlich			D-R model	
	$R_L^2$	$R_L$	$K_L$	$R_F^2$	$K_F$	$n$	$\beta$	$E$ (kJ/mol)
<b>Chlorophenol</b>								
PAN	0.7421	-0.6432	-0.0256	0.8447	55667	-0.508	0.0548	3.0206
PAN/PEI	0.8890	-0.5694	-0.0275	0.9306	7531	-0.727	0.0042	10.924
<b>Nitrophenol</b>								
PAN	0.9352	-0.2227	-0.0549	0.9012	132	-1.383	0.0881	2.3823
PAN/PEI	0.9063	-0.2514	-0.0498	0.9218	191	-1.317	0.0071	8.4156

### 3.4 Conclusion

Polyacrylonitrile nanofibres (PAN) were successfully synthesised and evaluated for removal of phenols from aqueous solutions. *In-situ* imination of the nanofibres (PEI-modification) enhanced the adsorption capacity of PAN nanofibres for the phenolic species tested. The optimum conditions for adsorption of the phenols onto PAN nanofibres were: pH of 7, initial nitrophenols or chlorophenols concentration of 80 mg/L, adsorbent dose of 25 mg, and contact time of 60 min, leading to adsorption capacities ranging from 27.25 to 38.37 mg/g for PAN and PEI-modified nanofibres, respectively. Due to the formation of stable phenolate ions at high pH conditions, the adsorption efficiency of nitrophenols was generally lower than that of chlorophenols. Multilayer adsorption of the phenolic species on the surface of the nanofibres was observed. Remarkably, the mechanism of adsorption between phenols and PAN or PEI-modified nanofibres was suggested as physisorption and chemisorption, respectively. The nanofibres efficiently removed phenolic species from aqueous solution during three regeneration cycles of the adsorbents. These results indicate that PEI-modified nanofibre membranes are the promising pretreatment materials for the removal of compounds bearing hydrophobic functional groups in MD processes. These nanofibres were therefore incorporated into the pretreatment filter for integrated MD purification of the environmental brackish water samples.

# CHAPTER 4

## ENHANCED FLUX IN DIRECT CONTACT MEMBRANE DISTILLATION USING SUPERHYDROPHOBIC PVDF NANOFIBRE MEMBRANES EMBEDDED WITH ORGANICALLY MODIFIED SiO<sub>2</sub> NANOPARTICLES

---

### 4.1 Introduction

Water scarcity and water quality are major threats currently impacting human populations in every continent (5,44,361,362). Water shortage is exacerbated by poor management and climate change, thus inducing droughts and the inability to meet the high water demand arising from rapid population growth (363,364). While 70% of the planet is covered with water (i.e., mainly occurring as seawater or brackish water), only 2.5% is available as fresh water. However, only 1% of fresh water is accessible since the rest is trapped in glaciers and icecaps. (4,56) Therefore, desalination of seawater and brackish water using alternative, economically viable, and sustainable processes is of paramount importance. Membrane Distillation (MD) is currently being envisaged as a promising cost-effective technology for the production of drinking water from saline solutions (164). A detailed description of MD technology is provided in **Chapter 2**. Despite extensive research and recent breakthroughs in the field of MD (38,39,103), membranes with combined high mechanical stability, porosity, and super-hydrophobicity to prevent wetting while maintaining high rejection and water flux have not been fully explored and require additional optimisation for a successful industrial implementation.

This chapter presents novel MD membranes bearing properties addressing the challenges associated with wetting and porosity. The synthesis of electrospun super-hydrophobic PVDF nanofibre membranes decorated with organically-modified silica nanoparticles (SiO<sub>2</sub>NPs) was conducted. The SiO<sub>2</sub>NPs were prepared using a novel green method involving the use of apple extract as the

reducing agent, followed by silane modification using octadecyltrimethoxysilane (OTMS), N-octadecyltrichlorosilane (ODTS), and chloro(dimethyl)-octadecylsilane (Cl-DMOS). These silane reagents are characterised by long-chain bulky alkyl groups, possess antiwetting properties (i.e., rendering surfaces superhydrophobic), form self-assembled layers on silicon dioxides (156,157,160), and have not been explored in the preparation of SiO<sub>2</sub>NPs-incorporated PVDF nanofibre membranes for their application in MD processes (156,157,160–162). The incorporation of these organically-modified SiO<sub>2</sub>NPs could provide PVDF nanofibres with a high void ratio, interconnected open structure, high surface area-to-volume ratio, highly ordered polymer chains with a more controlled structure, anti-wetting properties, and enhanced performance (i.e., higher salt rejection and water flux) (34).

## 4.2 Materials and Methods

### 4.2.1 Reagents

Polyvinylidene fluoride (PVDF) (MW = 534,000 g.mol<sup>-1</sup>), tetraethyl orthosilicate (TEOS) (reagent grade, 98%), N,N-dimethylacetamide (DMAc) (Puriss p.a., 99.5%), acetone (ACS reagent, 99.5%), absolute ethanol (ACS reagent, 99.9%), toluene (ACS reagent, 99.7%), octadecyltrimethoxysilane (OTMS) (technical grade, 90%), and 30 mL PP/PE eccentric tip syringe equipped with a blunt tip dispensing needle were purchased from Sigma Aldrich (Germany) while N-octadecyltrichlorosilane (ODTS) (reagent grade, 95%), chloro(dimethyl)-octadecylsilane (Cl-DMOS) (reagent grade, 95%) were purchased from Alfa Aesar (Ward Hill, USA). Granny Smith apple extract was purchased from Makolobane Farmers Enterprises (South Africa). Deionised water (Direct-Q®, Merck Millipore) was used for solution preparation.



#### 4.2.2 Synthesis of SiO<sub>2</sub>NPs

The SiO<sub>2</sub>NPs were prepared using a simplified and novel green chemical reduction method involving the use of apple extract as a reducing agent. Apple extract was used in excess to achieve a complete reduction reaction. Ethanol (25 mL), apple extract (10 mL), and 0.05 M NaOH (50 µL) were ultrasonicated in a conical flask for 2 h. Tetraethyl orthosilicate (TEOS) (2 mL) was added to the content of the flask and ultrasonication was continued for 5 h. The mixture of the products was centrifuged at 48 000 rpm. The resulting SiO<sub>2</sub>NPs were washed with ethanol and dried in an oven at 60°C for 24 h.

#### 4.2.3 Modification of SiO<sub>2</sub>NPs

The modification of the as-synthesised SiO<sub>2</sub>NPs was conducted by dispersing 10 g of pristine SiO<sub>2</sub>NPs in three conical flasks containing 100 mL of toluene. After adding the silane reagent (ODTS, OTMS, or Cl-DMOS) to flasks 1, 2, and 3, respectively, the flasks were stirred for 5 h under an inert atmosphere prior to centrifugation. To remove any excess silane reagent, the resultant modified SiO<sub>2</sub>NPs were washed twice with absolute ethanol. Finally, these organically-modified SiO<sub>2</sub>NPs were dried in an oven at 60°C for 24 h.

#### 4.2.4 Synthesis of PVDF nanofibre membranes

Nanofibre membranes were synthesised using an electrospinning technique following the previously reported studies (120,264). Briefly, 15% (w/v) PVDF prepared in an acetone/DMAc mixed solvent system (acetone/DMAc 3:2) was transferred to a 30 mL plastic syringe fitted with a 0.8 mm internal diameter needle. The syringe was placed on a single syringe pump. A high voltage generator was used to induce an electric field between the collecting plate and the tip of the needle. The positive terminal of the DC generator was connected to the tip of the syringe needle and the negative terminal was connected to the aluminium foil (rotating collecting plate). The nanofibres were synthesised under the following optimised electrospinning conditions: syringe injection flow rate of 1.0

mL/h (i.e. 25 h to electrospin 25 mL of PVDF solution), distance of 14 cm between the aluminium foil and the tip of the needle, and a voltage of 23 kV at room temperature. The electrospun PVDF nanofibres were dried in an oven at 40°C for 24 h to remove moisture. Also, PVDF nanofibre membranes were embedded with 1.0% (w/v) organically-modified SiO<sub>2</sub>NPs to enhance their super-hydrophobicity by blending the PVDF solution with 1.0% (w/v) SiO<sub>2</sub>NPs and electrospun *in situ*.

#### **4.2.5 Characterisation of PVDF nanofibre membranes and organically-modified SiO<sub>2</sub>NPs**

The dispersion, shape, and size of the organically-modified SiO<sub>2</sub>NPs were characterised using Transmission Electron Microscope (TEM, JEOL Jem-2010). ImageJ software was used to calculate the sizes of the NPs using the acquired TEM micrographs. A Scanning Electron Microscope (SEM, JEOL STM – IT300) and an Atomic Force Microscope (AFM, WITec Alpha 300 A, TS-150) were used to determine the surface morphology and roughness of the membranes. The hydrophobicity and the mechanical strength of the membranes were determined using contact angle measurements and stress-strain graphs. The contact angle was measured using a DSA30E Kruss drop shape analyzer (Kruss GmbH, Hamburg, Germany) while the stress-strain graphs were obtained using a Small Angle X-ray Scattering (SAXSpace, Anton Paar GmbH, Graz, Austria) system equipped with a universal extensional fixture. The Liquid Entry Pressure (LEP) was measured using a dead-end cell with an active membrane area of  $2 \times 10^{-3} \text{ m}^2$ . The cell was filled with saline water ( $30 \times 10^3 \text{ mg/L NaCl}$ ) and the inlet pressure of the feed solution was gradually increased to 2 kPa until the first liquid droplet appeared at the permeate side. The membrane pore sizes were measured using the dry-to-wet method in a liquid expulsion Capillary Flow Porometer (3G Series, Quantachrome Instruments, USA).

#### 4.2.6 Statistical analysis of organically-modified SiO<sub>2</sub>NPs sizes

One-way analysis of variance (ANOVA) was conducted to study the variation in sizes of the organically-modified SiO<sub>2</sub>NPs using Statistical Package for the Social Sciences (SPSS). However, One-way ANOVA is an omnibus test that does not indicate which groups are statistically different from each other in terms of size. Therefore, the Post-Hoc Test (Fisher's Least Significant Difference) was used to determine individual NPs differing in size. The formulated null hypothesis was set as  $\mu_1 = \mu_2 = \mu_3 = \mu_4$  (i.e., the mean size of SiO<sub>2</sub>NPs prepared under different modification methods are the same); while the alternative hypothesis would indicate a statistically significant difference in mean sizes.

#### 4.2.7 Performance of the PVDF nanofibre membranes

The performance of the PVDF nanofibre membranes embedded with organically-modified SiO<sub>2</sub>NPs was tested on a Direct Contact Membrane Distillation (DCMD) laboratory-scale set-up using a 30×10<sup>3</sup> mg/L NaCl solution, (i.e., slightly below the concentration of dissolved salts in seawater). The temperature of the feed was increased from 20°C to 80°C using a heating circulator (Polyscience, model 71, USA) while the permeate temperature was kept constant at 20°C in counter-current mode using a heating/cooling circulator (Julabo, F26, Germany). Each temperature condition was allowed 25 min to stabilise before recording measurements. A flow rate of 0.75 L/min was set for the NaCl solution (30×10<sup>3</sup> mg/L) and the coolant water (conductivity ≤ 0.10 μS/cm). The conductivity of the water was measured using a Shimadzu conductivity detector (Shimadzu Corporation, Kyoto Japan) to determine the salt rejection efficiencies. The water flux was calculated based on the mass of water transported from the feed (i.e., through SiO<sub>2</sub>NPs-embedded PVDF membrane; surface area: 1.25×10<sup>-2</sup> m<sup>2</sup>) to the permeate. The amount of water transported through the membrane in the state of vapour was determined by measuring the weight increment of the coolant water using a Kern & Sohn GmbH, EMB 3000\_1 weighing balance. The permeate flux ( $J_{\text{water}}$ ) and rejection efficiency (R) in MD were determined using the following **Equations** (108,365,366):

$$J_{water} = \frac{\Delta V}{\Delta t \cdot A_m} \quad (4.1)$$

where  $\Delta V$  is the volume of the permeate collected at a time interval  $\Delta t$ , and  $A_m$  is the membrane surface area. The difference in volume ( $\Delta V$ ) of the water collected could be calculated from the change in mass ( $\Delta m$ ) of the water collected (**Equation 4.2**), where 0.997 kg/L is used as the density ( $\rho$ ) of water at room temperature.

$$\Delta V = \frac{\Delta m}{\rho} \quad (4.2)$$

$$R(\%) = \frac{C_f - C_p}{C_f} * 100 \quad (4.3)$$

Where  $C_f$  is the concentration of the feed stream

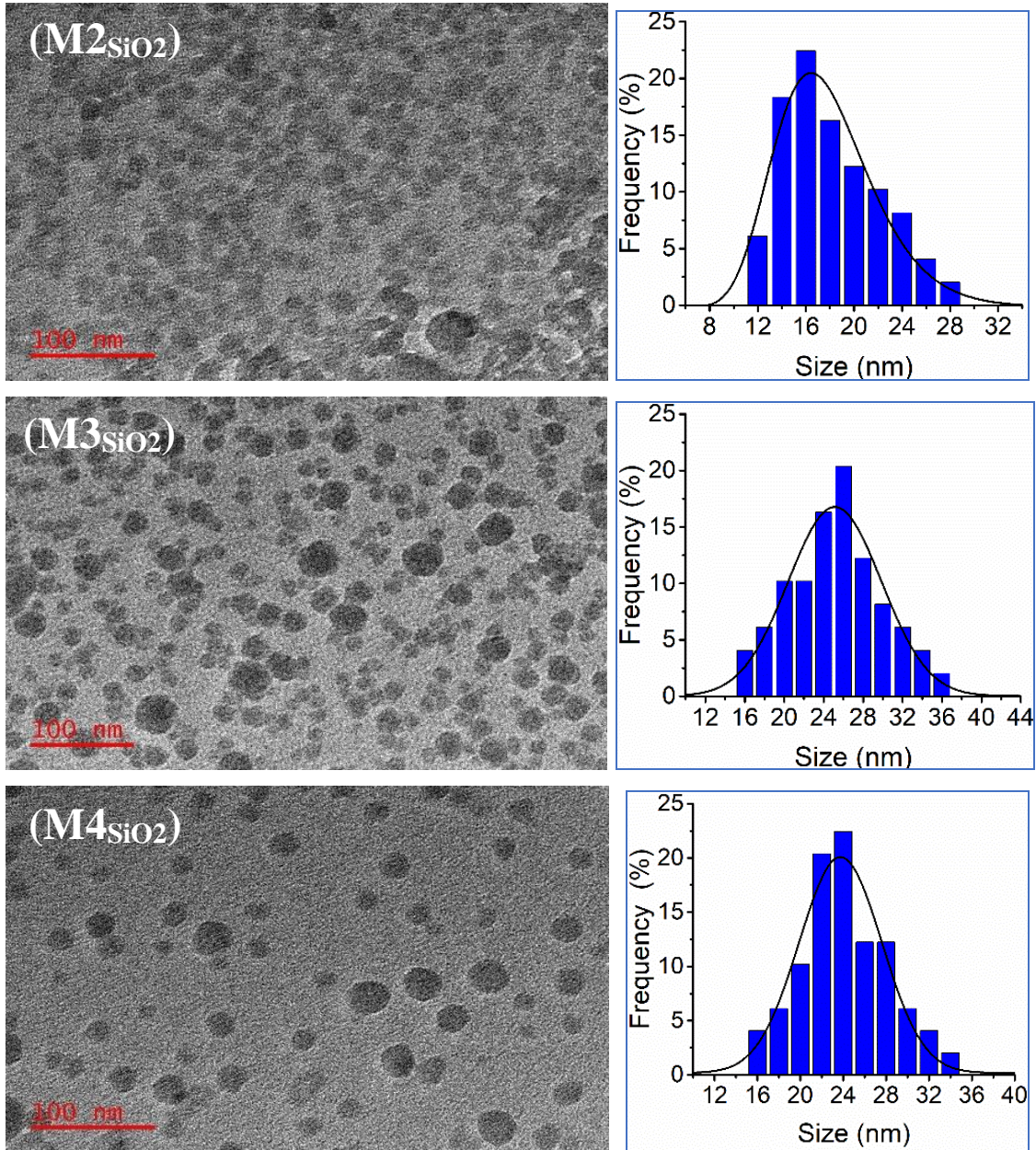
$C_p$  is the concentration of the permeate stream

### 4.3 Results and discussion

#### 4.3.1 Transmission Electron Microscopy (TEM) analysis of SiO<sub>2</sub>NPs

Transmission electron microscopy (TEM) was used to study the shapes and sizes of pristine and organically-modified SiO<sub>2</sub>NPs. All SiO<sub>2</sub>NPs generally showed a sphere-like morphology (**Figure 4.1**). The pristine SiO<sub>2</sub>NPs were showed to be slightly aggregated in comparison to their organically-modified counterparts. As indicated in the size distribution graphs, the mean sizes of the SiO<sub>2</sub>NPs were 17.4±3.9 nm, 24.5±4.8 nm, 23.7±4.4 nm and 24.9±7.1 nm for pristine, ODTs, OTMS, and CI-DMOS modified NPs, respectively (**Table 4.1**). These results are in agreement with previously reported SiO<sub>2</sub>NPs used in literature, and indicate an average polymer length of 3.5 nm (measured in vacuum) on the surface (367). An increase in the size of the organically-modified SiO<sub>2</sub>NPs and formation of

uniform structures could be ascribed to the self-assembled layer of the silane agent on the surface of the pristine SiO<sub>2</sub>NPs (161,162). Self-assembled monolayers of ODTS, OTMS, and Cl-DMOS on silica dioxide surfaces has been previously reported (157,160,161).



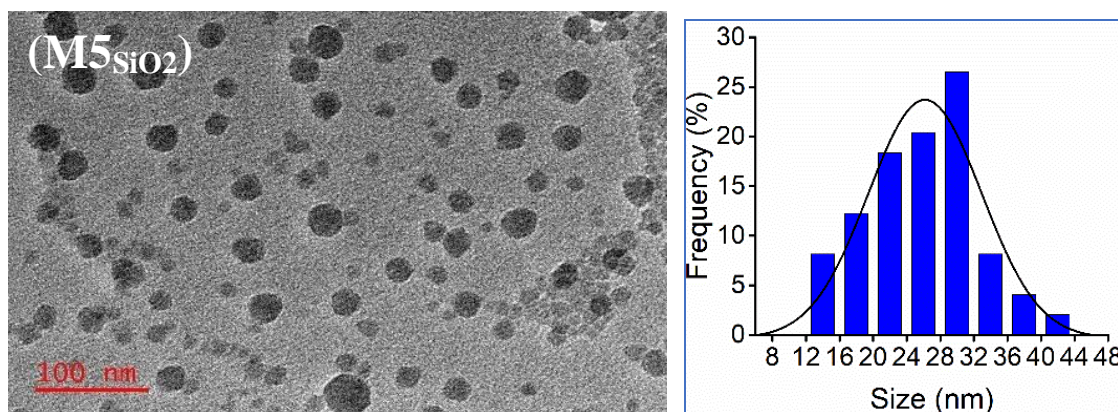


**Figure 4.1:** TEM images of SiO<sub>2</sub>NPs and their corresponding size distribution graphs: (M2SiO<sub>2</sub>): pristine SiO<sub>2</sub>NPs, (M3SiO<sub>2</sub>): ODTs-modified SiO<sub>2</sub>NPs, (M4SiO<sub>2</sub>): OTMS-modified SiO<sub>2</sub>NPs, (M5SiO<sub>2</sub>): Cl-DMOS-modified SiO<sub>2</sub>NPs.

#### 4.3.2 Statistical analysis of SiO<sub>2</sub>NPs sizes

The single variance ANOVA test was used to determine any significant difference in the sizes of SiO<sub>2</sub>NPs. The mean sizes and their corresponding standard deviations, the upper and lower bound at the 95% confidence interval for the mean, minimum, and maximum sizes of SiO<sub>2</sub>NPs are presented in **Table 4.1**. According to their mean values, modified SiO<sub>2</sub>NPs were bigger in size compared to their pristine counterpart. Therefore, to compare the mean sizes of the SiO<sub>2</sub>NPs, the Null hypothesis stated no statistically significant difference in the sizes of the SiO<sub>2</sub>NPs (i.e.,  $\mu_1 = \mu_2 = \mu_3 = \mu_4$ ; as the mean size values of pristine, ODTs, OTMS, and Cl-DMOS-modified SiO<sub>2</sub>NPs, respectively). The p-value of the test was 0.00, which was lower than 0.05; thus, indicating the rejection of the null hypothesis and suggesting that the sizes of the SiO<sub>2</sub>NPs were significantly different (**Table 4.2**).

The one-way ANOVA test did not indicate which NPs have significantly different mean values between groups (i.e., pristine SiO<sub>2</sub>NPs, ODTs, OTMS, and Cl-DMOS modified SiO<sub>2</sub>NPs). Therefore, Fisher's Least Significant Difference post-hoc test was conducted to determine the NPs that specifically have different mean values. The p-values (**Table 4.3**) indicated that there was a statistically significant difference in the mean value of the pristine SiO<sub>2</sub>NPs compared to the organically-

modified SiO<sub>2</sub>NPs. These p-values further demonstrated no statistically significant difference between the mean values of the organically-modified SiO<sub>2</sub>NPs.

**Table 4.1:** Side-by-side comparison of the descriptive statistics (M<sub>2SiO<sub>2</sub></sub>): pristine SiO<sub>2</sub>NPs, (M<sub>3SiO<sub>2</sub></sub>): ODTS-modified SiO<sub>2</sub>NPs, (M<sub>4SiO<sub>2</sub></sub>): OTMS-modified SiO<sub>2</sub>NPs, (M<sub>5SiO<sub>2</sub></sub>): CI-DMOS-modified SiO<sub>2</sub>NPs.

NPs	N	Mean	Std. Deviation	Std. Error	95% Confidence Interval for Mean		Minimum	Maximum
					Lower Bound	Upper Bound		
<b>M<sub>2SiO<sub>2</sub></sub></b>	50	17.228	3.920	.5544	16.114	18.342	11.430	26.190
<b>M<sub>3SiO<sub>2</sub></sub></b>	50	24.097	4.841	.6846	22.722	25.473	14.810	35.040
<b>M<sub>4SiO<sub>2</sub></sub></b>	50	23.512	4.380	.6194	22.268	24.756	15.450	33.120
<b>M<sub>5SiO<sub>2</sub></sub></b>	50	24.576	7.125	1.007	22.551	26.601	11.02	39.55

**Table 4.2:** Hypothesis test results of SiO<sub>2</sub>NPs sizes; One-way ANOVA test.

Sizes	Sum of Squares	df	Mean Square	F	Sig.
Between Groups	1779.647	3	593.216	21.817	.000
Within Groups	5329.334	196	27.190		
Total	7108.981	199			

**Table 4.3:** Least Significance Difference (LSD) of the mean sizes of SiO<sub>2</sub>NPs.

(I <sup>#</sup> ) Variables	(J <sup>#</sup> ) Variables	Mean Difference (I-J)	Std. Error	Sig.	95% Confidence Interval	
					Lower Bound	Upper Bound
<b>M<sub>2SiO<sub>2</sub></sub></b>	<b>M<sub>3SiO<sub>2</sub></sub></b>	-6.869*	1.043	.000	-8.926	-4.813
	<b>M<sub>4SiO<sub>2</sub></sub></b>	-6.283*	1.043	.000	-8.340	-4.227
	<b>M<sub>5SiO<sub>2</sub></sub></b>	-7.348*	1.043	.000	-9.405	-5.291
<b>M<sub>3SiO<sub>2</sub></sub></b>	<b>M<sub>2SiO<sub>2</sub></sub></b>	6.869*	1.043	.000	4.813	8.926
	<b>M<sub>4SiO<sub>2</sub></sub></b>	0.586	1.043	.575	-1.471	2.643
	<b>M<sub>5SiO<sub>2</sub></sub></b>	-0.478	1.043	.647	-2.535	1.578
<b>M<sub>4SiO<sub>2</sub></sub></b>	<b>M<sub>2SiO<sub>2</sub></sub></b>	6.283*	1.043	.000	4.227	8.340
	<b>M<sub>3SiO<sub>2</sub></sub></b>	-0.586	1.043	.575	-2.643	1.471
	<b>M<sub>5SiO<sub>2</sub></sub></b>	-1.064	1.043	.309	-3.121	0.992
<b>M<sub>5SiO<sub>2</sub></sub></b>	<b>M<sub>2SiO<sub>2</sub></sub></b>	7.348*	1.043	.000	5.291	9.405
	<b>M<sub>3SiO<sub>2</sub></sub></b>	0.478	1.043	.647	-1.578	2.535
	<b>M<sub>4SiO<sub>2</sub></sub></b>	1.064	1.043	.309	-0.992	3.121

\*. The mean difference is significant at the 0.05 level.

I<sup>#</sup> is the first factor in comparison and J<sup>#</sup> is the second factor in comparison

### 4.3.3 Scanning Electron Microscopy (SEM) analysis of the PVDF nanofibre membranes

Scanning electron microscopy (SEM) was used to study the surface morphology and cross-sectional view of the PVDF nanofibre membranes (**Figure 4.2**). PVDF nanofibre membranes not embedded with SiO<sub>2</sub>NPs were termed as M1; while PVDF nanofibre membranes modified with pristine SiO<sub>2</sub>NPs were termed as M2. Similarly, PVDF nanofibre membranes decorated with ODTs-SiO<sub>2</sub>NPs, OTMS-SiO<sub>2</sub>NPs, and Cl-DMOS-SiO<sub>2</sub>NPs were termed as M3, M4, and M5, respectively. Uniform non-beaded nanofibres were observed at the following optimised electrospinning conditions: (a) 15% (w/v) polymer concentration in a mixed solvent system of acetone:DMAc with a ratio of 56:44; (b) voltage of 23 kV; (c) flow rate of 1.0 mL/h; and (d) a distance of 14 cm between the tip of the needle and the rotating collector (**Figure 4.2, M1**). A polymer concentration of 15% (w/v) was the suitable concentration at which the critical concentration/viscosity for electrospinning of PVDF is possible. The voltage of 23 kV was the appropriate threshold voltage required to produce sufficient electric field at the distance of 14 cm, overcoming the polymer surface tension to eject the charged jet towards the collector. Under these conditions, the stabilisation of the polymer jet and formation of uniform molecular entanglement were achieved, leading to the production of uniform non-beaded polymers. However, these parameters were affected by the addition of modified SiO<sub>2</sub>NPs to the electrospinning solution (**Figure 4.2, M3-M5**). Similar electrospinning conditions of PVDF nanofibre membranes have been reported by Liao (102) which showed the formation of uniform microstructures. In the same study, it was observed that the incorporation of different additives affected the morphology of the nanofibres (i.e., bead formation) as a function of the additive concentrations (102). The SiO<sub>2</sub>NPs were added to the PVDF at a 1.0% relative concentration, which was the minimum SiO<sub>2</sub>NPs concentration affecting the morphology of the PVDF nanofibres while maintaining high contact angles (i.e., high hydrophobicity). Smooth and non-beaded nanofibres were obtained upon addition of pristine SiO<sub>2</sub>NPs to the electrospinning PVDF solution, which was consistent with previous studies

(37,367,368). However, slightly beaded nanofibres accompanied by electrospinning were observed upon addition of modified SiO<sub>2</sub>NPs (**Figure 4.2, M3-M5**).

With the aim of obtaining non-beaded nanofibres, the electrospinning parameters (i.e., polymer concentration, flow rate, voltage, and distance) were further varied after the addition of modified SiO<sub>2</sub>NPs to reduce beads formation. However, the morphology of the resulting nanofibres was negatively impacted by any change in these parameters. To this end, the original values of the electrospinning parameters were found optimum to produce slightly-beaded nanofibres accompanied by electrospinning upon addition of modified-SiO<sub>2</sub>NPs. The change in morphology was due to polymer stream breakdown and failure to stabilise the polymer jet, which affected the molecular entanglement (112). There are no reported studies on the effects of silane agents on the morphology of PVDF nanofibres. However, silane agents are known to affect the viscoelastic properties of the polymer (i.e., a property that determines the morphology of the nanofibres) (369). This provides an explanation for the formation of beaded PVDF nanofibres upon incorporation of SiO<sub>2</sub>NPs modified with silane agents (**Figure 4.2, M3-M5**). The corresponding intertwined nanofibre membranes observed in the cross-sectional SEM images indicated that the nanofibres were highly porous. An example of the embedment of SiO<sub>2</sub>NPs in the PVDF nanofibres shown on the high-resolution image on M5 (**Figure 4.2**).

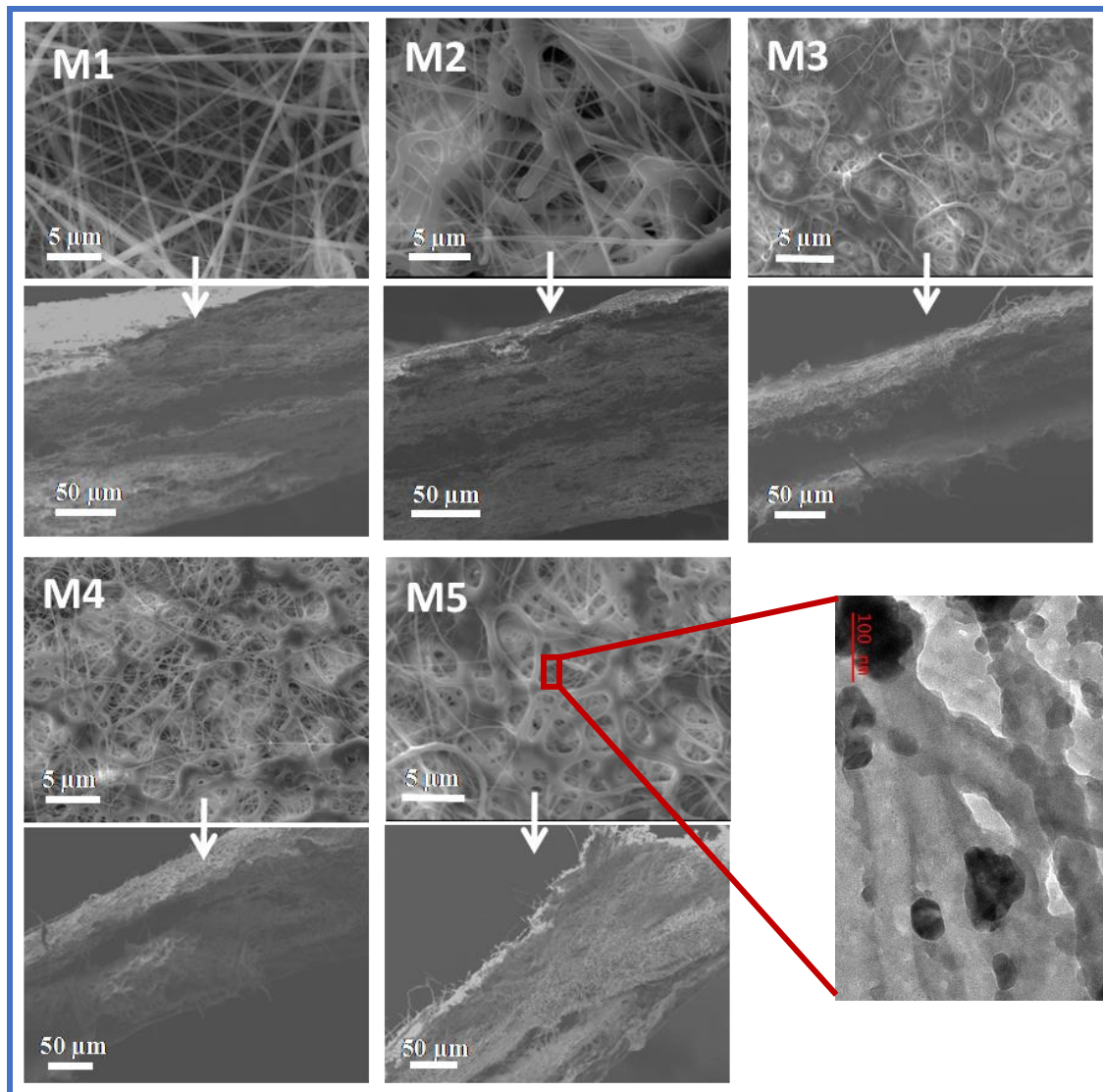


**Figure 4.2:** SEM images of PVDF electrospun nanofibre membranes embedded with SiO<sub>2</sub>NPs. (M1) pristine membrane, (M2), (M3), (M4), and (M5) membranes embedded with pristine SiO<sub>2</sub>NPs, ODTs-modified SiO<sub>2</sub>NPs, OTMS-modified SiO<sub>2</sub>NPs, and Cl-DMOS-modified SiO<sub>2</sub>NPs, respectively.

#### 4.3.4 Atomic Force Microscopy (AFM) analysis

The surface morphology of the PVDF nanofibre membranes was studied using AFM. The arithmetic mean height ( $R_a$ ) and the root mean square height ( $S_q$ ) of the voids on the surface of each membrane were used to provide information regarding the difference in height of each point compared to the arithmetical mean of the surface and the root mean square values of the ordinate values within the

defined membrane area. This information is important for determining the roughness of the membrane. The Ra values of M1, M2, M3, M4, and M5 were 96 nm, 161 nm, 212 nm, 205 nm, and 242 nm, respectively. The Sq values of M1, M2, M3, M4, and M5 were 140 nm, 194 nm, 283 nm, 278 nm, and 309 nm, respectively. The Ra and Sq values of the membranes increased with the addition of SiO<sub>2</sub>NPs to the electrospinning PVDF solution, indicating rougher membranes (**Figure 4.3**). The viscosity and the electric charge of the PVDF solution was affected by the addition of the SiO<sub>2</sub>NPs, which in turn resulted in the formation of slightly-beaded nanofibre membranes and rougher surfaces (37). The membrane morphology and roughness determine the distribution of the contact angle through the membrane. Rough membranes allow air entrapment in the membrane voids, which causes high repulsive forces between the membrane and water; thus, inducing a higher hydrophobicity (370,371). Furthermore, membranes with ununiform morphology and non-distributed surface roughness is likely to cause uneven distribution of the contact angles within the same membrane. Detailed information regarding these observations is outlined in the next section.

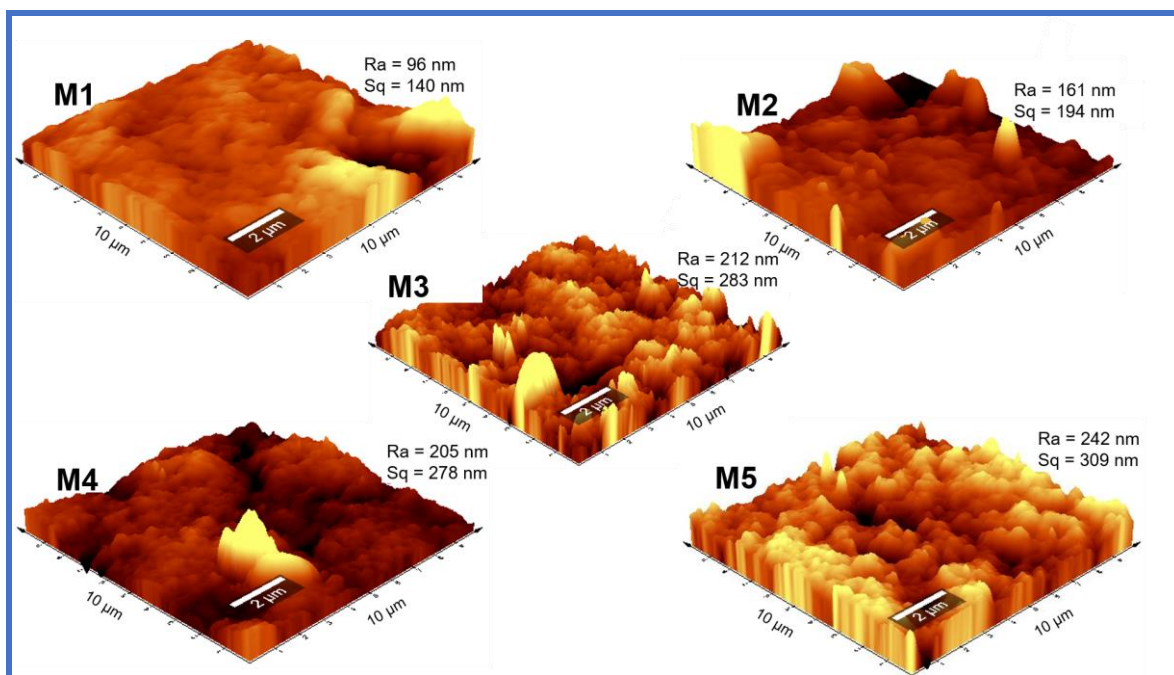


**Figure 4.3:** AFM micrographs of nanofibre membranes decorated with organically-modified SiO<sub>2</sub>NPs.

#### 4.3.5 Contact angle and tensile strength measurements

Contact angle measurements were conducted to investigate the interactions between water droplets and membrane surfaces arising from the hydrophobic or hydrophilic properties of the membranes. The properties of PVDF membranes range from hydrophilic to super-hydrophobic, depending on the synthesis methods conducted. The results of contact angle measurements indicated that the pristine PVDF membranes fall in the category of slightly hydrophobic materials (CA:  $92.8 \pm 1.5^\circ$ ) (**Figure 4.4**) (40). The embedment of pristine SiO<sub>2</sub>NPs into the PVDF membranes increased the membrane contact angle to  $109.1 \pm 1.9^\circ$ , inducing a higher hydrophobicity.(37) Similarly, a significant increase in the contact angle was observed for the ODTs, OTMS, Cl-DMOS-modified SiO<sub>2</sub>NPs embedded nanofibre membranes ( $156.4 \pm 2.4^\circ$ ,  $162.6 \pm 1.8^\circ$ ,  $151.7 \pm 2.1^\circ$ , respectively). Similar contact angles have been reported for PVDF membranes with 3 to 4% addition of SiO<sub>2</sub>NPs (37). These results clearly indicate that the silane agents (i.e., (CH<sub>3</sub>)<sub>3</sub> terminal groups of ODTs, OTMS, Cl-DMOS) significantly contributed to the formation of superhydrophobic PVDF nanofibre membranes at a low 1% NPs

concentration relative to the electrospinning solution. The advantage of superhydrophobicity does not only rely on the anti-wetting characteristics, but also on “lotus effect” process, which prevents membrane fouling by self-cleaning mechanisms (165). Membranes displaying high contact angles when alcohol was used as the non-solvent during phase inversion, have been reported (38,103). However, this process compromised the mechanical strength and porous nature of the membranes. Therefore, this study addressed such drawbacks by synthesizing mechanically strong and highly porous nanofibre membranes, as follows.

The mechanical strength of the membranes was measured using a SAXSpace instrument (Anton Paar, Graz, Austria). The Young's modulus of the nanofibre membrane was calculated from the elastic region of the stress-strain graphs (**Figure 4.4**). The Young's modulus of M1, M2, M3, M4, and M5 were  $48.3 \pm 2.1$  MPa,  $46.6 \pm 1.5$  MPa,  $42.1 \pm 1.8$  MPa,  $43.0 \pm 1.2$  MPa, and  $43.4 \pm 1.4$  MPa, respectively. Other studies have observed an increase in mechanical strength of the electrospun PVDF nanofibres upon addition of SiO<sub>2</sub>NPs (367,372). This observation was the result of the formation of uniform non-electrosprayed nanofibres with decreased diameters (373). Additionally, the nanofibre diameter generally decreased on addition of high charge carrying fillers at optimum concentrations (276). Nanofibres with smaller diameters are characterised by higher mechanical strength (367,372). Electrospinning and bead formation in electrospinning cause defects in the resultant nanofibres, hence reducing their mechanical strengths (374). Therefore, nanofibres of larger diameters and defects induced by a humid environment and electro-spraying results in the formation of weak (low mechanical strength) nanofibres (375,376). The underlying observation of the reduced mechanical strength of the PVDF membrane following the addition of organically-modified SiO<sub>2</sub>NPs was therefore associated with the formation of beaded nanofibres with increased diameter that were accompanied by spraying. The decreased membrane thickness reported on **Table 4.4** could also be another factor that influenced their mechanical strength. The thickness of M1, M2, M3, M4, and M5 membranes were found to be 151  $\mu\text{m}$ , 147  $\mu\text{m}$ , 129  $\mu\text{m}$ , 132  $\mu\text{m}$ , and 135  $\mu\text{m}$  respectively. The decline in the throughput of the nanofibre membrane would

be associated with electrospinning accompanied by a different degree of electrospinning upon addition of SiO<sub>2</sub>NPs, resulting in the formation of the thinner membrane characterised by lower mechanical strength (377). Although the incorporation of the organically modified SiO<sub>2</sub>NPs presented in this indicated the decrease in mechanical strength, the Young's modulus reported (42.1-43.4 MPa) are comparably greater than the previously reported studies (~10.6-28.2) (367,372), thus indicating their potential applications in low pressure-driven processes such as membrane distillation.

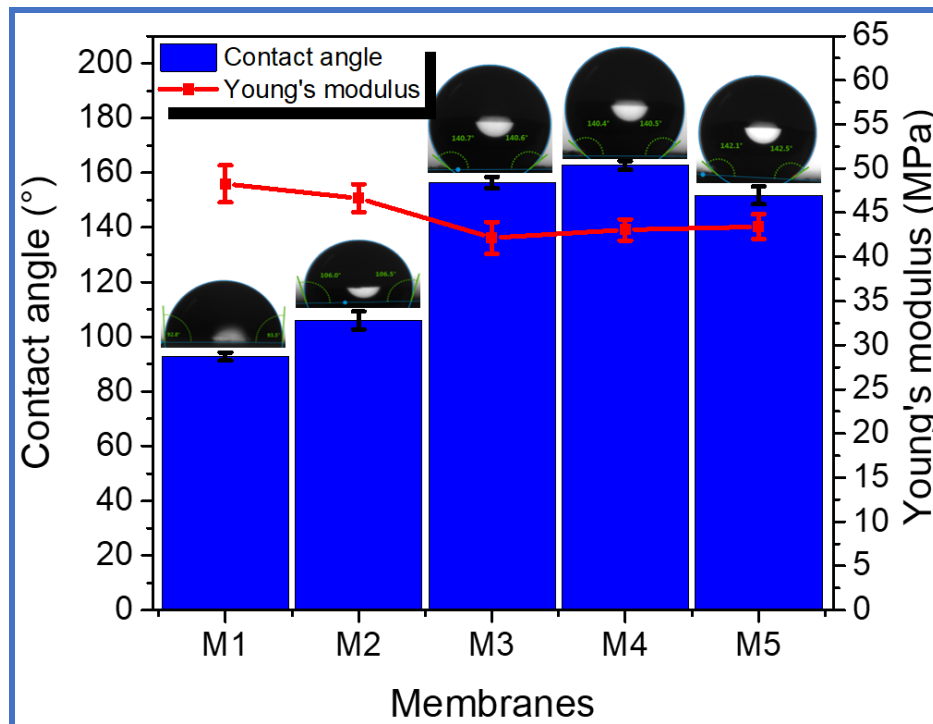


**Figure 4.4:** Contact angles and tensile strengths of nanofibre membranes.

#### 4.3.6 Liquid entry pressure (LEP) measurements

Liquid entry pressure (LEP) tests were conducted to determine the minimum pressure required to eject water (in liquid state) through SiO<sub>2</sub>NPs-embedded PVDF nanofibre membranes. The LEP is affected by several parameters including pore size, geometry, and membrane hydrophilicity (151). The LEP values

gradually increased from  $58.9 \pm 2.2$  kPa to  $84.2 \pm 2.8$  kPa for pristine PVDF nanofibre membrane (M1) and PVDF nanofibre membrane embedded with ODTS-modified SiO<sub>2</sub>NPs (M3), respectively (**Figure 4.5**). A decrease in LEP was observed from M3 to M5 (i.e.,  $84.2 \pm 2.8$  kPa to  $72.3 \pm 2.3$  kPa, respectively). These increases in LEP from pristine to SiO<sub>2</sub>NPs-embedded nanofibres would be the result of the electrospinning, which blocks the pores of the membrane or changes the geometry of the pores. A change in the LEP is also caused by cavitation induced by the hydrophobic nature of the SiO<sub>2</sub>NPs-embedded PVDF nanofibre membrane and the water polarity. Water becomes energetically unstable on hydrophobic surfaces, which increases with increasing membrane-water contact angle (378). This phenomenon results in the formation of water bubbles which consequently block the pores of the membrane, thus requiring more pressure to drive the water across the membrane. This increase in LEP has been previously reported during the incorporation of additives (e.g., graphene) in the electrospun PVDF nanofibres; where the LEP of superhydrophobic membrane and pristine PVDF nanofibres were  $130 \pm 5$  kPa and  $66 \pm 4$  kPa, respectively (171).

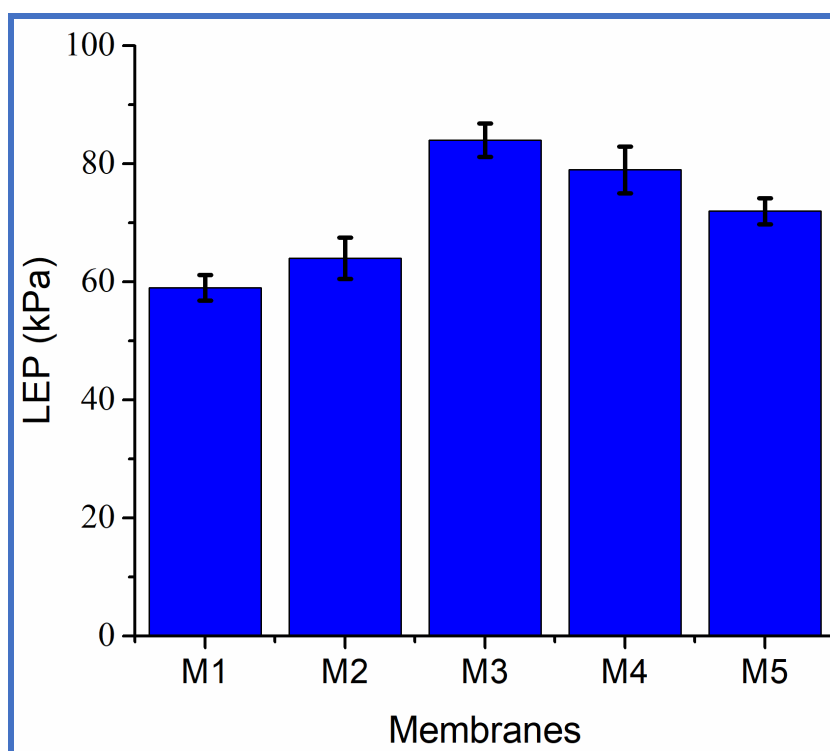


**Figure 4.5:** Liquid Entry Pressure of the PVDF nanofibre membranes.

#### 4.3.7 Membrane pore size and porosity measurements

Nanofibre membrane pore size measurements were conducted by a dry-to-wet method using a liquid expulsion capillary flow porometer. The average pore sizes of M1, M2, M3, M4, and M5 were 1.89  $\mu\text{m}$ , 1.48  $\mu\text{m}$ , 1.24  $\mu\text{m}$ , 1.41  $\mu\text{m}$ , and 1.27  $\mu\text{m}$ , respectively (**Figure 4.6**). This decline in pore structure from pristine to SiO<sub>2</sub>NPs-embedded membranes was associated with the formation of beaded nanofibres following the spraying process. Spraying blocks the pores of the sub-micron structures of the nanofibre mat, and thus reduces their water permeation. Although high porosity and large pore sizes are required for high fluxes in MD, they also pose the risk of wetting, which subsequently reduces the salts rejection efficiencies. Therefore, the ideal pore sizes and porosities for a better MD performance have been suggested as 0.1–1.5 $\mu\text{m}$  and 40–90%, respectively (24,34,102,151,163,182). The PVDF membrane porosities ranged from 82.6 $\pm$ 3.1% for pristine PVDF nanofibre membranes to 78.5 $\pm$ 2.9% for the nanofibres embedded with the organically-modified SiO<sub>2</sub>NPs (**Table 4.4**). This slight decline in porosity was also associated with the spraying on the nanofibres that somewhat blocked the pores of the membrane.

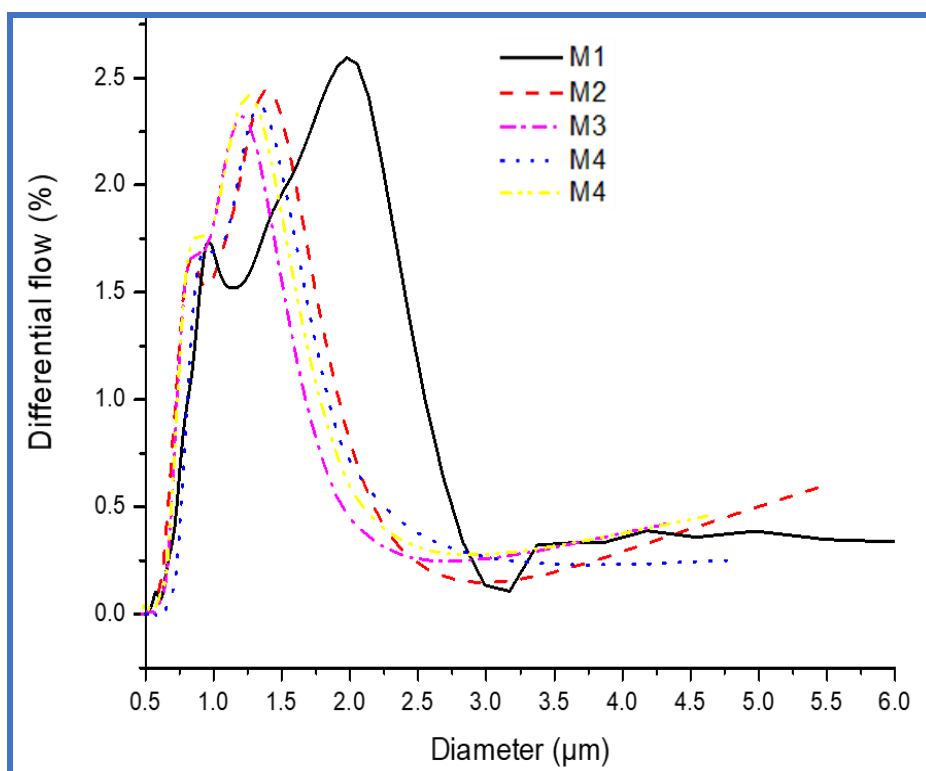


**Figure 4.6:** The pore size measurements of PVDF nanofibre membranes.

**Table 4.4:** Summary of properties of the PVDF nanofibre membranes.

Membranes	Thickness (µm)	Nanofibre diameter (nm)	Contact angle (°)	Young's modulus (MPa)	LEP (kPa)	Pore size (µm)	Porosity (%)
M1	151	641±157	92.8±1.5	48.3±2.1	58.9±2.2	1.89	82.6±3.1
M2	147	768±204	109.1±1.9	46.6±1.6	63.8±3.4	1.48	81.1±2.6
M3	129	882±326	156.4±2.4	42.1±1.8	84.2±2.8	1.24	79.3±2.3
M4	132	986±344	162.6±1.8	43.0±1.2	80.1±3.9	1.41	78.5±2.9
M5	135	953±318	151.7±2.1	43.4±1.4	72.3±2.3	1.27	79.9±2.5

#### 4.3.8 Salt (NaCl) rejections of the nanofibre membranes

The PVDF nanofibre membranes embedded with organically-modified SiO<sub>2</sub>NPs were evaluated for the rejection of NaCl on a DCMD configuration. A 99.9% salt rejection was recorded for the organically-modified superhydrophobic nanofibre membranes (**Figure 4.7**). A minimal decrease (99.8%) in salt rejection was

recorded for the membrane decorated with pristine SiO<sub>2</sub>NPs. Further losses in salt rejection, albeit minimal (from 99.9% to 99.4%), were recorded for the pristine PVDF nanofibre membrane. This slight decline in salt rejection would be attributed to possible wetting occurring inside the pores of the membrane whereby the less hydrophobic membrane would be more wetted. The main driving force behind the MD process is the vapour gradient across the two interfaces of the membrane (36). Therefore, wetting induces other separation driving forces such as concentration gradient, which allows the passage of salt from the feed side to the permeate side. As a result, a decrease in salt rejection occurs (**Figure 4.7**).

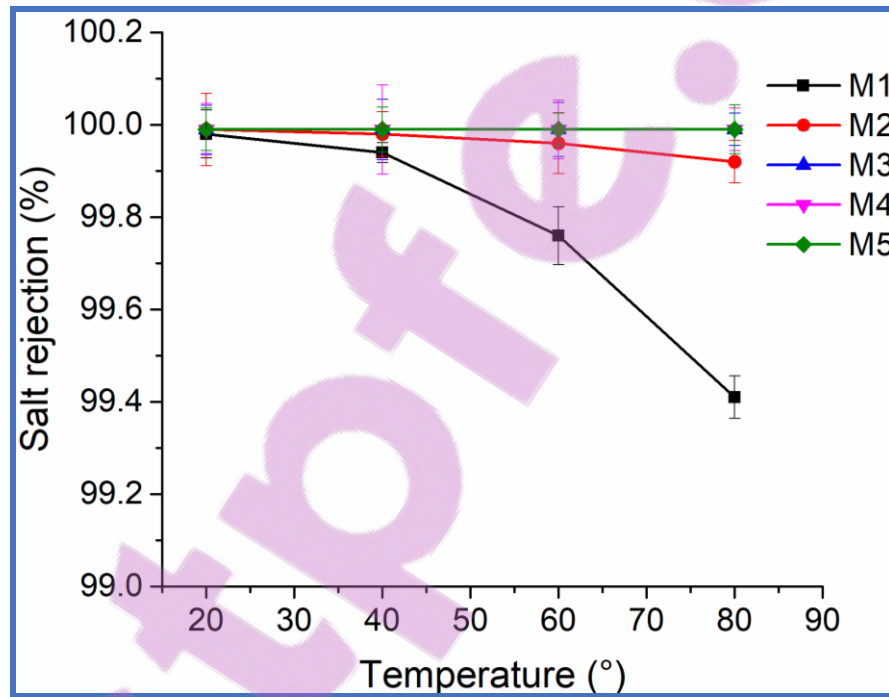


**Figure 4.7:** Salt (NaCl) rejection efficiencies of PVDF nanofibre membranes.

#### 4.3.9 Flux measurements

The flux of the salty water across the PVDF membranes embedded with and without organically-modified SiO<sub>2</sub>NPs is illustrated in **Figure 4.8**. The permeate temperature was kept at 20°C for all experiments. No water flux was observed when the feed temperature was kept at 20°C since the vapour gradient was zero

between the two interfaces at the same temperatures. The feed temperature of 20°C was tested to ensure that the driving force for the water passage was a vapour pressure difference as indicated in the previous studies, and not an osmotic water flux due to membrane wetting. The flux exponentially increased with an increase in the feed temperature in all membranes. The flux of all membranes embedded with organically-modified SiO<sub>2</sub>NPs was higher than those of M1 and M2. This result is ascribed to the possible occurrence of minimal membrane wetting on the feed side of M1 and M2 as opposed to M3, M4, and M5. The membranes M3, M4 and M5 are characterised by a contact angle higher than 150° which promotes water passage in the vapour state; thus, preventing membrane wetting. This wetting reduces the passage of water vapour as membranes are filled with liquid water, which subsequently minimises the water vapour flux (378).

Although M1 and M2 were characterised by larger pore sizes and higher porosity (i.e., properties required for the enhancement of water flux) than those of M3, M4, and M5, their thickness could be another factor associated with their lower fluxes. Thicker membranes promote the resistance of vapour transport across the membrane, which in turn results in flux decline (41). At a feed temperature of 60°C, the water fluxes of M1, M2, M3, M4, and M5 were 13.6 LMH, 19.4 LMH, 30.7 LMH, 33.9 LMH, and 34.2 LMH respectively. These results are in good agreement with previous studies reporting fluxes between 8.1 LMH and 35.8 LMH on different PVDF nanofibre membranes embedded with different SiO<sub>2</sub>NPs (41,95).

Additionally, fluxes were modelled as a function of temperature following an exponential decay fit, as  $Flux = A \times \exp\left(-\frac{T}{T_1}\right) + Flux_0$ . The R<sup>2</sup> of the fitting functions of PVDF fibre membranes embedded with organically-modified SiO<sub>2</sub>NPs showed high values (0.999), indicating a stable flux over a wide range of temperatures, as opposed to M1 and M2 (i.e., caused by wetting). The pre-exponential term A (i.e., defined as an experimental flux constant) was calculated as 0.6, 1.0, 8.5, 14.2, and 11.6 for M1, M2, M3, M4, and M5, respectively; indicating M4 (OTMS-SiO<sub>2</sub>NPs) as the most efficient membrane in terms of fluxes.

Such findings provide evidence an MD process with a higher water production rate that could be implemented at a higher scale for the production of fresh water from saline or brackish water.

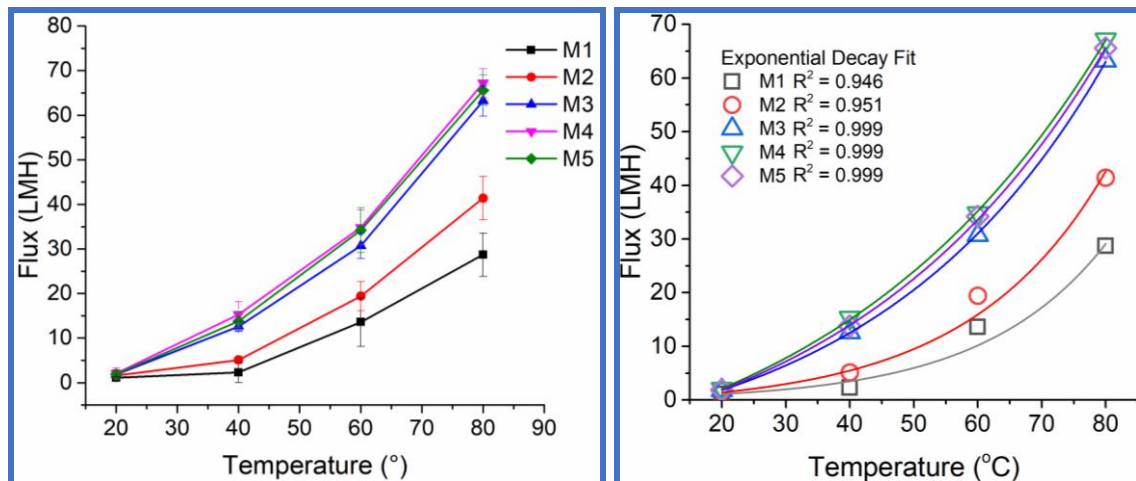


**Figure 4.8:** The water flux of salty water across PVDF nanofibre membranes embedded with organically modified SiO<sub>2</sub> NPs.

The water flux across the super-hydrophobic PVDF membranes was also studied as a function of time at feed and permeate temperatures of 60°C and 20°C, respectively. An unstable water flux that decreased with time was observed (**Figure 4.9**) and was attributed to temperature polarisation and artefact deviations. The loss of water flux in M1 and M2 was associated with the occurrence of wetting inside the pores of the membrane due to the poor hydrophobic nature of the membranes (379). At the low experimental pressures in MD, the wetted membranes blocked the passage of the water vapour, thus reducing the volume of water condensed at the permeate side of the membrane. The super-hydrophobic membranes M3, M4, and M5 were the least affected by wetting. When comparing the best performing membranes between M3, M4, and M5, in terms of water flux as a function of both temperature (**Figure 4.8**) and time (**Figure 4.9**), the efficiency of the membranes followed the trend: M4>M5>M3. The M4 membrane is the PVDF nanofibre membrane embedded with OTMS-modified SiO<sub>2</sub>NPs, where the OTMS molecule is characterised by a long aliphatic carbon chain (CH<sub>3</sub>(CH<sub>2</sub>)<sub>17</sub>- as in the case of other silane agents (ODTS and CI-DMOS) although their anchor functional groups are different. The anchor group on OTMS

is (-Si-OCH<sub>3</sub>)<sub>3</sub>, while (-Si-ClCH<sub>2</sub>)<sub>3</sub> and (-Si-Cl<sub>3</sub>)<sub>3</sub> are the anchor groups on ODTS and Cl-DMOS, respectively (156–162). The anchor groups on OTMS are more hydrophobic due to the presence of bulky nonpolar CH<sub>3</sub> groups. The presence of the strong electron-withdrawing atoms such as Cl and O in Cl-DMOS and ODTS cause uneven distribution of electrons, which subsequently induce a minimal polarity at one end of the molecule, hence reducing its hydrophobicity. These differences in the hydrophobic nature of the SiO<sub>2</sub>NPs give rise to the difference in performance observed in MD membranes (163,164).

To this end, a decline in the water flux in these membranes would be a result of temperature polarisation, which originates from the heat transfer occurring on both feed and the permeate sides of the membrane (379). Furthermore, the increase in the feed concentration was also associated with the flux decline. The initial concentration of NaCl was not maintained at its initial dilution in between hours and therefore caused concentration polarisation, resulting in different rates of flux decline in between membranes. Also, the changes in water activity were associated with flux decay. These observations have been previously reported where these fluctuations and decline in permeate fluxes were associated with both temperature and concentration polarisation (41,104).

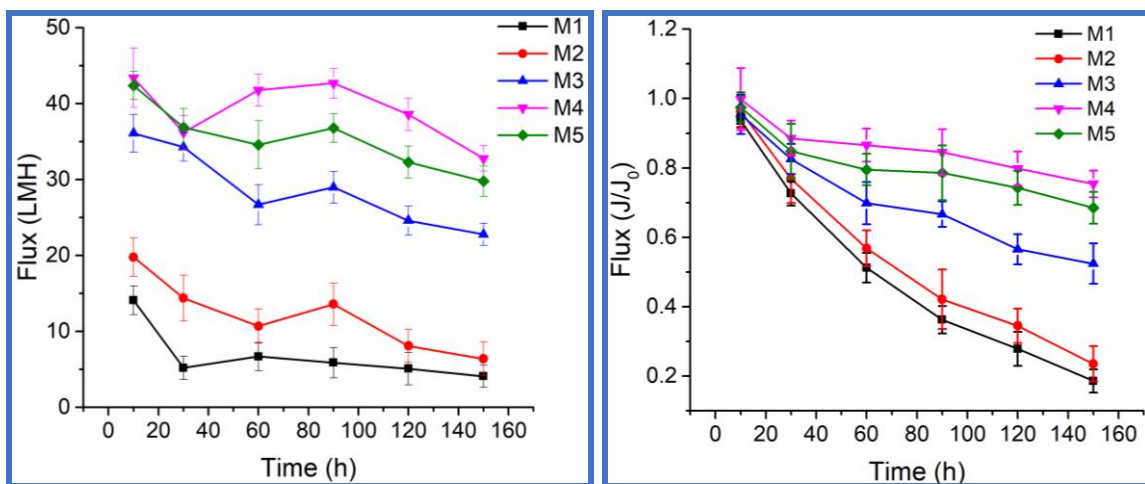


**Figure 4.9:** The effect of the long-term run of the DCMD using superhydrophobic PVDF membranes on water flux.

**Table 4.5** presents the comparison of the properties of PVDF-based nanofibre materials on MD performance and their LEP values. To attain efficient performance in MD operation, the MD membranes used should not be wetted by the process liquids and the membrane should be porous enough to allow water vapour permeability at reasonable rates (380). The membrane should be hydrophobic and the operating pressure should not exceed the LEP of the membrane (36,163,164,202,381). It has been reported that membranes used in MD should be characterized by the following properties: pore size (0.1-1.5  $\mu\text{m}$ ), porosity (40-90%), and LEP ( $\approx 250$  kPa) (24,102,151,163,381–385). The pore sizes and porosity of several PVDF-based nanofibre membranes are reported in **Table 4.5** and they include the findings of this study.

The LEP values of the PVDF-based nanofibre membranes reported in this study and in literature ( $\text{LEP} \leq 89$  kPa) are generally below the recommended values for use in MD. The highest LEP value ( $\approx 240$  kPa) obtained for PVDF-based nanofibre membranes was reported by Li *et al.* (2015) (386). The LEP value of the membranes is directly proportional to the membrane contact angle and inversely proportional to the membrane pore size and porosity (380). Therefore, the LEP values of PVDF nanofibre membranes obtained in the study and the reported literature could be improved by compromising the membrane pore sizes while enhancing the membrane hydrophobicity. The salt rejection and water flux reported in this study were comparable to the findings reported in literature (**Table 4.5**).

**Table 4.5:** Properties, LEP and performance comparison of PVDF-based nanofibre membranes in MD applications.

Nanofibre Membrane	Pore size (µm)	Porosity (%)	Contact angle (°)	LEP (kPa)	Salt rejection (%)	Flux (LMH)	Ref.
PVDF nanofibres on polyester substrate	1.90	91	150	43	99.9	31	(387)
f-SiO <sub>2</sub> NPs-modified PVDF nanofibre membrane	0.25	69	161	240	99.9	41	(386)
PVDF electrospun in LiCl	0.30	57	142	35	-	21	(102)
PVDF-coated PSF nanofibre	1.04	87	143	89	99.9	33	(388)
PVDF-co-HFP nanofibre	1.00	90	150	85	98.5	30	(214)
Pristine PVDF nanofibre	1.89	82	93	59	99.4	14	This study
SiO <sub>2</sub> NPs-modified PVDF	1.48	81	109	64	99.8	19	This study
f-SiO <sub>2</sub> NPs-modified PVDF	1.41	78	162	80	99.9	34	This study
Recommended operating conditions MD	0.1-1.5	40-90	≥150	250	≥99	-	(24,102,151,163,381–385)

#### 4.4 Conclusion

In the current study, membranes with combined high mechanical stability, porosity, and super-hydrophobicity were synthesised to prevent wetting while maintaining high salt rejection and water flux. The addition of organically-modified SiO<sub>2</sub>NPs synthesised by a novel green chemistry method as well as the manufacture of rough electrospun nanofibre membranes, resulted in superhydrophobic PVDF membranes with contact angles >150°. Remarkably, the concentration of modified SiO<sub>2</sub>NPs used to produce superhydrophobic PVDF nanofibre membrane was significantly lower (1% w/w) than those reported in previous studies (3–4% w/w), clearly indicating the efficiency of these silane reagents. These electrospun PVDF

fibre membranes embedded with organically-modified SiO<sub>2</sub>NPs displayed Young's modulus values of 42.1 MPa  $\geq E \geq$  43.4 MPa. The entangled and intertwined structures have also led to the formation of highly porous membranes (78.5–79.9%) with pore sizes ranging from 1.24 to 1.41  $\mu\text{m}$ , both parameters falling within previously suggested optimal ranges in MD (0.1–1.5 $\mu\text{m}$  and 40–90%, respectively). Additionally, LEP values of 72.3 $\pm$ 2.3 – 84.2 $\pm$ 2.8 kPa were recorded. These membranes were highly efficient in the removal of NaCl from water ( $\geq$ 99.9% removal) at a feed temperature of 60°C. In terms of flux as a function of both temperature and time, membranes embedded with OTMS-modified SiO<sub>2</sub>NPs (i.e., also showing the highest contact angle) were the most efficient, followed by Cl-DMOS-SiO<sub>2</sub>NPs and ODTs-SiO<sub>2</sub>NPs. The synthesis process of PVDF nanofibre membranes and silane modification of SiO<sub>2</sub>NPs described in the current investigation is a promising approach for a future implementation of MD for the desalination of brackish water/seawater at high recovery rates. However, further studies including fouling mitigations are still required. Therefore, surface modification of the membranes is presented in the forthcoming chapters to address membrane fouling propensities in MD.

## **CHAPTER 5**

# **SYNTHESIS OF SILVER NANOPARTICLES USING ONE-POT AND MICROWAVE-ASSISTED METHODS AND THEIR SUBSEQUENT EMBEDMENT ON PVDF NANOFIBRE MEMBRANES FOR GROWTH INHIBITION OF MESOPHILIC AND THERMOPHILIC BACTERIA**

---

### **5.1 Introduction**

Since its initial development, membrane technology has rapidly evolved and played a key role in the production of fresh water for human consumption (30). In the previous chapters, it was demonstrated that the modification of PVDF nanofibre membranes in MD distillation is a promising solution for production of high-quality water with improved fluxes. Despite extensive research and recent breakthroughs, fouling still remains the main limitation of membrane technology severely impacting its long-term performance. Four categories of membrane fouling have been clearly identified, namely: inorganic, organic, particle/colloidal, and biofouling (69,389). In particular, biofouling is largely attributed to the accumulation of soluble microbial products (SMP) and extracellular polymeric substances (EPS) produced by bacteria on membrane surfaces (67). Biofilms (i.e., structured and hydrated gels mainly consisting of proteins, polysaccharides, and natural organic matter) protect bacteria from biocides and hydrodynamic shear (67). The irreversibility and recalcitrance of biofouling have been extensively reported in the literature (70). Regardless of the type of feed, biofouling affects all kinds of membranes (e.g., membrane distillation, ultrafiltration, reverse osmosis) by increasing concentration polarisation, thus resulting in flux decline (67,390,391).

Due to their high toxicity to a wide range of bacteria, previous studies have focused on the synthesis of silver nanoparticles (AgNPs) as antibacterial agents for the prevention of biofilm formation on membranes during water purification

(68,392,393). For instance, in ultrafiltration, AgNPs-embedded polysulfone membranes did not only show improved resistance to water flux decline during the treatment of aqueous solutions containing bovine serum albumin (BSA) but also presented excellent antibacterial properties against *E. coli* and *B. subtilis* (149). Some AgNPs synthesis methods include the use of strong and toxic reducing agents, e.g., sodium borohydride ( $\text{NaBH}_4$ ) (394). Likewise, other non-green methods that have been reported in the literature for the reduction of silver ions into AgNPs involve the use of lithium aluminium hydride, hydrogen gas, and hydrazine (395–397). To circumvent the use of toxic chemicals, recent studies have focused on the use of environmentally benign reducing agents, e.g., ascorbic acid or citric acid (398,399).

Nevertheless, the use of green methods for the synthesis of AgNPs without assistive procedures has been found to be a slow process. Vanaja *et al.*, (2014) have demonstrated that an increase in reaction temperature significantly improved the rate of AgNPs production (400). Also, the formation of nanoparticles below 100 nm has been achieved with the use of plant extracts (e.g. *Arbutus unedo*, *Syzygium cumini* fruit, and *Pulicaria glutinosa*) (399). However, these nanoparticles tend to aggregate, thus compromising their antibacterial efficiency (401). Specifically, nanoparticles aggregation is influenced by the properties of the fluid, surface characteristics of the nanoparticles, and nanoparticles-fluid interactions (402). Moreover, the thermal distribution plays a critical role as it affects the rate of chemical reaction (402). In slower chemical reactions, metal ions form smaller nanoparticles which are characterised by high surface free energy. Such small nanoparticles aggregate to reduce their surface free energy while forming stable clusters in solution (402,403). Therefore, reducing agents and reaction conditions (i.e., including temperature, pressure, and reaction time) are of paramount importance to synthesise monodispersed AgNPs of controlled size and shape (404).

Remarkably, the microwave-assisted synthesis of monodispersed NPs of controlled morphology has been possible as shown in several studies (405–407).

For instance, Hasanpoor *et al.* (2015), demonstrated the formation of ultrafine needle-like NPs of uniform structure and of homogeneous size distribution (405). In contrast, NPs prepared using a one-pot synthesis method were characterised by different levels of aggregation and a variety of shapes ranging from spherical, triangular, hexagonal and tetragonal. These were prepared in one synthesis procedure using different concentrations of the reducing agents (408). Despite the substantial research conducted in: a) pressure-driven membranes impregnated with AgNPs for improved biofouling resistance, and b) green methods for the synthesis of AgNPs of controlled shape/size, key knowledge gaps still remain in these fields and need to be addressed (409).

This chapter reports on the use of Granny Smith apple extract as a widely available and novel reducing agent for the green synthesis of AgNPs. The beneficial effects of apple extracts on human health have been extensively investigated (410,411). Further advantages of apple extracts include their abundant availability at low cost, biodegradability, biocompatibility, and being less harmful to the environment (398,412,413). In addition, thermal-assisted one-pot and microwave-assisted methods were used under controlled conditions to increase the production rate of AgNPs, where the properties of the resulting AgNPs were compared.

The green synthesis route ensured that the following principles of Green Chemistry and Engineering were met: (a) waste reduction at molecular level by maximizing the use nanoscale materials), (b) synthesis of less hazardous chemicals by use of environmental benign reducing agents, (c) use of safer solvents such as plant extracts (d) use of the least energy intensive route, (e) use of the renewable resources, *e.g.* plants resources, (f) reduction of the intermediate steps for synthesis of AgNPs, (g) real time pollution prevention by ensuring that the AgNPs are not leached from the dispersing substrate, and (h) selection of chemicals that are safer and minimize the risk of accidents.

The AgNPs-embedded polyvinylidene fluoride (PVDF) nanofibre membranes were developed and their antibacterial activities towards thermophilic Gram-positive *Geobacillus stearothermophilus* and mesophilic Gram-positive *Staphylococcus aureus* and Gram-negative *Pseudomonas aeruginosa* and *Klebsiella pneumoniae* were evaluated. As far as the literature is concerned, there is no reported studies regarding the biocidal effect of AgNPs on thermophilic bacteria. Therefore, the main motivation behind the selection of thermophilic *G. stearothermophilus* and mesophilic *P. aeruginosa*, *K. pneumoniae* and *S. aureus* is the potential scenario of biofilm formation (i.e., and subsequent biofouling) in thermally-driven membrane processes (e.g., membrane distillation applications) during seawater/brackish water desalination and water treatment/purification. This latter scenario is not well established in the literature and would highly assist in identifying research directions that are necessary to minimise biofouling in membrane distillation.

## 5.2 Materials and methods

### 5.2.1 Reagents

Polyvinylidene fluoride (PVDF, MW=534,000 g.mol<sup>-1</sup>), N,N-dimethylacetamide (DMAc, Puriss p.a., 99.5%), acetone (ACS reagent, 99.5%), ethanol absolute (ACS reagent, 99.9%), silver nitrate (AgNO<sub>3</sub>, ACS reagent, 99.0%), 30 mL PP/PE eccentric tip syringe equipped with a blunt tip dispensing needle, and aluminium foil (thickness: 3.0x10<sup>-4</sup> m) were purchased from Sigma Aldrich, Germany. The Granny Smith apples were purchased from Makolobane Farmers Enterprises (Pty) LTD (Senekal, South Africa). Gram-negative *Pseudomonas aeruginosa* (ATCC# 27853), *Klebsiella pneumoniae* (ATCC# 33495) and Gram-positive *Geobacillus stearothermophilus* (ATCC# 12980), *Staphylococcus aureus* (ATCC# 25923) were purchased from the American Type Culture Collection (ATCC, USA). Ultrapure water was produced from Direct-Q® system (resistivity: 18 MΩ·cm, Merck, Millipore). All reagents were used as received.

## 5.2.2 Synthesis of AgNPs

The AgNPs were prepared following a modified green chemistry method (399) where apple extract (414) was used as the reducing agent. The apple extracts are characterised by a wide range of organic acids such as malic, quinic, isocitric, shikimic, citric and chlorogenic acids which can inevitably reduce the metal ions to their respective NPs when subjected to controlled chemical reactions (415–418). The chemical reaction was carried out by adding an excess amount of the reducing agent for a complete reduction of  $\text{Ag}^+$  ions. To a conical flask containing 30 mL of 0.1 M silver nitrate, 50 mL of apple extract was added. The reduction of  $\text{Ag}^+$  ions to AgNPs was performed using two different experimental setups, namely a) the thermally-assisted one-pot method conducted at 100°C in a thermal reactor, and b) the microwave-assisted method as previously described by Pal *et al* (2009) (419). (**Figure 5.1**). The resulting AgNPs from the two methods were centrifuged at 48,000 rpm to separate them from the supernatant. The AgNPs were further washed with deionised water to remove unreacted Ag and dried in the oven at 50°C for 24 h.

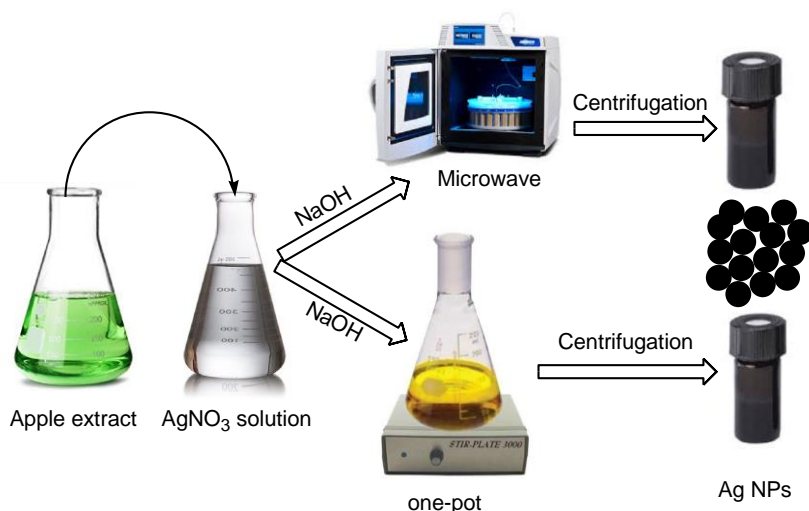


**Figure 5.1:** Schematic representation of the synthesis of AgNPs using thermally-assisted one-pot and microwave-assisted reduction methods.

### 5.2.3 Synthesis of PVDF nanofibre membranes

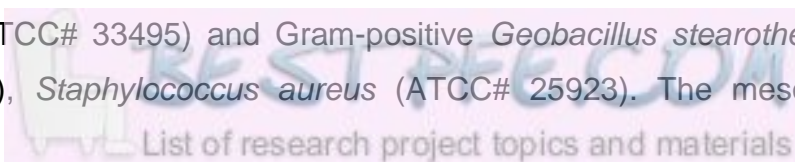
The PVDF nanofibre membranes were synthesised using the electrospinning technique described in **Chapter 4, subsection 4.2.4**. For the synthesis of AgNPs-embedded PVDF nanofibres, the AgNPs were added to the electrospinning solution at a 2% concentration relative to the PVDF. Embedding AgNPs at 2% to the membranes was found to be effective for growth inhibition of bacteria including *E. coli* (336,420–422). The electrospun PVDF nanofibres were dried in an oven at 40°C for 24 h to remove moisture.

### 5.2.4 Characterisation of AgNPs and PVDF membranes

The formation of AgNPs was confirmed by a PerkinElmer UV-Vis spectrometer Lambda 6505, Energy Dispersive X-ray spectroscopy (EDS, Oxford X-MAXN), and X-ray diffraction (XRD, Rigaku SmartLab X-Ray Diffractometer) using CuK $\alpha$  radiation ( $\lambda = 0.154$  nm) at 45 kV and 200 mA. The XRD patterns were qualitatively analysed using PDXL software (Rigaku Corporation) equipped with Powder Diffraction File from the Joint Committee on Powder Diffraction Standards (JCPDS-PDF-2) database. A scanning electron microscope (SEM, JEOL JSM-IT300) was used to study the surface morphology of the nanofibre membranes. The dispersion, morphology, and size of the AgNPs were characterised using transmission electron microscope (TEM, JEOL Jem-2010). ImageJ software was used to calculate the diameter of the AgNPs from the acquired TEM micrographs. Student's t-test was used to compare the mean diameter of the resulting AgNPs prepared under one-pot and microwave-assisted reduction methods.

### 5.2.5 Antibacterial tests using AgNPs-embedded PVDF membranes

The biocidal effect of AgNPs-embedded PVDF nanofibre membranes was tested against Gram-negative *Pseudomonas aeruginosa* (ATCC# 27853), *Klebsiella pneumoniae* (ATCC# 33495) and Gram-positive *Geobacillus stearothermophilus* (ATCC# 12980), *Staphylococcus aureus* (ATCC# 25923). The mesophiles *P.*



*aeruginosa*, *K. pneumoniae*, *S. Aureus* and the thermophile *G. stearothermophilus* were initially cultured on a Petri dish and incubated under aseptic conditions for 24 h at 37°C and 55°C, respectively. The resulting bacterial strains were grown in culture media by direct inoculation in Mueller-Hinton broth (423). The inoculated media were slowly shaken at 37°C for *P. aeruginosa*, *K. pneumoniae*, *S. Aureus* and 55°C for *G. stearothermophilus*, respectively, until an optical density (OD<sub>600</sub>) of 0.6 was reached.

Disk-diffusion agar experiments were conducted to test the biocidal effectiveness of AgNPs-embedded PVDF nanofibre membranes on the bacterial strains. Briefly, 100 µL of a bacterial suspension (OD<sub>600</sub>: 0.6) was spread uniformly over the surface of the agar in a Petri dish (culture plate); thereafter, nanofibre membranes of equal sizes were placed on the surface of the soft agar. The plates containing the nanofibre membranes were then incubated at 37°C for *P. aeruginosa*, *K. pneumoniae*, *S. Aureus* and 55°C for *G. stearothermophilus* for 24 h. The bacterial growth inhibition was then assessed by determining the growth inhibition area around the nanofibre membranes.

To determine the minimum concentration of the AgNPs on the PVDF nanofibre membranes needed to induce growth inhibition on bacteria, minimum inhibitory concentration (MIC) tests were performed in a closed 96-well microtitre plates under sterile conditions. The AgNPs produced at different reduction kinetics were tested for their MIC to determine the differences in biotoxicity of NPs towards *P. aeruginosa*, *K. pneumoniae*, *S. Aureus* and *G. stearothermophilus*. The nanofibre membranes were ground and dispersed in de-ionised water. Ultra-pure water (100 µL) was added to the first well of the first row. Neomycin (antibiotic control; 100 µL) was added to the first well of the second row. Ground AgNPs-embedded PVDF nanofibre membranes suspended in ultra-pure water (100 µL) were added to the first well of the third row. This suspension was serially two-fold diluted by transferring 50 µL of the sample to the following well containing 50 µL of de-ionised water until reaching 32X dilution. Cultures of *P. aeruginosa*, *K. pneumoniae*, *S. Aureus* and *G. stearothermophilus* bacterial cultures (50 µL,



### 5.3.2 Kinetics of AgNPs formation: UV-Vis analysis

The UV-Vis spectroscopic analysis of AgNPs was conducted to gain an understanding of the rate of formation of AgNPs with and without the assistance of microwave irradiation and using apple extract as a reducing agent. The UV-Vis absorption spectra and maximum absorption plots of AgNPs are presented in **Figure 5.2**. The produced AgNPs absorbed UV light over the wavelength range of 392–398 nm with a maximum peak at approximately 396 nm (i.e., characteristic absorption peak of AgNPs) (264). These observations are in agreement with those of other previously reported studies (148,396,401,424). The absorption peaks of the one-pot-synthesised AgNPs broadened over time, indicating the change in size distribution of the NPs (420). Also, the absorption peaks shifted from lower to higher wavelengths during the reduction period indicating the conversion of Ag<sup>+</sup> ions to AgNPs (148,264,301).

The surface plasmon resonance increased with increasing thermal and microwave irradiation of AgNO<sub>3</sub>. The increase in the intensity of the absorbance (i.e., caused by the irradiation time) directly correlated to an increase in the concentration of AgNPs produced (**Figure 5.2a and b**). Nevertheless, the rate of reduction of the Ag<sup>+</sup> ions (or rate of production of AgNPs) decreased at higher irradiation times (between 72–96 h in the thermally-assisted one-pot reduction and 2–2.5 h in the microwave-assisted reduction), indicating that the reaction was reaching equilibrium due to the depletion of Ag<sup>+</sup> ions (**Figure 5.2**). The kinetics of AgNPs formation were much faster in the microwave-assisted reaction than in the thermally-assisted one-pot reaction. The reaction reached equilibrium after 2.5 h in the microwave and proceeded towards equilibrium in 96 h (4 days) in the thermally-assisted one-pot synthesis. This phenomenon was associated with the selective heating of the reaction components, rapid heating rates, and the superheating of the solvents which resulted in an accelerated reaction rate in microwave-assisted reduction compared to that of conventional thermally-assisted one-pot reaction (425,426). Previous investigations using plant extracts as reducing agents with no reaction-assisted methods have reported slow kinetics ranging from several days to two months (427,428). This highlights the necessity

for reaction rate enhancement by introducing the microwave-assisted method and other techniques for the high production rate of AgNPs with controlled shape and size.

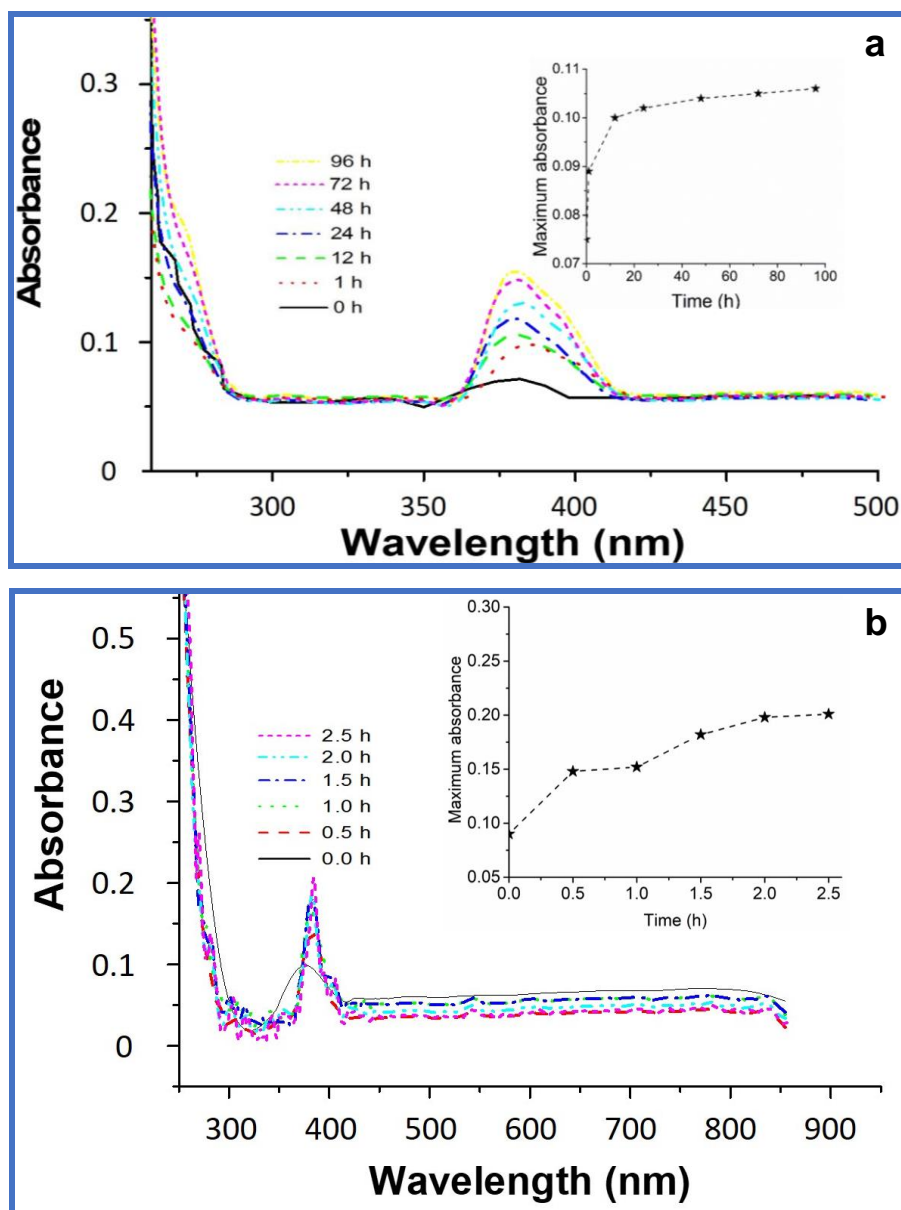


**Figure 5.2:** UV-Vis absorption spectra of AgNPs synthesised using (a) thermally assisted one-pot and (b) microwave-assisted reduction methods.

### 5.3.3 XRD characterisation of AgNPs and nanofibre membranes

The XRD patterns of AgNPs and AgNPs-embedded PVDF nanofibres are presented in **Figure 5.3**. The JCPDS card values for the following planes (111), (200), (220), (311) and (222) at  $2\theta = 38.3^\circ$ ,  $44.5^\circ$ ,  $64.8^\circ$ ,  $77.7^\circ$ , and  $82.1^\circ$  corresponded to the characteristic diffraction peaks of the AgNPs (**Figure 5.3a**). The diffraction peak of the AgNPs shifted to  $2\theta = 21.7^\circ$  with the JCPDS card value of (111) due to the chemical surroundings of the AgNPs induced by the PVDF nanofibre membranes (**Figure 5.3b**) (301). The JCPDS card values for the plane (020) at  $2\theta = 20.9^\circ$  was associated with the diffraction patterns of the PVDF (429).

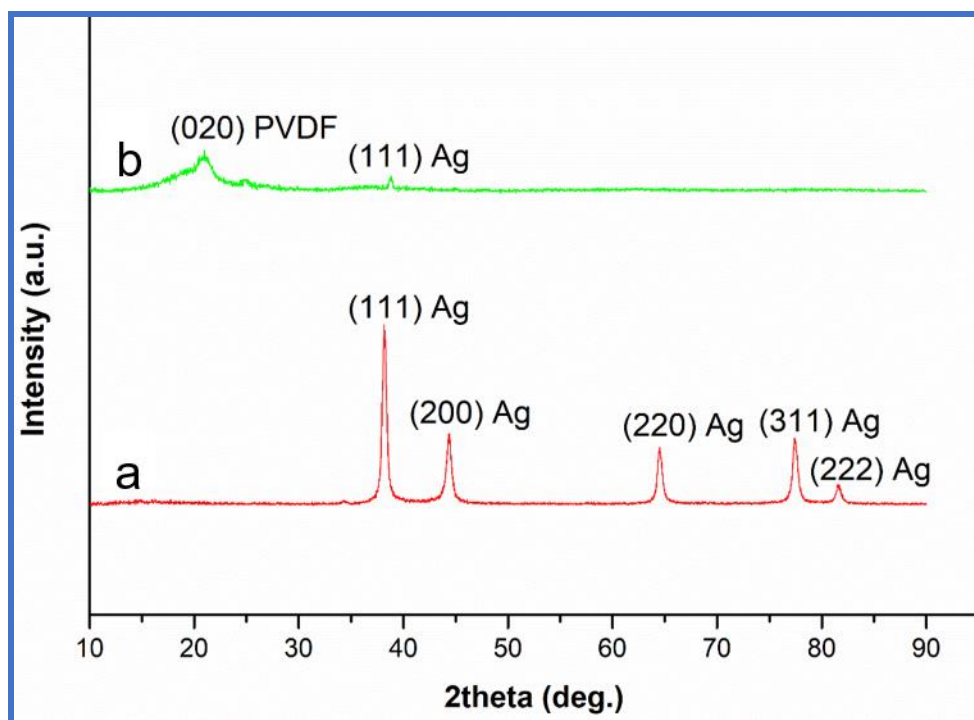


**Figure 5.3:** The XRD patterns of (a) AgNPs, and (b) PVDF nanofibres embedded with AgNPs.

#### 5.3.4 Morphological and chemical analysis by SEM-EDS

**Figure 5.4.** presents the surface morphology of the AgNPs-embedded PVDF nanofibres prepared under optimised electrospinning conditions. Uniform and non-beaded nanofibres were obtained under the optimised electrospinning parameters as provided in the experimental section including polymer concentration, injection flow rate, and distance between the collector and the needle. These conditions were explained in the previous chapter 4 and 5 (**Figure 5.4a**). Nevertheless, the addition of AgNPs affected the surface tension of the PVDF solution which subsequently led to the formation of nanofibres with electrospaying (**Figure 5.4b**). This change in the morphology of PVDF nanofibres was caused by a polymer stream breakdown induced by the failure to stabilise the polymer jet, thus leading to an electrospinning with minimal electrospaying (112). The size distribution plots of the PVDF nanofibre membranes are presented in **Figure 5.4c**). The mean diameters of the PVDF nanofibres and AgNPs-embedded PVDF nanofibres were  $345 \pm 79$  nm and  $448 \pm 84$  nm respectively. The increase in nanofibre diameter from PVDF to AgNPs-embedded PVDF membranes was associated with the electrospaying of the nanofibres. The sizes of the nanofibres obtained in this study were comparable to those obtained from the previous chapters as well as in previous studies (430,431).

The elemental composition of the AgNPs-embedded PVDF nanofibre membranes was characterised using energy-dispersive X-ray spectroscopy (EDS). Along with F and C as elemental components of PVDF (**Figure 5.4d**), elemental Ag was detected. This result confirmed the presence of AgNPs in the nanofibre membranes. The dispersion of the AgNPs and their size distributions were subsequently determined by TEM analysis.

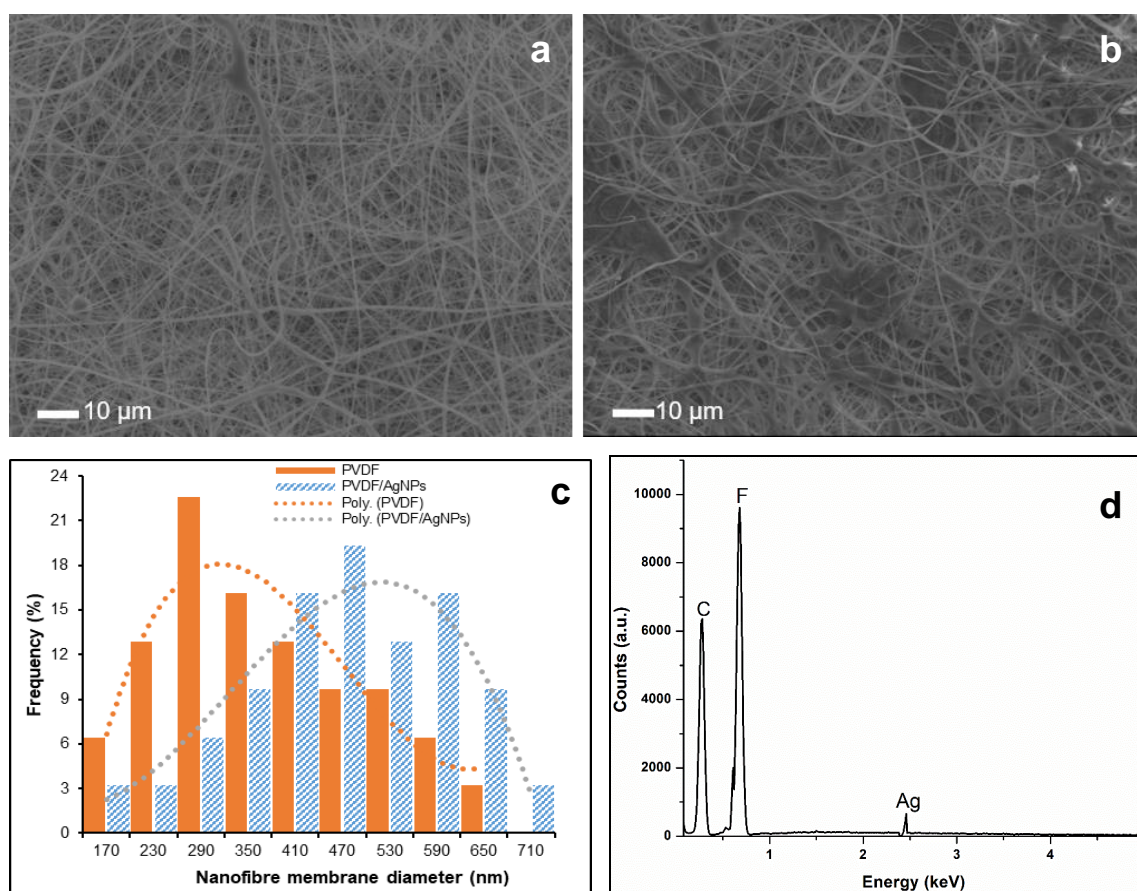


**Figure 5.4:** SEM images of PVDF and AgNPs-embedded nanofibre membranes: (a) PVDF nanofibre membranes; (b) AgNPs-embedded PVDF nanofibre membranes; (c) nanofibre size distribution graphs; and (d) EDS spectra of AgNPs-embedded PVDF nanofibre membranes.

### 5.3.5 Size, morphology, and dispersity of AgNPs: TEM analysis

The mean diameter, size distribution, and morphology of the AgNPs were examined by transmission electron microscopy (TEM) (**Figure 5.5**). The mean diameter of the AgNPs and the corresponding size distribution were determined using the TEM micrographs and ImageJ software. The AgNPs were elongated and spherical-like in shape with diameters of  $28.24 \pm 2.35$  and  $22.05 \pm 3.05$  nm for the thermally-assisted one-pot and microwave-assisted methods, respectively (**Figure 5.5**). The elongation of the AgNPs observed during the thermally-assisted one-pot reduction was caused by the aggregation of the AgNPs during the synthesis process (i.e., fusion of AgNPs during nucleation and growth) (432). In the case of

the microwave-assisted reduction, the AgNPs were evenly dispersed on the PVDF nanofibre membranes with few indications of AgNPs clustering together. In slow chemical reactions, metal ions form smaller nanoparticles which are characterised by a high surface free energy. Such nanoparticles aggregate to reduce their surface free energy while forming stable clusters in solution as explained in previous studies (402,403). Another factor that could possibly result in the formation of the clustered AgNPs is Van der Waals forces. These forces exist between molecules of the same substance. Even though van der Waals is a very weak interaction, it however, has a greater influence for smaller molecules at shorter length scales. Albeit Van der Waals forces are likely to exist between nanoparticles of the same type, the mechanism is believed to be dominated by electrostatic, covalent or surface energy interactions (433,434).

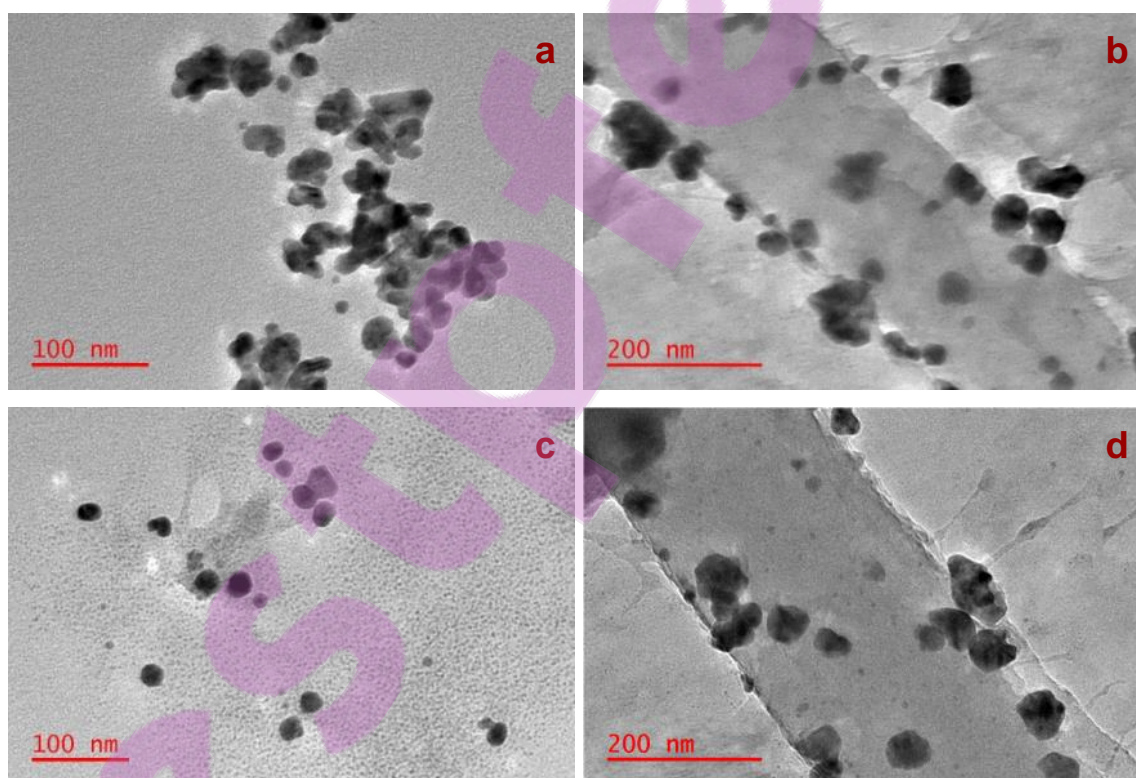


**Figure 5.5:** TEM images of AgNPs and AgNPs-embedded PVDF nanofibre membrane (a) AgNPs synthesised by thermally-assisted one-pot method; (b) one-pot synthesised AgNPs embedded in the PVDF nanofibre membranes; (c) AgNPs synthesised by microwave-assisted method; and (d) microwave-assisted synthesised AgNPs embedded in the PVDF nanofibre membranes.

**Figure 5.6** presents the size distribution (i.e., probability density functions) plots of the synthesised AgNPs. The sizes of the AgNPs were uniformly distributed on a Gaussian probability density function with size diameters ranging from 22.2–37.2 nm and 14.7–29.6 nm for the AgNPs synthesised by one-pot and microwave-assisted methods respectively. The size distribution of the NPs is of paramount importance in understanding their physicochemical properties (435). The nucleation, growth, and morphology of the AgNPs affect their loading on the PVDF nanofibre membranes, and hence determine their biocidal effects on the growth inhibition of the bacteria (436). The two-tailed student t-test was used to determine the differences in sizes for the AgNPs prepared under one-pot and microwave-assisted reduction methods. The null hypothesis was originally stated as  $\mu_1 = \mu_2$  (i.e., the mean size of the AgNPs prepared under these two methods is the same). The obtained p-value was 0.003, which was lower than the test value of 0.05. This result indicated that the null hypothesis should be rejected indicating a statistically significant difference in the mean diameter of the AgNPs prepared using these two methods.

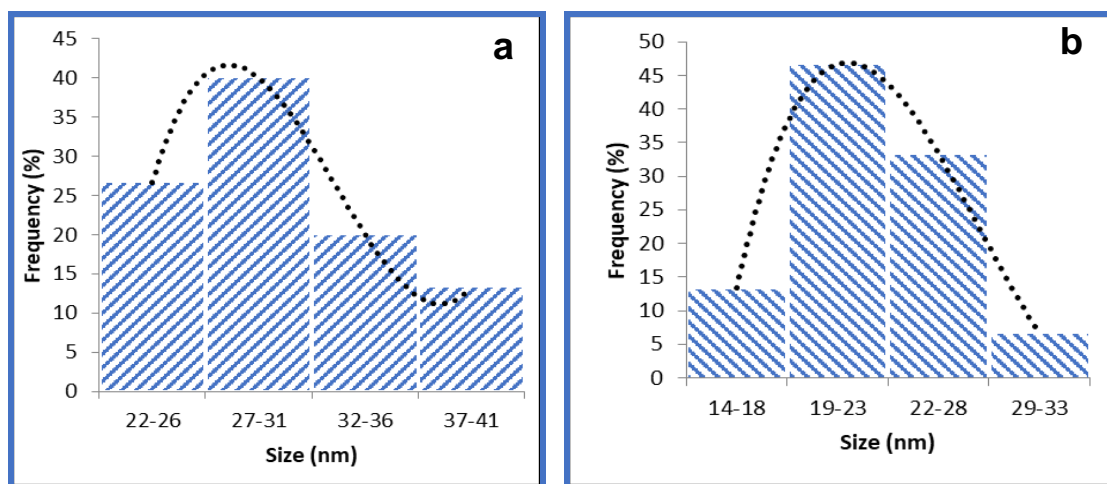


**Figure 5.6:** The size distribution of the AgNPs: (a) thermally-assisted one-pot and (b) microwave-assisted synthesis.

### 5.3.6 Antibacterial tests

#### 5.3.6.1 Disk-diffusion agar experiments

The antibacterial activities of the AgNPs-embedded PVDF nanofibre membranes were evaluated against mesophiles *P. aeruginosa*, *K. pneumoniae*, *S. Aureus* and thermophile *G. stearothermophilus* using a modified disk-diffusion method (264). The mesophilic bacteria *P. aeruginosa*, *K. pneumoniae*, *S. Aureus* can resist high temperatures of up to 50°C (437) while the thermophile *G. stearothermophilus* can resist even higher temperatures ranging between 90–100°C (438). Mesophilic and thermophilic bacteria are among the strains suggested to cause biofouling in thermally-driven membrane processes (e.g., membrane distillation) (437,439). Although it is hypothesised that microbial growth is hindered by the high process temperatures in membrane distillation (MD), the deposition of microbial foulants has been clearly identified (390). Even though biofoulants impact the general performance of MD, the dynamics and succession of biofouling are not known. Therefore, high-temperature resistant bacteria are the possible sources of biofouling in MD. As such, it is imperative to test the bacterial tactic response to the AgNPs prior to real applications in MD systems (66,390). The bacteria *P. aeruginosa*, *K. pneumoniae*, *S. Aureus* and *G. stearothermophilus* are known to be non-resistant to neomycin antibiotic (440,441). which was used as control in this study. The inhibitory effect of the AgNPs-embedded PVDF nanofibres on bacterial growth is presented in **Figure 5.7**. The bare PVDF nanofibre membrane (i.e., absence of AgNPs) did not show an inhibitory effect on the growth of bacteria (**Figure 6.7.**). Conversely, neomycin produced a wide inhibition zone on all bacteria due to the possible diffusion of antibiotic within the agar (**Figure 5.7**). A clear inhibition zone was observed in three areas (**Figure 5.7 a<sub>1,2,4</sub>, b<sub>1,2,3</sub>, c<sub>1,2,3</sub> and d<sub>1,2,3</sub>**) where the AgNPs-embedded PVDF nanofibre membranes came into contact with the culture media (442,443). No inhibition was observed on one of the AgNPs-embedded nanofibre membranes (**Figure 5.7 a<sub>3</sub>, b<sub>4</sub>, c<sub>4</sub> and d<sub>4</sub>**). This phenomenon was associated with the distribution of the AgNPs; specifically, the nanofibre membrane containing uneven distribution of AgNPs resulting in the nonappearance of the AgNPs at certain areas of the nanofibres demonstrated no

bacterial growth inhibition. The inhibition zone of the AgNPs-embedded PVDF nanofibres was significantly smaller than that of neomycin. Specifically, the AgNPs were bound to the nanofibre membrane, hence they did not diffuse within the culture media to produce a wider zone of bacterial growth inhibition. However, the bacterial growth inhibition zone observed in the disk-diffusion agar experiments demonstrated that the AgNPs-embedded PVDF nanofibre membrane could potentially prevent bacterial growth during water purification, hence reducing the formation of the biofilms.

### 5.3.6.2 Minimum inhibitory concentration

The disk-diffusion method does not indicate the minimum concentration loading of the AgNPs that would produce a foreseeable growth inhibition of bacteria. Therefore, a 96-well plate assay was used to determine the minimum concentration loading of the AgNPs to inhibit bacterial growth. The AgNPs were produced at different reduction times of the one-pot and microwave-assisted reduction processes; these were subsequently embedded in the PVDF nanofibre membranes. The nanofibre membranes containing AgNPs were ground to enable their serial dilution for the determination of the minimum inhibitory concentration (MIC). The MIC tests were conducted on *G. stearothermophilus*, *P. aeruginosa*, *S. Aureus*, and *K. pneumoniae*. The MIC assay is a useful technique that provides information about the lowest concentration of the antibacterial agents that will inhibit the visible growth of the test isolates after incubation over 24 h (444). The development of a purple colour in the growth media upon addition of p-iodonitrotetrazolium chloride indicated the presence of metabolically active bacteria. Neomycin antibiotic was found to inhibit the growth of *G. stearothermophilus*, *P. aeruginosa*, *S. Aureus*, and *K. pneumoniae* at the minimum concentration of  $1.8 \mu\text{g}\cdot\text{mL}^{-1}$  (**Figure 5.8**). The AgNPs-embedded PVDF nanofibres inhibited the growth of *G. stearothermophilus*, *P. aeruginosa*, *S. Aureus*, and *K. pneumoniae* at the minimum concentration range of (3.04–5.51 mg/mL) (**Figure 5.8**). These nanofibres are characterised by active antibacterial AgNPs with a concentration range of 0.06–0.11 mg/mL (i.e., 2% AgNPs relative to

PVDF nanofibres) as shown on **Figure 5.8**. The free  $\text{Ag}^+$  ions at zero h of reduction generally showed a growth inhibition at higher concentrations compared to their AgNPs counterpart. This finding can be explained by the antibacterial mechanism where both  $\text{Ag}^+$  ions and AgNPs are known to interact with the thiol groups and nucleic acids of the bacteria, binding to their enzymes, and damaging their cell envelopes or inhibiting the enzyme activity thus, resulting in cell inactivation (145–147). The  $\text{Ag}^+$  ions and AgNPs also bind to the thiol groups found in the bacteria enzymes, and inhibit the enzyme activity, which consequently generate the reactive oxygen species (ROS) that cause damage to the DNA of the bacteria. The silver ions are highly reactive compared to their AgNPs counterparts. The  $\text{Ag}^+$  ions react with bacterial proteins leading to the formation of insoluble Ag(protein) complexes which in turn cause a significant decrease in their antibacterial activities. This explains the need for the high concentrations of the  $\text{Ag}^+$  ions to produce a foreseeable bacterial log reduction compared to AgNPs. Therefore, it is of high importance to synthesise AgNPs for antibacterial purposes using a green synthesis route.

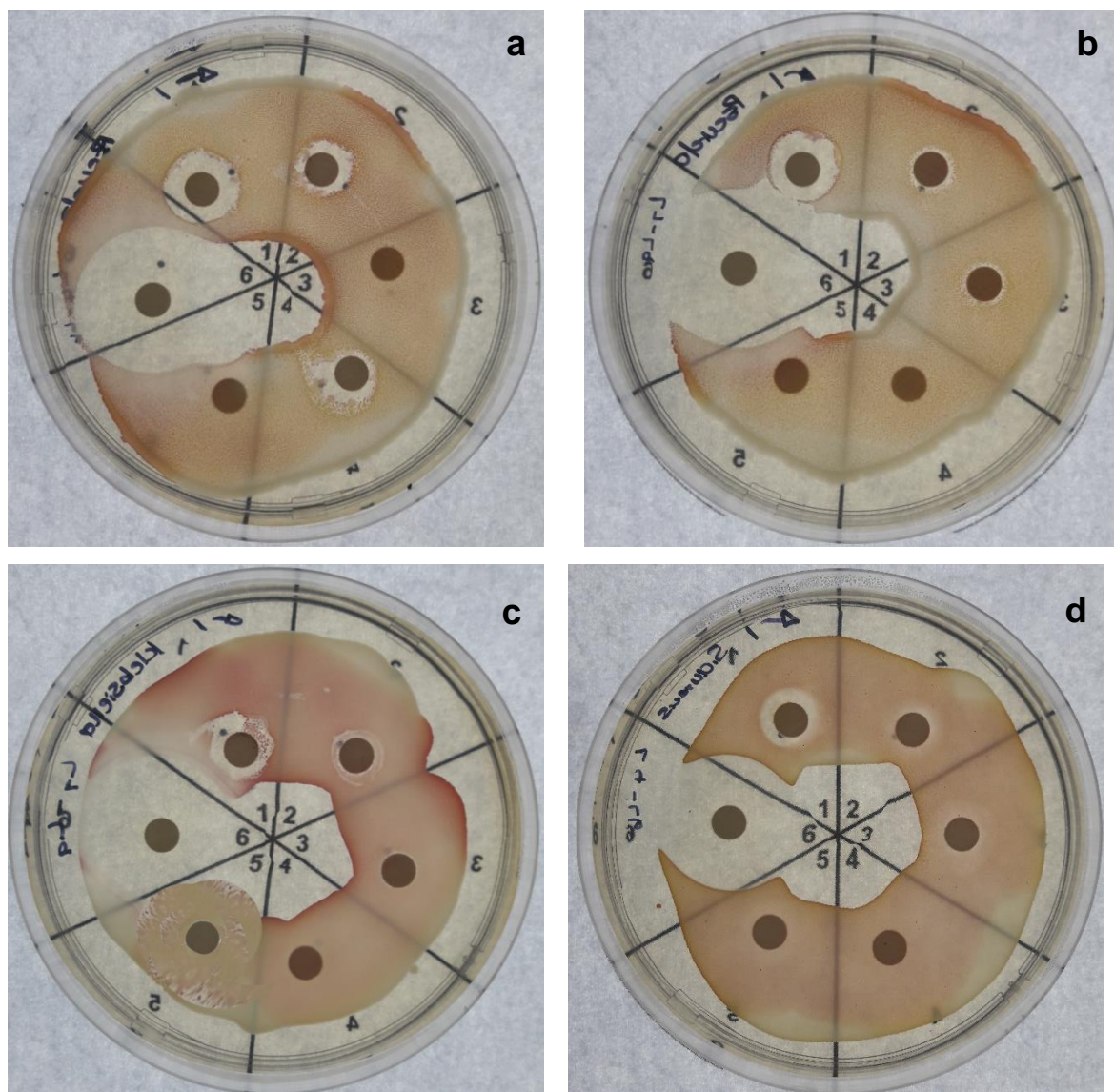


**Figure 5.7:** The disk-diffusion method showing the growth inhibition of: (a) *G. stearothermophilus*; (b) *P. aeruginosa*; (c) *K. pneumoniae*; and (d) *S. aureus* using the AgNPs supported on the PVDF nanofibres where 1-4 are AgNPs on the nanofibres, 5 is the nanofibre without antibacterial AgNPs and 6 is the antibiotic (neomycin).

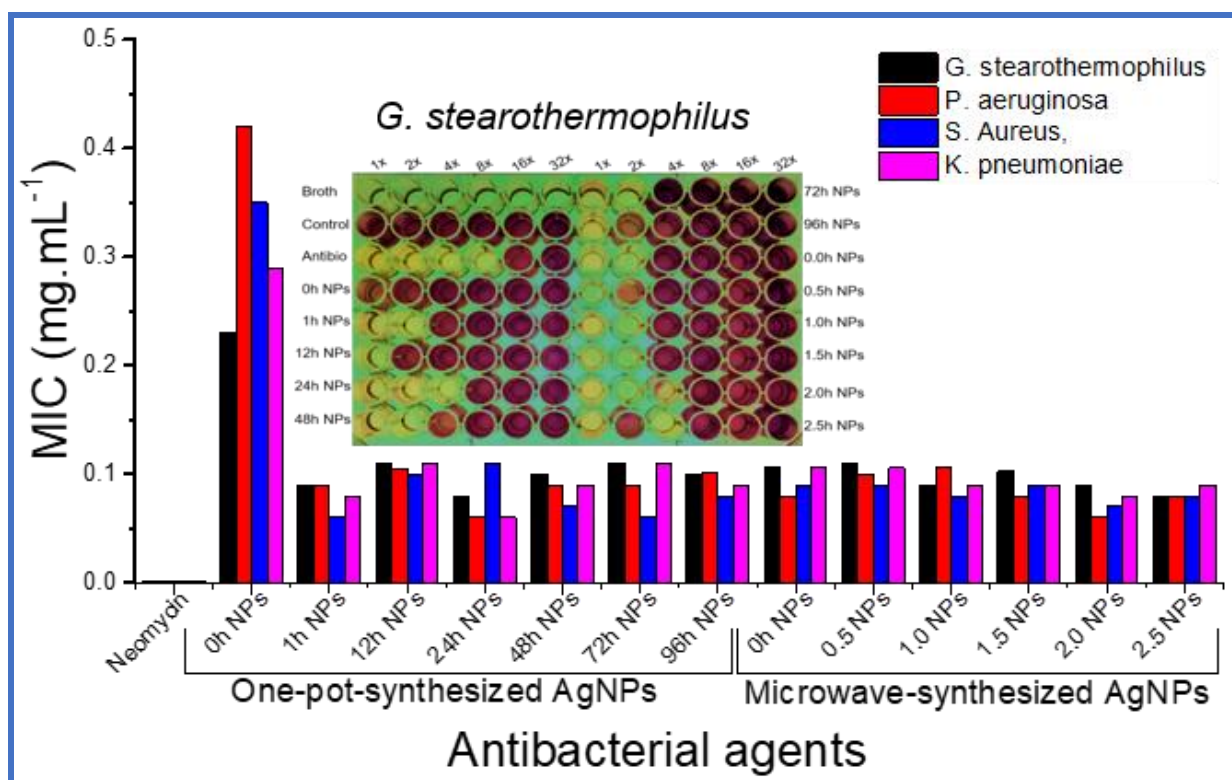


**Figure 5.8:** The minimum inhibitory concentration (MIC) of AgNPs reduced at different times on *Geobacillus stearothermophilus*, *Staphylococcus aureus*, *Pseudomonas aeruginosa*, and *Klebsiella pneumoniae*.

#### 5.4 Conclusion

Bacterial contamination of potable water is not only a health threat but also negatively affects the performance of several membrane-based processes (e.g., ultrafiltration, nanofiltration, desalination, membrane distillation). As a result, biofilms develop on the surface of membranes, thus reducing their rate of water recovery. Therefore, it is imperative to test the responses of biofilm-forming bacteria on the membranes towards AgNPs antibacterial activities prior to real applications in MD systems. In this study, the AgNPs were synthesised using both thermally-assisted one-pot and microwave-assisted reduction methods where apple extract was used as a novel reducing agent. The microwave-assisted method was found to produce highly dispersed AgNPs with particle sizes smaller than those produced using thermally-assisted one-pot method. The AgNPs were produced within 2.5 h in a microwave-assisted reduction and approximately 96 h

(4 days) in the thermally assisted one-pot reduction. This observation indicated that microwave-assisted reduction is an effective and efficient method for the synthesis of the AgNPs. The resultant AgNPs which were successfully embedded in the PVDF nanofibre membranes has demonstrated their capabilities in preventing the growth of mesophilic and thermophilic bacteria on the membranes at the minimum inhibition concentration of 0.06 – 0.11 mg/mL. These materials are therefore a one-step solution in preventing the formation of the biofilms on membrane surfaces in water purification systems that are subject to contamination by mesophilic and thermophilic bacteria. However, the real application for the prevention of biofilm formation is still required to determine the effect of thermophilic and mesophilic bacteria on water flux in MD.

# CHAPTER 6

## SUPERHYDROPHOBIC PVDF NANOFIBRE MEMBRANES COATED WITH AN ORGANIC FOULING RESISTANT HYDROPHILIC ACTIVE LAYER FOR DIRECT CONTACT MEMBRANE DISTILLATION

---

### 6.1 Introduction

Chapter 4 demonstrated high salt rejection and water flux in MD. Interestingly, the incorporation of functionalised nanoparticles such as silica (f-SiO<sub>2</sub>NPs) enhanced the hydrophobicity of PVDF nanofibre membranes (i.e., displaying contact angles  $\approx 160^\circ$ ) to mimic the self-cleaning mechanism of materials with strong water-repellent properties (the lotus effect) (38,103). However, it has been previously reported that performance of these superhydrophobic NP-modified PVDF nanofibre membranes is significantly affected by fouling (445). Specifically, hydrophobic polymers induce hydrophobic-hydrophobic interactions between foulants and the membrane, causing adsorption and resulting pore blocking and changes in membrane surface characteristics (i.e., conditioning film formation) (359). This fouling aggravates due to the accumulation of organic, inorganic and colloidal substances and the development of biofilms, resulting in enhanced wettability of the membranes and thus impacting the diffusion of water vapour through the membrane and compromising its rejection efficiency (37,93,446).

The literature survey has demonstrated that membranes with self-cleaning mechanisms should be characterised by contact angles  $\approx 180^\circ$  and a hysteresis of contact angle  $\leq 10^\circ$  (165,167,168,380,447–449). The membranes bearing these properties have not been achieved to this end. Therefore, the synthesis of high-performance PVDF membranes (i.e., fouling and wetting resistant) for the recovery of water from saline solutions remains the main challenge for the successful full-scale implementation of MD processes. Wang *et al.* (2016) demonstrated that membranes used in MD could also be modified to mimic antifouling properties of a

fish scales, clamshells, and shark skins due to their hydrophilic surface chemistry (94). This work and other related reports where the hydrophobic membranes were coated with a hydrophilic layer, has demonstrated that the membranes become wetted on the active hydrophilic surface while the hydrophobic layer prevents the passage of the water in liquid state and allows vapour permeability (94,138,139).

Therefore, this chapter and forthcoming chapters present the synthesis of a PVDF nanofibre membrane consisting of: i) a superhydrophobic separation layer, and ii) an antifouling hydrophilic active layer. The superhydrophobic layer comprised of a PVDF nanofibre membrane embedded with silanised-SiO<sub>2</sub>NPs, for exclusively allowing the transport of water vapour. The hydrophilic layer consisted of a PVDF membrane embedded with carboxylated multi-walled carbon nanotubes (f-MWCNTs) and silver nanoparticles (AgNPs), to provide hydrophilic and biocidal (i.e., biofouling control) properties, respectively. Active layers with similar characteristics (i.e., fouling control) have been extensively evaluated in other membrane-based purification systems (e.g., reverse osmosis, nanofiltration, and forward osmosis) (450–452). Both SiO<sub>2</sub>NPs and AgNPs were synthesised using a novel green-chemistry method. Additionally, the morphology of NPs and membranes and chemical structure were rigorously characterised by X-Ray photoelectron spectroscopy (XPS), Transmission Electron Microscopy (TEM), Scanning Electron Microscopy (SEM), X-Ray Diffraction (XRD), Raman Spectroscopy, and Fourier Transform Infra-Red Spectroscopy (FTIR); while their performance (salt rejection and water flux) was assessed. There is little information regarding the synthesis of highly-porous superhydrophobic PVDF nanofibre membranes coated with a thin hydrophilic (active) layer to impart fouling resistance properties in MD.

## **6.2 Materials and methods**

### **6.2.1 Reagents**

Polyvinylidene fluoride (PVDF) (MW = 534 000 g/mol), tetraethyl orthosilicate (TEOS) (reagent grade, 98%), N,N-dimethylacetamide (DMAc) (Puriss p.a.,

99.5%), acetone (ACS reagent, 99.5%), absolute ethanol (ACS reagent, 99.9%), toluene (ACS reagent, 99.7%), bovine serum albumin (BSA, lyophilised powder, 95%, MW = 66 000 g/mol) octadecyltrimethoxysilane (OTMS) (technical grade, 90%), 30 mL PP/PE eccentric tip syringe equipped with a blunt tip dispensing needle, and aluminium foil (thickness:  $3.0 \times 10^{-4}$  m) were purchased from Sigma Aldrich (Germany). Granny Smith apple extract was purchased from Makolobane Farmers Enterprises (Senekal, South Africa). Deionised water was produced in the laboratory using Direct-Q® Millipore system (Merck Millipore). All reagents were used as received.

### **6.2.2 Synthesis of silver nanoparticles (AgNPs) and silica nanoparticles (SiO<sub>2</sub>NPs)**

Silver nanoparticles were prepared using a modified green synthesis method as reported by Shaik *et al.* (2008) where apple extract was used as the reducing agent [28,29]. This synthesis method was previously described in **Chapter 5**. Silica nanoparticles were prepared using a one-pot green chemical reduction method involving apple extract (i.e., reducing agent) as described in **Chapter 4**.

### **6.2.3 Surface modification of SiO<sub>2</sub>NPs**

The surface modification of the SiO<sub>2</sub>NPs (i.e., silanisation) was performed by dispersing 10 mg of pristine SiO<sub>2</sub>NPs in a conical flask containing 20 mL of toluene, followed by the addition of 1 mL of octadecyltrimethoxysilane (OTMS). The flask was stirred for 5 h under an inert atmosphere prior to centrifugation. The resultant organically-modified SiO<sub>2</sub>NPs were rinsed twice with absolute ethanol to remove any excess silane (OTMS) reagent, dried in an oven at 60°C for 24 h prior to isolation, and termed f-SiO<sub>2</sub>NPs. This method was also discussed in **Chapter 4**.

#### **6.2.4 Synthesis and oxidation of Multi-walled Carbon Nanotubes (MWCNTs)**

Multi-walled carbon nanotubes (MWCNTs) with an average diameter of 7 nm were synthesised following the previously reported procedure (263,265,453). The MWCNTs were oxidised to MWCNTs-COOH using a concentrated acid mixed solvent solution ( $\text{H}_2\text{SO}_4/\text{HNO}_3$ ) during purification and termed f-MWCNTs. During the purification and oxidation process, 0.2 g of MWCNTs were added into a 25 mL solution of sulphuric acid/nitric acid mixture (3:1) in a 50 mL round-bottom flask equipped with a starfish condenser. The mixture of MWCNTs and acid solvent was refluxed at 120°C for 24 h. The resultant f-MWCNTs were separated from the acid solvent by diluting the mixture to 1 000 mL with deionised water and thereafter filtered. The f-MWCNTs were washed several times with deionised water until a neutral pH was reached and were finally dried in an oven at 110°C for 24 h.

#### **6.2.5 Synthesis of PVDF nanofibre membranes**

The PVDF nanofibre membranes were synthesised using an electrospinning technique as previously described in **Chapter 4**. The top surface of the f-SiO<sub>2</sub>NPs-modified PVDF nanofibre membrane was coated with a thin hydrophilic layer as follows. The f-SiO<sub>2</sub>NPs-modified PVDF nanofibre membrane was placed on a casting plate. The casting knife was adjusted to a distance of 20 µm above the nanofibre membrane surface. A PVDF solution containing 1% (w/v) f-MWCNTs, 2% (w/v) AgNPs, and 4% deionised water (i.e., as the hydrophilic, antibacterial, and pore-forming agents, respectively) was cast on the top surface of the f-SiO<sub>2</sub>NPs-modified PVDF nanofibre membrane. The resulting membrane was then immersed in a water bath for coagulation and dried in an oven at 50°C for 24 h and termed AgNPs/f-MWCNTs coated PVDF nanofibre membrane.

#### **6.2.6 Characterisation of nanoparticles and PVDF nanofibre membranes**

The dispersion, shape, and size of AgNPs, MWCNTs, f-MWCNTs, SiO<sub>2</sub>NPs, and f-SiO<sub>2</sub>NPs were characterised using a transmission electron microscope (TEM,

JEOL Jem-2010). ImageJ software was used to calculate the sizes of the NPs using the acquired TEM micrographs. The chemical characteristics and functionalisation of the f-MWCNTs, SiO<sub>2</sub>NPs were confirmed using Fourier Transform Infrared (Perkin Elmer FTIR) and X-Ray Photoelectron Spectroscopy (AXIS Supra™ XPS). A Scanning Electron Microscope (SEM, JEOL STM – IT300) was used to study the surface morphology of the membranes, while the dry membrane samples were examined using X-ray Diffraction (XRD) (Rigaku 124 Ultimate IV X-ray diffractometer) to obtain information on their crystal structure. The XRD patterns were qualitatively analysed using integrated X-ray powder diffraction software (PDXL), provided with the Powder Diffraction File from the Joint Committee on Powder Diffraction Standards (JCPDS-PDF2) database. The thermal degradation of the membranes was monitored using a Perkin-Elmer TGA 4000 thermogravimetric analyser. Raman spectra of the MWCNTs were obtained in the range between 3500 and 100 cm<sup>-1</sup> on a Bruker FT Raman RFS 100/S spectrophotometer system equipped with a 785 and 1064 nm dual-channel laser at a resolution of 1 cm<sup>-1</sup>. Finally, stress-strain graphs were obtained using an AG-Plus Universal tester on a rectangular-shaped membrane sample (100×65 mm<sup>2</sup>). The Young's modulus ( $E = \frac{\delta}{\epsilon}$ ) was calculated from the elastic region before materials reach the yield strength, where  $\delta$  was the force applied per membrane area (A) and  $\epsilon$  was the dimensionless membrane displacement (proportional deformation). The leaching of AgNPs was tested using a PerkinElmer UV-Vis spectrometer Lambda 6505. The test samples were analysed from the MD permeate solution while the control test solution was the solution of reduced AgNPs presented in **Chapter 5**.

### 6.2.7 Performance of PVDF nanofibre membranes

The direct contact membrane distillation (DCMD) process was used to evaluate the salt rejection and water flux for: a) pristine, b) f-SiO<sub>2</sub>NPs-modified, and c) AgNPs/f-MWCNTs-coated PVDF nanofibre membrane (surface area ≈ 0.0125 m<sup>2</sup>). The test solution was composed of 30×10<sup>3</sup> mg/L NaCl, 5.0 mg/L CaCl<sub>2</sub> and 50 mg/L bovine serum albumin BSA. The feed and permeate temperatures were kept

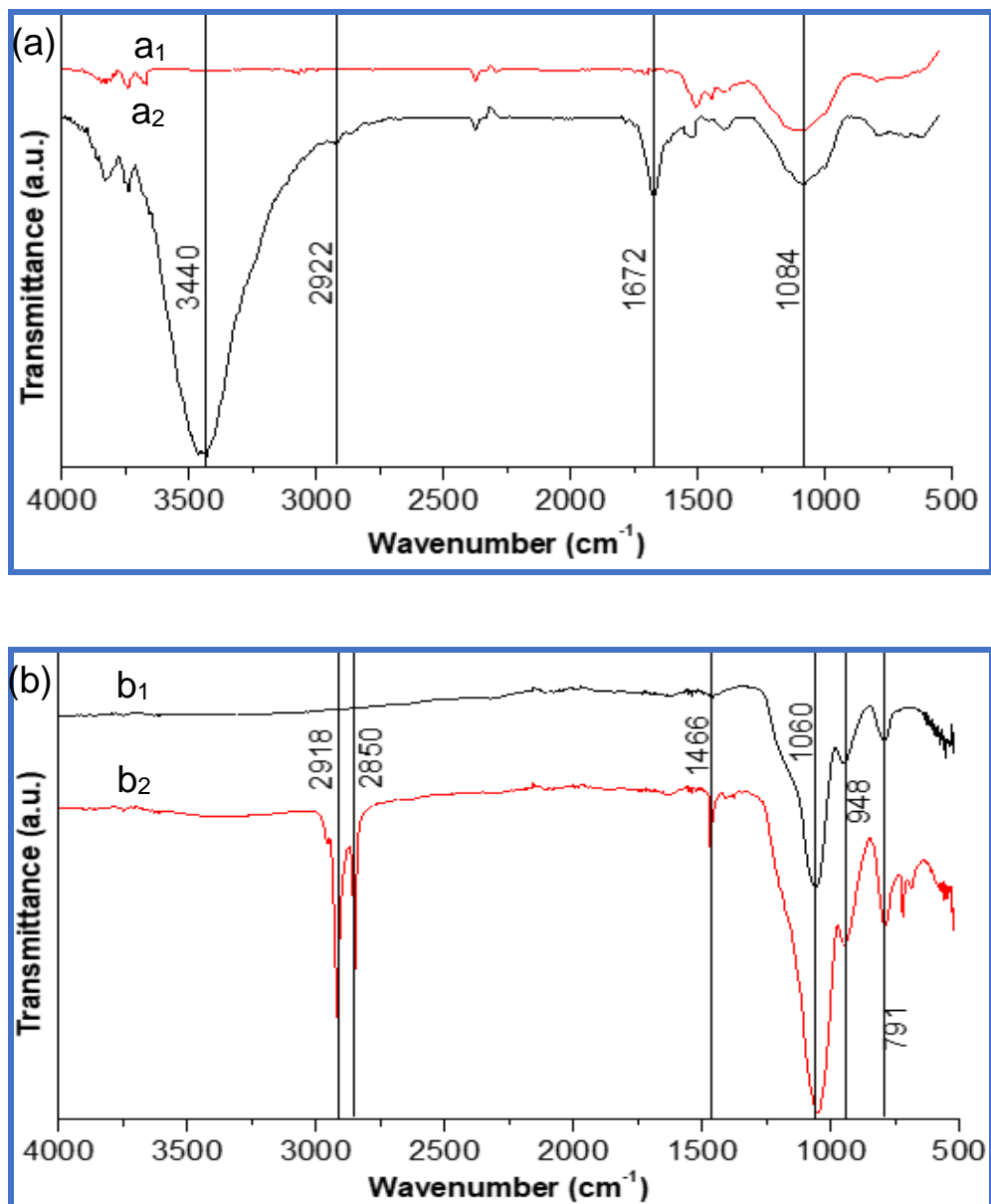
at 60°C and 20°C, respectively. The water was circulated at a flow rate of 0.75 L/min and the conductivity of the water solutions was continuously measured using a Shimadzu conductivity meter to determine the average salt concentration at the feed and permeate side of the membranes. The amount of water passing through the membrane in the form of vapour was determined by measuring the weight increment of the coolant water using a Kern & Sohn GmbH, EMB 3000\_1 weighing balance. **Equations 4.1** and **4.3** were used to calculate the water flux and salt rejection respectively.

### 6.3 Results and discussion

#### 6.3.1 Structural analysis of pristine and modified PVDF nanofibre membranes, MWCNTs, and SiO<sub>2</sub>NPs by FTIR

Structural information of pristine and modified MWCNTs, SiO<sub>2</sub>NPs, and PVDF membranes was obtained from FTIR analysis over a spectral range of 4 000 – 500 cm<sup>-1</sup>. Infrared absorption peaks of functional groups were compared to the IR spectra of common functional groups reported by McMurry (2008) (346). Specifically, the peaks at 1 084 cm<sup>-1</sup> and 2 922 cm<sup>-1</sup> were due to the stretching vibrations of C-C and C-H of the MWCNTs (**Figure 6.1a<sub>1</sub>**). The functionalisation of MWCNTs (f-MWCNTs) was identified by the presence of two peaks at 3 440 cm<sup>-1</sup> and 1 672 cm<sup>-1</sup> which corresponded to the stretching frequencies of O-H and C=O (**Figure 6.1a<sub>2</sub>**). These stretching frequencies are characteristic bonds in the -COOH functional group (454). In the case of SiO<sub>2</sub>, the Si-O-Si symmetric and asymmetric bands were observed at 791 cm<sup>-1</sup> and 1 060 cm<sup>-1</sup>. The peak at 946 cm<sup>-1</sup> was attributed to the Si-O stretching vibration (**Figure 6.1b<sub>1</sub>**). The intense peaks at 2 918 cm<sup>-1</sup> and 2 850 cm<sup>-1</sup> were ascribed to the C-H stretching vibration of the long molecular chains of the alkyl groups in octadecyltrimethoxysilane (CH<sub>3</sub>(CH<sub>2</sub>)<sub>17</sub>Si(OCH<sub>3</sub>)<sub>3</sub>) (**Figure 6.1b<sub>2</sub>**). The CH<sub>2</sub> band of the octadecyltrimethoxysilane (OTMS) was observed at 1 466 cm<sup>-1</sup> (455,456). The presence of the α-form of PVDF was ascertained by the bands at 1 171 cm<sup>-1</sup> and 876 cm<sup>-1</sup> that corresponded to the -CF<sub>2</sub>- stretching and bending (**Figure 6.1c<sub>1</sub>**). The bands at 1 401 and 2 925 were associated with the C-F and C-H stretching

frequencies, respectively (457,458). No new peaks were observed upon addition of f-MWCNTs and f-SiO<sub>2</sub>NPs to the PVDF membrane (**Figure 6.1c<sub>2</sub>-c<sub>3</sub>**), indicating that these particles were physically bound to the resultant PVDF nanocomposite fibres. However, the grafting of OTMS onto SiO<sub>2</sub>NPs (superhydrophobic fillers) and the carboxylation of MWCNTs (hydrophilic fillers) were further confirmed using X-ray photoelectron spectroscopy (XPS).



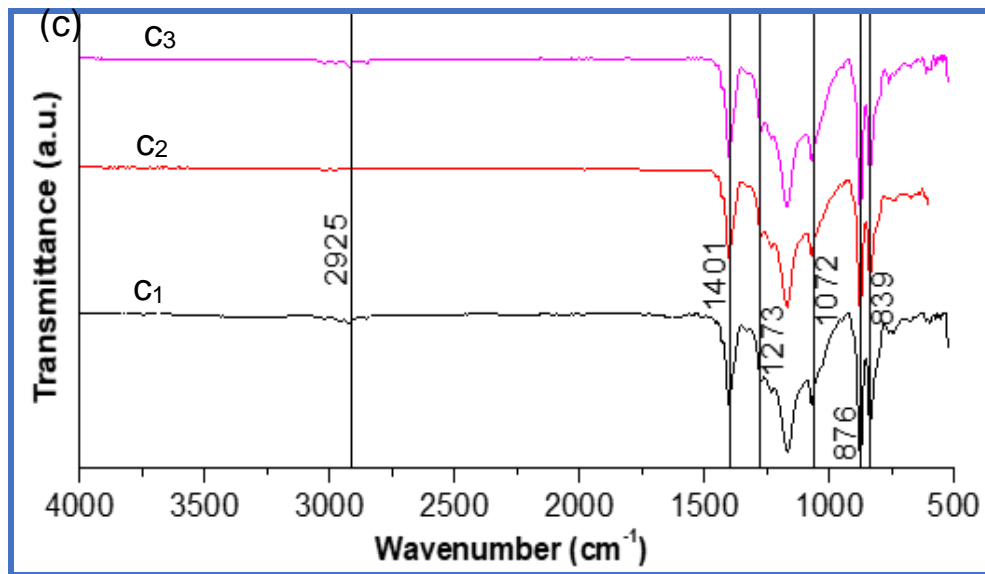


**Figure 6.1:** FTIR spectra of: (a<sub>1</sub>) MWCNTs; (a<sub>2</sub>) f-MWCNTs; (b<sub>1</sub>) SiO<sub>2</sub>NPs; (b<sub>2</sub>) f-SiO<sub>2</sub>NPs; (c<sub>1</sub>) pristine PVDF nanofibre membrane; (c<sub>2</sub>) AgNPs/f-MWCNTs coated PVDF nanofibre membrane; and (c<sub>3</sub>) f-SiO<sub>2</sub>NPs-modified PVDF nanofibre membrane.

### 6.3.2 Raman spectroscopic analysis of MWCNTs

The oxidation of the as-synthesised MWCNTs using a H<sub>2</sub>SO<sub>4</sub>/HNO<sub>3</sub> acid solution decreased the catalyst impurities, thus resulting in the decrease of distortions of MWCNTs structures. The graphite peaks (G bands) of the MWCNTs, f-MWCNTs, and AgNPs/f-MWCNT-coated PVDF nanofibres membranes were observed at 1 569 cm<sup>-1</sup>, 1 572 cm<sup>-1</sup>, and 1 582 cm<sup>-1</sup>, respectively (**Figure 6.2**). The distortion peaks (D bands) of these materials were observed at 1 345 cm<sup>-1</sup>, 1 353 cm<sup>-1</sup> and 1 343 cm<sup>-1</sup>, respectively. The corresponding Raman shifts of each spectrum and the derived ratios of the intensities of the D and G bands ( $I_D/I_G$ ) are provided in **Table 6.1**. The  $I_D/I_G$  ratio of the MWCNTs decreased after acid treatment, indicating that there was a decrease in impurities which consequently induced the grain boundaries between the C-C bonds of the MWCNTs. However, the incorporation of f-MWCNTs into the PVDF nanofibres indicated the alteration of the grain

boundaries as demonstrated by the increase in  $I_D/I_G$  ratio. These results are in agreement with previously reported findings (459–462).

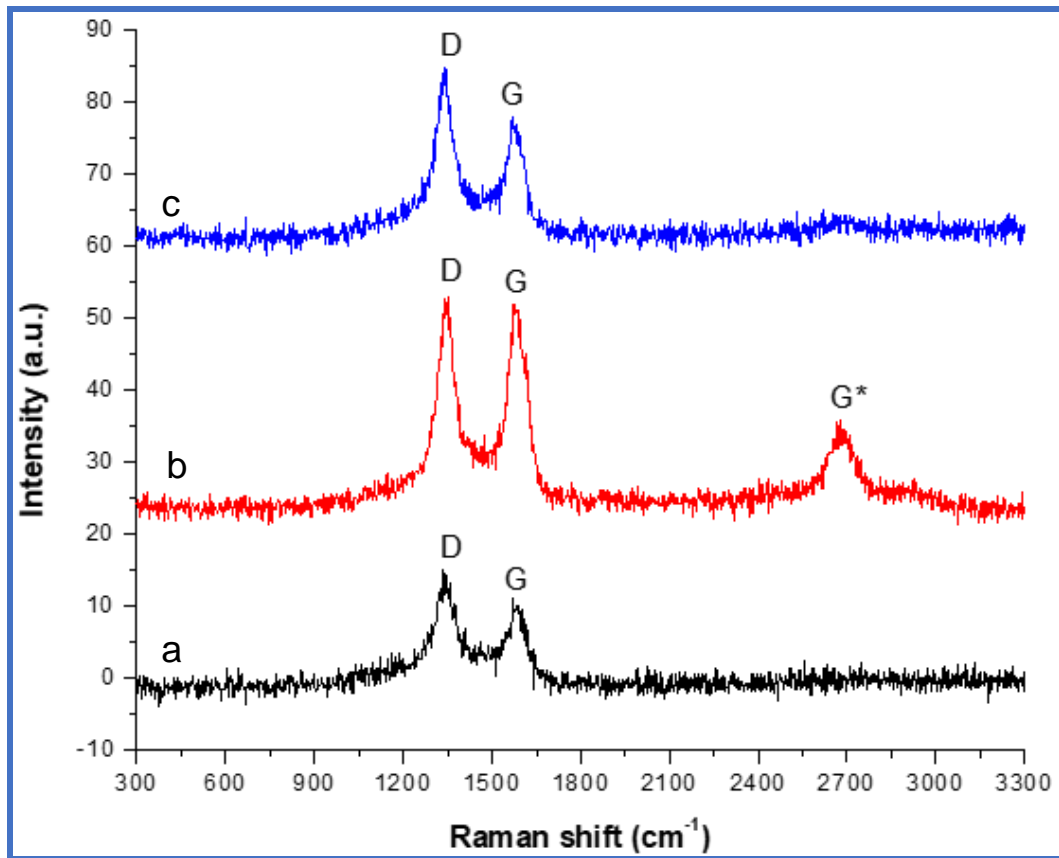


**Figure 6.2:** Raman spectra of: (a) MWCNTs; (b) f-MWCNTs; and (c) AgNPs/f-MWCNT-coated PVDF nanofibre membrane.

**Table 6.1:**  $I_D/I_G$  ratios of the MWCNTs used to modify PVDF nanofibre membranes.

Materials	Raman shift ( $\text{cm}^{-1}$ )		$I_D/I_G$
	Distortion (D band)	Graphite (G band)	
MWCNTs	1 345	1 569	1.32
f-MWCNTs	1 353	1 572	1.07
AgNPs/f-MWCNTs PVDF	1 343	1 582	1.47

### 6.3.3 XRD analysis of modified PVDF nanofibre membranes

The PVDF nanofibre membranes were analysed using XRD to confirm the embedment of f-MWCNTs, f-SiO<sub>2</sub>NPs and AgNPs. The XRD patterns of these nanomaterials are presented in **Figure 6.3**. The JCPDS card values for the observed planes (210) at  $2\theta = 29.98^\circ$  corresponded to the broad diffraction pattern of the SiO<sub>2</sub> (**Figure 6.3c**). The diffraction patterns of the f-MWCNTs were observed at  $2\theta = 25.79^\circ$  and  $43.08^\circ$  with the JPCDS card values for the planes (002) and (100) (**Figure 6.3b**). The card values for the planes (111), (200), (220), (331), (222) at  $2\theta = 38.17^\circ, 44.39^\circ, 64.50^\circ, 77.42^\circ, 81.69^\circ$  were characteristic XRD patterns of the AgNPs (**Figure 6.3a**). The PVDF nanofibre membranes decorated with f-MWCNTs, f-SiO<sub>2</sub>NPs, and AgNPs showed the diffraction patterns of the PVDF, MWCNTs, SiO<sub>2</sub>NPs, and AgNPs at the planes (020), (002), (210), and (111) with a slight shift to the  $2\theta = 20.96^\circ, 25.92^\circ, 28.76^\circ, \text{ and } 38.14^\circ$ , respectively (**Figure 6.3d**).

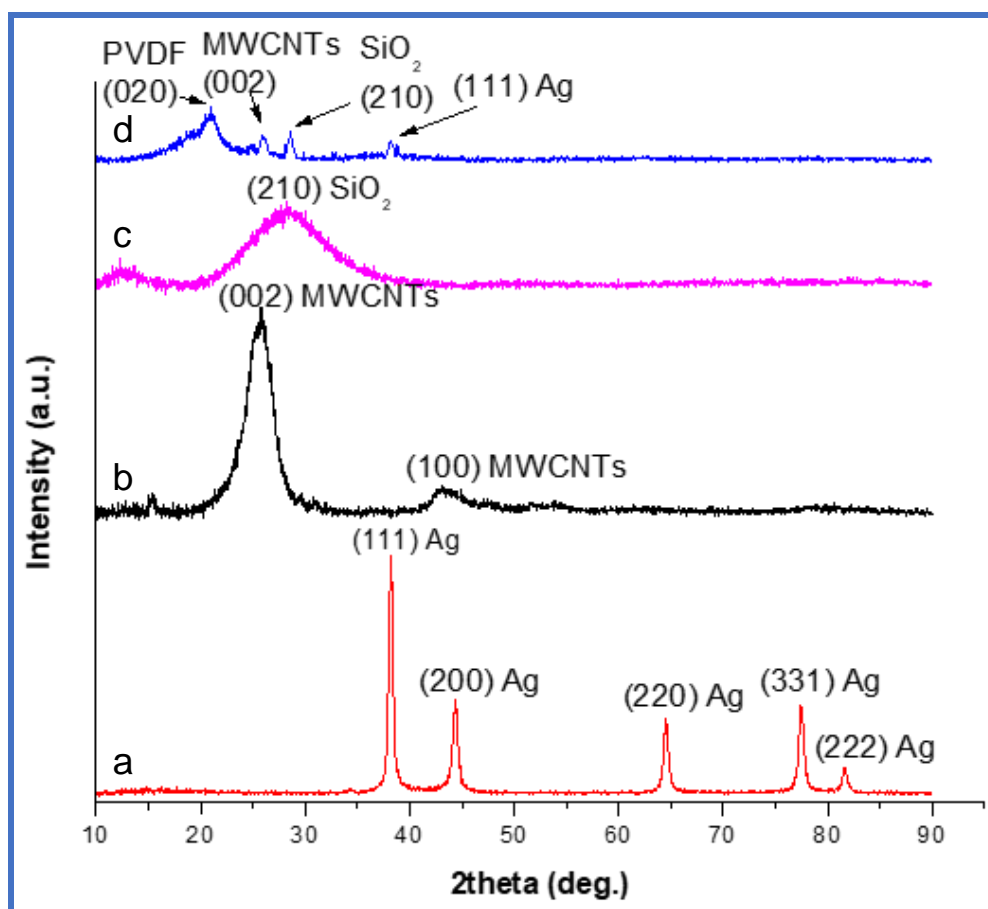


**Figure 6.3:** XRD spectra of: (a) AgNPs; (b) f-MWCNTs; (c) f-SiO<sub>2</sub>NPs; and (d) AgNPs/f-MWCNTs coated PVDF nanofibre membrane.

### 6.3.4 XPS analysis of the SiO<sub>2</sub>NPs and MWCNTs

The elemental composition of SiO<sub>2</sub>NPs and f-SiO<sub>2</sub>NPs was also studied using X-ray photoelectron spectroscopy (XPS). The standard survey scan of SiO<sub>2</sub>NPs and f-SiO<sub>2</sub>NPs is presented in **Figure 6.4**. The spectra of the survey scan exhibited four distinct peaks at 101 eV, 152 eV, 282 eV, and 530 eV, corresponding to Si2p, Si2s, C1s and O1s, respectively. An increase in the atomic fraction of Si and O was observed after the modification of the SiO<sub>2</sub>NPs using octadecyltrimethoxysilane (OTMS) (**Table 6.2**). This increase would be attributed to the incorporation of the Si and O carrying OTMS that was grafted onto SiO<sub>2</sub>NPs. The binding energy of C1s at 281.8 eV was observed on SiO<sub>2</sub>NPs. Upon modification of the SiO<sub>2</sub>NPs, the C1s peaks at binding energies of 282.2 – 282.0

eV, 284.1 eV, and 285.6 eV corresponding to the bonding of Si-C, C-C, and C-O, respectively, were identified (**Figure 6.5**) (160,463–467). Additionally, the O1s peak at binding energy of 530.0 eV corresponding to the bonding of Si-O was identified. The C1s, O1s, and Si2p spectra of the SiO<sub>2</sub>NPs were deconvoluted and were further presented on **Figure 6.5**. The binding energies of C1s, O1s and Si2p, C1s and O1s on SiO<sub>2</sub>NPs were 100.9 eV, 281.8 eV, and 529.2 eV, respectively (**Figure 6.5a,c,e**). Upon modification of SiO<sub>2</sub>NPs (i.e. f-SiO<sub>2</sub>NPs), the binding energy peaks of Si2p were 99.9 eV, 99.5 eV, and 99.3 eV which corresponded to C-O-Si, Si-C, and Si-Si bonds (**Figure 6.5f**). All these binding energies indicated the successful grafting of the OTMS onto SiO<sub>2</sub>NPs. The self-assembled monolayer of OTMS on the SiO<sub>2</sub>NPs would be expected to improve the hydrophobicity of membranes due to their long-chain aliphatic non-polar CH<sub>3</sub> anchored on the SiO<sub>2</sub>NPs (39,156,157,160–162).

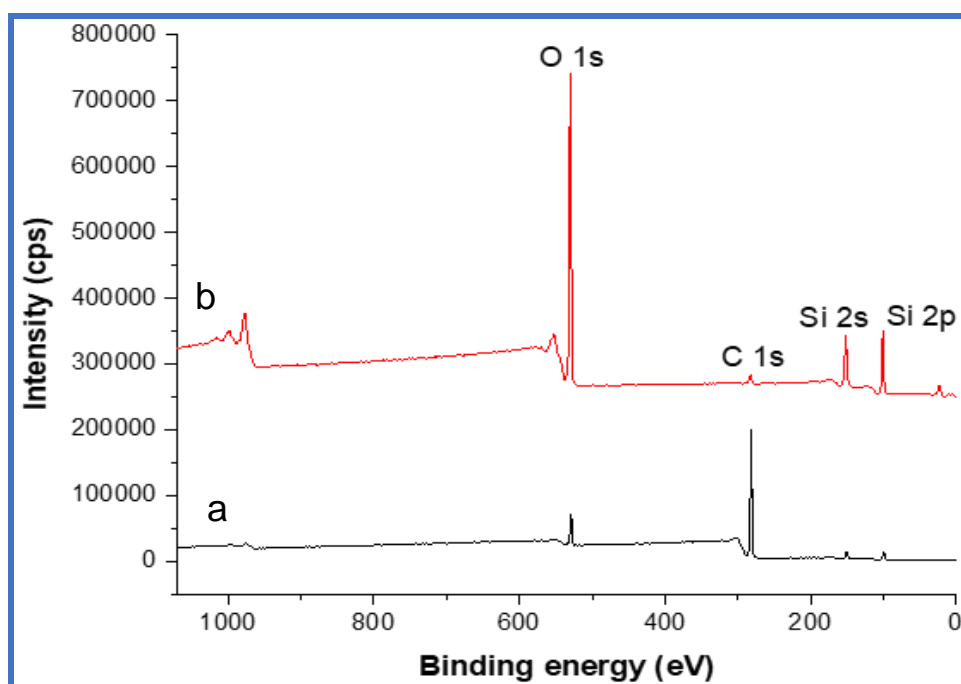


**Figure 6.4:** XPS survey spectra of (a) SiO<sub>2</sub>NPs and (b) f-SiO<sub>2</sub>NPs.

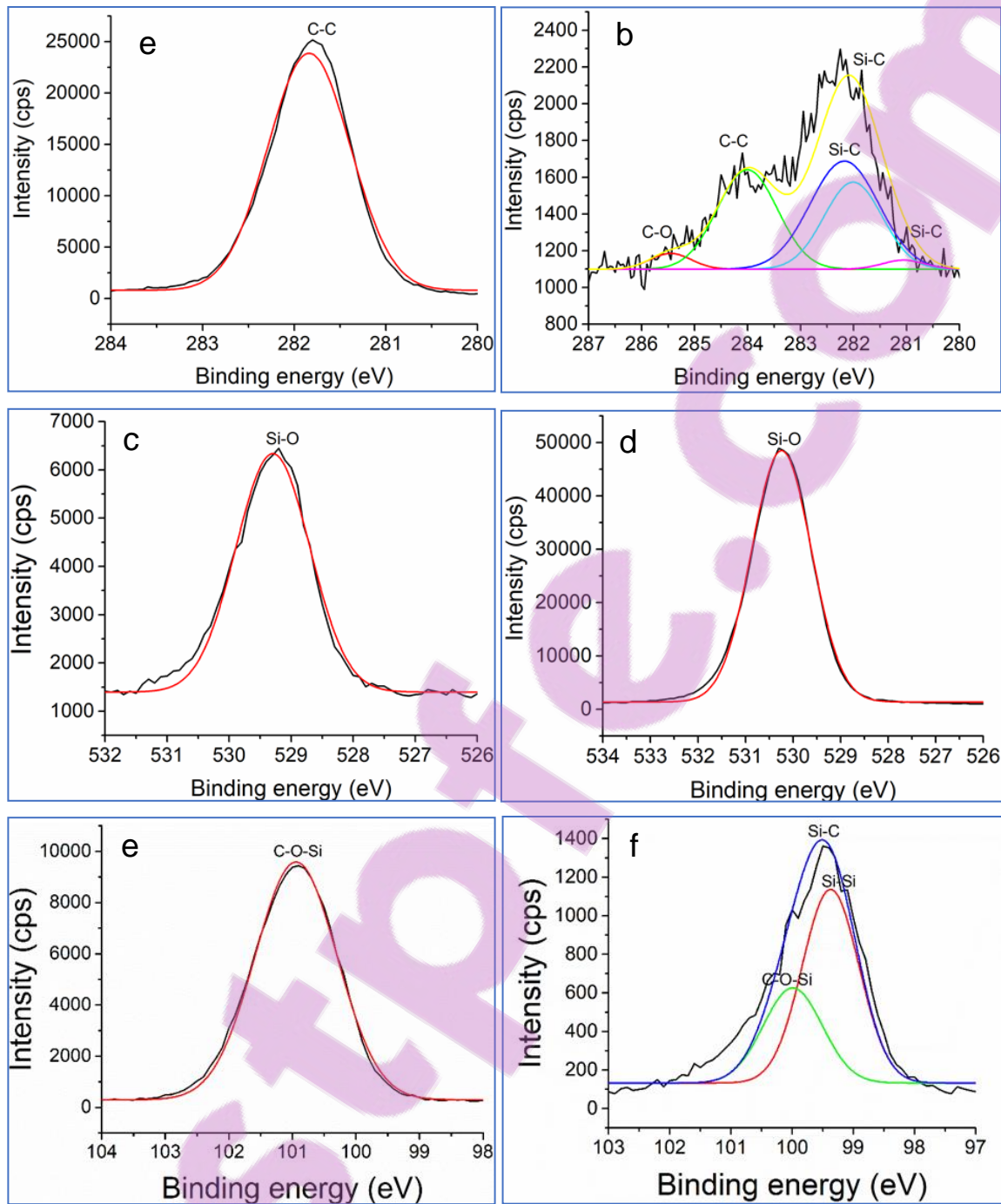


**Figure 6.5:** XPS spectra of SiO<sub>2</sub>NPs and f-SiO<sub>2</sub>NPs indicating the deconvoluted peaks of (a-b) C1s, (c-d) O1s, and (e-f) Si2p.

**Table 6.2:** Atomic concentration of the elements in SiO<sub>2</sub>NPs.

Atoms	SiO <sub>2</sub> NPs (%)	f-SiO <sub>2</sub> NPs (%)
Si2p	5.75±0.20	30.15±0.28
C1s	85.23±0.31	6.25±0.47
O1s	9.02±0.26	63.61±0.39

### 6.3.5 TEM analysis of AgNPs and SiO<sub>2</sub>NPs

The physical properties of nanoparticles (i.e., size and shape) have been previously reported to affect their properties (468). Depending on the synthesis method, nanoparticles would occur in varied shapes (e.g., spheres, cubes, rods, and platelets) and sizes below 100 nm (468). The TEM images of AgNPs, SiO<sub>2</sub>NPs, and f-SiO<sub>2</sub>NPs indicated the formation of sphere-like nanoparticles (**Figure 6.6**). AgNPs were slightly dispersed with few loose aggregates while pristine and f-SiO<sub>2</sub>NPs were monodispersed (**Figure 6.6a-c**). The sizes (diameters) of AgNPs, pristine SiO<sub>2</sub>NPs and f-MWCNTs followed a lognormal distribution with mean diameters of 22.1±4.1 nm, 17.2±3.9 nm, and 6.7±2.1 nm, respectively (**Figure 6.7a,b,d**). The size of f-SiO<sub>2</sub>NPs followed a Gaussian distribution with a mean diameter of 23.5±4.3 nm (**Figure 6.7c**). The SiO<sub>2</sub>NPs reported in this chapter are comparable with the ones reported on chapter 4. The increase in diameters of the f-SiO<sub>2</sub>NPs was previously described to be caused by the self-assembly layer formation on the pristine SiO<sub>2</sub>NPs leading to visual differences under transmission electron microscope.

The organic modification of SiO<sub>2</sub>NPs (OTMS self-assembled layer) would have resulted in an increase in the size of the SiO<sub>2</sub>NPs (**Figure 6.6c**). Conversely, tube-like structures were observed for both MWCNTs and f-MWCNTs, indicating the formation of nanotubes (**Figure 6.6d-e**). Also, the size distribution plots of AgNPs, SiO<sub>2</sub>NPs, and MWCNTs followed lognormal and Gaussian functions (SI); where both pristine and oxidised MWCNTs showed similar mean diameters (6.7±2.1 nm). Interestingly, the TEM images of pristine MWCNTs showed traces of catalyst

deposit (**Figure 6.6d**). Nevertheless, upon acid treatment of MWCNTs (i.e., resulting in f-MWCNTs), the catalyst traces were significantly reduced (**Figure 6.6e**).

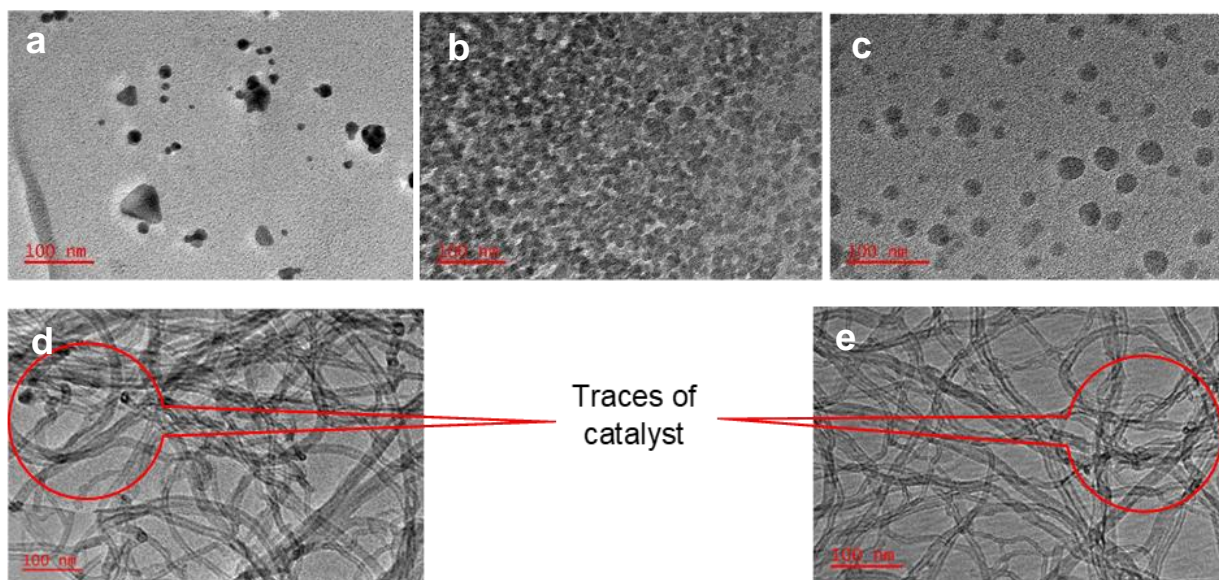


**Figure 6.6:** TEM images of: (a) AgNPs; (b) pristine SiO<sub>2</sub>NPs; (c) f-SiO<sub>2</sub>NPs; (d) MWCNTs; and (e) f-MWCNTs.

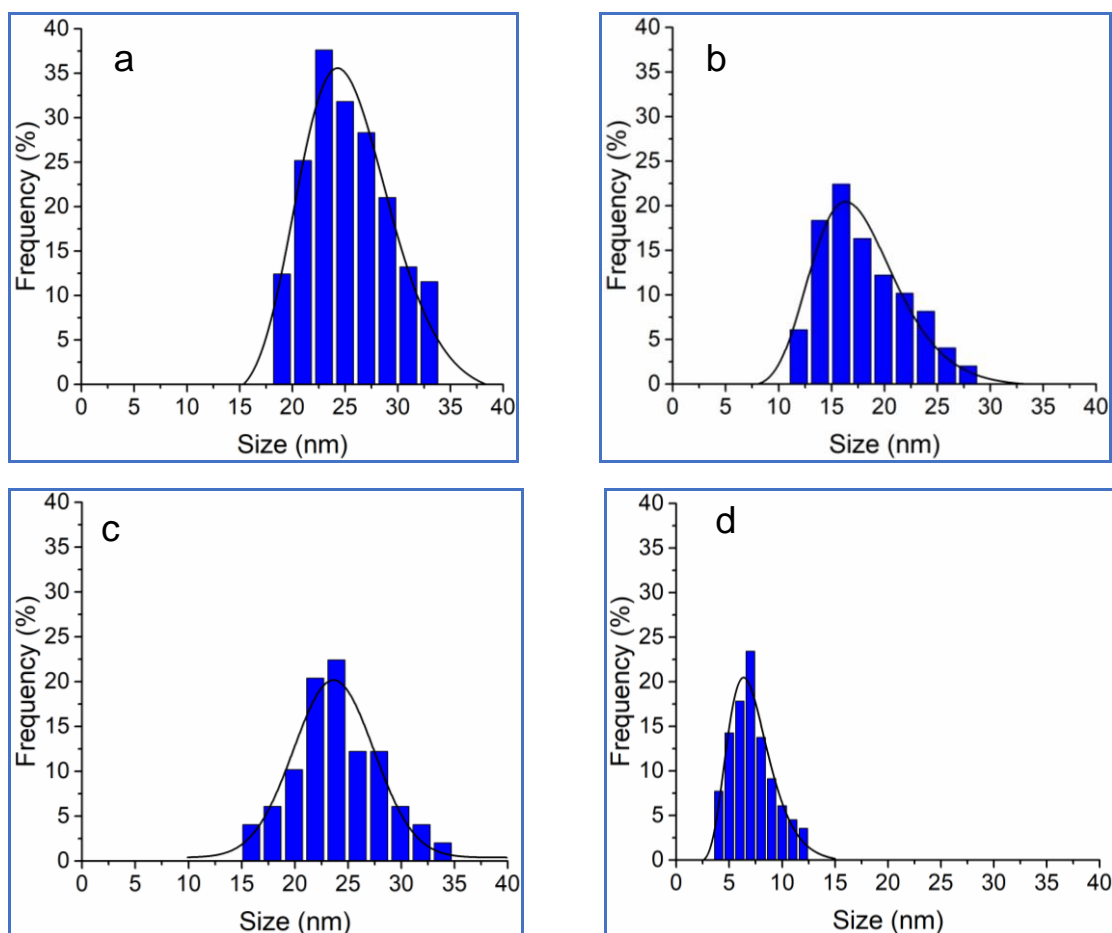


**Figure 6.7:** Size distributions of (a) AgNPs, (b) SiO<sub>2</sub>NPs, (c) f-SiO<sub>2</sub>NPs, and (d) f-MWCNTs.

### 6.3.6 Morphological analysis of pristine and modified PVDF nanofibre membranes by SEM

The morphology of pristine and modified PVDF nanofibre membranes (i.e., surfaces and cross-sections) was studied by SEM. SEM micrographs showed uniform and bead-free pristine PVDF nanofibres synthesised under optimised electrospinning conditions as described in Section 2.2.2 (**Figure 6.8a**). The addition of the f-SiO<sub>2</sub>NPs affected the viscoelasticity of the PVDF electrospinning solution. This change in viscoelasticity led to a stream breakdown process and failure to stabilise the polymer jet which affected the molecular entanglement of the nanofibres, thus resulting in slightly-beaded nanofibre membranes with non-uniform structures (112). Remarkably, the resultant PVDF nanofibre membranes

were characterised by monodispersed f-SiO<sub>2</sub>NPs (**Figure 6.8b**). A cross-section of the f-SiO<sub>2</sub>NPs-modified PVDF nanofibre membrane coated with a thin hydrophilic AgNPs/f-MWCNTs layer is presented in **Figure 6.8c**. The thickness of this thin hydrophilic layer was approximately 16  $\mu\text{m}$  while that of the electrospun f-SiO<sub>2</sub>NPs-modified PVDF nanofibre was approximately 116  $\mu\text{m}$ , resulting in a combined thickness of approximately 135  $\mu\text{m}$ . An efficient contact between the thin layer and the nanofibre membrane was observed, which eventually led to difficulty in estimating the exact thickness of the thin active layer. The thin layer was also characterised by a high pore size distribution as evidenced in the high-resolution SEM micrograph (**Figure 6.8d**). Further details on the membrane pore size and porosity are presented in the next section.

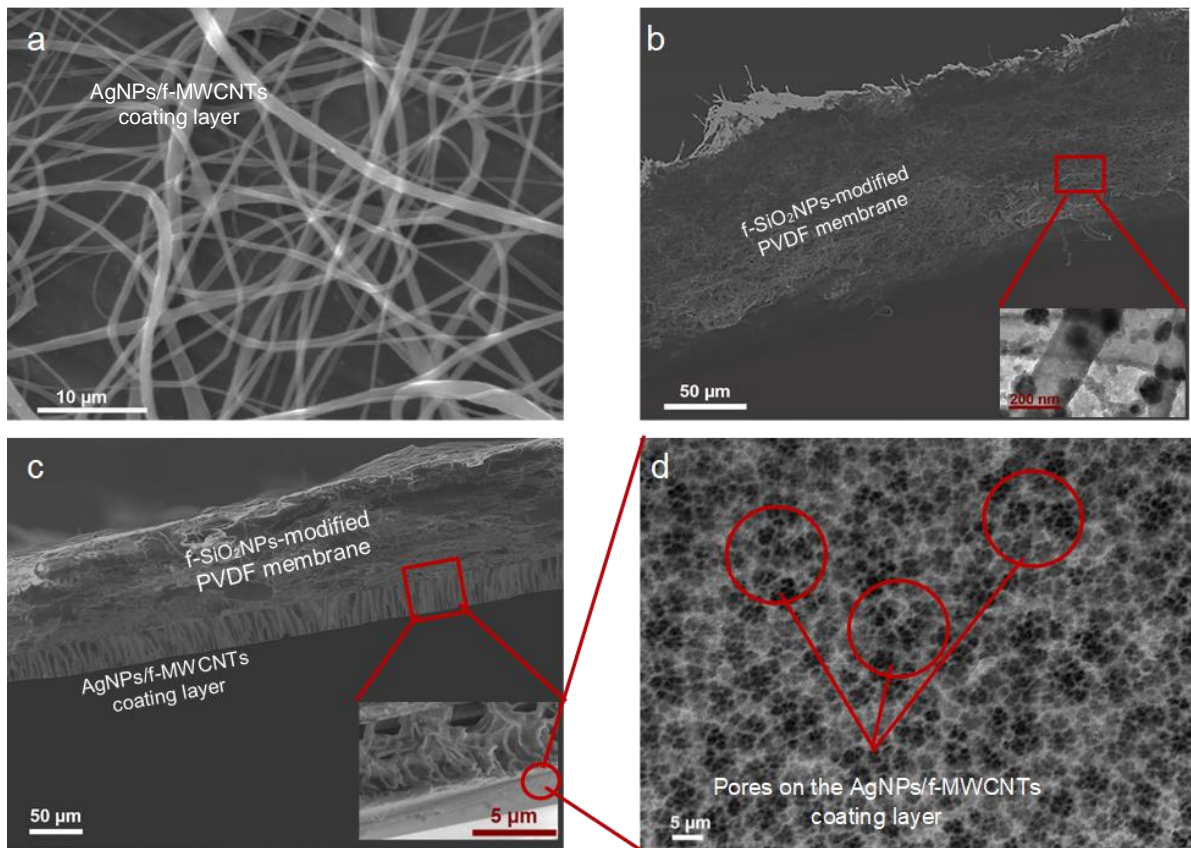


**Figure 6.8:** SEM micrographs of: (a) pristine PVDF nanofibre membrane; (b) cross-section of f-SiO<sub>2</sub>NPs-modified PVDF nanofibre membrane; (c) cross-section of AgNPs/f-MWCNTs coated PVDF nanofibre membrane; and (d) top surface of the AgNPs/f-MWCNTs coating layer.

### 6.3.7 Contact angles, porosity and pore sizes of pristine and modified PVDF nanofibre membranes

The contact angles, porosity and pore sizes of the PVDF nanofibre membranes are presented in **Figure 6.9**. The PVDF membranes were either hydrophobic or hydrophilic, depending on the synthesis methods used and the additives incorporated in the membrane. This degree of hydrophobicity/hydrophilicity was determined by contact angle measurements. The contact angle of water on pristine PVDF nanofibre membranes was  $93\pm 5^\circ$  (**Figure 6.9**). However, the embedment of f-SiO<sub>2</sub>NPs in the PVDF nanofibre membranes significantly increased their contact angle to  $151\pm 7^\circ$ . On the other hand, the contact angle of water on the AgNP/f-MWCNTs coating layer was considerably decreased to  $57\pm 4^\circ$ . The high contact angle of the f-SiO<sub>2</sub>NPs-modified PVDF nanofibre membrane is associated with a possible air-entrapment in the nano-web structures of the electrospun membranes as well as the incorporation of superhydrophobic f-SiO<sub>2</sub>NPs. Conversely, the low contact angle ( $57^\circ$ ) of the AgNP/f-MWCNTs coating layer was due to the presence of the hydrophilic short-chain alkyl carboxylic acid (COOH) on the f-MWCNTs and the AgNPs. These observations have also been previously reported (460,469). Remarkably, the incorporation of AgNPs not only enhanced the hydrophilicity of membranes but also significantly improved membrane resistance to biofouling due to the biocidal effect of Ag (469,470).

Pristine, f-SiO<sub>2</sub>NPs-modified, and AgNP/f-MWCNTs coated PVDF nanofibre membranes displayed reasonably high porosity values (i.e., 83%, 80%, and 81%, respectively) (**Figure 6.9**). The highly distributed microvoids of the thin layer observed in the SEM micrographs provided evidence of the high porosity of the cast layer. This is ascribed to the fact that the porosity measurements are obtained from the open data area. According to Idris and co-workers (2017), the high porosity measurements in membranes are due to a slow solvent demixing rate during phase separation (471). In the current study, the casting solution was mixed with 4% ultrapure water to ensure a low demixing rate during phase inversion. Furthermore, the porosity of the electrospun PVDF nanofibre membrane was lower than that of the thin hydrophilic layer. This was associated with electrospaying on

the electrospun nanofibre membranes which may result in the obstruction of the microvoids. However, the pore sizes measured in the pristine and f-SiO<sub>2</sub>NP-modified PVDF nanofibre membranes were larger than those of the AgNP/f-MWCNTs coating layer, i.e.,  $1.34 \pm 0.02 \mu\text{m}$ ,  $1.26 \pm 0.03 \mu\text{m}$ , and  $0.65 \pm 0.02 \mu\text{m}$ , respectively. Both membrane porosity and pore sizes play a critical role during mass transfer in MD separation processes. Nevertheless, a high porosity tend to decrease the mechanical strength of membranes, thus potentially affecting their performance (472).

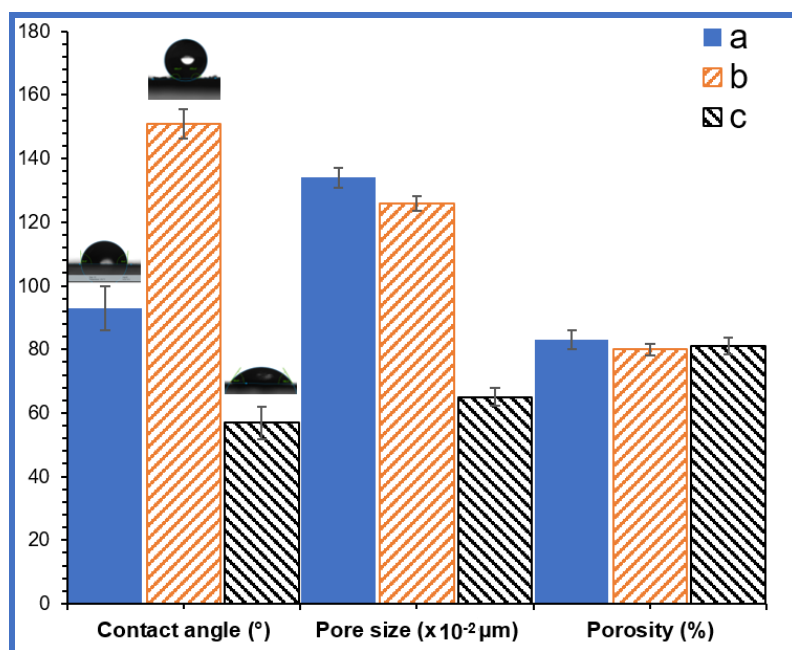


**Figure 6.9:** Contact angle measurements, porosity, and pore size of: (a) pristine PVDF nanofibre membrane; (b) f-SiO<sub>2</sub>NP-modified PVDF nanofibre membranes and (c) AgNP/f-MWCNTs coated PVDF nanofibre membrane.

### 6.3.8 Liquid entry pressure (LEP) measurements of modified membranes

The liquid entry pressure (LEP) of the modified membranes was evaluated and the results are presented in **Figure 6.10**. The LEP of the porous PVDF nanofibre membranes was recorded as  $61.7 \pm 2.9 \text{ kPa}$ . The LEP of the superhydrophobic membranes was increased to  $86.5 \pm 2.8 \text{ kPa}$ . These results were consistent with the values reported in Chapter 4, indicating their successful reproducibility. Further

increase in LEP was observed on the superhydrophobic membranes coated with a thin hydrophilic layer. The LEP of the coated membrane was  $139.1 \pm 4.6$  kPa. This increase in LEP was associated with the decrease in membrane pore size reported in **Figure 6.9**. Although membrane coating resulted to an increased LEP of the membrane, it worth noting that the LEP recommended in MD was not achieved (473–475). To achieve high LEP values, superhydrophobic membranes with smaller pore sizes are recommended. Therefore, optimization of the nanofibre membrane pore sizes is required prior to hydrophilic coating.

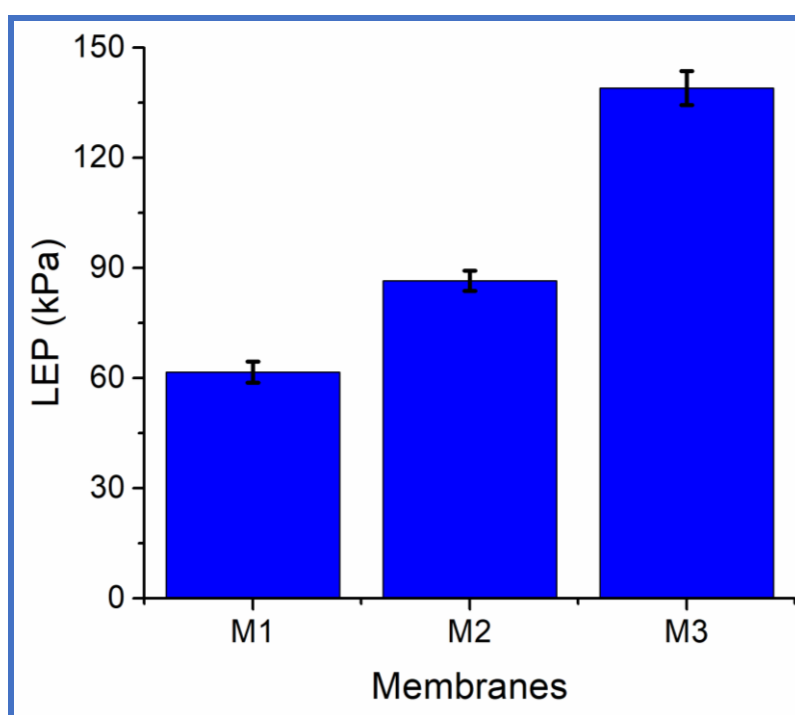


**Figure 6.10:** The LEP measurements of the nanofibre membranes: (a) pristine PVDF nanofibre membrane; (b) f-SiO<sub>2</sub>NP-modified PVDF nanofibre membranes and (c) AgNP/f-MWCNTs coated PVDF nanofibre membrane.

### 6.3.9 Thermal degradation of pristine and modified PVDF nanofibre membranes

The thermal stress resistance of membrane is a key parameter for a successful thermally-driven membrane separation process. The thermal degradation of

pristine and modified PVDF nanofibre membranes is presented in **Figure 6.11**. One-step rapid thermal degradation of pristine PVDF and Si<sub>2</sub>ONP-modified PVDF nanofibre membranes was recorded over the temperature range of 401–530°C, and 442–547°C with a mass loss of 84% and 78%, respectively. The minimal weight losses observed at temperatures below 200°C were associated with the removal (evaporation) of water bound within the membrane. A complete thermal degradation of pristine PVDF membranes was observed along with no remaining residues, while that of Si<sub>2</sub>ONP-modified PVDF nanofibre membrane was characterised by a mass of approximately 5% associated with residual carbon formed during combustion and non-degraded SiO<sub>2</sub>NPs. The incorporation of AgNP/f-MWCNTs slightly increased the degradation temperature compared to that of pristine PVDF nanofibre membrane, where the first mass loss (54%) due to depolymerisation of the PVDF was observed at the temperature range between 491°C and 546°C. Additional weight losses at the temperature range between 550°C and 866°C (i.e., resulting in a total weight loss of 26%) were associated with further degradation of the PVDF and an initial degradation of f-MWCNTs. The remaining mass (10%) below 1 000°C was associated with residual carbon, AgNPs, and f-SiO<sub>2</sub>NPs that were incorporated in the membrane. The addition of f-SiO<sub>2</sub>NPs, AgNPs, and f-MWCNTs generally increased the thermal stability of the PVDF nanofibre membrane. These observations confirmed several findings reported in previous studies (160,469,476,477).

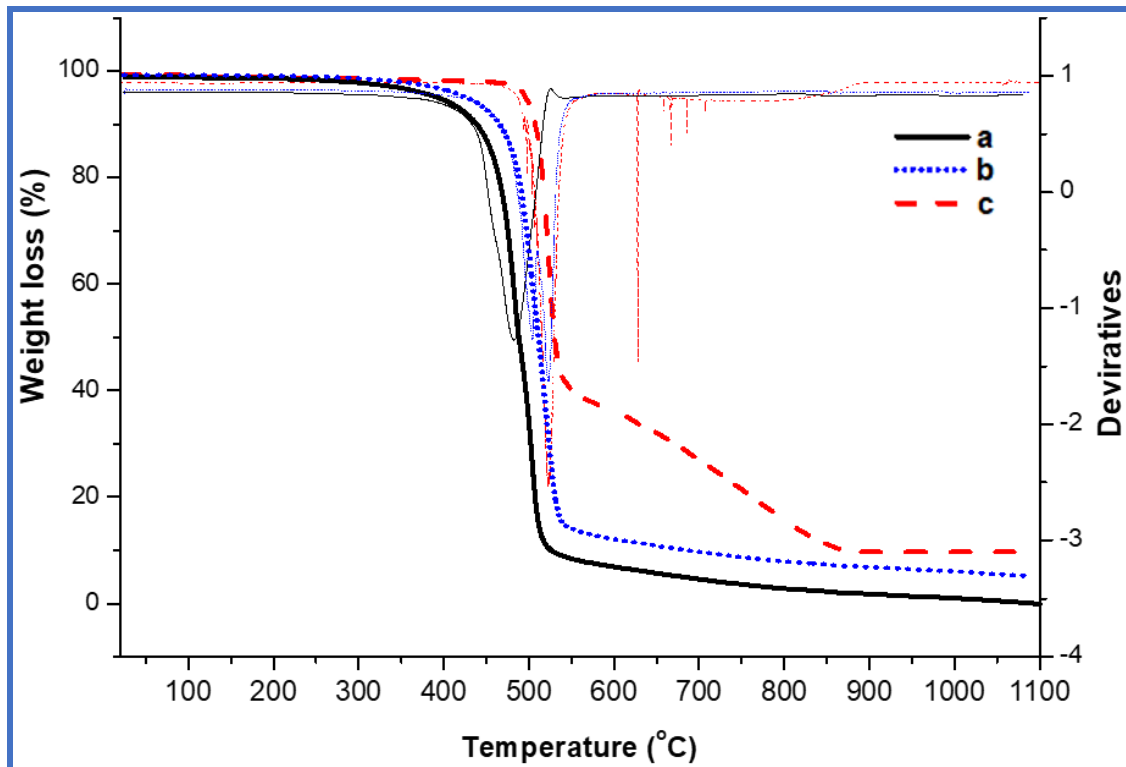


**Figure 6.11:** Thermal degradation of: (a) pristine PVDF nanofibre membrane; (b) f-SiO<sub>2</sub>NP-modified PVDF nanofibre membrane; and (c) AgNP/f-MWCNTs coated PVDF nanofibre membrane.

### 6.3.10 Mechanical stability of pristine and modified PVDF nanofibre membranes

Although MD operates at low pressures, the hydraulic impact and large-scale applications may negatively impact the mechanical stability of membranes (i.e., rupture of the membranes) (299). This highlights the necessity to synthesise mechanically strong membranes. The stress-strain plots of pristine and modified PVDF nanofibre membranes are presented in **Figure 6.12**, while the mechanical strength data is summarised in **Table 6.3**. The tensile strengths of pristine and f-SiO<sub>2</sub>NP-modified PVDF nanofibre membranes were 2.24 N and 2.13 N, with a corresponding Young's modulus of 45.6 MPa and 41.3 MPa, respectively. The coating of f-SiO<sub>2</sub>NP-modified PVDF nanofibre membrane with a thin (approximately 16  $\mu\text{m}$ ) AgNP/f-MWCNTs layer increased the tensile strength of

the PVDF nanofibre membranes to 2.38 N, resulting in a Young's modulus of 54.7 MPa. The Young's modulus of the membrane samples was determined at their elastic region, where the proportional deformations were 13%, 26%, and 30% for pristine, f-SiO<sub>2</sub>NP-modified, and AgNP/f-MWCNT-coated PVDF nanofibre membranes, respectively. The lower proportional deformation of the coated PVDF nanofibre membrane resulted in a higher Young's modulus of 54.7 MPa compared to that of pristine (45.6 MPa) and f-SiO<sub>2</sub>NP-modified (41.3 MPa) membranes. This result demonstrated that the coating of nanofibre membranes with an AgNP/f-MWCNTs layer improved their mechanical strength as was previously reported (460). The percentage elongation at break (fracture strain) of pristine, f-SiO<sub>2</sub>NP-modified, and AgNP/f-MWCN-coated PVDF nanofibre membranes was 98.3%, 94.4%, and 92.1%, respectively. The mechanical properties of the PVDF nanofibre membranes reported in the current study are consistent with those of previous studies evaluating in MD applications (299,367,372).

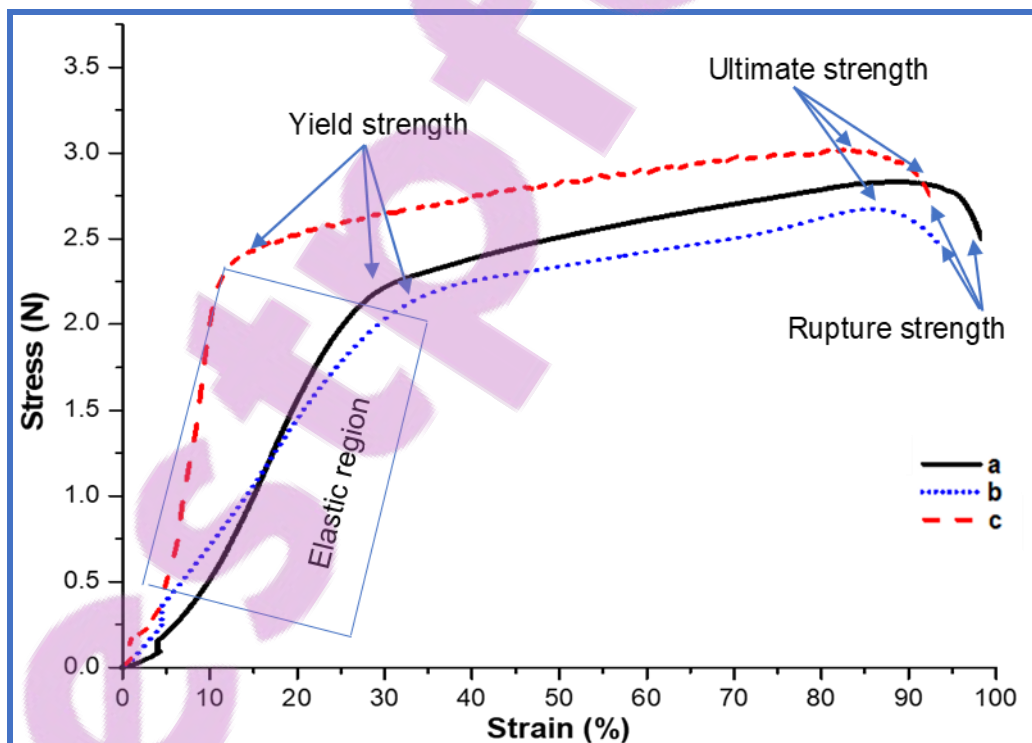


**Figure 6.12:** Stress-strain curves for: (a) pristine PVDF nanofibre membrane; (b) f-SiO<sub>2</sub>NP-modified PVDF nanofibre membrane; and (c) AgNP/f-MWCNTs coated PVDF nanofibre membrane.

**Table 6.3:** Mechanical properties of: (a) pristine PVDF membrane; (b) f-SiO<sub>2</sub>NP-modified membrane; and (c) AgNP/f-MWCNTs coated PVDF membranes.

Membrane sample	Thickness ( $\mu\text{m}$ )	Tensile strength (N)	Elongation at yield (%)	Elongation at break (%)	Young's modulus (MPa)
pristine PVDF membrane	121	2.24	13	98.3	45.6
f-SiO <sub>2</sub> NP-modified membrane	116	2.13	26	94.4	41.3
AgNP/f-MWCNTs-coated membrane	135	2.38	30	92.1	54.7

### 6.3.11 Fouling experiments

Pristine and modified PVDF nanofibre membranes were evaluated for their resistance towards flux decline using a solution containing bovine serum albumin (BSA) as an organic/protein model foulant in the presence of Ca<sup>2+</sup> cations, while simultaneously measuring salt rejection efficiency. In addition to van der Waals and electrostatic interactions, it has been widely suggested that adsorption of proteins (*e.g.* BSA) on membranes is mainly due hydrophobic effects (*i.e.*, favourable interactions between non-polar hydrophobic regions in both membranes and proteins) (445). Additionally, Ca<sup>2+</sup> cations have been suggested to form inner-sphere complexes with carboxyl groups on organics and the membranes, thus, exacerbate membrane fouling through cation-bridging mechanisms (478–480). The flux profiles of these membranes and their corresponding average rejection efficiency at (feed temperature = 60 °C and permeate temperature = 20°C) are presented in **Figure 6.13**. The initial water fluxes ( $t=0$  h) of pristine, f-SiO<sub>2</sub>NP-modified, and AgNP/f-MWCNT-coated PVDF nanofibre membranes were 18.0 LMH, 40.3 LMH, and 13.1 LMH, respectively. Remarkably, the embedment of f-SiO<sub>2</sub>NP on PVDF nanofibre membranes resulted in a 2.25-fold increase in water flux, thus providing evidence of the high potential of nanoparticles functionalisation of membranes for flux enhancement. Nevertheless, the flux of AgNP/f-MWCNT-coated PVDF nanofibre membrane was 27% lower than that of the pristine membrane. This low flux would be directly

associated with the considerable decrease in membrane pore size due to surface coating of the nanofibre membranes (i.e., from  $1.26 \pm 0.03 \mu\text{m}$  to  $0.65 \pm 0.02 \mu\text{m}$ ) and the increase in thickness. The result indicates the importance of pore size for achieving high fluxes. The three membrane samples experienced flux declines as a function of operation time; however, at different rates. These flux declines were described as exponential decay, following the **equation**:  $\text{Flux} = A \times \exp(-t/\kappa)$ , where  $A$  is a pre-exponential term describing the y-axis intercept,  $t$  is time (hours), and  $\kappa$  is the fitting parameter describing the exponential flux decay. Pristine membranes showed a decrease in water flux of 87% after 120 h of operation (i.e., following a  $\kappa=37.2$  h), indicating the impact of fouling. However, a more pronounced flux decline (i.e., 92% flux decrease after 120 h of operation, and following a  $\kappa=20.6$  h) was observed in the superhydrophobic f-SiO<sub>2</sub>NP-modified PVDF. This result could be attributed to the superhydrophobicity of the membrane itself (480). The superhydrophobicity (contact angle  $\approx 151^\circ$ ) of the f-SiO<sub>2</sub>NP-modified PVDF nanofibre membrane resulted in favourable hydrophobic interactions between the membrane and BSA, thus promoting cake formation and a subsequent decrease in membrane permeability. The hydrophobicity of membranes inducing organic and colloidal fouling have been extensively reported in previous studies (481,482). Despite its lowest initial flux, the AgNP/f-MWCNT-coated PVDF nanofibre membrane also showed the lowest flux decline (i.e., 69%, and following a  $\kappa=67.4$  h). It worth noting that although membrane coating improved the flux decay, these results are not the best but a promising approach that requires further optimization to attain stable resistances to flux decay. Although this AgNP/f-MWCNT coating layer was slightly hydrophilic, it decreased membrane fouling and subsequent pore wetting. The salt rejection of the membrane samples also followed different trends. Pristine membranes showed an already high salt rejection of 98.6%. Despite its higher fluxes, f-SiO<sub>2</sub>NP-modified PVDF nanofibre membrane showed a slightly lower salt rejection of 97.2%. This decline in salt rejection efficiency of the latter demonstrated that the adsorption of foulants changed the surface characteristics of the membrane (i.e., conditioning film), resulting in the passage of water in the liquid state rather than in the vapour form, thus reducing its rejection efficiency (36). It worth noting that huge difference

in salt rejections for SiO<sub>2</sub>NP and f-SiO<sub>2</sub>NP-modified PVDF nanofibre membranes reported in the previous chapter and the current chapter was due to differences in water sampling for measurement. In the previously chapter the measurements were taken after every 25 min, while in the current chapter, the measurements were taken after 120 h of MD operation. Notably, the highest salt rejection was observed for the AgNP/f-MWCNT-coated PVDF nanofibre membrane (99.8%), indicating the potential of this approach for decreasing fouling and enhancing salt rejection.

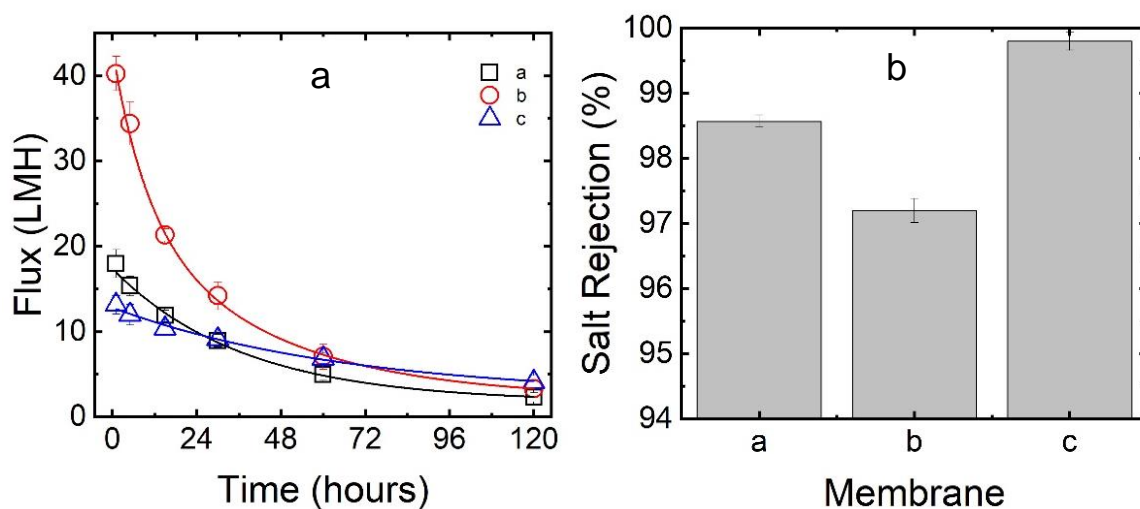


**Figure 6.13:** Flux of PVDF membranes as a function of time (a) and their corresponding average salt rejection (b): (a) pristine PVDF membrane; (b) f-SiO<sub>2</sub>NP-modified membrane; and (c) PVDF membrane coated with AgNP/f-MWCNTs.

### 6.3.12 AgNPs leaching experiments

Although AgNPs are used as active antibacterial agents in many fields, their impact due to their release into the environment is not fully known. Therefore, the release of AgNPs from the PVDF nanofibre membranes was investigated and the results are presented in **Figure 6.14**. The synthesized AgNPs were used as a control while AgNPs determined in the permeate solution after MD experiments were measured as the test for leaching. The synthesized AgNPs (control) absorbed the UV-Vis light at the wavelength range 385-419 nm with a maximum

absorption peak at 406 nm (i.e. the characteristic peak of AgNPs) (120,336,421). The test experiment presented a low-density UV-Vis absorption peak below 350 nm that corresponded to a low concentration of the Ag<sup>+</sup> ions. The low concentration of the Ag<sup>+</sup> ions demonstrated their gradual release to the environment while AgNPs were tightly bound on the PVDF nanofibre membranes, thus demonstrating their stability for longer operations.

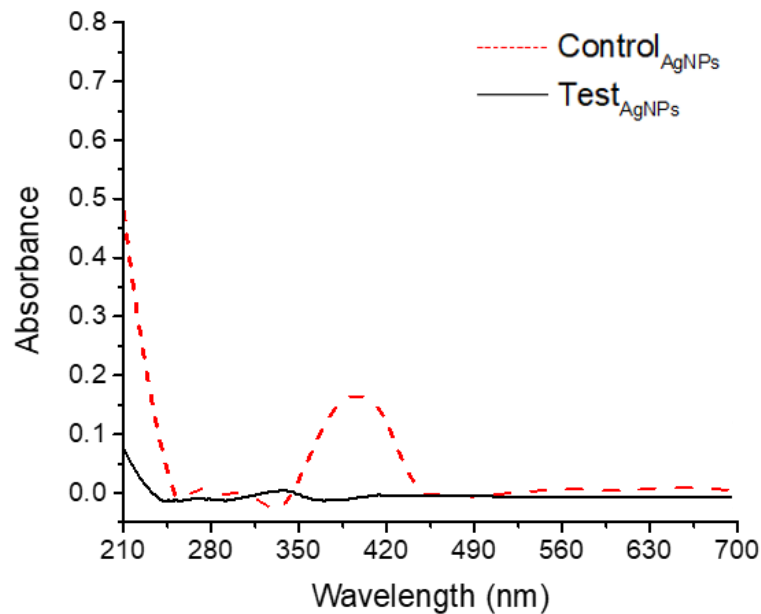


**Figure 6.14:** UV-Vis absorption spectra of AgNPs tested for leaching.

## 6.4 Conclusion

The efficient control of membrane fouling with optimised cleaning and replacement remains a major obstacle in the long-term operation of MD processes. It is therefore imperative to develop fouling-resistant membranes towards a wide range of foulants. In the current study, the synthesis of a superhydrophobic PVDF nanofibre membrane exhibiting a significant decrease in BSA fouling was successfully achieved. The surface of an f-SiO<sub>2</sub>NPs-modified PVDF membrane was coated with a polymer solution containing AgNPs/f-MWCNTs. These AgNPs and carboxylated-MWCNTs enhanced the hydrophilicity on this active surface and

also improved the thermal degradation and mechanical stability of the resultant membrane. The AgNPs/f-MWCNTs coated PVDF nanofibre membrane exhibited a higher resistance to flux decline relative to pristine and superhydrophobic f-SiO<sub>2</sub>NP-modified PVDF nanofibre membrane; while maintaining high average salt rejection. Nevertheless, AgNPs/f-MWCNTs coated PVDF nanofibre membrane displayed a lower water flux than pristine and f-SiO<sub>2</sub>NPs-modified PVDF membranes induced by the smaller average pore size of its active layer.

Despite the promising results of the current study, additional research is essential to improve the permeability of this hydrophilic active layer. In conclusion, superhydrophobic f-SiO<sub>2</sub>NP-modified PVDF nanofibre membranes are demonstrated to be severely impacted by fouling, leading to a drastic decline in water flux. Although membrane coating significantly improved the resistance towards flux decay, further improvements are required to improve the use of this membranes in MD. Additionally, biofouling, organic and colloidal fouling experiments are still required to ascertain the resistance of this coated membrane towards flux decline and salt rejection.

# CHAPTER 7

## HYDROPHILIC THIN-LAYER COATING OF A SUPERHYDROPHOBIC PVDF NANOFIBRE MEMBRANE FOR ORGANIC, COLLOIDAL AND BIOFOULING MITIGATION IN DIRECT CONTACT MEMBRANE DISTILLATION

---

### 7.1 Introduction

Although fouling has been established in MD applications, further research studies focusing on innovative low-fouling superhydrophobic PVDF nanofibre membranes is imperative. The fouling studies reported in MD are dominated by organic and inorganic fouling (70,151). In addition to colloidal, organic, and inorganic fouling, biofouling has been observed in MD. However, the current research on biofouling in MD is slowly growing (66), mainly influenced by the perception that the operating conditions, *e.g.*, high operating temperatures ( $\geq 60^\circ$ ) and saline feed waters, do not allow the growth and accumulation of bacteria (66). Nevertheless, some wastewaters discharged from thermophilic bioreactor systems find their way into natural aquifers (152,264,301,483). The previous chapter has demonstrated the growth inhibition of thermophilic bacteria on AgNPs-embedded PVDF nanofibre membranes.

This chapter reports on the preparation of superhydrophobic SiO<sub>2</sub>NPs-embedded PVDF nanofibre membranes. Their fouling resistance was evaluated in DCMD mode. Furthermore, these superhydrophobic SiO<sub>2</sub>NPs-embedded PVDF nanofibre membranes were coated using a thin hydrophilic layer impregnated with carboxylated multiwalled carbon nanotubes (f-MWCNTs) and silver nanoparticles (AgNPs) to induce membrane fouling resistance towards thermophilic bacteria, colloidal and organic fouling. This hydrophilic coating layer would provide a

promising approach and research direction for mitigation of organic, colloidal and biofouling in DCMD processes.

## 7.2 Methods and materials

### 7.2.1 Reagents

Polyvinylidene fluoride (PVDF) ( $MW = 534,000 \text{ g}\cdot\text{mol}^{-1}$ ), tetraethyl orthosilicate (TEOS) (reagent grade, 98%), N,N-dimethylacetamide (DMAc) (Puriss p.a., 99.5%), acetone (ACS reagent, 99.5%), absolute ethanol (ACS reagent, 99.9%), toluene (ACS reagent, 99.7%), octadecyltrimethoxysilane (OTMS) (technical grade, 90%), sodium alginate (medium viscosity), LUDOX® AS-40 colloidal silica (40 wt. % suspension in  $\text{H}_2\text{O}$ ), and a 30 mL PP/PE eccentric tip syringe equipped with a blunt tip dispensing needle were purchased from Sigma Aldrich (Germany). N-octadecyltrichlorosilane (ODTS) (reagent grade, 95%) and chloro(dimethyl)-octadecylsilane (Cl-DMOS) (reagent grade, 95%) were purchased from Alpha Aesar (USA). Granny Smith apple extract were purchased from Makolobane Farmers Enterprises (Senekal, South Africa). Deionised water (Direct-Q®, Merck Millipore) was used for solution preparation.

### 7.2.2 Synthesis and modification of $\text{SiO}_2$ NPs and PVDF nanofibre membranes

Experimental procedure for synthesis and modification of  $\text{SiO}_2$ NPs was described in **Chapter 4**. Likewise, synthesis of PVDF nanofibre membranes was described in **Chapter 4**. Modifications of the PVDF nanofibre was also described in **Chapter 5 and 6**. Coated PVDF nanofibre membranes were prepared by coating pristine,  $\text{SiO}_2$ NPs-modified, or f- $\text{SiO}_2$ NPs-modified PVDF nanofibre membranes with a solution containing 2% AgNPs and 1% f-MWCNTs to produce an antibacterial and hydrophilic thin layer. Due to their strong binding energy, the f-MWCNTs did not leach out of the polymer as previously demonstrated (484). The uncoated membranes: pristine PVDF,  $\text{SiO}_2$ NPs-modified PVDF, ODTS-functionalised

SiO<sub>2</sub>NPs-modified PVDF; OTMS-functionalised SiO<sub>2</sub>NPs-modified PVDF, Cl-DMOS-functionalised SiO<sub>2</sub>NPs-modified PVDF and coated membranes were termed M1, M2, M3, M4 and M5 respectively. The coated pristine, coated SiO<sub>2</sub>NPs-modified PVDF, coated ODTs-functionalised SiO<sub>2</sub>NPs-modified, and coated OTMS-functionalised SiO<sub>2</sub>NPs-modified PVDF, coated Cl-DMOS-functionalised SiO<sub>2</sub>NPs-modified PVDF nanofibre membranes were termed M6, M7, M8, M9 and M10 respectively. OTMS-functionalised SiO<sub>2</sub> improved the contact angles of the PVDF nanofibres membranes and they are therefore referred as the f-SiO<sub>2</sub>NPs throughout the entire manuscript.

### **7.2.3 Characterisation of virgin and fouled nanofibre membranes**

The morphology of virgin and fouled PVDF nanofibre membranes was investigated using Scanning Electron Microscope (SEM, JEOL STM – IT300). The samples were fixed on a conductive carbon tape and carbon-coated. Energy-dispersive X-ray Spectroscopy (EDS) was used to investigate the elemental composition of the membranes. In addition, the surface roughness of the membranes was studied using atomic force microscopy (AFM, WITec Alpha 300 A, TS-150). The membranes were scanned in an area of 10.0 μm × 10.0 μm. The membranes fouled with biofilms were prepared for confocal microscopy using an in-house protocol. Live/dead cells were visualised using a Nikon A1R laser scanning microscope. The samples were placed in a sterile Petri dishes immediately after removal from the operating MD module and stained using LIVE/DEAD® BacLight™ Bacterial Viability Kit. The water contact angle (CA) of the PVDF membranes was measured using a DSA30E Kruss drop shape analyser (GmbH) on virgin and fouled membranes by the sessile drop method. In all experiments, 5 μL of probe liquids was used. To determine the surface energy (surface tension) component of the membranes, contact angles on these membranes were determined with three well-characterised probe liquids (de-ionised water, glycerol and diiodomethane). Diiodomethane was used as the dispersive (non-polar) liquid while de-ionised water and glycerol were used as polar liquids.

## **7.2.4 Preparation of the feed solutions**

### **7.2.4.1 Sodium alginate and colloidal silica as model organic and colloidal foulants**

The test solution was composed of 5.0 mg/L  $\text{CaCl}_2$  and 20 mg/L sodium alginate. NaCl was added to the feed solution until a conductivity of 47 mS/cm was attained mimicking the total conductivity of brackish water. The feed solution containing colloidal silica was prepared as follows.  $\text{CaCl}_2$  and colloidal silica were added to de-ionised water at 5.0 mg/L and 40 wt%, respectively while NaCl was further added to this feed solution to attain a total ionic conductivity of 47 mS/cm. The feed solutions were sonicated prior to use.

### **7.2.4.2 Model biofoulants**

Feed solutions used for biofouling tests were collected from thermophilic bacteria from a thermophilic reactor effluent at Innolab CVBA (Ghent, Belgium). The plastic containers used to collect the water samples were rinsed three times with the respective effluent prior to collection. The samples were pretreated by a 10  $\mu\text{m}$  filter (Millipore™ Isopore™, TCTP). The filters were continuously replaced to mitigate any cake formation. Calcium chloride ( $\text{CaCl}_2$ ) was added to the pretreated solution to reach a final concentration of 5.0 mg/L. Furthermore, sodium chloride was added to the pretreated solution until a total ionic conductivity of 47 mS/cm was attained in the feed solution.

## **7.2.5 Performance of the PVDF nanofibre membranes**

The performance of the PVDF nanofibre membranes embedded with organically-modified  $\text{SiO}_2\text{NPs}$  was evaluated on a Direct Contact Membrane Distillation (DCMD) laboratory-scale set-up using a solution characterised by the model foulants presented above. The total ionic conductivity of each solution was adjusted to 47 mS/cm using NaCl (i.e., slightly below the concentration of

dissolved salts in seawater). The temperature of the feed was 60°C while the permeate temperature was kept constant at 20°C in counter mode. A flow rate of 0.75 L/min was set for the feed solution and the coolant water (conductivity of the latter  $\leq 0.10 \mu\text{S/cm}$ ). The conductivity of the water was measured using a Shimadzu conductivity meter to determine the salt rejection efficiencies. The water flux was calculated based on the mass of water transported from the feed (i.e., modified PVDF membrane; surface area:  $1.25 \times 10^{-2} \text{ m}^2$ ) to the permeate. The amount of water transported through the membrane in the state of vapour was determined by measuring the weight increment of the coolant water using a Kern & Sohn GmbH, EMB 3000\_1 weighing balance. **Equations 4.1** and **4.3** were used to calculate the water flux ( $J_{\text{water}}$ ) and salt rejection (R). The experiments were conducted continuously, and measurements were taken at 5 h time interval. A new nomenclature of fouled nanofibre membranes was developed as follows: colloidal fouling on (M1) pristine PVDF, (M2) f-SiO<sub>2</sub>NPs-modified PVDF and (M3) coated f-SiO<sub>2</sub>NPs-modified PVDF; biofouling on (M4) pristine PVDF, (M5) f-SiO<sub>2</sub>NPs-modified PVDF and (M6) coated f-SiO<sub>2</sub>NPs-modified PVDF; alginate fouling on (M7) pristine PVDF, (M8) f-SiO<sub>2</sub>NPs-modified PVDF and (M9) coated f-SiO<sub>2</sub>NPs-modified PVDF.

### 7.2.6 Fouling of MD membranes

In order to understand the membrane and foulant interactions, the van Oss model was used (107,480,485). In this model, three probe liquids were used to determine the surface free energy of the membrane and the interfacial free energy between the membrane and the foulant (solute). The used probe liquids were de-ionised water, glycerol and diiodomethane. Diiodomethane was used as the dispersive (non-polar) liquid while de-ionised water and glycerol were used as polar liquids. The surface tension components of the probe liquids were given in **Table 7.1** (486). Additionally, the total polar ( $\sigma_i^p$ ) and the total surface energy ( $\sigma_i^{\text{TOT}}$ ) components were provided. The total surface tension ( $\sigma_i^{\text{TOT}}$ ) was expressed as:

$$\sigma_l^{TOT} = \sigma_l^D + \sigma_l^P \quad (7.1)$$

Where

$$\sigma_l^P = 2\sqrt{\sigma_l^+ \sigma_l^-} \quad (7.2)$$

**Table 7. 1:** The surface tension properties of the probe liquids at 20°C (486).

Probe liquids	$\sigma_L^D$ (mJ·m <sup>-2</sup> )	$\sigma_L^+$ (mJ·m <sup>-2</sup> )	$\sigma_L^-$ (mJ·m <sup>-2</sup> )	$\sigma_L^P$ (mJ·m <sup>-2</sup> )	$\sigma_L^{TOT}$ (mJ·m <sup>-2</sup> )
Water	21.8	25.5	25.5	51.0	72.8
Glycerol	34.0	3.9	57.4	30.0	64.0
Diiodomethane	50.8	0.0	0.0	0.0	50.8

The surface tension parameters of the solid surface ( $\sigma_s^D, \sigma_s^-, \sigma_s^+$ ) were determined through the measured contact angles of the probe liquids characterised by the tension parameters given in **Table 7.2** using Young Dupre **Equation**.

$$\sigma_L^{TOT} (1 + \cos \theta) = 2 \left( \sqrt{\sigma_s^D \sigma_l^D} + \sqrt{\sigma_s^+ \sigma_l^-} \sqrt{\sigma_s^- \sigma_l^+} \right) \quad (7.3)$$

where:  $\sigma_l^D$  was the dispersive component of the surface tension of the liquid,  $\sigma_l^+$  was the acid component of the surface tension of the liquid,  $\sigma_l^-$  was the base component of the surface tension of the liquid,  $\sigma_s^D$  was the dispersive component of the surface energy of the solid,  $\sigma_s^+$  was the acid component of the surface energy of the solid, and  $\sigma_s^-$  was the base component of the surface energy of the solid.

In order to determine each surface tension parameter of the solid surface, **Equation 7.3** was broken down into the following:

$$\sigma_L^{TOT} (1 + \cos \theta) = 2 \left( \sqrt{\sigma_s^D \sigma_l^D} \right) \quad (7.4)$$

Where the contact angle of the dispersive liquid was used to calculate the dispersive component of the surface

$$\sigma_L^{TOT} (1 + \cos \theta) = 2 \left( \sqrt{\sigma_s^D \sigma_l^D} + \sqrt{\sigma_s^+ \sigma_l^-} \right) \quad (7.5)$$

Where the contact angle of the liquid that has the base component was used to calculate the acid component of the surface.

$$\sigma_L^{TOT} (1 + \cos \theta) = 2 \left( \sqrt{\sigma_s^D \sigma_l^D} + \sqrt{\sigma_s^+ \sigma_l^-} \sqrt{\sigma_s^- \sigma_l^+} \right) \quad (7.6)$$

Where the contact angle of the liquid that has the acid component was used to calculate the base component of the surface.

The interfacial free energy for interaction between the membrane (*m*) and the solute (foulant) (*s*) in water (*w*) was therefore estimated using the following **Equations.**

$$\Delta G_{swm}^D = 2 \left( \sqrt{\sigma_w^D} - \sqrt{\sigma_s^D} \right) \left( \sqrt{\sigma_m^D} - \sqrt{\sigma_w^D} \right) \quad (7.7)$$

$$\Delta G_{swm}^P = 2\sqrt{\sigma_w^+} \left( \sqrt{\sigma_s^-} + \sqrt{\sigma_m^-} - \sqrt{\sigma_w^-} \right) + 2\sqrt{\sigma_w^-} \left( \sqrt{\sigma_s^+} + \sqrt{\sigma_m^+} - \sqrt{\sigma_w^+} \right) - 2\sqrt{\sigma_s^+ \sigma_m^-} - 2\sqrt{\sigma_s^- \sigma_m^+} \quad (7.8)$$

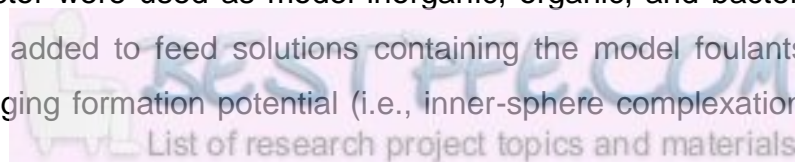
$$\Delta G_{swm}^{TOT} = \Delta G_{swm}^D + \Delta G_{swm}^P \quad (7.9)$$

Where  $\Delta G_{swm}^{TOT}$  was the total free energy of cohesion.

## 7.3 Results and discussion

### 7.3.1 SEM-EDS analysis of the fouled membranes

Cake formation leading to membrane fouling was investigated using SEM analysis. Colloidal silica, sodium alginate, and the effluent from the thermophilic bacteria bioreactor were used as model inorganic, organic, and bacterial fouling. Ca<sup>2+</sup> ions were added to feed solutions containing the model foulants owing to their cation bridging formation potential (i.e., inner-sphere complexation) between



ionised functional groups on foulants and membranes; thus, leading to high fouling propensities as previously reported (359,480,487). After 50 h of operation, the membranes were characterised by layer formation and deposition of the particulate matter. The colloidal silica particles were deposited in the internal microstructures of PVDF nanofibre membranes; while their deposition was lower on the membrane coated with a thin hydrophilic layer (**Figure 7.1, M1 and M2**). The SEM micrographs of the fouled membranes revealed severe fouling on both alginate and bio-fouled pristine PVDF and f-SiO<sub>2</sub>NPs-modified PVDF nanofibre membranes (**Figure 7.1, M4, M5, M7 and M8**). A similar observation was also reported by Zarebska and co-workers (2014) (488). The cake formation was significantly lower in all membranes coated with a thin hydrophilic layer, suggesting minimal fouling occurring on the surface of the membrane (**Figure 7.1, M3, M6 and M9**). The investigated bio-fouled membranes were characterised by rod-like structures, which indicated the presence of bacteria on the surface of the membranes.

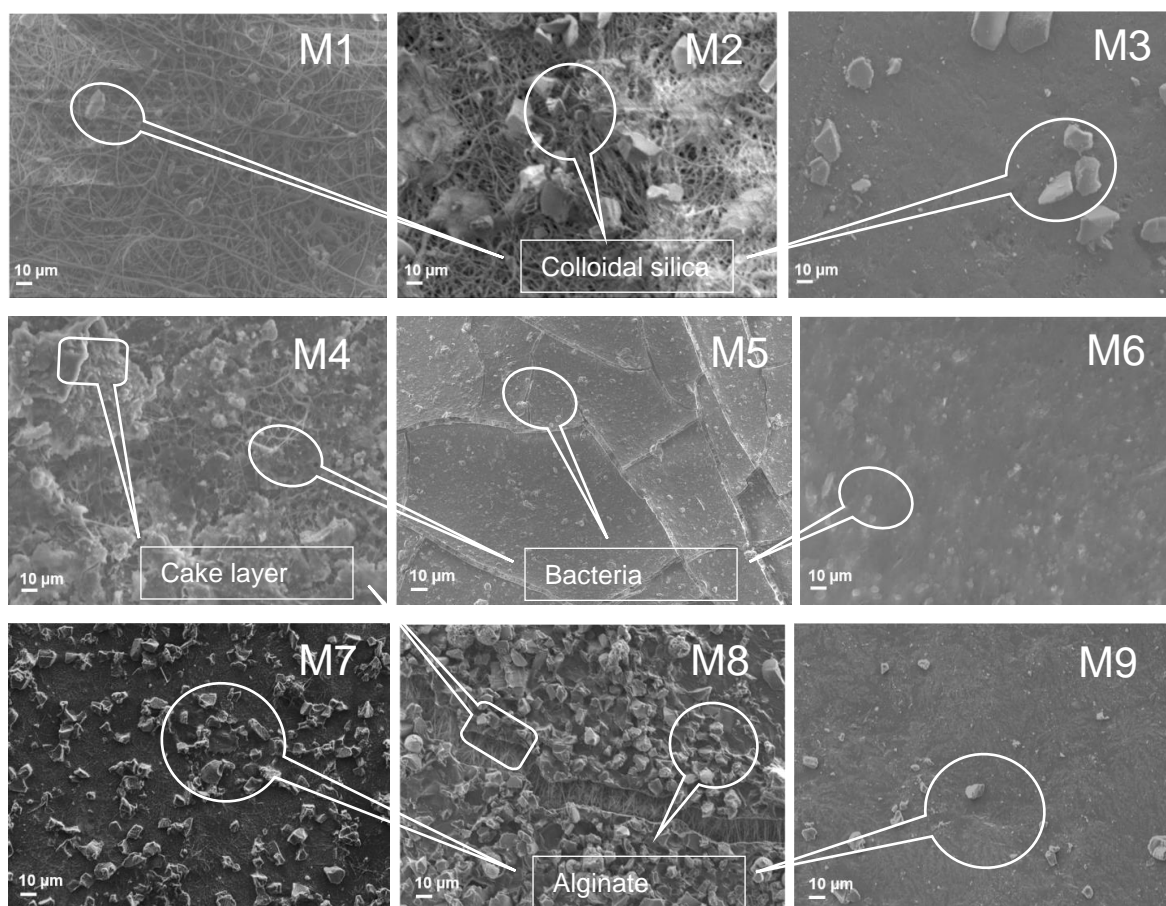


**Figure 7.1:** SEM images of: colloidal silica fouling on (M1) pristine PVDF nanofibre, (M2) f-SiO<sub>2</sub>NPs-modified PVDF nanofibre, and (M3) thin hydrophilic layer-coated PVDF nanofibre membrane; biofouling on (M4) pristine PVDF nanofibre, (M5) f-SiO<sub>2</sub>NPs-modified PVDF nanofibre, and (M6) thin hydrophilic layer-coated PVDF nanofibre membrane; and alginate fouling on (M7) pristine PVDF nanofibre, (M8) f-SiO<sub>2</sub>NPs-modified PVDF nanofibre, and (M9) thin hydrophilic layer-coated PVDF nanofibre membrane.

Remarkably, the surface of pristine PVDF and f-SiO<sub>2</sub>NPs-modified PVDF nanofibre membranes were fully covered by a cake layer of alginate and biofilms. However, the f-MWCNTs/AgNPs coating significantly reduced the deposition and cake formation on the surface of the membrane. The cross-section of membranes was recorded to elucidate the degree of cake formation on the fouled membranes. The cross-sections (**Figure 7.2**) showed a layer with thickness of 53 nm on the membrane surface for pristine PVDF and PVDF-f-SiO<sub>2</sub>NPs membranes.

Interestingly, the thickness of the cake layer is rarely reported on literature in MD. However, fouling experiments conducted on humic acid in electro-coagulation/oxidation membrane reported the formation of a cake layer with thickness  $\approx 30$  nm (142). In this study, the alginate fouling resulted in a 90% flux decay on the f-SiO<sub>2</sub>NPs-modified PVDF nanofibre membrane. **Figure 7.2, M2** shows the cross-section of coated f-SiO<sub>2</sub>NPs subjected to alginate solution in DCMD. Interestingly, membrane coating significantly reduced alginate fouling due to lower membrane surface roughness and hydrophobicity. Furthermore, alginate was unable to interact with silanol groups and causing cake formation as the silanol groups were not accessible due to the hydrophilic coating (480).

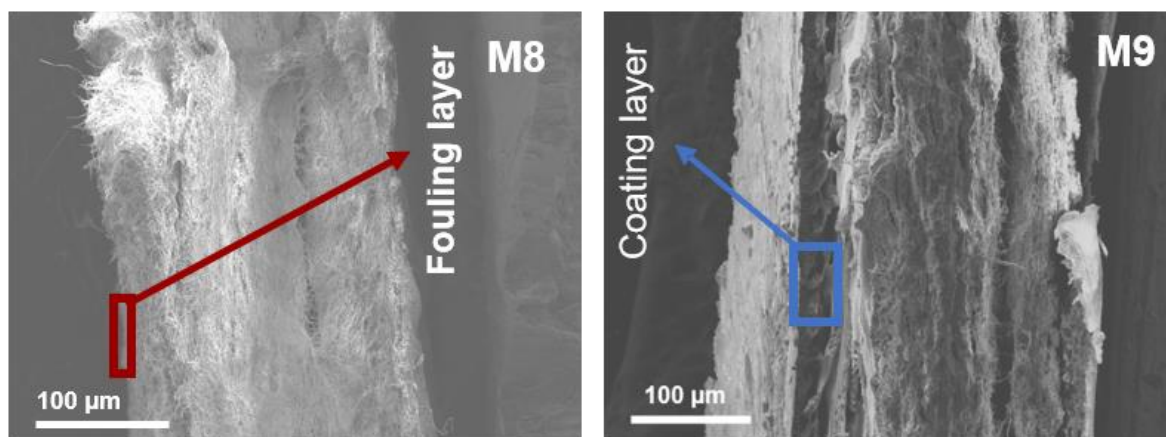


**Figure 7.2:** Cross-sectional view of alginate-fouled membranes: (M8) f-SiO<sub>2</sub>NPs-modified PVDF and (M9) coated f-SiO<sub>2</sub>NPs-modified PVDF nanofibre membranes.

### 7.3.2 EDS analysis of fouled membranes

The EDX spectra (i.e., elemental components) of the fouled membranes are presented in **Figure 7.3**. The following elements were identified in colloidal silica-fouled pristine PVDF nanofibre membrane: C, O, F, Na, Si, Cl, and Ca, which are the elemental components of pristine PVDF nanofibre membranes and the feed solution (**Figure 7.3, M1**). Similarly, these elements were observed on biofouled f-SiO<sub>2</sub>NPs-modified PVDF nanofibre membranes (**Figure 7.3, M8**). Additionally,

elemental Ag was observed on the membrane coated with a thin hydrophilic layer, which plays a key anti-bacterial fouling role (**Figure 7.3, M6**).

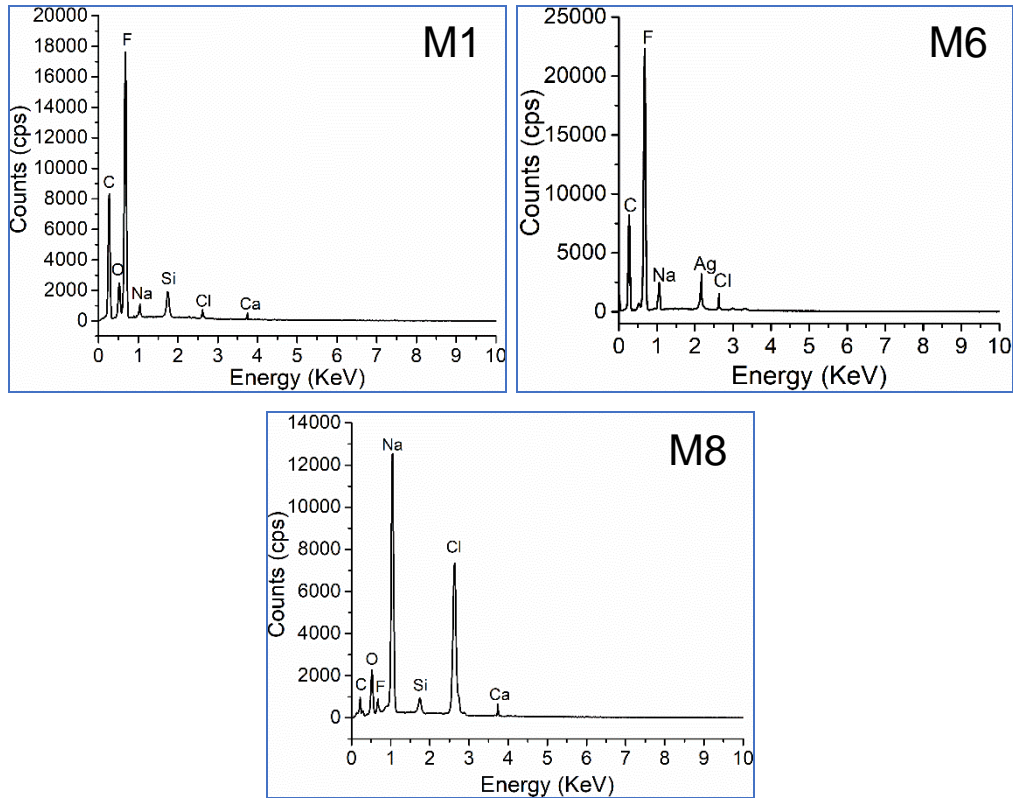


**Figure 7.3:** EDX spectra of: (M1) colloidal silica-fouled pristine PVDF nanofibre membrane, (M6) biofouling on coated PVDF nanofibre membrane, and (M8) alginate-fouled f-SiO<sub>2</sub>NPs-modified PVDF nanofibre membrane.

### 7.3.3 Confocal laser scanning microscopy analysis of bio-fouled membranes

The viability of the microorganisms affected by the properties of the membrane surface was determined using a confocal laser scanning microscope. The proliferation of live cells (stained green) were considerably higher on the pristine PVDF nanofibre membrane than that of dead cells (stained red), as observed in **Figure 7.4, M4**. This high cell viability observed indicates that pristine PVDF nanofibre membrane promoted the growth of microorganisms on its surface, i.e. favourable adsorption of cells and their extracellular polymeric substance (EPS)

known as biofilm. This cell growth and accumulation exacerbated membrane fouling. However, the concentration of dead cells (stained red) was significantly higher on the f-MWCNTs/AgNPs-coated PVDF nanofibre membrane, as shown in **Figure 7.4, M6**. This result confirmed the cytotoxicity of the coated membrane towards microorganisms; leading to a decrease in cell viability and controlled membrane fouling. The inactivation of cells was explained by the antimicrobial mechanism where AgNPs interact with the thiol groups and nucleic acids of the micro-organisms (*e.g.*, bacteria), binding to their enzymes, and damaging their cell envelopes or inhibiting the enzyme activity; thus, resulting in cell inactivation (145–147). The confocal microscopy results were in agreement with the SEM micrographs of fouled membranes, indicating that f-MWCNTs/AgNPs membrane coating promoted bacterial cell inactivation, and resistance to biofilm formation and growth. The current confocal microscopy results were consistent with those previously reported by other studies (66,68,489).

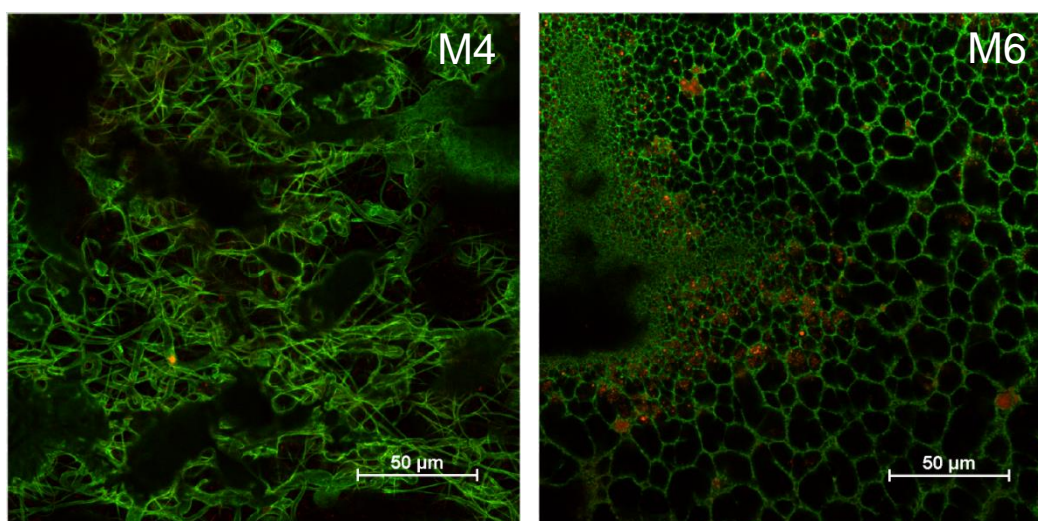


**Figure 7.4:** Confocal laser scanning microscopy spectra of cells on: (M4) Pristine PVDF nanofibre membrane and (M6) f-MWCNTs/AgNPs-coated PVDF nanofibre membrane.

#### 7.3.4 AFM analysis of fouled membranes

The surface morphology of fouled membranes was studied using AFM. The arithmetic mean height ( $R_a$ ) and the root mean square height ( $S_q$ ) of the voids on the surface of each membrane were used to estimate the effect of fouling towards membrane surface roughness. The  $R_a$  values of M1, M2, M3, M4, M5, M6, M7, M8, M9 were 154 nm, 238 nm, 47 nm, 81 nm, 79 nm, 34 nm, 73 nm, 96 nm, and 41 nm, respectively (**Figure 7.5**). The  $R_a$  and  $S_q$  values of colloidal silica-fouled membranes were slightly higher than those of virgin membranes that were previously presented. This observation was supported by the deposition of colloidal particles presented on SEM micrographs. However, the  $R_a$  and  $S_q$  values of alginate-fouled and bio-fouled membranes were lower than those of their virgin membranes counterpart, indicating that alginate and bio-foulants formed a smooth layer at the surface of the membranes. During membrane drying, cracks were recorded on fouled membranes by AFM images (typically in M4, M5, M7, and M8). Furthermore, the nanofibre membrane coating using a solution containing f-MWCNTs and AgNPs decreased the surface roughness of the fouled membranes. These observations are in good agreement with those previously reported by other studies (38,150,490,491).

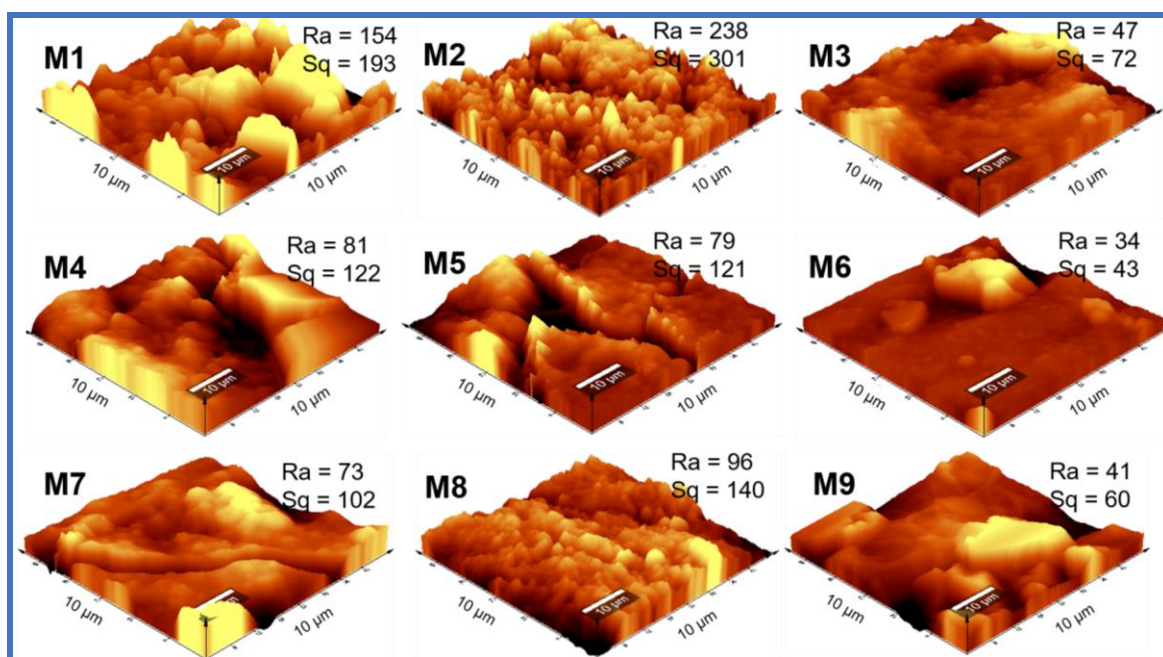


**Figure 7.5:** AFM images of fouled membranes: colloidal silica fouling on (M1) pristine PVDF nanofibre, (M2) f-SiO<sub>2</sub>NPs-modified PVDF nanofibre, and (M3) thin hydrophilic layer-coated PVDF nanofibre membranes; biofouling on (M4) pristine PVDF nanofibre, (M5) f-SiO<sub>2</sub>NPs-modified PVDF nanofibre, and (M6) thin hydrophilic layer-coated PVDF nanofibre membrane; and alginate fouling on (M7) pristine PVDF nanofibre, (M8) f-SiO<sub>2</sub>NPs-modified PVDF nanofibre, and (M9) thin hydrophilic layer-coated PVDF nanofibre membrane.

### 7.3.5 Contact angles of fouled membranes

The effect of fouling on membrane hydrophobicity was investigated using contact angles of virgin and fouled membranes. The results are presented on **Table 7.2**. The foulants (colloidal silica, alginate, and biological communities) showed different effects towards membrane hydrophobicity. The contact angles of the virgin membranes (membranes before MD experiments) on M1, M2, and M3 were  $96 \pm 4^\circ$ ,  $159 \pm 9^\circ$  and  $68 \pm 3^\circ$  respectively. There was no significant difference between the contact angles of the membranes fouled by colloidal silica. However, the membranes fouled by alginate showed a decrease in hydrophobicity. The contact angles were measured as  $84 \pm 6^\circ$ ,  $147 \pm 7^\circ$  and  $63 \pm 4^\circ$  on M7, M8, and M9,

respectively. Likewise, the contact angles of membranes fouled by biological communities changed to  $96\pm 3^\circ$ ,  $164\pm 8^\circ$ , and  $67\pm 3^\circ$  on M4, M5, and M6 respectively. A decrease in membrane contact angles induced by the accumulation of alginate would be ascribed to the hydrophilic moieties ( $\text{COO}^-$  and  $-\text{OH}$ ) present in alginate (492,493). However, the contact angles of membranes fouled by biological communities were either slightly lower on coated  $\text{f-SiO}_2$ -modified PVDF nanofibre membranes or also higher on  $\text{f-SiO}_2$ -modified PVDF nanofibre membranes compared to virgin (clean) membranes. The cell membranes of most bacteria are characterised by amphipathic phospholipids containing a hydrophobic tail and a hydrophilic head (494). Furthermore, water contact angles of bacterial cell surfaces range from hydrophilic to hydrophobic which inevitably affects the hydrophobic nature of the membrane by either lowering or increasing the membrane contact angles (495,496). The effect of fouling on membrane hydrophobicity has been reported in previous studies and is consistent with the findings of this research (14,70,142,469).

**Table 7. 2:** The water contact angles of virgin and fouled membranes.

Fouling type	Membrane	Contact angle ( $^\circ$ )
Virgin	M1	$96\pm 4$
	M2	$159\pm 9$
	M3	$68\pm 3$
Colloidal fouled	M1	$94\pm 6$
	M2	$155\pm 11$
	M3	$69\pm 5$
Biofouled	M4	$96\pm 4$
	M5	$164\pm 8$
	M6	$67\pm 3$
Alginate fouled	M7	$84\pm 3$
	M8	$147\pm 7$
	M9	$63\pm 4$

(M1) pristine PVDF nanofibre, (M2)  $\text{f-SiO}_2$ NPs-modified PVDF nanofibre, and (M3) thin hydrophilic layer-coated PVDF nanofibre membranes; biofouling on (M4) pristine PVDF nanofibre, (M5)  $\text{f-SiO}_2$ NPs-modified PVDF nanofibre, and (M6) thin hydrophilic layer-coated PVDF nanofibre membrane; and alginate fouling on (M7) pristine PVDF nanofibre, (M8)  $\text{f-SiO}_2$ NPs-modified PVDF nanofibre, and (M9) thin hydrophilic layer-coated PVDF nanofibre membrane.

### 7.3.6 Determination of membrane-foulant interfacial free energy

The contact angles of fouled membranes were measured using three probe liquids to calculate the interfacial free energy between membranes and solutes (foulants) and the results are presented on **Table 7.2**. The surface free energies of the dispersive components were higher than those of the polar components on virgin M1 and M2, suggesting a hydrophobic membrane. The surface free energy of the polar components increased on the membrane coating using a solution containing f-MWCNTs and AgNPs, indicating a hydrophilic membrane (**M3**) (107). The fouling on the membrane lowered the surface free energy of the dispersive components below that of the polar components, suggesting a clear modification of the membrane (485). Furthermore, the interfacial free energies ( $\Delta G$ ) between the membrane and foulants were calculated and tabulated in **Table 7.3**. The negative values of  $\Delta G$  indicated that the attractive interaction between membranes and foulants was favourable (480). These membrane-foulants attractive interactions led to a decline in water flux, suggesting that long-term operations would not be ideal due to a decrease in water permeability.

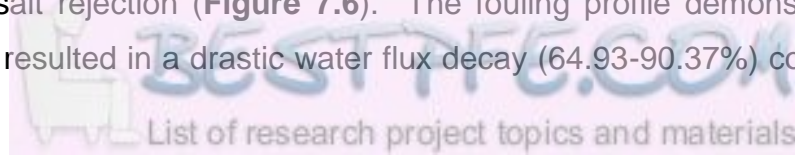
**Table 7.3:** Membrane-foulants interfacial free energy determining the initial membrane fouling.

Interactive type	Surface free energy components			$\Delta G$ (mJ/m <sup>2</sup> )
	$\sigma_s^-$ (mJ/m <sup>2</sup> )	$\sigma_s^+$ (mJ/m <sup>2</sup> )	$\sigma_s^D$ (mJ/m <sup>2</sup> )	
Virgin membranes				
M1	9.37	-27.8	28.9	-
M2	-0.13	-48.9	49.5	-
M3	8.74	1.19	1.57x10 <sup>-6</sup>	-
Colloidal				
M1	12.1	1.62	0.0004	-25.6
M2	15.2	0.38	0.044	-63.3
M3	10.9	1.62	0.028	-31.7
Biological				
M4	9.54	2.24	1.04	-43.9
M5	5.69	7.40	1.04	-70.0
M6	9.87	1.08	0.004	-34.3
Alginate				
M7	14.9	0.25	0.01	-35.1
M8	16.0	0.11	0.06	-103.2
M9	8.61	0.97	0.66	-82.5

$\sigma_s^-$  = base component of the surface energy of the solid,  $\sigma_s^+$  = acid component of the surface energy of the solid,  $\sigma_s^D$  = dispersive component of the surface energy of the solid,  $\Delta G$  = Interfacial free energy, (M1) pristine PVDF nanofibre, (M2) f-SiO<sub>2</sub>NPs-modified PVDF nanofibre, and (M3) thin hydrophilic layer-coated PVDF nanofibre membranes; biofouling on (M4) pristine PVDF nanofibre, (M5) f-SiO<sub>2</sub>NPs-modified PVDF nanofibre, and (M6) thin hydrophilic layer-coated PVDF nanofibre membrane; and alginate fouling on (M7) pristine PVDF nanofibre, (M8) f-SiO<sub>2</sub>NPs-modified PVDF nanofibre, and (M9) thin hydrophilic layer-coated PVDF nanofibre membrane.

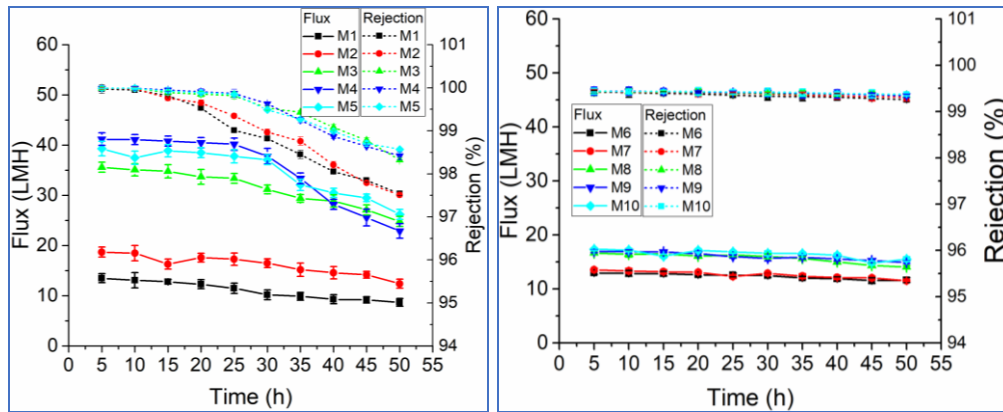
### 7.3.7 Effect of membrane fouling on water flux and salt rejection

Fouling is a major problem that affects all membrane-based processes. It is defined as the accumulation of solutes on the surface of the membrane during separation (70). The model foulants studied were colloidal silica, alginic acid sodium salt, and microbial communities collected from the thermophilic bacteria effluent. Generally, all three model foulants induced a decline in water flux as well as a decay in salt rejection (**Figure 7.6**). The fouling profile demonstrated that alginate-fouling resulted in a drastic water flux decay (64.93-90.37%) compared to

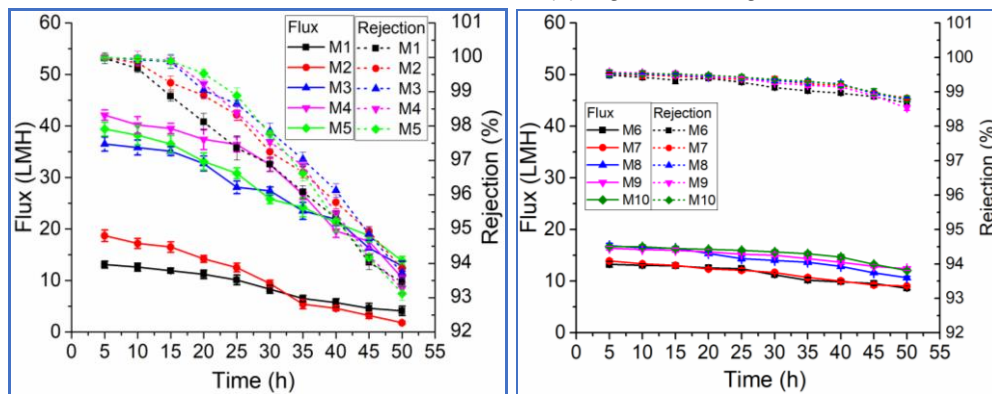


a moderate decay caused by biofouling (50.49-71.85%) and colloidal fouling (30.34-44.42%) (**Figure 7.6, M1-5**). Fouling was observed to intensify on the SiO<sub>2</sub>NPs-modified PVDF nanofibre due to the silanol-alginate interactions where bridge formation between the membrane and the alginate was induced by the presence of Ca<sup>2+</sup> ions (480). The SEM results showed a cake formation of alginate and growth of biofilms on the membrane surface, which are the key explanations for the deterioration of the water flux within the first 50 hours of operation. These observations were also reported on polypropylene membrane by Zarebska and co-workers (2014) (488). Furthermore, colloidal silica particles penetrate into the membrane pores, causing a severe pore blockage in flat sheet membranes (243). However, due to the bigger pore sizes (1-2.5µm) in nanofibre membranes, the colloidal silica particles have little effect on the decrease of water flux. The decay in salt rejection is an evidence of membrane wetting which subsequently decreases the quality of the permeate. The effect of the foulants towards the rejection decays followed the order of: alginate (6.13-6.87%) > biofouling (3.14-4.11%) > colloidal silica (1.42-2.48%) (**Figure 7.6, M1-5**). These observations are in agreement with those previously reported by other studies (14,70,93,445,488). A sustainable MD performance was observed during the use of the coated membrane where both flux and salt rejection efficiencies remained almost stable in the first 50 h of operation. It should be noted that a rejection efficiency below 99% in MD is an indication of an inefficient process (139,379,497). In this case, the flux decay induced by alginate, biofouling, and colloidal silica was observed to be 24.22-36.87%, 19.40-31.37%, and 10.39-15.60% respectively (**Figure 7.6, M6-10**). On the other hand, the salt rejection declined by 0.75-1.04%, 0.52-0.67%, and 0.07-0.16% due to alginate, biofouling, and colloidal fouling, respectively. The oxidised MWCNTs and AgNPs coating of the surface rendered the superhydrophobic PVDF membranes resistant to adhesion of microbiological communities while preventing silanol-alginate interactions. These findings were also previously reported in the literature, where membrane fouling caused decays in water flux and rejection efficiencies during the oil-water separation and water desalination (104,183).

(a) Colloidal fouling on uncoated membranes (b) Colloidal fouling on coated membranes



(c) Alginate fouling on uncoated membranes (d) Alginate fouling on coated membranes



(e) Biofouling on uncoated membranes (f) Biofouling on coated membranes

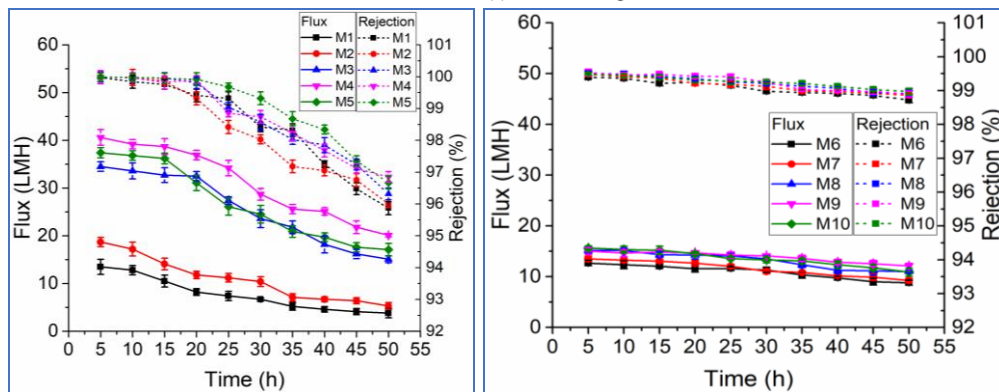


**Figure 7.6:** Effect of colloidal, organic, and biofouling on MD permeate flux and salt rejection efficiency. Uncoated membranes: (M1) Pristine membrane, membrane modified with (M2) pristine SiO<sub>2</sub>NPs, (M3) ODTs-functionalised SiO<sub>2</sub> NPs, (M4) OTMS-functionalised SiO<sub>2</sub>NPs, and (M5) CI-DMOS-functionalised SiO<sub>2</sub>NPs; coated membranes: (M6) Pristine membrane, membrane modified with (M7) pristine SiO<sub>2</sub>NPs, (M8) ODTs-functionalised SiO<sub>2</sub> NPs, (M9) OTMS-functionalised SiO<sub>2</sub>NPs, and (M10) CI-DMOS-functionalised SiO<sub>2</sub>NPs.

## 7.4 Conclusion

In Chapter 4, it was demonstrated that the incorporation of the f-SiO<sub>2</sub>NPs successfully improved the hydrophobicity of PVDF nanofibre membranes. The SiO<sub>2</sub>NPs were modified using three silane reagents, namely; ODTs, OTMS, and Cl-DMOS. The contact angles were found to increase from 94° to 162°. To mitigate the fouling propensities of the membrane while maintaining membrane resistance to wetting, the superhydrophobic membranes were coated with a thin layer containing f-MWCNTs and AgNPs. The hydrophobic membranes were characterised by the formation of a cake layer induced by the alginate and biofouling. Furthermore, particulate colloids were deposited on the surface of the uncoated membranes. Notably, cake formation formed a smooth topology on the surface of the membrane while colloidal silica increased membrane surface roughness to above the surface roughness of their counterpart virgin membranes. It was observed that, membrane coating reduced the cake formation. Furthermore, the presence of the AgNPs on the coating layer inhibited the growth of microorganisms, hence improved membrane resistance towards bio-fouling. The contact angles of the fouled membranes were used to estimate the type of interactions between the membranes and the foulants. It was observed that, alginate slightly decreased the membrane contact angles while biofouling and colloidal silica slightly increased the water-membrane contact angles. The interfacial free energy values were all negative, indicating that the membrane-foulant interactions were attractive. This phenomenon agreed with SEM micrographs, which demonstrated the formation of a cake layer on the surface of the membranes. Consequently, the 30-90% flux decays were recorded within 50 h. of operation. Furthermore, salt rejection was reduced by 1.4-6.1%. Although, membrane coating decreased the initial water flux from 43-45 LMH to 16-17LMH, stable water fluxes were observed within 50 h of operation where the decays of 19-31% flux decays were recorded. Auspiciously, stable salt rejection was observed with salt decline of 0.1-1.0%. Although, these results are an indication of a promising fouling and wetting mitigations in MD, further research is required to ensure non-occurrence of membrane wetting within the membrane pores. Additionally, long-term operating conditions (a minimum of 600 h) are essential to

determine their effect towards membrane wetting. The flux and salt rejection decline on coated membrane further demonstrates that possible fouling is taking place. Therefore, designing an efficient pretreatment filter is of paramount importance. Although the membrane modifications showed the feasibility of developing a fouling-resistant MD membrane to mitigate the challenges associated with MD processes, the cost analysis of this technology that involves the use of expensive materials such as Ag need further investigation. However, it is noteworthy to mention that these materials are used in relatively low percentages relative to the PVDF polymer, thus their cost in a final product should not be high. The advantage of using nanomaterials is the ability to do more with less.

## CHAPTER 8

# HYDROPHOBIC PVDF NANOFIBRE MEMBRANES COATED WITH A FOULING-RESISTANT HYDROPHILIC LAYER FOR PURIFICATION OF ENVIRONMENTAL WATER SAMPLES IN MEMBRANE DISTILLATION

---

### 8.1 Introduction

A sustainable and efficient management of water resources is the most suitable alternative to meet the water quantity and quality demands of the growing global population (16). In the previous chapters, it was demonstrated that MD equipped modified PVDF nanofibre membranes can effectively remove the salts from water. However, an integrated MD purification system equipped with a pretreatment step is required for treatment of environmental brackish water samples. This follows a scenario of membrane fouling observed on the use of synthetic water samples.

This chapter demonstrates the use of developed novel MD membranes comprising of porous electrospun nanofibre membrane coated with a thin hydrophilic layer for purification of complex environmental brackish water samples. The synthesis of electrospun super-hydrophobic PVDF nanofibre membranes involves the incorporation of the organically-functionalised silica nanoparticles (f-SiO<sub>2</sub>NPs). The incorporation of these organically-modified SiO<sub>2</sub>NPs provided PVDF nanofibres with a high void ratio, interconnected open structure, high surface to mass ratio, highly ordered polymer chains with a more controlled structure, and enhanced performance (i.e., higher rejection and water flux) (34). To reduce membrane fouling, the modified PVDF nanofibre membranes were coated with a hydrophilic layer consisting of silver nanoparticles (AgNPs) and carboxylated multi-walled carbon nanotubes (f-MWCNTs).

## 8.2 Methods

### 8.2.1 Reagents

Polyvinylidene fluoride (PVDF) ( $MW = 534,000 \text{ g}\cdot\text{mol}^{-1}$ ), tetraethyl orthosilicate (TEOS) (reagent grade, 98%), N,N-dimethylacetamide (DMAc) (Puriss p.a., 99.5%), acetone (ACS reagent, 99.5%), absolute ethanol (ACS reagent, 99.9%), toluene (ACS reagent, 99.7%), octadecyltrimethoxysilane (OTMS) (technical grade, 90%), and a 30 mL PP/PE eccentric tip syringe equipped with a blunt tip dispensing needle were purchased from Sigma Aldrich (Germany), while N-octadecyltrichlorosilane (ODTS) (reagent grade, 95%) was purchased from Alfa Aesar (USA). Granny Smith apple extract was purchased from Makolobane Farmers Enterprises (Senekal, South Africa). Deionised water (Direct-Q®, Merck Millipore) was used for solution preparation.

### 8.2.2 Water samples

The feed water samples were collected from two sampling points along the Scheldt estuary at Terneuzen in Netherlands (GPS coordinates: 51°19'26.6"N 3°49'30.4"E) and Antwerp (Belgium, GPS coordinates: 51°13'43.7"N 4°24'02.3"E) and Nandoni Dam (South Africa). Briefly, the fresh water from the Scheldt river mixes with the North Sea water producing brackish water of high salinity at Terneuzen and of low salinity at Antwerp. Therefore, the brackish water samples collected at Terneuzen and Antwerp were termed high salinity (HS) and low salinity (LS), respectively. The water samples for laboratory analysis and MD purification were collected at 1-m depth from the surface of the estuary water and kept in a cooler box during transportation to the laboratories. The samples were characterised the same day of sampling. The physicochemical properties of the water samples were characterised by total organic carbon (TOC), total carbon (TC), total inorganic carbon (TIC), temperature, conductivity, pH, total dissolved solids (TDS), and microbial cell density (**Table 8.1**). Additionally, the detailed experimental description of the water samples collected from Nandoni Dam was

provided in chapter 1. The detailed description of the water quality collected from the Nandoni Dam is reported elsewhere (56,498)

**Table 8.1:** Physicochemical properties and microbial cell density of the low salinity (LS) and high salinity (HS) brackish water samples.

Physicochemical and biological parameters	LS	HS
Total organic carbon (mg/L)	2.21±0.08	0.36±0.03
Total carbon (mg/L)	57.44±0.18	40.06±0.21
Total inorganic carbon (mg/L)	55.24±0.25	39.69±0.12
Temperature (°C)	19.75±0.21	19.70±0.14
Conductivity (mS/cm)	13.38±0.06	39.10±0.16
pH	7.80±0.01	7.95±0.01
Total dissolved solids (mg/L)	9,176±48	25,412±162
Cell density (cells/mL)	1.62*10 <sup>6</sup> ±3.21*10 <sup>4</sup>	1.18*10 <sup>6</sup> ±2.95*10 <sup>4</sup>

LS = low salinity water, HS = high salinity water

### 8.2.3 Synthesis of pristine and modified PVDF nanofibre membranes

Pristine and modified PVDF nanofibres membranes were synthesised using previously reported procedures (**Chapter 4**). Coating of the superhydrophobic PVDF nanofibre membranes was also reported in **Chapter 5 and 6**. The coating solution was prepared using 10% PVDF. Therefore, the nanotubes were physically bound as fillers to a coating layer. The casting layer was spread on the surface of the PVDF nanofibre membrane followed by phase inversion in a water bath. Due to its strong binding energy, the MWCNTs do not leach out of the polymer as previously demonstrated (484). Uncoated membranes: (M1) pristine, (M2) SiO<sub>2</sub>NPs-modified, (M3) f-SiO<sub>2</sub>NPs-modified; and coated membranes: (M4) coated pristine, (M5) coated SiO<sub>2</sub>NPs-modified, and (M6) coated f-SiO<sub>2</sub>NPs-modified PVDF nanofibre membranes were dried in an oven for 24 h before experiments.

#### 8.2.4 Effect of the composition of brackish water samples on water fluxes and salt rejections performance of PVDF nanofibre membranes

The performance of the PVDF nanofibre membranes (membrane surface area  $\approx 0.0125 \text{ m}^2$ ) was evaluated on a Direct Contact Membrane Distillation (DCMD) unit to determine the impact of fouling on salt rejection efficiencies and water flux. The feed solutions (**Table 8.1**) were pretreated using a candle filter (pore size  $\sim 100 \mu\text{m}$ ) equipped with polyethyleneimine-functionalised polyacrylonitrile nanofibre membranes to reduce particulate and dissolved organic/inorganic compounds. During MD experiments, the temperatures of the feed and permeate were kept at  $60^\circ\text{C}$  and  $20^\circ\text{C}$ , respectively. The water was circulated at a flow rate of  $0.75 \text{ L/min}$  and the conductivity of the solutions was continuously measured using a Shimadzu conductivity meter to determine the salt concentration at the feed and at the permeate sides of the membranes. The volume of water transported through the membrane in the form of vapor was determined by measuring the weight increment of the permeate using a Kern & Sohn GmbH, EMB 3000\_1 weighing balance. **Equations 4.1 and 4.3** were used to calculate water flux ( $J_{\text{water}}$ ) and salt rejection (R).

#### 8.2.5 Characterisation of PVDF nanofibre membranes

The morphology of the PVDF nanofibre membrane was investigated using JEOL STM – IT300 Scanning Electron Microscope (SEM). The samples were fixed on a conductive carbon tape and carbon-coated. Energy-dispersive X-ray (EDX) mapping was used to determine the elemental composition of the membranes. In addition, the surface roughness of the membranes was studied using the atomic force microscopy (AFM, WITEc Alpha 300 A, TS-150). The membranes were measured with a similar tip at a scan area of  $10.0 \mu\text{m} \times 10.0 \mu\text{m}$ . The water contact angle of the PVDF membrane samples was measured using a DSA30E Kruss drop shape analyser (GmbH) on virgin and MD-used membranes by a sessile drop method. In all experiments,  $5 \mu\text{L}$  of the probe liquids was used. On one hand, the sliding angle was determined using a built-in tilting specimen. The

membrane was attached to the glass slide and fixed on the tilting specimen. A 10  $\mu\text{L}$  water droplet was placed on the membrane and the plate was inclined until the droplet started to move. The tilt angle at which the droplet starts sliding was called a sliding contact angle (hysteresis of contact angle). To determine the surface energy (surface tension) component of the membranes, the contact angles were measured using three well characterised three probe liquids (de-ionised water, glycerol and diiodomethane). Diiodomethane was used as the dispersive (non-polar) liquid while de-ionised water and glycerol were used as polar liquids. The surface tension components of the probe liquids are given in **Table 7.1**. Furthermore, the interfacial free energy between estimated using **Equations 7.1 – 7.9**.

### **8.3 Results and discussion**

#### **8.3.1 Atomic force microscopy (AFM) analysis**

The surface morphology of the PVDF nanofibre membranes was studied using AFM. The results presented were AFM results of pristine PVDF nanofibre membrane, f-SiO<sub>2</sub>NPs-modified PVDF nanofibre membrane, and coated f-SiO<sub>2</sub>NPs-modified PVDF nanofibre membrane (**Figure 8.1**). The surface roughness was determined from the arithmetic mean height (Ra) and the root mean square height (Sq) values of the voids on the surface of the membranes. The Ra values of M1, M3 and M6 were found to be 104 nm, 141 nm, and 67 nm respectively. The Sq values of M1, M3, and M6 were 136 nm, 172 nm, and 93 nm respectively. The addition of the f-SiO<sub>2</sub>NPs to electrospinning solution of PVDF resulted to an increase in the Ra and Sq values, indicating an increase in membrane surface roughness. However, the coating of the membranes demonstrated a decrease in membrane surface roughness as depicted using the recorded Ra and Sq values. The hydrophobicity of the rough membrane was enhanced due to the presence of the entrapped air within their micro-voids (370,371). The rougher membranes are therefore more hydrophobic compared to their counterpart smooth membranes. These observations were therefore confirmed using contact angle measurements.

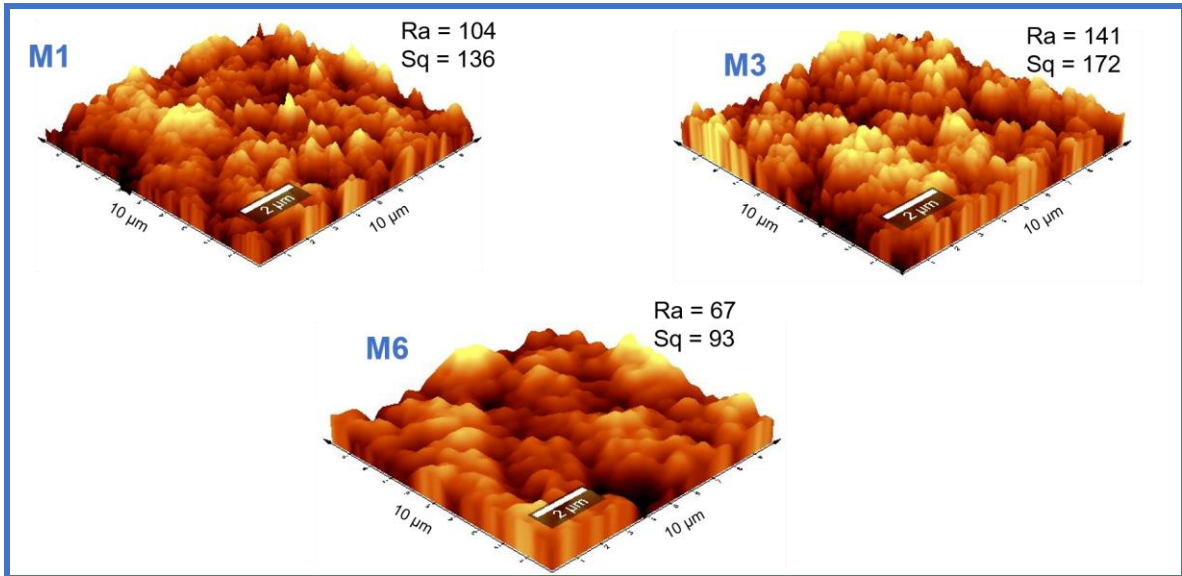


**Figure 8.1:** AFM micrographs of PVDF nanofibre membranes: (M1) Pristine PVDF nanofibre membrane, (M3) f-SiO<sub>2</sub>NPs-modified PVDF nanofibre membrane, (M6) coated f-SiO<sub>2</sub>NPs-modified PVDF nanofibre membrane.

### 8.3.2 Morphology of modified and fouled membranes by Scanning Electron Microscopy (SEM)

The SEM micrographs of uncoated and coated PVDF nanofibre membranes before and after MD treatment with low salinity (LS) and high salinity (HS) feed waters are given in **Figure 8.2**. The SEM micrographs of pristine PVDF nanofibre (M1), f-Si-modified PVDF nanofibre (M3), and coated f-Si-modified PVDF nanofibre membranes (M6) before and after MD treatment (**Figure 8.2 and 8.3**) were examined in detail to determine the morphology of the membrane surface and the cake layer. The investigation of cake layer formation and the effect of fouling on membrane hydrophobicity on M1, M3 and M6 was based on the following observations: (a) M1 showed the lowest initial flux, lowest salt rejection, and lowest flux decay due to non-functionalisation, (b) M3 showed the highest initial flux, salt rejection, and high water flux decay, and (c) M6 showed high initial water flux and salt rejections, and reduced water flux decay.

Pristine PVDF nanofibres membranes were characterised by uniform nanofibres and low beads formation. However, after MD filtration of both LS and HS feed solutions, granular deposits with low cake formation observed. The entrapment of deposits was associated with the surface roughness of the intertwined structures of the PVDF nanofibre membrane (499). The micro-sized particulate matter observed in the pristine membrane pores was possibly due to the presence of inorganic particles in the feed solution. The deposits were associated with the sparingly soluble salts precipitating on the surface of the membrane thus causing flux decline (158). Also, supersaturation of the soluble salts could form salts deposition on the surface of the membrane due to concentration polarization and reduce the water flux. Likewise, cake layer formation was found to be more intense on the f-SiO<sub>2</sub>NPs-modified PVDF nanofibre membrane (M3) suggesting the likelihood of pore blockage beyond 50 h of operation for both LS and HS feeds. This observation would be associated with the surface roughness and super-hydrophobic nature of the f-SiO<sub>2</sub>NPs-modified PVDF nanofibre membrane (M3). Specifically, strong interactions between the hydrophobic moieties of the foulants and the super-hydrophobic membrane surface would occur (57). The hydrophilic coating layer on the f-SiO<sub>2</sub>NPs-modified PVDF nanofibre membrane (M6) decreased the roughness and hydrophobicity of the membrane surface; thus, resulting in a lower adsorption of foulants for both LS and HS feeds. These observations are also in good agreement with previous studies (103,445,500), demonstrating that the addition of a hydrophilic coating layer has the potential to reduce fouling in MD membranes.

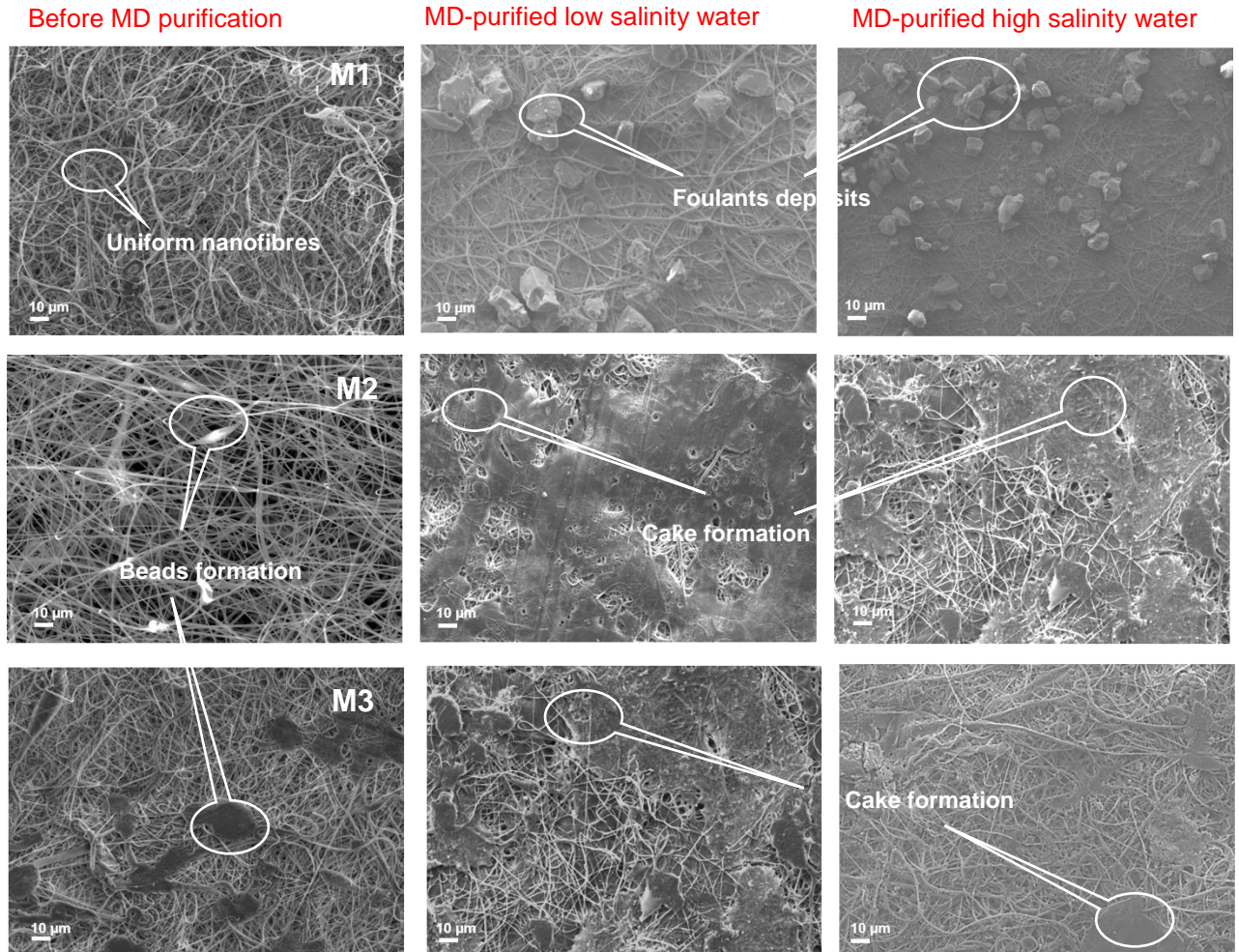


**Figure 8.2:** SEM micrographs of uncoated PVDF membranes before and after MD treatment with low salinity (LS) and high salinity (HS) feed waters: (M1) Pristine PVDF nanofibre membrane: (M2), SiO<sub>2</sub>NPs-modified PVDF nanofibre membrane: (M3) f-SiO<sub>2</sub>NPs-modified PVDF nanofibre membrane.

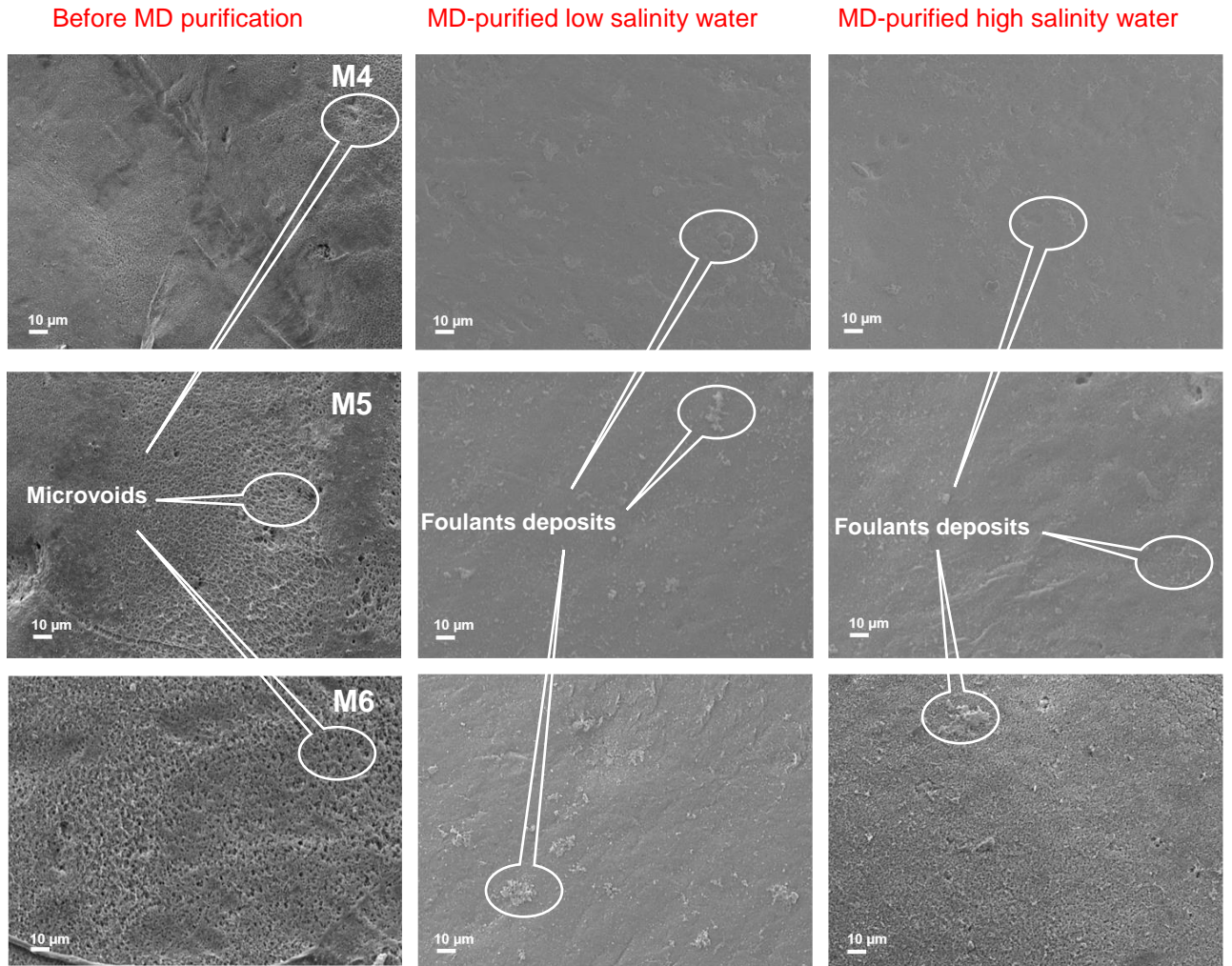


**Figure 8.3:** SEM micrographs of coated PVDF membranes before and after MD treatment with low salinity (LS) and high salinity (HS) feed waters. (M4) Pristine PVDF nanofibre membrane, (M5), SiO<sub>2</sub>NPs-modified PVDF nanofibre membrane, (M6) f-SiO<sub>2</sub>NPs-modified PVDF nanofibre membrane.

### 8.3.3 EDS analysis of fouled membranes

Energy-dispersive X-ray spectroscopy (ED) analysis of fouled membranes was conducted to investigate the elemental composition of the foulants. The experiments were conducted on pristine PVDF nanofibre membranes under LS and HS feed conditions (**Figure 8.4**). In addition to C and F (i.e., elemental components of the PVDF polymer) and Na and Cl (i.e., elements of the feed solution), the following elements were identified: Magnesium (Mg), potassium (K), and zinc (Zn) when using low salinity/brackish feed and Mg, Si, Ca, and Zn when using the high salinity/brackish feed solution. Mg and K are naturally occurring

elements which are mostly found in river waters and river catchments (19,228). Silica is also abundantly available in the sea water in different forms including colloidal silica (243,482). In addition, although, Zn naturally occurs in water, concentrations are on the increase due to additions of Zn through anthropogenic activities including waste disposal (44,501,502).

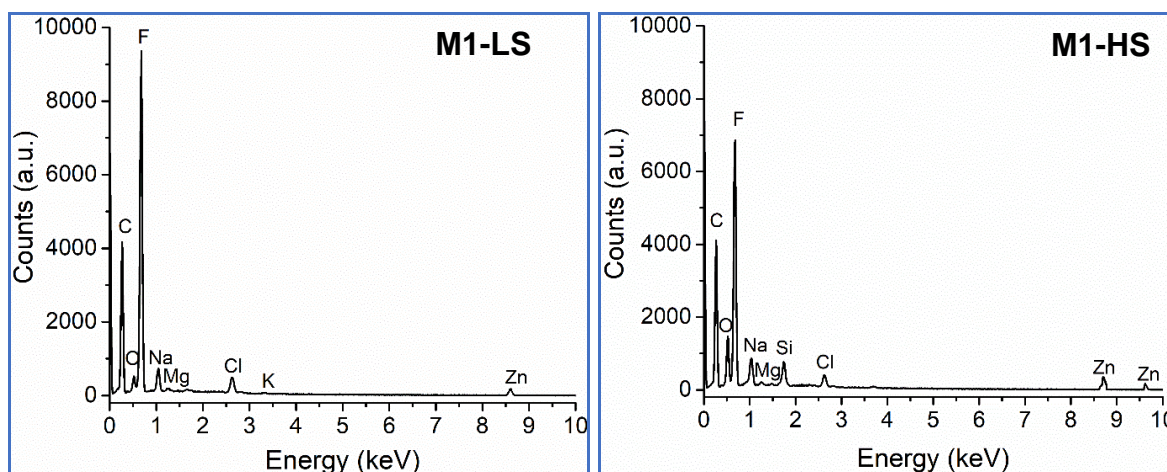


**Figure 8.4:** EDX spectra of pristine PVDF membranes (M1) after MD filtration of low salinity water (M1-LS), and high salinity water (M1-HS).

### 8.3.4 Contact angle measurements

Membrane wetting induced by cake formation has a direct influence of MD membrane separation efficiency. Therefore, the contact angles of the membranes were analysed to determine the effect of membrane fouling on membrane hydrophobicity/hydrophilicity. The water contact angles of M1, M2, M3, M4, M5 and M6 were found to be  $94\pm 3^\circ$ ,  $113\pm 5^\circ$ ,  $156\pm 6^\circ$ ,  $59\pm 3^\circ$ ,  $58\pm 2^\circ$ , and  $63\pm 4^\circ$ , respectively, before MD purification (**Figure 8.5**). The high contact angle of M3 (f-SiO<sub>2</sub>NPs-modified PVDF nanofibre membrane) indicated the super-hydrophobic nature of its surface. Conversely, the low contact angle of M6 (coated f-SiO<sub>2</sub>NPs-modified PVDF nanofibre membrane) indicated the hydrophilic properties of the coating layer embedded with silver nanoparticles (AgNPs) and functionalised multi-walled carbon nanotubes (f-MWCNTs). However, after MD separation of the low salinity/brackish feed solution, the contact angles were decreased to  $80\pm 4^\circ$ ,

102±37°, 126±5°, 57±3°, 56±5°, and 59±6°, respectively (**Figure 8.5**). The highest impact of the MD purification process on contact angle values was recorded for M3 membrane contact angles of M3 membrane. Notably, the contact angle values of the M6 (i.e. the coated M3) were observed to decrease only slightly after the MD process. Furthermore, the high salinity (HS) feed water induced a lower decrease in contact angle values compared to those of the low salinity (LS) water solution. This phenomenon was due to the higher concentrations of inorganic/organic components present in the low salinity (LS) feed water; thus, negatively impacting the hydrophobic nature of the membrane. Hysteresis of contact angle (HCA or sliding angle) is another important parameter that defines membrane suitability in MD application. High contact angles ( $\approx 160^\circ$ ) and lower HCA ( $\leq 10^\circ$ ) are indicative membranes with self-cleaning mechanism of the membrane, a process known as the lotus effect (40,165,171,499). A decrease in HCA was observed on addition of the SiO<sub>2</sub>NPs to PVDF nanofibre membranes. A further decrease in HCA (7-9°) was observed in the coated f-SiO<sub>2</sub>NPs-modified PVDF nanofibre membrane (**Figure 8.5**). The decrease in HCA was due to the easy roll-off of the liquid droplet on the smooth surface of the coated membrane compared to the rougher uncoated membranes. These observations were supported by the previously reported findings (37,40,171).

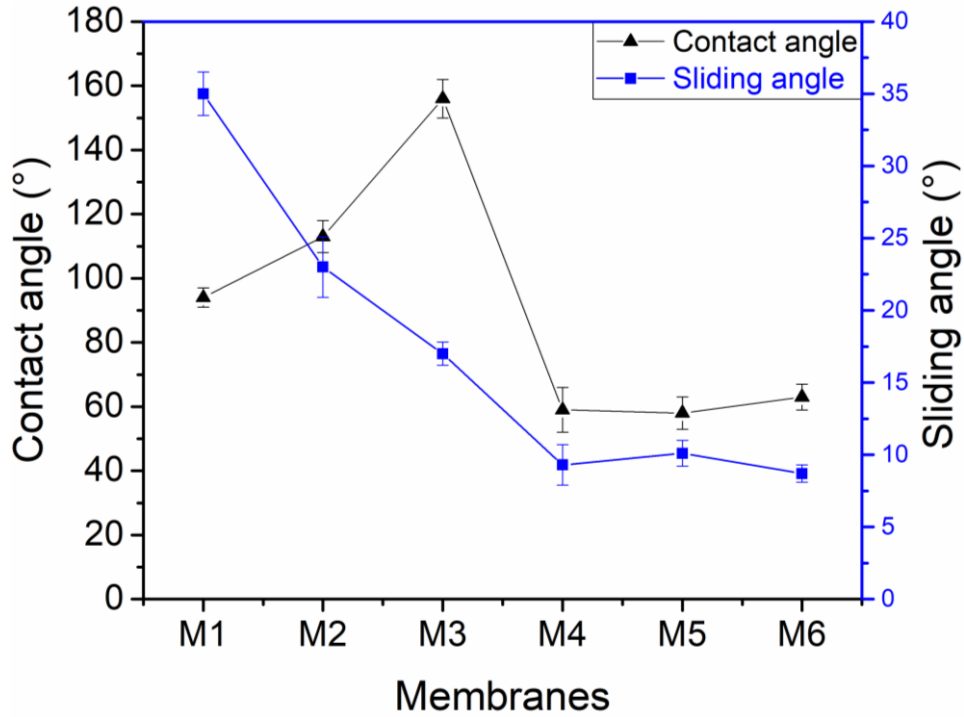


**Figure 8.5:** Contact angles and sliding angles (HCA) of PVDF membranes before MD purification test when using low salinity (LS) and high salinity (HS) feed water. (M1) Pristine PVDF; (M2) SiO<sub>2</sub>NPs-modified PVDF (M3) f-SiO<sub>2</sub>NPs-modified PVDF; (M4) coated pristine PVDF; (5) coated SiO<sub>2</sub>NPs-modified PVDF (M6) coated f-SiO<sub>2</sub>NPs-modified PVDF nanofibre membranes.

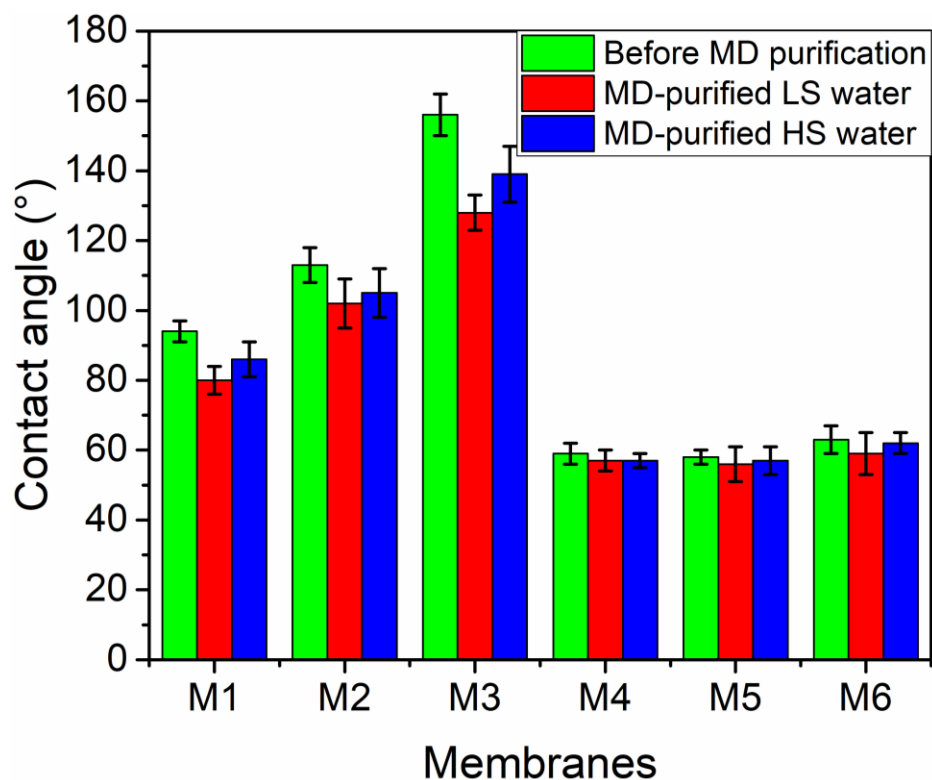


**Figure 8.6:** Contact angles of fouled PVDF membranes before and after MD purification test when using low salinity (LS) and high salinity (HS) feed water. (M1) Pristine PVDF; (M2) SiO<sub>2</sub>NPs-modified PVDF (M3) f-SiO<sub>2</sub>NPs-modified PVDF; (M4) coated pristine PVDF; (5) coated SiO<sub>2</sub>NPs-modified PVDF (M6) coated f-SiO<sub>2</sub>NPs-modified PVDF nanofibre membranes.

### 8.3.5 Membrane and foulants interactions

The contact angle measurements of the pristine and fouled membranes were used to determine the surface tension components of the membranes and solutes (foulants). The results are presented in **Table 8.2**. The surface tension components of the liquids, membrane and solutes were used to compute the interfacial free energies of the membrane and the solutes. The polar interactions of the surface energy/tension were found to be higher than dispersive interactions, indicating the possible attractive interactions between the membranes and the foulants (107,485).

**Table 8.2:** Surface free energy components of clean and fouled membrane surfaces.

Membrane	Surface tension on clean membrane			Surface tension after MD-purified LS water			Surface tension after MD-purified HS water		
	$\sigma_m^D$	$\sigma_m^+$	$\sigma_m^-$	$\sigma_s^D$	$\sigma_s^+$	$\sigma_s^-$	$\sigma_s^D$	$\sigma_s^+$	$\sigma_s^-$
M1	1.30	0.33	8.41	$0.16 \times 10^{-7}$	0.26	11.2	$0.74 \times 10^{-3}$	$0.39 \times 10^{-2}$	12.1
M2	0.14	1.51	11.2	$0.74 \times 10^{-3}$	1.62	9.34	$0.45 \times 10^{-2}$	0.02	8.93
M3	0.16	1.06	9.86	0.23	0.90	9.51	0.97	0.03	8.48
M4	0.12	0.07	15.8	0.085	1.20	11.7	$0.20 \times 10^{-2}$	0.73	9.14
M5	$0.74 \times 10^{-4}$	0.92	9.05	0.29	0.01	16.80	0.08	0.13	16.7
M6	0.12	1.52	16.5	$0.16 \times 10^{-7}$	0.61	9.11	0.12	0.91	16.1

The total interfacial free energy  $\Delta G_{swm}^{TOT}$  provides an estimation of the interaction between the membrane and the solutes (foulants). It therefore determines quantitative definition of the overall hydrophobicity and hydrophilicity of the membranes (57). The more the negative value  $\Delta G_{swm}^{TOT}$ , the stronger interactions between membrane and foulant interaction (Figure 8.7) (107,480,485). The interfacial free energy demonstrated high interactions between the electrospun nanofibre membranes compared to the coated membranes in all feed solutions. This was ascribed to the high surface roughness of the membranes as well as the hydrophobic nature of the membranes. Additionally, hysteresis of contact angle (HCA) is another factor that affects the foulant removal from the membrane surface. The higher the membrane contact angle and the lower the value of HCA ( $<10^\circ$ ), thus improving the membrane self-cleaning mechanism, and the lower the membrane and foulant interaction (40,503). For the uncoated M1, M2, and M3, high contact angles, surface roughness, and HCA were observed, and they are believed to be the main reasons for high membrane and foulant interactions. The values of  $\Delta G_{swm}^{TOT}$  were increased after membrane coating using the thin layer containing f-MWCNTs and AgNPs. The increase in  $\Delta G_{swm}^{TOT}$  demonstrated the reduction in the membrane and solute interaction. Therefore, coating of the superhydrophobic membrane using hydrophilic materials is a one-step solution to membrane fouling. These observations were in good agreement with those reported in other studies (57,503–505).

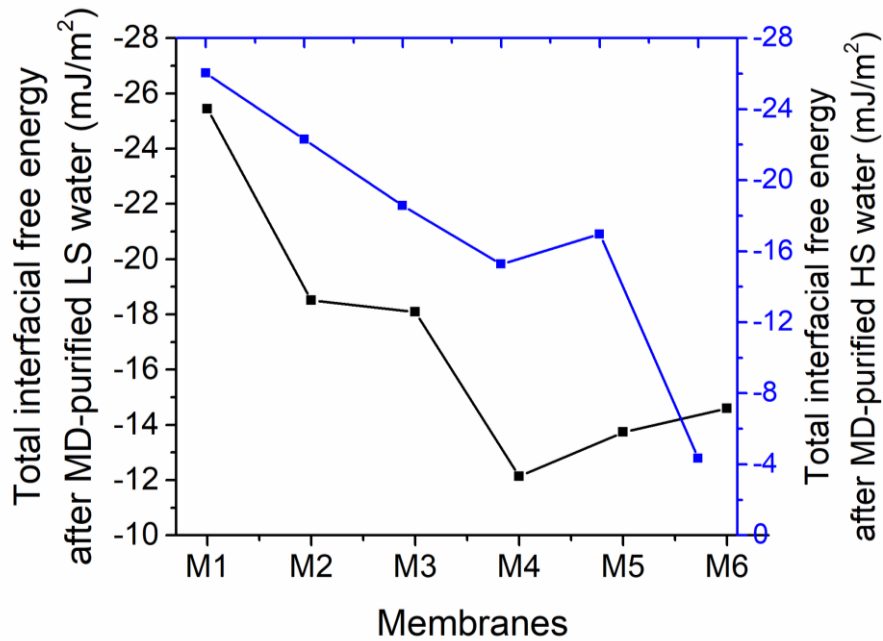


**Figure 8.7:** Various membrane-foulant (or solute) interactions determining initial membrane fouling.

### 8.3.6 Fouling studies using the water samples collected from the estuary in Belgium

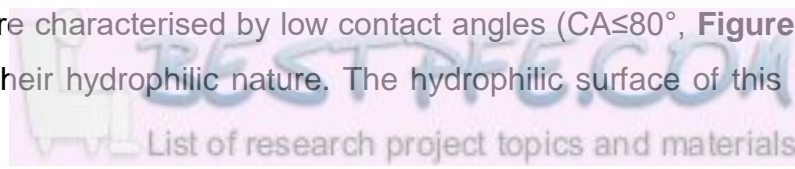
#### 8.3.6.1 Flux decay on modified PVDF nanofibre membranes

The water flux of brackish water samples (LS and HS) across uncoated (M1, M2, and M3) and coated (M4, M5, and M6) PVDF nanofibre membranes was studied using a DCMD setup. All experiments were characterised by flux declines on all membranes (**Figure 8.8**). Severe flux declines were observed in uncoated membranes as well as with low salinity (LS) water samples. After, 50 h of operation, the flux decays on uncoated membrane samples (M1, M2, and M3) with low salinity (LS) brackish water were found to be 73.6%, 75.6%, and 62.1%, respectively while with high salinity (HS) flux decays of 50.0%, 59.8%, and 42.3% respectively were recorded. The difference in flux decay caused by the LS and HS feed samples could be explained by their total organic carbon (TOC) content. The low salinity feed solution was characterised by a higher concentration of TOC ( $2.21 \pm 0.08$  mg/L) than that of the high salinity feed solution ( $0.36 \pm 0.03$  mg/L). This

difference could be attributed to the high dilution effect towards organic solutes induced by the seawater on the river water. The higher TOC content in LS would cause membrane fouling and consequently membrane wetting; thus, leading to higher flux declines. Notably, the f-SiO<sub>2</sub>NPs-modified PVDF nanofibre membranes (M3) showed the highest initial water flux under both LS and HS solution conditions. The initial water flux on M1, M2, and M3 with LS feed solution was 12.9 LMH, 15.6 LMH, and 36.4 LMH respectively. Similar observations were recorded with HS feed solution where the water flux was 13.6 LMH, 14.2 LMH, and 37.1 LMH, respectively. These results indicate the efficiency of the organic modification (i.e., silanisation process) on silica nanoparticles, and thus, enhanced flux performance was observed in modified PVDF nanofibre membranes.

Similarly, the higher organic content of the LS feed solution was also found to have a negative impact on water flux across coated nanofibre membranes (M4, M5, and M6). After 50 h of operation, the flux decays in M4, M5, and M6 with low salinity (LS) feed solution were found to be 33.5%, 42.9%, and 26.6%, respectively; while with high salinity (HS) feed solution, flux decays of 22.1%, 24.7%, 20.8% respectively were recorded. Also, the initial water flux of all coated membranes was similar in magnitude and ranged from 13.7 LMH to 14.7 LMH. Nevertheless, the lower flux decays shown by all coated membranes (i.e., compared to flux decays recorded for uncoated membranes) indicated the significant effect of the hydrophilic coating layer on the performance of pristine, SiO<sub>2</sub>NPs-modified, and f-SiO<sub>2</sub>NPs-modified PVDF nanofibre membranes.

Due to its higher level of total organic carbon (TOC), LS brackish water exacerbated the flux decline on all coated and uncoated membranes. This was attributed to hydrophobic-hydrophobic interactions between the hydrophobic surfaces of the PVDF nanofibre membranes and the hydrophobic moieties (e.g., aromatic rings) in the organic matter present in the feed solution. This phenomenon was found to be particularly more severe on uncoated PVDF nanofibre membranes (M1, M2, and M3). However, all coated PVDF nanofibre membranes were characterised by low contact angles ( $CA \leq 80^\circ$ , **Figure 8.6**); thus, demonstrating their hydrophilic nature. The hydrophilic surface of this hydrophilic



coating layer reduced the adsorption of inorganic/organic matter on the surface of the membranes and subsequently reduced membrane fouling and flux decays (506). These results are consistent with results reported in previous studies (452,507) and will be further discussed in the sections given below.

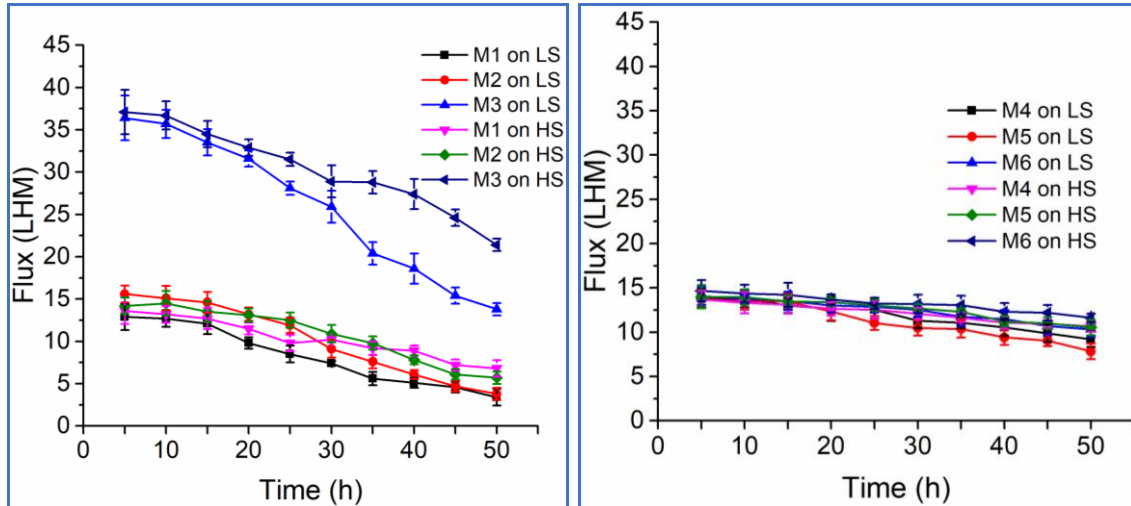


**Figure 8.8:** Water flux of LS and HS across PVDF nanofibre membranes. Uncoated membranes: (M1) pristine, (M2) SiO<sub>2</sub>NPs-modified, (M3) f-SiO<sub>2</sub>NPs-modified; and coated membranes: (M4) coated pristine, (M5) coated SiO<sub>2</sub>NPs-modified, and (M6) coated f-SiO<sub>2</sub>NPs-modified PVDF nanofibre membranes.

### 8.3.6.2 Salt rejection of modified PVDF nanofibre membranes

The impact of fouling on the rejection of salts by the modified PVDF nanofibre membranes was investigated. The initial salt rejections of uncoated membranes M1, M2, and M3 with low salinity (LS) feed solution was found to be 99.97%, 99.98%, and 99.99%; while with low salinity feed solution was 99.99%, 99.98%, and 99.99%, respectively (**Figure 8.9**). After 50 h of operation, the salt rejection of uncoated membranes M1, M2, M3 with low salinity (LS) brackish water declined by 5.4%, 5.7%, and 6.3%, respectively, while with high salinity (HS) brackish water (i.e. feed solution characterized by low concentrations of TOC) the salt rejection declined by 2.3%, 3.1%, and 4.6%, respectively. The lower salt rejection decays observed with high salinity feed solution was associated with a lower membrane fouling propensity. Specifically, organic fouling would reduce the membrane

hydrophobicity and would promote membrane wetting; consequently, reducing the salt rejection efficiency (32). Coated membranes showed lower initial salt rejection than uncoated membranes but the decays in salt rejection after 50 h of operation was observed to be much lower in coated membranes.

The initial salt rejections of coated membranes M4, M5, and M6 with low salinity (LS) feed solution was found to be 99.58%, 99.62%, and 99.63%; while with high salinity (HS) feed solution, the initial salt rejection was 99.59%, 99.58%, and 99.61%, respectively. It worth noting that the initial salt rejection of coated membranes was observed to be slightly lower than that of uncoated membranes. However, after 50 h of operation, the decay in salt rejection of coated membranes was observed to be significantly lower than that of uncoated membranes. After 50 h of operation, the salt rejection of coated membranes M4, M5, and M6 with low salinity (LS) brackish feed water declined by 0.9%, 1.6%, and 1.4%, while with high salinity (HS) feed water, salt rejections declined by 0.7%, 0.6%, and 0.9% respectively.

The results of salt rejection and water flux studies were comparable with previously reported studies where the functionalised membranes demonstrated almost stable flux and salt rejection fluctuations (183,243,469,488). Briefly, Huang and the co-workers prepared a Janus membrane using a positively charged cetyltrimethylammonium bromide / Poly(vinylidene fluoride-co-hexafluoropropylene (CTAB/PVDF-HFP) fibrous substrate which was subsequently decorated with fluorinated SiNPs and coated with a solution containing perfluorooctanoate (PFO)/chitosan (CTS)/ SiNPs blend (183). The Janus membrane demonstrated the ability to maintain stable water flux compared to virgin membranes. These findings were in agreement with the findings of this study. However, the preparation method for synthesis of the Janus membrane was not environmentally friendly due to the use of toxic and costly fluorinated materials such as perfluorooctanoate (508).

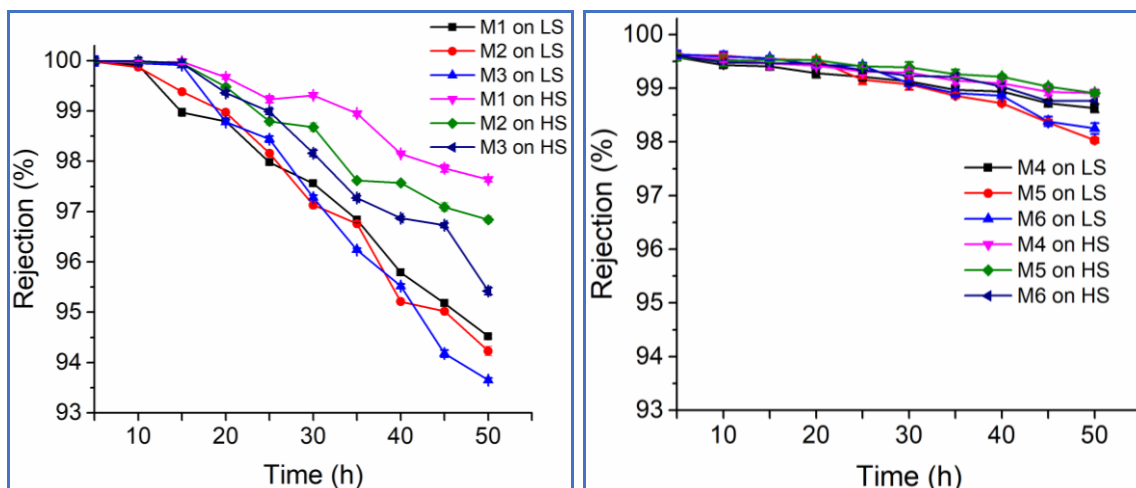


**Figure 8.9:** Salt rejections of PVDF nanofibre membranes. Uncoated membranes: (M1) pristine, (M2) SiO<sub>2</sub>NPs-modified, (M3) f-SiO<sub>2</sub>NPs-modified; and coated membranes: (M4) coated pristine, (M5) coated SiO<sub>2</sub>NPs-modified, and (M6) coated f-SiO<sub>2</sub>NPs-modified PVDF nanofibre membranes.

### 8.3.7 Fouling studies using the water samples collected at Nandoni Dam in South Africa

#### 8.3.7.1 Flux decay on modified PVDF nanofibre membranes

The flux decay was further studied on water samples collected from Nandoni Dam in South Africa. The feed water samples were collected at the inlet and the outlet of the dam. The experiments conducted using the uncoated (M1, M2, and M3) were characterised by flux decline. After 50 h of operation, the water flux of M1, M2, and M3 using the inlet water samples declined by 61.1%, 55.7% and 40.3%, respectively while with outlet water samples, the water flux of M1, M2, and M3 declined by 36.4%, 54.9% and 36.3%, respectively (**Figure 8.10**). The environmental water samples collected from the dam inlet were characterised by high levels of total organic carbon (TOC) compared to the dam outlet water samples. The average TOC concentration at the dam inlet was  $4.77 \pm 0.32$  mg/L while that of the dam outlet water samples was  $3.13 \pm 0.10$  mg/L. This difference in organic compound concentration was related to the decline in water flux. The higher concentration of organic compounds in dam inlet water samples would

cause membrane fouling leading to flux decline. Similarly, the f-SiO<sub>2</sub>NPs-modified PVDF nanofibre membranes (M3) showed the highest initial water flux under both inlet and outlet water feed conditions. The coated membranes (M4, M5, and M6) were continuously characterised by the reduction in flux decay during the 50 h of operation. Briefly, after 50 h of operation, the water flux of M4, M5, and M6 using the dam inlet feed solution declined by 22.3%, 26.2%, and 20.6%, respectively, while the water flux of M4, M5, and M6 using the dam outlet feed solution declined by 21.4%, 18.3%, and 18.2% respectively (**Figure 8.10**). Although, the initial water flux of all coated membranes was lower in magnitude compared to that observed for uncoated membranes, their resistance to flux decline is an indication of their sustainable use in MD operation.

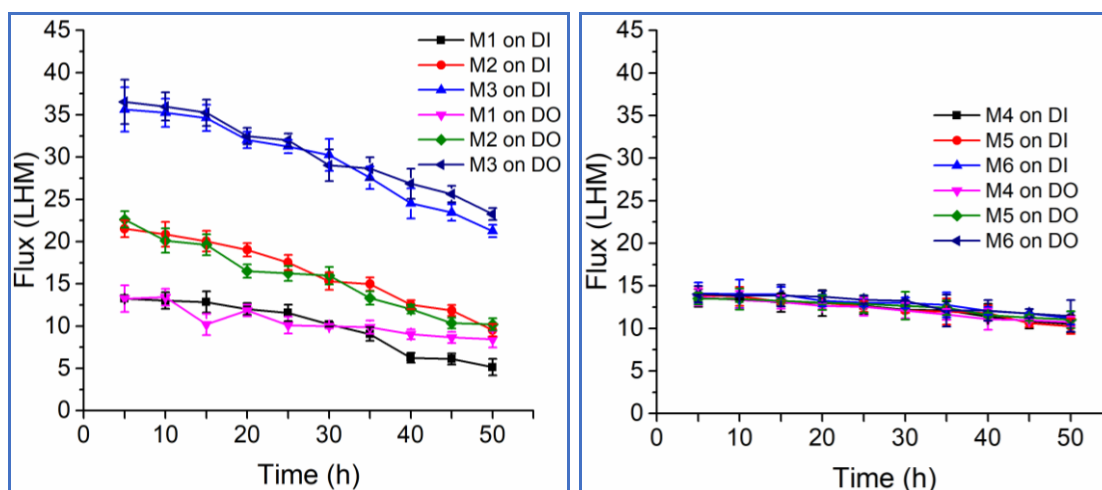


**Figure 8.10:** Water flux decay of PVDF nanofibre membranes using dam inlet (DI) and dam outlet (DO) water samples. Uncoated membranes: (M1) pristine, (M2) SiO<sub>2</sub>NPs-modified, (M3) f-SiO<sub>2</sub>NPs-modified; and coated membranes: (M4) coated pristine, (M5) coated SiO<sub>2</sub>NPs-modified, and (M6) coated f-SiO<sub>2</sub>NPs-modified PVDF nanofibre membranes.

### 8.3.7.2 Salt rejection decay of modified PVDF nanofibre membranes

The water samples collected from Nandoni Dam were further used to study their effect on salt rejection and results are presented in **Figure 8.11**. The salt rejection

of uncoated M1, M2, and M3 when using dam inlet feed water declined by 3.0%, 2.8% and 3.1%, respectively. Similarly, the decays in salt rejection of uncoated M1, M2, and M3 when using dam outlet feed water were declined by 2.9%, 2.8% and 3.4% respectively. There were no statistically significant differences in salt rejection decays caused by the two feed solutions as compared to the flux studies. This phenomenon is an indication of similar effects of membrane fouling towards wetting of the used membranes. (32). Likewise, the salt rejection on coated membranes was slightly lower than that observed in uncoated membranes. However, the salt rejection decays of coated membranes were significantly lower than those of uncoated membranes. After 50 h of operation, the salt rejection of coated membranes M4, M5, and M6 with dam inlet feed water declined by 0.8%, 0.9%, and 0.6%, respectively while that with dam outlet feed water declined by 0.8%, 0.6%, and 0.7% respectively. These salt rejection and water flux findings were comparable with results previously reported by other studies where the functionalised membranes demonstrated almost stable flux and salt rejection fluctuations (183,243,469,488).

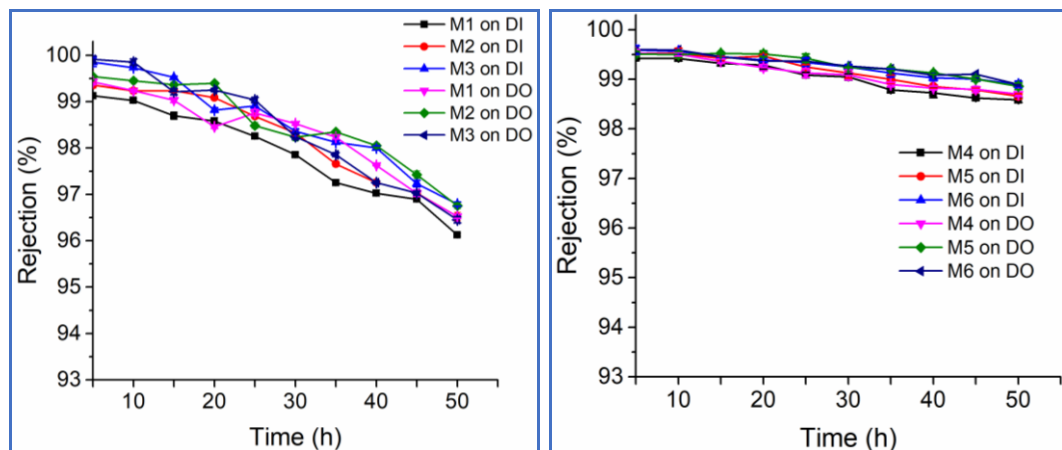


**Figure 8.11:** Salt rejection of PVDF nanofibre membranes using dam inlet (DI) and dam outlet (DO) water samples. Uncoated membranes: (M1) pristine, (M2) SiO<sub>2</sub>NPs-modified, (M3) f-SiO<sub>2</sub>NPs-modified; and coated membranes: (M4) coated pristine, (M5) coated SiO<sub>2</sub>NPs-modified, and (M6) coated f-SiO<sub>2</sub>NPs-modified PVDF nanofibre membranes.

### 8.3.8 Comparison of the water flux and salt rejection decay of PVDF nanofibre membranes using water samples collected from the Scheldt estuary in Belgium and Nandoni Dam in South Africa

The water flux and salt rejection decays of the PVDF nanofibre membranes using water samples collected from the estuary in Belgium and Nandoni Dam in South Africa were compared and the results are presented in **Table 8.3**. The water flux decay was significantly different while the salt rejection decay was significantly similar when using high salinity water collected from the estuary in Belgium, the Nandoni Dam inlet and outlet streams. The differences in flux declines induced by the feed solutions collected from the estuary and the dam water were due to a number of parameters that include the chemistry of foulants present in these feed solutions. For instance, the presence of sparingly soluble salts such as calcium sulphate ( $\text{CaSO}_4$ ) that float around the membrane causes membrane fouling regardless of the superhydrophobic nature of the membrane. (242). It was therefore indicated that the module design and cross-flow conditions are the key parameters for attainment of a stable water flux and high rejection efficiencies even when the desalination process is subjected to precipitating salts floating around the membranes (131). These parameters are yet to be exploited in the future MD studies. The results obtained in this study were compared with results reported in the literature where the environmental water samples were used as the feed solution (**Table 8.4**). The results demonstrated that flux was severely impacted when superhydrophobic membranes were used (449,509,510). However, hydrophilic coating of the membranes reduced the flux decays indicating a promising approach towards MD performance. Therefore, the findings of this study were in agreement with the reported literature.

**Table 8.3:** Comparison of water flux and salt rejection decay of PVDF nanofibre membranes using the water samples collected from the estuary in Belgium and Nandoni Dam in South Africa.

Membranes	Flux decay (%)				Salt rejection decay (%)			
	LS	HS	DI	DO	LS	HS	DI	DO
M1	73.6	50.0	61.1	36.3	5.4	2.3	3.0	2.9
M2	75.6	59.8	55.7	54.9	5.7	3.1	2.8	2.8
M3	62.1	42.3	40.3	36.3	6.3	4.6	3.1	3.4
M4	33.5	22.1	22.3	21.4	0.9	0.7	0.8	0.8
M5	42.8	24.7	23.2	18.3	1.6	0.6	0.9	0.6
M6	26.6	20.8	20.6	18.2	1.4	0.9	0.6	0.7

LS = low salinity water, HS = high salinity water, DI = dam inlet water, DO = dam outlet water

**Table 8.4:** Comparison of flux decays when real water samples were purified in MD.

Membranes	Water source	Configuration	Duration (h)	Initial flux (LMH)	Final flux (LMH)	Ref.
PVDF	Shale oil water	DCMD	-	30	17.5	(509)
PVA-coated PVDF	Shale oil water	DCMD	-	30	24.5	(509)
PVDF/SiO <sub>2</sub> NPs	Shale oil water	DCMD	-	26	15	(509)
PVDF	Oily saline wastewater	DCMD	1000	11	0	(449)
PVDF/SiO <sub>2</sub> NPs	Oily saline wastewater	DCMD	1000	10	0	(449)
Hydrophilic coated PVDF/SiO <sub>2</sub> NPs	Oily saline wastewater	DCMD	1000	4	2	(449)
PVDF hollow fibre	Rubber industry waste water	DCMD	150	7.4	1.5	(510)
PVDF/f-SiO <sub>2</sub> NPs	HS water from estuary	DCMD	50	37.1	21.4	This study
Hydrophilic-coated PVDF/f-SiO <sub>2</sub> NPs	HS water from estuary	DCMD	50	14.7	11.6	This study
PVDF/f-SiO <sub>2</sub> NPs	Nandoni Dam water	DCMD	50	36.7	23.8	This study
Hydrophilic-coated PVDF/f-SiO <sub>2</sub> NPs	Nandoni Dam water	DCMD	50	14.2	11.9	This study

## 8.4 Conclusion

The incorporation of organically functionalised silica nanoparticles (f-SiO<sub>2</sub>NPs) on PVDF nanofibre membranes proved to be a suitable technique to improve the properties of MD membranes for low and high salinity (collected from the estuary) as well as the feed water samples collected from Nandoni Dam. However, it was found that the performance of f-SiO<sub>2</sub>NPs-modified PVDF membranes was still negatively impacted by the adsorption of foulants. The hydrophilic coating layer on the MD membranes provided anti-fouling properties to the PVDF membranes, resulting in decreased flux decay, cake layer formation, and a lower decline in salt rejection. However, the initial water flux of these coated membranes significantly decreased in comparison to those of superhydrophobic f-SiO<sub>2</sub>NPs-modified PVDF membranes suggesting that there is still room for research and improvement (e.g., enhanced permeability and salt rejection) particularly for these hydrophilic coating layers. Despite the fouling challenges observed, this technique showed great potential for the development of antifouling MD membranes towards the successful implementation of MD processes.

## CHAPTER 9

### GENERAL CONCLUSIONS AND RECOMMENDATIONS

---

The level of water salinity at Nandoni dam was assessed to determine the suitability of this water source for drinking purposes. The water conductivity and TDS concentrations indicated that water in Nandoni Dam was partially brackish with few exceptions at the dam outlet and the water treatment plant. Additionally, the concentrations of some phenols were found to be higher than SANS 241 drinking water standards while that of the PAHs fell within the acceptable limits. These findings indicated that the water sourced from the Nandoni Dam does not only require qualitative and quantitative analyses but also engineering, economic, legal, ecological social aspects and advanced purification processes to manage it holistically. Furthermore, advanced energy-efficient water purification technologies are of paramount importance to solve water quality problems. The MD is one such technology that could be adopted and is proposed for the municipality.

Membrane distillation is envisaged as a promising advanced and cost-effective membrane technology for desalination of brackish water. The membranes used in MD include PVDF nanofibre membranes among others. The current study synthesized f-SiO<sub>2</sub>NPs-modified PVDF nanofibre membranes with superhydrophobicity properties (contact angles >150°) to prevent wetting while maintaining high rejection and water flux. These electrospun PVDF nanofibre membranes embedded with organically-modified SiO<sub>2</sub>NPs displayed Young's modulus values of 42.1 MPa ≤ E ≤ 43.4 MPa. The entangled and intertwined structures have also led to the formation of highly porous membranes (78.5–79.9%) with pore sizes ranging from 1.24 to 1.41 μm, both parameters falling within previously suggested optimal ranges in MD (40–90% and 0.1–1.5μm, respectively).

However, the LEP values of 72.3±2.3 – 84.2±2.8 kPa recorded in this study were below the recommended LEP values (≥250 kPa) in MD. These membranes were

highly efficient in the removal of NaCl from water ( $\geq 99.9\%$  removal) at a feed temperature of  $60^\circ$ . In terms of flux as a function of both temperature and time, membranes embedded with Cl-DMOS, ODTS, OTMS-modified  $\text{SiO}_2$ NPs (also showing the highest contact angle) were the most efficient. However, the performance of these membranes was negatively impacted by the adsorption of foulants, followed by the change in membrane characteristics where flux and salt rejection decays of 30-90% and 1.4-6% were reported respectively. Therefore, coating of superhydrophobic membrane with a hydrophilic layer consisting of silver nanoparticles (AgNPs) and carboxylated multi-walled carbon nanotubes (f-MWCNTs) was evaluated.

Membrane coating effectively reduced the overall flux and salt rejection decays. Although, membrane coating decreased the initial water flux from 43-45 LMH to 16-17LMH, stable water fluxes were observed within 50 h of operation where the decays of 19-31% flux decays and 0.1-1.0% salt rejection decays were recorded. The decrease in flux decay was ascribed to reduction of biofilm formation, membrane-organic and membrane-colloidal interactions enhanced by the antibacterial AgNPs and hydrophilic f-MWCNTs respectively.

To further address fouling observed in MD, iminated polyacrylonitrile nanofibres (PAN) were synthesised and tested for the removal of volatile compounds with hydrophobic moieties from water sources. The model volatile organic compounds were o-chlorophenol and p-nitrophenol. The optimum conditions for adsorption of the phenols onto iminated PAN nanofibres were: pH 7, initial nitrophenol or chlorophenol concentration of 80 mg/L, adsorbent dose of 25 mg, and contact time of 60 min, leading to an adsorption capacity of 38.37 mg/g. These materials were incorporated into a candle filter and used in the MD pretreatment step to remove organic, particulate and colloidal particles.

The flux decays recorded on the MD integrated to a pretreatment step were in the range of 18.2-26.6% when the environmental samples were used as the feed samples. Therefore, it was concluded that the nanoparticle-modified membranes are a one-step solution to address many challenges associated with MD.

Nanoparticle-incorporated membranes also create a path for achieving superhydrophobic membranes with contact angles above 150°. Carefully designed methods for the incorporation of nanoparticles into these membranes offer the possibility of developing high-performance MD water recovery technologies.

It is worth noting that although the findings of this study are a promising approach to mitigate fouling, wetting and low rate of water recovery in MD, there is still room for research and improvement (e.g., enhanced permeability and salt rejection) particularly for these hydrophilic coating layers. Therefore, surface modifications need further exploration. Plasma coating with a thin layer ( $\leq 10$  nm) is recommended. The rapid deteriorations of the water flux could be achieved by use of a superhydrophilic coating (contact angle  $\leq 30^\circ$ ) on the superhydrophobic membranes. Furthermore, optimization of pore size, pore structure and nanofibre diameters of the nanofibre membranes is recommended to improve the LEP of the membranes.

Nanofibre membranes suffer critical challenges of low industrial throughput. Therefore, the production of high-throughput and low cost nanofibre requires future consideration. Additionally, long-term operating conditions (a minimum of 600 h) are required to determine the stability of the synthesized materials in MD applications. Although the membrane modifications done showed the feasibility of developing a fouling-resistant membrane to mitigate the challenges associated with MD processes, the cost analysis of this technology that involves the use of expensive materials such as Ag need further investigation. It is imperative to systematically develop even more cost-effective purification systems that are integrated with emerging membranes to produce high quality water at large industrial throughput.

## REFERENCES

---

1. Aulenbach DB. Water our second most important natural resource. In: Boston College Law Review. 1968. 535–52.
2. Collins JF, Brown JP, Alexeeff G V, Salmon AG. Potency equivalency factors for some polycyclic aromatic hydrocarbons and polycyclic aromatic hydrocarbon derivatives. Regul Toxicol Pharmacol. 1998;28(1):45–54.
3. Muller M, Schreiner B, Smith L, Koppen B Van, Sally H, Aliber M, et al. Water security in South Africa. Development Planning Division Working Paper Series. 2009;12(12):1–40.
4. Mishra RK, Dubey SC. Fresh water availability and it's global challenge. Int J Eng Sci Invent Res Dev. 2015;2:351–407.
5. Hoekstra AY, Mekonnen MM, Chapagain AK, Mathews RE, Richter BD. Global monthly water scarcity: Blue water footprints versus blue water availability. PLoS One. 2012;7(2):1–9.
6. Rajaram T, Das A. Water pollution by industrial effluents in India: Discharge scenarios and case for participatory ecosystem specific local regulation. Futures. 2008;40(1):56–69.
7. Lemieux PM, Lutes CC, Santoianni DA. Emissions of organic air toxics from open burning: A comprehensive review. Prog Energy Combust Sci. 2004;30(1):1–32.
8. Ali SM, Sabae SZ, Fayez M, Monib M, Hegazi NA. The influence of agro-industrial effluents on River Nile pollution. J Adv Res. 2011;2(1):85–95.
9. Vengosh A. Salinization and saline environments. In: Treatise on Geochemistry. 2nd ed. 2013. 325–78.
10. Marie A, Vengosh A. Sources of salinity in underground water from Jericho area, Jordan Valley. Ground Water. 2001;39(2):240–8.
11. Konečný F, Boháček Z, Müller P, Kovářová M, Sedláčková I. Contamination of soils and groundwater by petroleum hydrocarbons and volatile organic

- compounds - Case study: ELSLAV BRNO. *Bull Geosci.* 2003;78(3):225–39.
12. Mclin SG. Evaluation of aquifer contamination from salt water disposal wells. *Proc Oklahoma Acad Sci.* 1986;61:53–61.
  13. Edokpolo B, Yu QJ, Connell D. Health risk assessment of ambient air concentrations of benzene, toluene and xylene (BTX) in service station environments. *Int J Environ Res Public Health.* 2014;11(6):6354–74.
  14. Naidu G, Jeong S, Kim SJ, Kim IS, Vigneswaran S. Organic fouling behavior in direct contact membrane distillation. *Desalination.* 2014;347:230–9.
  15. Haque SA. Salinity problems and crop production in coastal regions of Bangladesh. *Pakistan J Bot.* 2006;38(5 SPEC. ISS.):1359–65.
  16. Rijsberman FR. Water scarcity: Fact or fiction? *Agric Water Manag.* 2006;80:5–22.
  17. Xing L, Huang L, Hou X, Yang L, Chi G, Xu J, et al. Groundwater hydrochemical zoning in inland plains and its genetic mechanisms. *Water.* 2018;10:2–18.
  18. Zuurbier KG, Stuyfzand PJ. Consequences and mitigation of saltwater intrusion induced by short-circuiting during aquifer storage and recovery in a coastal subsurface. *Hydrol Earth Syst Sci.* 2017;21:1173–88.
  19. Cucci G, Lacolla G, Mastro MA, Caranfa G. Leaching effect of rainfall on soil under four-year saline water irrigation. *Soil Water Res.* 2016;11(3):181–9.
  20. Joshi DC, Toth T, Sari D. Spatial variability of electrical conductivity of soils irrigated with brackish water in the arid region of Rajasthan, India. *Ann Arid Zone.* 2006;45(1):9–17.
  21. Morillo J, Usero J, Rosado D, El Bakouri H, Riaza A, Bernaola FJ. Comparative study of brine management technologies for desalination plants. *Desalination.* 2014;336(1):32–49.
  22. Clayton ME, Stillwell AS, Webber ME. Implementation of brackish groundwater desalination using wind-generated electricity: A case study of the energy-water nexus in Texas. *Sustainability.* 2014;6:758–78.

23. Tidwell VC, Moreland BD, Zemlick KM, Roberts BL, Passell HD, Jensen D, et al. Mapping water availability, projected use and cost in the western United States. *Environ Res Lett.* 2014;9:1–11.
24. Camacho LM, Dumée L, Zhang J, Li J de, Duke M, Gomez J, et al. Advances in membrane distillation for water desalination and purification applications. *Water.* 2013;5(1):94–196.
25. Valavala R, Sohn J, Han J, Her N, Yoon Y. Pretreatment in reverse osmosis seawater desalination: A short review. *Environ Eng Res.* 2011;16(4):205–12.
26. Al-Sahali M, Ettouney H. Developments in thermal desalination processes: Design, energy, and costing aspects. *Desalination.* 2007;214:227–40.
27. Manjula S, Subramanian R. Membrane technology in degumming, dewaxing, deacidifying, and decolorizing edible oils. *Crit Rev Food Sci Nutr.* 2006;46(7):569–92.
28. Geise GM, Lee HS, Miller DJ, Freeman BD, Mcgrath JE, Paul DR. Water purification by membranes: The role of polymer science. *J Polym Sci Part B Polym Phys.* 2007;45:1390–8.
29. Singh B, Kochkodan V, Hashaikeh R, Hilal N. A review on membrane fabrication: Structure, properties and performance relationship. *Desalination.* 2013;326:77–95.
30. Le NL, Nunes SP. Materials and membrane technologies for water and energy sustainability. *Sustain Mater Technol.* 2016;7:1–28.
31. Khayet M, Gordino MP, Mengual JI. Theoretical and experimental studies on desalination using membrane distillation. *Desalination.* 2003;157:297–305.
32. Kullab A, Martin A. Membrane distillation and applications for water purification in thermal cogeneration plants. *Sep Purif Technol.* 2011;76:231–7.
33. Thomas N, Mavukkandy MO, Loutatidou S, Arafat HA. Membrane distillation research and implementation: Lessons from the past five decades. *Sep Purif Technol.* 2017;189:108–27.
34. Kang G, Cao Y. Application and modification of poly(vinylidene fluoride)

- (PVDF) membranes – A review. *J Memb Sci.* 2014;463:145–65.
35. Khayet M. Solar desalination by membrane distillation: Dispersion in energy consumption analysis and water production costs (a review). *Desalination.* 2013;308:89–101.
  36. Curcio E, Drioli E. Membrane distillation and related operations—A review. *Sep Purif Rev.* 2005;34:35–86.
  37. Dong Z-Q, Ma X-H, Xu Z-L, Gu Z-Y. Superhydrophobic modification of PVDF–SiO<sub>2</sub> electrospun nanofiber membranes for vacuum membrane distillation. *RSC Adv.* 2015;5:67962–70.
  38. Munirasu S, Banat F, Ahmed A, Abu M. Intrinsically superhydrophobic PVDF membrane by phase inversion for membrane distillation. *Desalination.* 2017;417:77–86.
  39. Chen Y, Tian M, Li X, Wang Y, An AK, Fang J, et al. Anti-wetting behavior of negatively charged superhydrophobic PVDF membranes in direct contact membrane distillation of emulsified wastewaters. *J Memb Sci.* 2017;535:230–8.
  40. Razmjou A, Arifin E, Dong G, Mansouri J, Chen V. Superhydrophobic modification of TiO<sub>2</sub> nanocomposite PVDF membranes for applications in membrane distillation. *J Memb Sci.* 2012;415–416:850–63.
  41. An AK, Lee EJ, Guo J, Jeong S, Lee JG, Ghaffour N. Enhanced vapor transport in membrane distillation via functionalized carbon nanotubes anchored into electrospun nanofibres. *Sci Rep.* 2017;7:1–11.
  42. Kiss AA, Kattan Readi OM. An industrial perspective on membrane distillation processes. *J Chem Technol Biotechnol.* 2018;93(8):2047–55.
  43. Bessong PO, Nyathi E, Mahopo TC, Netshandama V. Development of the Dzimauli community in Vhembe District, Limpopo Province of South Africa, for the MAL-ED cohort study. *Clin Infect Dis.* 2014;59:317-S324.
  44. Nthunya LN, Masheane ML, Malinga SP, Nxumalo EN, Mamba BB, Mhlanga SD. Determination of toxic metals in drinking water sources in the Chief Albert Luthuli Local Municipality in Mpumalanga, South Africa. *Phys Chem*

- Earth. 2017;100:94–100.
45. Frankson L. Department ready to start Giyani water project \_ Infrastructure news. Infrastructureene.ws and service delivery. 2015 [cited 2017 Nov 24]. Available from: <http://www.infrastructurene.ws/2015/08/21/departement-ready-to-start-giyani-water-project/>
  46. Fouche PSO, Vlok W, Roos JC, W L-P, A J. Establishing the fishery potential of Lake Nandoni in the Luvuvhu River, Limpopo Province. Water Research Commission, 1-135; 2013.
  47. Edokpayi JN, Rogawski ET, Kahler DM, Hill CL, Reynolds C, Nyathi E, et al. Challenges to sustainable safe drinking water: A case study of water quality and use across seasons in rural communities in Limpopo Province, South Africa. *Water (Switzerland)*. 2018;10(2):1–18.
  48. Edokpayi JN, Odiyo JO, Popoola OE, Msagati TAM. Determination and distribution of polycyclic aromatic hydrocarbons in rivers, sediments and wastewater effluents in Vhembe District, South Africa. *Int J Environ Res Public Health*. 2016;13(4):1–12.
  49. Gumbo JR, Dzaga RA, Nethengwe NS. Impact on water quality of Nandoni water reservoir downstream of municipal sewage plants in Vhembe district, South Africa. *Sustain*. 2016;8(7):1–16.
  50. Mukwevho N. Water crisis hits Limpopo villagers hard. *Health-E News*. 2017 [cited 2019 Jan 21]. 1–2. Available from: <https://www.health-e.org.za/2017/02/01/water-crisis-hits-limpopo-villagers-hard/>
  51. Nduvheni S. Limpopo Mirror \_ News \_ Water shortages causes dissatisfaction in unit E. *Limpopo Mirror*. 2015 [cited 2019 Jan 21]. 1–3. Available from: <https://limpopomirror.co.za/articles/news/31306/2015-06-05/water-shortages-causes-dissatisfaction-in-unit-e>
  52. Kanduti D, Sterbenk P, Artnik A. Fluoride: a review of use and effects on health. *Mater Socio Medica*. 2016;28(2):133.
  53. Ha SK. Dietary salt intake and hypertension. *Electrolyte Blood Press*. 2014;12:7–18.

54. Aburto NJ, Ziolkovska A, Hooper L, Elliott P, Cappuccio FP, Meerpohl JJ. Effect of lower sodium intake on health: Systematic review and meta-analyses. *BMJ*. 2013;346:1–20.
55. Rabofire M. Polokwane hit by severe water shortage. *News24*. 2016. Available from: <http://www.infrastructurene.ws/2016/01/11/polokwane-hit-by-severe-water-shortage/>
56. Nthunya LN, Maifadi S, Mamba, Bhekie B, Verliefde AR, Mhlanga SD. Spectroscopic determination of water salinity in brackish surface water in Nandoni Dam, at Vhembe District, Limpopo Province, South Africa. *Water*. 2018;10:1–13.
57. Zhang M, Liao B qiang, Zhou X, He Y, Hong H, Lin H, et al. Effects of hydrophilicity/hydrophobicity of membrane on membrane fouling in a submerged membrane bioreactor. *Bioresour Technol*. 2015;175:59–67.
58. NGWA. Brackish Groundwater. 2010 [cited 2018 Jan 3]. 1–4. Available from: [http://www.ngwa.org/Media-Center/briefs/Documents/Brackish\\_water\\_info\\_brief\\_2010.pdf](http://www.ngwa.org/Media-Center/briefs/Documents/Brackish_water_info_brief_2010.pdf)
59. WHO. Guidelines for drinking-water quality. Vol. 1, World Health Organization. 2008.
60. Del Rio D, Rodriguez-Mateos A, Spencer JPE, Tognolini M, Borges G, Crozier A. Dietary (Poly)phenolics in Human Health: Structures, Bioavailability, and Evidence of Protective Effects Against Chronic Diseases. *Antioxid Redox Signal*. 2013;18(14):1818–92.
61. Azevedo D de A, Gerchon E, dos Reis EO. Monitoring of pesticides and polycyclic aromatic hydrocarbons in water from Paraiba do Sul River, Brazil. *J Braz Chem Soc*. 2004;15(2):292–9.
62. Agency for Toxic Substances and Disease Registry. Toxicological profile for styrene. 2010 [cited 2017 Aug 19]. 1–236. Available from: <https://www.atsdr.cdc.gov/toxprofiles/tp53.pdf>
63. Babich H, Davis DL. Phenol : A review of environmental and health risks. *Regul Toxicol Pharmacol*. 1981;1:90–109.

64. Grimmer G, Brune H, Dettbarn G, Naujack KW, Mohr U, Wenzel-Hartung R. Contribution of polycyclic aromatic compounds to the carcinogenicity of sidestream smoke of cigarettes evaluated by implantation into the lungs of rats. *Cancer Lett.* 1988;43(3):173–7.
65. Ye B, Yang L, Li Y, Wang W, Li H. Water sources and their protection from the impact of microbial contamination in rural areas of Beijing, China. *Int J Environ Res Public Health.* 2013;10:879–91.
66. Zodrow KR, Bar-Zeev E, Giannetto MJ, Elimelech M. Biofouling and microbial communities in Membrane Distillation and Reverse Osmosis. *Environ Sci Technol.* 2014;48:13155–64.
67. Nguyen T, Roddick FA, Fan L. Biofouling of water treatment membranes: A review of the underlying causes, monitoring techniques and control measures. *Membranes (Basel).* 2012;2:804–40.
68. Biswas P, Bandyopadhyaya R. Biofouling prevention using silver nanoparticle impregnated polyethersulfone (PES) membrane: E. coli cell-killing in a continuous cross-flow membrane module. *J Colloid Interface Sci.* 2017;491:13–26.
69. Landaburu-aguirre J, García-pacheco R, Molina S, Rodríguez-sáez L, Rabadán J, García-calvo E. Fouling prevention , preparing for re-use and membrane recycling . Towards circular economy in RO desalination. *Desalination.* 2016;393:16–30.
70. Tijing LD, Woo YC, Choi JS, Lee S, Kim SH, Shon HK. Fouling and its control in membrane distillation-A review. *J Memb Sci.* 2015;475:215–44.
71. Lowe BM, Skylaris CK, Green NG. Acid-base dissociation mechanisms and energetics at the silica-water interface: An activationless process. *J Colloid Interface Sci.* 2015;451:231–44.
72. Hassanali A, Prakash MK, Eshet H, Parrinello M. On the recombination of hydronium and hydroxide ions in water. *Proc Natl Acad Sci.* 2011;108(51):20410–5.
73. Theeuwes NE, Solcerová A, Steeneveld GJ. Modeling the influence of open

- water surfaces on the summertime temperature and thermal comfort in the city. *J Geophys Res Atmos.* 2013;118:8881–96.
74. Malmberg CG. Electrical conductivity of dilute solutions of sea water from 5 to 120 degree celcius. *J Res Natl Bur Stand - A Phys Chem.* 1965;69(1):39–43.
75. Rusydi AF. Correlation between conductivity and total dissolved solid in various type of water: A review. *IOP Conf Ser Earth Environ Sci.* 2018;118(1):1–6.
76. Jonsson J, Smedfors K, Nyholm L, Thornell G. Towards Chip-Based Salinity Measurements for Small Submersibles and Biologgers. *Int J Oceanogr.* 2013;2013:1–11.
77. Sharma A, Kundu SS, Tariq H, Kewalramani N, Yadav RK. Impact of total dissolved solids in drinking water on nutrient utilisation and growth performance of Murrah buffalo calves. *Livest Sci.* 2017;198:17–23.
78. Yan N, Marschner P, Cao W, Zuo C, Qin W. Influence of salinity and water content on soil microorganisms. *Int Soil Water Conserv Res.* 2015;3:316–23.
79. Eng MH, Ita MK, Urata KM. Quantitative analysis of chloride in brackish water: An application to the hyperchromic effect of copper (II) ion with chloride ion. *Anal Sci.* 2005;21:95–9.
80. Alley WM. Desalination of ground water: earth science perspectives. Ground-water resources for the future. Department of the interior U.S. Geological Survey, Denver, CO, USA, USGS Fact Sheet 075-03. 2003 [cited 2018 Jan 2]. 1–4. Available from: <https://pubs.usgs.gov/fs/fs075-03/>
81. Harris RR. Aspects of sodium regulation in a brackish-water and a marine species of the isopod genus *Sphaeroma*. *Mar Biol.* 1972;12(1):18–27.
82. Srimuk P, Lee J, Fleischmann S, Choudhury S, Jäckel N, Zeiger M, et al. Faradaic deionization of brackish and sea water via pseudocapacitive cation and anion intercalation into few-layered molybdenum disulfide. *J Mater Chem A.* 2017;5(30):15640–9.
83. Florescu D, Iordache AM, Costinel D, Horj E, Ionete RE, Culea M. Validation

- procedure for assessing the total organic carbon in water samples. *Rom J Phys.* 2013;58(1–2):211–9.
84. Ndiweni SN, Chys M, Chaukura N, Van Hulle SWH, Nkambule TTI. Assessing the impact of environmental activities on natural organic matter in South Africa and Belgium. *Environ Technol.* 2019;13(40):1756–68.
85. Doull J, Andelman J, Characklis W, Christman R, Cohen S, Engelbrecht R, et al. *Drinking Water and Health*. Vol. 4, National Academies Press. Washington D.C: National Academy Press; 1982. 1–312.
86. Krupadam RJ, Khan MS, Wate SR. Removal of probable human carcinogenic polycyclic aromatic hydrocarbons from contaminated water using molecularly imprinted polymer. *Water Res.* 2010;44(3):681–8.
87. Keith L, Telliard W. ES&T special report: Priority pollutants: I-a perspective view. *Environ Sci Technol.* 1979;13(4):416–23.
88. WHO. Polycyclic Aromatic Hydrocarbons in Drinking-Water; Background Document for Development of WHO Guidelines for Drinking-Water Quality. Vol. 2, Who/Sde/Wsh/03.04/59. Geneva, Switzerland; 2003.
89. Meleiro Porto AL, Zelayarán Melgar G, Consiglio Kasemodel M, Nitschke M. Biodegradation of Pesticides. In: *Pesticides in the Modern World - Pesticides Use and Management*. Brazil: INTECH; 2010. 407–39.
90. Mangat SS, Elefsiniotis P. Biodegradation of the herbicide 2,4-dichlorophenoxyacetic acid (2,4-d) in sequencing batch reactors. *Water Res.* 1999;33(3):861–7.
91. Blue drop statistics in Vhembe District Municipality. Vhembe District Municipality. 2010 [cited 2016 Jun 10]. Available from: [http://www.ewisa.co.za/ewisawaterworks/misc/municipalcontacts/defaultLIM\\_Vembe.htm](http://www.ewisa.co.za/ewisawaterworks/misc/municipalcontacts/defaultLIM_Vembe.htm)
92. Gilron J, Song L, Sirkar KK. Design for cascade of crossflow direct contact membrane distillation. *Ind Eng Chem Res.* 2007;46:2324–34.
93. Thomas N, Mavukkandy MO, Loutatidou S, Arafat HA. Membrane distillation research & implementation: Lessons from the past five decades. *Sep Purif*

- Technol. 2017;189:108–27.
94. Wang Z, Hou D, Lin S. Composite membrane with underwater-oleophobic surface for anti- oil-fouling membrane distillation. *Environ Sci Technol.* 2016;50:3866–74.
  95. Bonyadi S, Chung TS. Flux enhancement in membrane distillation by fabrication of dual layer hydrophilic-hydrophobic hollow fiber membranes. *J Memb Sci.* 2007;306:134–46.
  96. Aydiner C, Imer DYK, Oncel S, Dogan EC, Narci AO, Cakmak S, et al. Marmara seawater Desalination by Membrane Distillation: Direct Consumption Assessment of produced drinking water. In: *Desalination.* London: INTECH; 2017. 2–29.
  97. Mohammadi T, Bakhteyari O. Concentration of l-lysine monohydrochloride (l-lysine-HCl) syrup using vacuum membrane distillation. *Desalination.* 2006;200(1–3):591–4.
  98. Drioli E, Ali A, Macedonio F. Membrane distillation: Recent developments and perspectives. *Desalination.* 2015;356:56–84.
  99. Bourouni K, Chaibi MT. Application of geothermal energy for brackish water desalination in the South of Tunisia. In: *Proceedings World Geothermal Congress 2005.* Turkey, 24-29 2005: Antalya; 2005. 1–6.
  100. Khayet M. Membranes and theoretical modeling of membrane distillation: A review. Vol. 164, *Advances in Colloid and Interface Science.* 2011. 56–88.
  101. Lim JW, Lee JM, Yun SM, Park BJ, Lee YS. Hydrophilic modification of polyacrylonitrile membranes by oxyfluorination. *J Ind Eng Chem.* 2009;15(6):876–82.
  102. Liao Y, Wang R, Tian M, Qiu C, Fane AG. Fabrication of polyvinylidene fluoride (PVDF) nanofiber membranes by electro-spinning for direct contact membrane distillation. *J Memb Sci.* 2013;425–426:30–9.
  103. Wu X, Zhao B, Wang L, Zhang Z, Li J, He X, et al. Superhydrophobic PVDF membrane induced by hydrophobic SiO<sub>2</sub> nanoparticles and its use for CO<sub>2</sub> absorption. *Sep Purif Technol.* 2018;190:108–16.

104. Zhang J, Song Z, Li B, Wang Q, Wang S. Fabrication and characterization of superhydrophobic poly (vinylidene fluoride) membrane for direct contact membrane distillation. *Desalination*. 2013;324:1–9.
105. Ebewele RO. *Polymer Science and Technology*. Chapman & Hall/CRC Press LLC, U.S.A., pp 295-315, 2000;
106. Xiong Z, Lin H, Liu F, Xiao P, Wu Z, Li T, et al. Flexible PVDF membranes with exceptional robust superwetting surface for continuous separation of oil/water emulsions. *Sci Rep*. 2017;7:1–12.
107. Khumalo N, Nthunya L, Derese S, Motsa M, Verliefe A, Kuvarega A, et al. Water recovery from hydrolysed human urine samples via direct contact membrane distillation using PVDF/PTFE membrane. *Sep Purif Technol*. 2019;211:610–7.
108. Khumalo NP, Nthunya LN, De Canck E, Derese S, Verliefe AR, Kuvarega AT, et al. Congo red dye removal by direct membrane distillation using PVDF/PTFE membrane. *Sep Purif Technol*. 2019;211:578–86.
109. Jurczuk K, Galeski A, Mackey M, Hiltner A, Baer E. Orientation of PVDF  $\alpha$  and  $\gamma$  crystals in nanolayered films. *Colloid Polym Sci*. 2015;293:1289–97.
110. Ruan L, Yao X, Chang Y, Zhou L, Qin G, Zhang X. Properties and Applications of the  $\beta$  Phase Poly(vinylidene fluoride). *Polymers*. 2018;10(228):1–27.
111. Wang X, Sun F, Yin G, Wang Y, Liu B, Dong M. Tactile-sensing based on flexible PVDF nanofibers via electrospinning: A review. *Sensors*. 2018;18(2):2–16.
112. Reneker DH, Yarin AL. Electrospinning jets and polymer nanofibers. *Polymer (Guildf)*. 2008;49(10):2387–425.
113. Li M, Katsouras I, Piliago C, Glasser G, Lieberwirth I, Blom PWM, et al. Controlling the microstructure of poly(vinylidene-fluoride) (PVDF) thin films for microelectronics. *J Mater Chem C*. 2013;1(46):7695–702.
114. Bao JJ, Zou BK, Cheng Q, Huang YP, Wu F, Xu GW, et al. Flexible and free-standing LiFePO<sub>4</sub>/TPU/SP cathode membrane prepared via phase

- separation process for lithium ion batteries. *J Memb Sci.* 2017;541:633–40.
115. Tomaszewska M. Preparation and properties of flat-sheet membranes from poly(vinylidene fluoride) for membrane distillation. *Desalination.* 1996;104:1–11.
116. Feng CY, Khulbe KC, Matsuura T, Ismail AF. Recent progresses in polymeric hollow fiber membrane preparation, characterization and applications. *Sep Purif Technol.* 2013;111:43–71.
117. Haase MF, Jeon H, Hough N, Kim JH, Stebe KJ, Lee D. Multifunctional nanocomposite hollow fiber membranes by solvent transfer induced phase separation. *Nat Commun.* 2017;8(1):1–7.
118. Vonch J, Yarin A, Megaridis CM. Electrospinning: A study in the formation of nanofibers. *J Undergrad Res.* 2007;1(1):1–5.
119. Jaworek A. Electro spray droplet sources for thin film deposition. *J Mater Sci.* 2007;42:266–97.
120. Nthunya LN, Masheane ML, Malinga SP, Edward N, Barnard TG, Kao M, et al. Greener approach to prepare electrospun antibacterial cyclodextrin/cellulose acetate nanofibres for removal of bacteria from water. *ACS Sustain Chem Eng.* 2016;5(1):153–60.
121. Fong H, Chun I, Reneker DH. Beaded nanofibers formed during electrospinning. *Polymer.* 1999;40:4585–92.
122. Tijing LD, Chul Y, Shim W, He T, Choi J, Kim S, et al. Superhydrophobic nanofiber membrane containing carbon nanotubes for high-performance direct contact membrane distillation. *J Memb Sci.* 2016;502:158–70.
123. Lee E, Kyoungjin A, Hadi P, Lee S, Chul Y. Advanced multi-nozzle electrospun functionalized titanium dioxide / composite membranes for direct contact membrane distillation. *J Memb Sci.* 2017;524:712–20.
124. Zafar M, Najeeb S, Khurshid Z, Vazirzadeh M, Zohaib S, Najeeb B, et al. Potential of electrospun nanofibers for biomedical and dental applications. *Materials.* 2016;9:1–21.
125. Bhattacharya A, Misra BN. Grafting : a versatile means to modify polymers

- Techniques , factors and applications. *Prog Polym Sci.* 2004;29:767–814.
126. Wu J, Wang N, Zhang HC, Wang L, Dong H, Zhao Y, et al. Acrylic acid grafted porous polycarbonate membrane with smart hydrostatic pressure response to pH. *J Mater Chem A.* 2013;1:4642–6.
127. Korolkov I V., Gorin YG, Yeszhanov AB, Kozlovskiy AL, Zdorovets M V. Preparation of PET track-etched membranes for membrane distillation by photo-induced graft polymerization. *Mater Chem Phys.* 2018;205:55–63.
128. Puppolo MM, Hughey JR, Weber B, Dillon T, Storey D, Cerkez E, et al. Plasma modification of microporous polymer membranes for application in biomimetic dissolution studies. *AAPS Open.* 2017;3(9):1–13.
129. Akhavan B, Jarvis K, Majewski P. Plasma polymer-functionalized silica particles for heavy metals removal. *ACS Appl Mater Interfaces.* 2015;7:4265–74.
130. Song L, Li B, Sirkar KK, Gilron JL. Direct Contact Membrane Distillation-Based Desalination : Novel Membranes , Devices , Larger-Scale Studies , and a Model. *Ind Eng Chem Res.* 2007;46:2307–23.
131. Song L, Ma Z, Liao X, Kosaraju PB, Irish JR, Sirkar KK. Pilot plant studies of novel membranes and devices for direct contact membrane distillation-based desalination. *J Memb Sci.* 2008;323:257–70.
132. Morgan PW. Interfacial Polymerization. In: *Encyclopedia Of Polymer Science and Technology - Wiley Online Library.* New York: John Wiley & Sons, Inc.; 2011. 1–125.
133. Park SJ, Choi W, Nam SE, Hong S, Lee JS, Lee JH. Fabrication of polyamide thin film composite reverse osmosis membranes via support-free interfacial polymerization. *J Memb Sci.* 2017;526:52–9.
134. Gohil JM, Ray P. A review on semi-aromatic polyamide TFC membranes prepared by interfacial polymerization: Potential for water treatment and desalination. *Sep Purif Technol.* 2017;181:159–82.
135. Petersen RJ. Composite reverse osmosis and nanofiltration membranes. *J Memb Sci.* 1993;83(1):81–150.

136. Yimsiri P, MacKley MR. Spin and dip coating of light-emitting polymer solutions: Matching experiment with modelling. *Chem Eng Sci.* 2006;61(11):3496–505.
137. Chen S, Lu X, Hu Y, Lu Q. Biomimetic honeycomb-patterned surface as the tunable cell adhesion scaffold. *Biomater Sci.* 2015;3:85–93.
138. Zuo G, Wang R. Novel membrane surface modification to enhance anti-oil fouling property for membrane distillation application. *J Memb Sci.* 2013;447:26–35.
139. García JV, Dow N, Milne N, Zhang J, Naidoo L, Gray S, et al. Membrane distillation trial on textile wastewater containing surfactants using hydrophobic and hydrophilic-coated polytetrafluoroethylene (PTFE) membranes. *Membranes (Basel).* 2018;8:1–15.
140. Krajewski SR, Kujawski W, Bukowska M, Picard C, Larbot A. Application of fluoroalkylsilanes (FAS) grafted ceramic membranes in membrane distillation process of NaCl solutions. *J Memb Sci.* 2006;281:253–9.
141. Zhang Y, Wang X, Cui Z, Drioli E, Wang Z. Enhancing wetting resistance of poly (vinylidene fluoride) membranes for vacuum membrane distillation. *Desalination.* 2017;415:58–66.
142. Sun J, Hu C, Zhao K, Li M, Qu J, Liu H. Enhanced membrane fouling mitigation by modulating cake layer porosity and hydrophilicity in an electro-coagulation/oxidation membrane reactor (ECOMR). *J Memb Sci.* 2018;550:72–9.
143. Soyekwo F, Zhang Q, Gao R, Qu Y, Lin C, Huang X, et al. Cellulose nanofiber intermediary to fabricate highly-permeable ultrathin nano filtration membranes for fast water purification. *J Memb Sci.* 2017;524:174–85.
144. Buzea C, Blandino IIP, Robbie K. Nanomaterials and Nanoparticles: Sources and Toxicity. *Biointerphases.* 2007;2(4):1–103.
145. Li WR, Xie XB, Shi QS, Zeng HY, Ou-Yang YS, Chen Y Ben. Antibacterial activity and mechanism of silver nanoparticles on *Escherichia coli*. *Appl Microbiol Biotechnol.* 2010;85(4):1115–22.

146. Schreurs WJA, Hosenberg H. Effect of silver ions on transport and retention of phosphate by *Escherichia coli*. *J Bacteriol.* 1982;152:7–13.
147. Prabhu S, Poulouse EK. Silver nanoparticles: mechanism of antimicrobial action, synthesis, medical applications, and toxicity effects. *Int Nano Lett.* 2012;2:1–10.
148. Son WK, Youk JH, Park WH. Antimicrobial cellulose acetate nanofibers containing silver nanoparticles. *Carbohydr Polym.* 2006;65(4):430–4.
149. Huang L, Zhao S, Wang Z, Wu J, Wang J, Wang S. In situ immobilization of silver nanoparticles for improving permeability, antifouling and anti-bacterial properties of ultrafiltration membrane. *J Memb Sci.* 2016;499:269–81.
150. Dong C, Wang Z, Wu J, Wang Y, Wang J, Wang S. A green strategy to immobilize silver nanoparticles onto reverse osmosis membrane for enhanced anti-biofouling property. *Desalination.* 2017;401:32–41.
151. Ahmad NA, Leo CP, Ahmad AL, Ramli WKW. Membranes with great hydrophobicity: A review on preparation and characterization. *Sep Purif Rev.* 2015;44(2):109–34.
152. Phattaranawik J, Fane AG, Pasquier ACS, Bing W. A novel membrane bioreactor based on membrane distillation. *Desalination.* 2008;223:386–95.
153. Frock AD, Kelly RM. Extreme thermophiles: Moving beyond single-enzyme biocatalysis. *Curr Opin Chem Eng.* 2012;1:363–72.
154. Hao YQ, Wang YF, Weng YX. Particle-size-dependent hydrophilicity of TiO<sub>2</sub> nanoparticles characterized by marcus reorganization energy of interfacial charge recombination. *J Phys Chem C.* 2008;112(24):8995–9000.
155. Koparde VN, Cummings PT. Molecular dynamics study of water adsorption on TiO<sub>2</sub> nanoparticles. *J Phys Chem C.* 2007;111:6920–6.
156. Wang Y, Lieberman M. Growth of ultrasooth octadecyltrichlorosilane self-assembled monolayers on SiO<sub>2</sub>. *Langmuir.* 2003;19(4):1159–67.
157. Iwasa J, Kumazawa K, Aoyama K, Suzuki H, Norimoto S, Shimoaka T, et al. In situ observation of a self-assembled monolayer formation of octadecyltrimethoxysilane on a silicon oxide surface using a high-speed

- atomic force microscope. *J Phys Chem C*. 2016;120:2807–13.
158. Koga Y, Westh P, Nishikawa K, Subramanian S. Is a methyl group always hydrophobic? Hydrophilicity of trimethylamine-N-oxide, tetramethyl urea and tetramethylammonium Ion. *J Phys Chem B*. 2011;115:2995–3002.
159. Menger FM, Chlebowski ME. Is the ether group hydrophilic or hydrophobic? *Langmuir*. 2005;21:2689–95.
160. Escorihuela J, Pujari SP, Zuilhof H. Organic monolayers by B(C<sub>6</sub>F<sub>5</sub>)<sub>3</sub>-catalyzed siloxanation of oxidized silicon surfaces. *Langmuir*. 2017;33:2185–93.
161. Sugimura H, Saito N, Ishida Y, Ikeda I, Hayashi K, Takai O. Photochemical reaction of organosilane self-assembled monolayer as studied by scanning probe microscopy. *J Vac Sci Technol A Vacuum, Surfaces, Film*. 2004;22:1428–32.
162. Kumar V, Puri P, Nain S, Bhat KN, Sharma NN. Self assembled monolayers of octadecyltrichlorosilane for dielectric materials. In: *AIP Conference Proceedings*. 2016. 2–7.
163. Eykens L, De Sitter K, Dotremont C, Pinoy L, Van der Bruggen B. Membrane synthesis for membrane distillation: A review. *Sep Purif Technol*. 2017;182:36–51.
164. Alkhudhiri A, Darwish N, Hilal N. Membrane distillation: A comprehensive review. *Desalination*. 2012;287:2–18.
165. Zhang M, Feng S, Wang L, Zheng Y. Lotus effect in wetting and self-cleaning. *Biotribology*. 2016;5:31–43.
166. Gould P. Smart, clean surfaces. *Mater Today*. 2003;6:44–8.
167. Latthe SS, Terashima C, Nakata K, Fujishima A. Superhydrophobic surfaces developed by mimicking hierarchical surface morphology of lotus leaf. *Molecules*. 2014;19(4):4256–83.
168. Samaha MA, Tafreshi HV, Gad-el-Hak M. Superhydrophobic surfaces: From the lotus leaf to the submarine. Vol. 340, *Comptes Rendus - Mecanique*. 2012. 18–34.

169. Rezaei M, Samhaber W. Wetting behaviour of superhydrophobic membranes coated with nanoparticles in membrane distillation. *Chem Eng Trans.* 2016;47:373–8.
170. Mahdi S, Shahabadi S, Rabiee H, Mojtaba S, Mokhtare A, Brant JA. Superhydrophobic dual layer functionalized titanium dioxide/polyvinylidene fluoride-co-hexafluoropropylene (TiO<sub>2</sub>/PH) nano fibrous membrane for high flux membrane distillation. 2017;537(December 2016):140–50.
171. Moradi R, Karimi-Sabet J, Shariaty-Niassar M, Koochaki MA. Preparation and characterization of polyvinylidene fluoride/graphene superhydrophobic fibrous films. *Polymers.* 2015;7:1444–63.
172. Aihara J ichi, Yamabe T, Hosoya H. Aromatic character of graphite and carbon nanotubes. *Synth Met.* 1994;64:309–13.
173. Schravendijk P, van der Vegt NFA. From hydrophobic to hydrophilic solvation: An application to hydration of benzene. *J Chem Theory Comput.* 2005;1:643–52.
174. Vatanpour V, Ghadimi A, Karimi A, Khataee A, Yekavalangi ME. Antifouling polyvinylidene fluoride ultrafiltration membrane fabricated from embedding polypyrrole coated multiwalled carbon nanotubes. *Mater Sci Eng C.* 2018;89:41–51.
175. Safarpour M, Khataee A, Vatanpour V. Preparation of a novel polyvinylidene fluoride (PVDF) ultrafiltration membrane modified with reduced graphene oxide / titanium dioxide (TiO<sub>2</sub>) nanocomposite with enhanced hydrophilicity and antifouling properties. *Ind Eng Chem Res.* 2014;53:13370–82.
176. Jiricek T, Komárek M, Chaloupek J, Lederer T. Flux Enhancement in Membrane Distillation Using Nanofiber Membranes. *J Nanomater.* 2016;2016:1–7.
177. Fang J, Wang H, Wang X, Lin T. Superhydrophobic nanofibre membranes: Effects of particulate coating on hydrophobicity and surface properties. *J Text Inst.* 2012;103:937–44.
178. Huang Y, Wang Z, Hou D, Lin S. Coaxially electrospun super-amphiphobic

- silica-based membrane for anti- surfactant-wetting membrane distillation. *J Memb Sci.* 2017;531:122–8.
179. Liao Y, Loh C, Wang R, Fane AG. Electrospun Superhydrophobic Membranes with Unique Structures for Membrane Distillation. *ACS Appl Mater Interfaces.* 2014;6:16035–16048.
180. Attia H, Alexander S, Wright CJ, Hilal N. Superhydrophobic electrospun membrane for heavy metals removal by air gap membrane distillation (AGMD). *Desalination.* 2017;420:318–29.
181. Hou D, Lin D, Ding C, Wang D, Wang J. Fabrication and characterization of electrospun superhydrophobic PVDF- HFP / SiNPs hybrid membrane for membrane distillation. *Sep Purif Technol.* 2017;189:82–9.
182. Prince JA, Singh G, Rana D, Matsuura T, Anbharasi V, Shanmugasundaram TS. Preparation and characterization of highly hydrophobic poly (vinylidene fluoride) – Clay nanocomposite nanofiber membranes (PVDF – clay NNMs) for desalination using direct contact membrane distillation. *J Memb Sci.* 2012;397–398:80–6.
183. Huang Y, Wang Z, Jin J, Lin S. Novel Janus Membrane for Membrane Distillation with Simultaneous Fouling and Wetting Resistance. *Environ Sci Technol.* 2017;51:13304–10.
184. Lee E, Kyoungjin A, He T, Chul Y, Kyong H. Electrospun nano fiber membranes incorporating fluorosilane-coated TiO<sub>2</sub> nanocomposite for direct contact membrane distillation. 2016;520:145–54.
185. Chul Y, Tijing LD, Shim W, Choi J, Kim S, He T, et al. Water desalination using graphene-enhanced electrospun nano fiber membrane via air gap membrane distillation. *J Memb Sci.* 2016;520:99–110.
186. Efome JE, Rana D, Matsuura T, Lan CQ. Enhanced performance of PVDF nanocomposite membrane by nano fiber coating: A membrane for sustainable desalination through. *Water Res.* 2016;89:39–49.
187. Zolotarev PP, Ugrozov VV, Volkina IB, Nikulin VM. Treatment of waste water for removing heavy metals by membrane distillation. *J Hazard Mater.*

- 1994;37(1):77–82.
188. Criscuoli A, Zhong J, Figoli A, Carnevale MC, Huang R, Drioli E. Treatment of dye solutions by vacuum membrane distillation. *Water Res.* 2008;42:5031–7.
189. Ding Z, Liu L, Liu Z, Ma R. The use of intermittent gas bubbling to control membrane fouling in concentrating TCM extract by membrane distillation. *J Memb Sci.* 2011;372(1–2):172–81.
190. Alkhudhiri A, Darwish N, Hilal N. Treatment of saline solutions using Air Gap Membrane Distillation: Experimental study. *Desalination.* 2013;323:2–7.
191. Tomaszewska M. Membrane distillation-examples of applications in technology and environmental protection. *Polish J Environ Stud.* 2000;9(1):27–36.
192. Ashoor BB, Mansour S, Giwa A, Dufour V, Hasan SW. Principles and applications of direct contact membrane distillation (DCMD): A comprehensive review. *Desalination.* 2016;398:222–46.
193. Lee H, He F, Song L, Gilron J, Sirkar KK. Desalination with a cascade of Ccross-flow hollow fiber Membrane Distillation devices integrated with a heat exchanger. 2011;57(7).
194. Alsaadi AS, Ghaffour N, Li JD, Gray S, Francis L, Maab H, et al. Modeling of air-gap membrane distillation process: A theoretical and experimental study. *J Memb Sci.* 2013;445:53–65.
195. Bajáková J, Chaloupek J, Lukáš D, Lacarin M. “Drawing” - Drawing’ - the production of individual nanofibers by experimental method. *Int Conf Nanomater - Res Appl.* 2011;9:21–3.
196. Onsekizoglu P. Membrane distillation: Principle, advances, limitations and future prospects in food industry. In: *Distillation - Advances from Modeling to Applications.* London: INTECH; 2012. 233–67.
197. Boukhriss M, Zhani K, Bacha H Ben. State Of The Art of Various Configurations of the Membrane Distillation Unit for Distilling The Seawater. *Int J Emerg Technol Adv Eng.* 2014;4(5):340–57.

198. Khaled F, Chaouachi B, Hidouri K. Study of vacuum membrane distillation coupled with solar energy. In: International Conference on Green Energy and Conversion Systems, GECS 2017. 2017. 1–5.
199. Mericq J, Laborie S, Cabassud C. Evaluation of systems coupling vacuum membrane distillation and solar energy for seawater desalination. *Chem Eng J*. 2011;166(2):596–606.
200. Boubakri A, Hafiane A, Bouguecha SAT. Direct contact membrane distillation: Capability to desalt raw water. *Arab J Chem*. 2017;10:S3475–81.
201. Rochd S, Zerradi H, Mizani S, Dezairi A, Ouaskit S. Modélisation of Membrane Distillation: Mass and Heat Transfer in Air Gap Membrane Distillation. *J Membr Sci Technol*. 2016;6(2):1–9.
202. Salehi MA, Rostamani R. Review of membrane distillation for the production of fresh water from saline water. *J Nov Appl Sci*. 2013;2:1072–5.
203. Drioli E, Criscuoli A, Molero LP. Membrane Distillation. *Water Wastewater Treat Technol*. 2009;3:1–14.
204. Boonyaroj V, Chiemchaisri C, Chiemchaisri W, Theepharaksapan S. Toxic organic micro-pollutants removal mechanisms in long-term operated membrane bioreactor treating municipal solid waste leachate. *Bioresour Technol*. 2012;113:174–80.
205. Sivakumar M, Ramezani-pour M. Mine Water Treatment Using a Vacuum Membrane Distillation System. *APCBEE Procedia*. 2013;5:157–62.
206. Moradi R, Monfared SM, Amini Y, Dastbaz A. Vacuum enhanced membrane distillation for trace contaminant removal of heavy metals from water by electrospun PVDF/TiO<sub>2</sub> hybrid membranes. *Korean J Chem Eng*. 2016;33(7):2160–8.
207. Otitoju TA, Ahmad AL, Ooi BS. Polyvinylidene fluoride ( PVDF ) membrane for oil rejection from oily wastewater: A performance review. *J Water Process Eng*. 2016;14:41–59.
208. Chiam C, Sarbatly R. Vacuum membrane distillation processes for aqueous solution treatment — A review. *Chem Eng Process Process Intensif*.

- 2013;74:27–54.
209. Macedonio F, Ali A, Poerio T, El-Sayed E, Drioli E, Abdel-Jawad M. Direct contact membrane distillation for treatment of oilfield produced water. *Sep Purif Technol.* 2014;126:69–81.
210. Shaulsky E, Nejati S, Boo C, Perreault F. Post-fabrication modification of electrospun nanofiber mats with polymer coating for membrane distillation applications. *J Memb Sci.* 2017;530:158–65.
211. Mokhtar NM, Lau WJ, Ismail AF, Veerasamy D. Membrane distillation technology for treatment of wastewater from rubber industry in Malaysia. *Procedia CIRP.* 2015;26:792–6.
212. Zuo J, Bonyadi S, Chung T. Exploring the potential of commercial polyethylene membranes for desalination by membrane distillation. *J Memb Sci.* 2016;497:239–47.
213. Wang J, Sun X, Yuan Y, Chen H, Wang H, Hou D. A novel microwave assisted photo-catalytic membrane distillation process for treating the organic wastewater containing inorganic ions. *J Water Process Eng.* 2016;9:1–8.
214. Tijing LD, Woo YC, Johir MAH, Choi JS, Shon HK. A novel dual-layer bicomponent electrospun nanofibrous membrane for desalination by direct contact membrane distillation. *Chem Eng J.* 2014;256:155–9.
215. Ji Z. Treatment of heavy-metal wastewater by vacuum membrane distillation: effect of wastewater properties. In: *IOP Conference Series: Earth and Environmental Science PAPER.* IOP Publishing; 2017. 2–6.
216. Ke H, Feldman E, Guzman P, Cole J, Wei Q, Chu B, et al. Electrospun polystyrene nano fibrous membranes for direct contact membrane distillation. *J Memb Sci.* 2016;515:86–97.
217. Asif MB, Hai FI, Kang J, Merwe JP Van De, Leusch FDL, Yamamoto K, et al. Degradation of Trace Organic Contaminants by a Membrane Distillation — Enzymatic Bioreactor. *Appl Sci.* 2017;7:1–15.
218. Shi X, Zhou W, Ma D, Ma Q, Bridges D, Ma Y, et al. Electrospinning of

- Nanofibers and Their Applications for Energy Devices. *J Nanomater.* 2015;2015:1–20.
219. Nayak R, Padhye R, Kyratzis IL, Truong YB, Arnold L. Recent advances in nanofibre fabrication techniques. *Text Res J.* 2012;82(2):129–47.
220. Zafar M, Najeeb S, Khurshid Z, Vazirzadeh M, Zohaib S, Najeeb B, et al. Potential of electrospun nanofibers for biomedical and dental applications. *Materials (Basel).* 2016;9(2):1–21.
221. Kenry, Lim CT. Nanofiber technology: current status and emerging developments. *Prog Polym Sci.* 2017;70:1–17.
222. Brinkmann T, Pohlmann J, Withalm U, Wind J, Wolff T. Theoretical and experimental investigations of flat sheet membrane module types for high capacity gas separation applications. *Chemie-Ingenieur-Technik.* 2013;85(8):1210–20.
223. Faria LFF, Di Luccio M, Nobrega R, Borges CP. Development and characterization of microfiltration hollow-fiber modules for sterilization of fermentation media. *Brazilian J Chem Eng.* 2002;19(2):141–50.
224. Krzeminski P, Antonio J, Nieuwenhuijzen AF Van. Flat sheet or hollow fibre — comparison of full-scale membrane bio-reactor configurations. *Desalin Water Treat.* 2012;42:100–6.
225. Bergdahl ME, Bergdahl LA. A comparison of flat-sheet and hollow-fiber membrane oxygenators. *Texas Hear Inst J.* 1989;16(1):27–31.
226. Geng X, Kwon O-H, Jang J. Electrospinning of chitosan dissolved in concentrated acetic acid solution. *Biomaterials.* 2005 Sep;26(27):5427–32.
227. Martinová L, Lubasová D. Electrospun Chitosan Based Nanofibers. 2008;12(2).
228. Mpenyana-monyatsi L, Onyango MS, Momba MNB. Groundwater quality in a South African rural community: A possible threat to public health. *Polish J Environ Stud.* 2012;21(5):1349–58.
229. Irr A, Irr A. CAplus Core Journal Coverage CAplus Core Journal Coverage List CAplus Core Journal Coverage. 2014;1–59.

230. Subramani A, Jacangelo JG. Emerging desalination technologies for water treatment: A critical review. *Water Res.* 2015;75:164–87.
231. Hrnčič MK, Cör D, Verboten MT, Knez Ž. Application of supercritical and subcritical fluids in food processing. *Food Qual Saf.* 2018;2(2):59–67.
232. He Q, Tu T, Yan S, Yang X, Duke M, Zhang Y, et al. Relating water vapor transfer to ammonia recovery from biogas slurry by vacuum membrane distillation. *Sep Purif Technol.* 2018;191:182–91.
233. Li Z, Ren X, Zuo J, Liu Y, Duan E, Yang J, et al. Struvite precipitation for ammonia nitrogen removal in 7-aminocephalosporanic acid wastewater. *Molecules.* 2012;17:2126–39.
234. Khayet M, Velázquez A, Mengual JI. Direct contact membrane distillation of humic acid solutions. *J Memb Sci.* 2004;240(1–2):123–8.
235. Chen TH, Huang YH. Dehydration of diethylene glycol using a vacuum membrane distillation process. *J Taiwan Inst Chem Eng.* 2017;74:233–7.
236. Carnevale MC, Gnisci E, Hilal J, Criscuoli A. Direct Contact and Vacuum Membrane Distillation application for the olive mill wastewater treatment. *Sep Purif Technol.* 2016;169:121–7.
237. Tu KL, Nghiem LD, Chivas AR. Coupling effects of feed solution pH and ionic strength on the rejection of boron by NF/RO membranes. *Chem Eng J.* 2011;168(2):700–6.
238. Hu J, Pu Y, Ueda M, Zhang X, Wang L. Charge-aggregate induced (CAI) reverse osmosis membrane for seawater desalination and boron removal. *J Memb Sci.* 2016;520:1–7.
239. Güler E, Kaya C, Kabay N, Arda M. Boron removal from seawater: State-of-the-art review. *Desalination.* 2015;356:85–93.
240. Criscuoli A, Rossi E, Cofone F, Drioli E. Erratum to Boron removal by membrane contactors: The water that purifies water (*Clean Techn Environ Policy*, 10.1007/s10098-009-0221-8). *Clean Technol Environ Policy.* 2010;12(1):63–63.
241. Wang P, Chung TS. Recent advances in membrane distillation processes:

- Membrane development, configuration design and application exploring. *J Memb Sci*. 2015;474:39–56.
242. He F, Gilron J, Lee H, Song L, Sirkar KK. Potential for scaling by sparingly soluble salts in crossflow DCMD. *J Memb Sci*. 2008;311:68–80.
243. Qin W, Zhang J, Xie Z, Ng D, Ye Y, Gray SR, et al. Synergistic effect of combined colloidal and organic fouling in membrane distillation: Measurements and mechanisms. *Environ Sci Water Res Technol*. 2017;3:119–27.
244. Ali A, Drioli E, Macedonio F. Membrane engineering for sustainable development: A perspective. *Appl Sci*. 2017;7(10):1026.
245. Kesieme UK, Milne N, Aral H, Yong C, Duke M. Economic analysis of desalination technologies in the context of carbon pricing, and opportunities for membrane distillation. *Desalination*. 2013;323:66–74.
246. Banat F, Jwaied N. Economic evaluation of desalination by small-scale autonomous solar-powered membrane distillation units. *Desalination*. 2008;220:566–73.
247. Chang H, Chang C, Hung C, Cheng T, Ho C. Optimization study of small-scale solar membrane distillation desalination systems (s-SMDDS). *Int J Environ Res Public Health*. 2014;11:12064–87.
248. van der Bruggen B. Desalination by distillation and by reverse osmosis — trends towards the future. *Membr Technol*. 2003;2003:6–9.
249. Bouguecha S, Hamrouni B, Dhahbi M. Small scale desalination pilots powered by renewable energy sources: Case studies. *Desalination*. 2005;183(1–3):151–65.
250. Meindersma GW, Guijt CM, de Haan AB. Desalination and water recycling by air gap membrane distillation. *Desalination*. 2006;187:291–301.
251. Pangarkar BL, Deshmukh SK, Guddad M V. Economic assessment of multi-effect membrane distillation (MEMD) for water treatment. *Int J Eng Res Technol*. 2017;10(1):253–7.
252. El-Zanati E, El-Khatib KM. Integrated membrane – based desalination

- system. *Desalination*. 2007;205:15–25.
253. Drioli E, Laganh F, Criscuolo A, Barbieri G. Integrated membrane operations in desalination processes. *Desalination*. 1999;122:141–5.
254. Gazagnes L, Cerneaux S, Persin M, Prouzet E, Larbot A. Desalination of sodium chloride solutions and seawater with hydrophobic ceramic membranes. *Desalination*. 2007;217:260–6.
255. Al-Karaghoul A, Kazmerski LL. Energy consumption and water production cost of conventional and renewable-energy-powered desalination processes. *Renew Sustain Energy Rev*. 2013;24:343–56.
256. Baker JS, Dudley LY. Biofouling in membrane systems - A review. *Desalination*. 1998;118:81–90.
257. Wang J, Qu D, Tie M, Ren H, Peng X, Luan Z. Effect of coagulation pretreatment on membrane distillation process for desalination of recirculating cooling water. *Sep Purif Technol*. 2008;64:108–15.
258. Wang J, Kim SC, Pui DYH. Investigation of the figure of merit for filters with a single nanofiber layer on a substrate. Vol. 39, *Journal of Aerosol Science*. 2008. 323–34.
259. Work WJ, Horie K, Hess M, Stepto RFT. Definitions of Terms Related to Polymer Blends, Composites, and Multiphase Polymeric Materials. *Pure Appl Chem*. 2007;76(11):1985–2007.
260. Li Y, Wan W. Exploring polymer nanofiber mechanics. *IEEE Nanotechnol Mag*. 2017;11:16–28.
261. Baturalp Y, Yener F, Cengiz-Callioglu F, Jirsak O. Effect of concentration and salt additive on Taylor cone structure. Brno, Czech Republic, EU. 2012;10:23–5.
262. Wang G, Yu D, Kelkar AD, Zhang L. Progress in Polymer Science Electrospun nanofiber: Emerging reinforcing filler in polymer matrix composite materials. *Prog Polym Sci*. 2017;75:73–107.
263. Nthunya LN, Masheane ML, Malinga SP, Nxumalo EN, Mhlanga SD. Environmentally benign chitosan-based nanofibres for potential use in water

- treatment. *Cogent Chem.* 2017;3(1):1–17.
264. Nthunya LN, Masheane ML, Malinga SP, Barnard TG, Nxumalo EN, Mamba BB, et al. UV-assisted reduction of in situ electrospun antibacterial chitosan-based nanofibres for removal of bacteria from water. *RSC Adv.* 2016;6:95936–43.
265. Nthunya LN, Masheane ML, Malinga SP, Nxumalo EN, Mamba BB, Mhlanga SD. Thermally and mechanically stable cyclodextrin/cellulose acetate nanofibers synthesized using an environmentally benign procedure. *Int J Smart Nano Mater.* 2017;8(1):1–19.
266. Persano L, Camposeo A, Tekmen C, Pisignano D. Industrial upscaling of electrospinning and applications of polymer nanofibers: A review. *Macromol Mater Eng.* 2013;298(5):504–20.
267. Jeong SI, Krebs MD, Bonino C a, Samorezov JE, Khan S a, Alsberg E. Electrospun chitosan-alginate nanofibers with in situ polyelectrolyte complexation for use as tissue engineering scaffolds. *Tissue Eng Part A.* 2011;17:59–70.
268. Zhijiang C, Xianyou S, Qing Z, Yuanpei L. Amidoxime surface modification of polyindole nanofiber membrane for effective removal of Cr ( VI ) from aqueous solution. *J Mater Sci.* 2017;52(9):5417–34.
269. Hardick O, Stevens B, Bracewell GD. Nanofiber fabrication in a temperature and humidity controlled environment for improved fibre consistency. In: *Nature Precedings.* 2010. 1–11.
270. Toskas G, Cherif C, Hund RD, Laourine E, Mahltig B, Fahmi A, et al. Chitosan(PEO)/silica hybrid nanofibers as a potential biomaterial for bone regeneration. *Carbohydr Polym.* 2013;94(2):713–22.
271. Huang Z, Zhang Y, Kotaki M, Ramakrishna S. A review on polymer nanofibers by electrospinning and their applications in nanocomposites. *Compos Sci Technol.* 2003;63:2223–53.
272. Balamurugan R, Sundarrajan S, Ramakrishna S. Recent Trends in Nanofibrous Membranes and Their Suitability for Air and Water Filtrations.

- Membranes (Basel). 2011;1:232–48.
273. Agarwal S, Wendorff JH, Greiner A. Use of electrospinning technique for biomedical applications. *Polymer (Guildf)*. 2008;49:5603–21.
274. Rogina A. Electrospinning process: Versatile preparation method for biodegradable and natural polymers and biocomposite systems applied in tissue engineering and drug delivery. *Appl Surf Sci*. 2014;296:221–30.
275. Ahmed FE, Lalia BS, Hashaikh R. A review on electrospinning for membrane fabrication: Challenges and applications. *Desalination*. 2015;356:15–30.
276. Haider A, Haider S, Kang IK. A comprehensive review summarizing the effect of electrospinning parameters and potential applications of nanofibers in biomedical and biotechnology. *Arab J Chem*. 2015;
277. Ma Z, Kotaki M, Ramakrishna S. Electrospun cellulose nanofiber as affinity membrane. *J Memb Sci*. 2005;265(1–2):115–23.
278. Chan CK, Liao S, Li B, Lareu RR, Larrick JW, Ramakrishna S, et al. Early adhesive behavior of bone-marrow-derived mesenchymal stem cells on collagen electrospun fibers. *Biomed Mater*. 2009;4:1–10.
279. Morrison RW. Overview of current collective protection filtration technology. In: 2002 NBC Defense Collective Protection Conference. USA: U.S. Army Soldier and Biological Chemical Command; 2003. 1–9.
280. Kyoungjin A, Guo J, Lee E, Jeong S, Zhao Y, Wang Z, et al. PDMS / PVDF hybrid electrospun membrane with superhydrophobic property and drop impact dynamics for dyeing wastewater treatment using membrane distillation. *J Memb Sci*. 2017;525:57–67.
281. Chakraborty A, Deva D, Sharma A, Verma N. Adsorbents based on carbon microfibers and carbon nanofibers for the removal of phenol and lead from water. *J Colloid Interface Sci*. 2011;359(1):228–39.
282. Tao X, Zhou G, Zhuang X, Cheng B, Li X, Li H. Solution blowing of activated carbon nanofibers for phenol adsorption. *RSC Adv*. 2015;5(8):5801–8.
283. Nthunya LN, Masheane ML, Malinga SP, Nxumalo EN, Mhlanga SD.

- Electrospun chitosan-based nanofibres for removal of phenols from drinking water. *Water SA*. 2018;44(3):377–86.
284. Horzum N, Shahwan T, Parlak O, Demir MM. Synthesis of amidoximated polyacrylonitrile fibers and its application for sorption of aqueous uranyl ions under continuous flow. *Chem Eng J*. 2012;213:41–9.
285. Rad LR, Momeni A, Ghazani BF, Irani M, Mahmoudi M, Noghreh B. Removal of Ni<sup>2+</sup> and Cd<sup>2+</sup> ions from aqueous solutions using electrospun PVA/zeolite nanofibrous adsorbent. *Chem Eng J*. 2014;256:119–27.
286. Qi FF, Cao Y, Wang M, Rong F, Xu Q. Nylon 6 electrospun nanofibers mat as effective sorbent for the removal of estrogens: Kinetic and thermodynamic studies. *Nanoscale Res Lett*. 2014;9(1):1–10.
287. Habiba U, Siddique TA, Talebian S, Lee JLL, Salleh A, Ang BC, et al. Effect of deacetylation on property of electrospun chitosan/PVA nanofibrous membrane and removal of methyl orange, Fe(III) and Cr(VI) ions. *Carbohydr Polym*. 2017;177:32–9.
288. Akduman C, Akçakoca Kumbasar EP, Morsunbul S. Electrospun nanofiber membranes for adsorption of dye molecules from textile wastewater. In: *IOP Conference Series: Materials Science and Engineering*. Greece: IOP Publishing Ltd; 2017. 1–7.
289. Wen B, Shan XQ. Improved immobilization of 8-hydroxyquinoline on polyacrylonitrile fiber and application of the material to the determination of trace metals in seawater by inductively coupled plasma mass spectrometry. *Anal Bioanal Chem*. 2002;374:948–54.
290. Aliabadi M, Irani M, Ismaeili J, Piri H, Parnian MJ. Electrospun nanofiber membrane of PEO/Chitosan for the adsorption of nickel, cadmium, lead and copper ions from aqueous solution. *Chem Eng J*. 2013;220:237–43.
291. Saeed K, Haider S, Oh TJ, Park SY. Preparation of amidoxime-modified polyacrylonitrile (PAN-oxime) nanofibers and their applications to metal ions adsorption. *J Memb Sci*. 2008;322:400–5.
292. Zhengyang L, Tingting L, Libao A, Pengfei F, Cangjian G, Zhiming Z. Highly

- efficient chromium(VI) adsorption with nanofibrous filter paper prepared through electrospinning chitosan/polymethylmethacrylate composite. *Carbohydr Polym.* 2016;137:119–26.
293. Razzaz A, Ghorban S, Hosayni L, Irani M, Aliabadi M. Chitosan nanofibers functionalized by TiO<sub>2</sub> nanoparticles for the removal of heavy metal ions. *J Taiwan Inst Chem Eng.* 2016;58:333–43.
294. Habiba U, Siddique TA, Li Lee JJ, Joo TC, Ang BC, Afifi AM. Adsorption study of methyl orange by chitosan/polyvinyl alcohol/zeolite electrospun composite nanofibrous membrane. *Carbohydr Polym.* 2018;191:79–85.
295. Nthunya LN, Masheane ML, Malinga SP, Nxumalo EN, Mhlanga SD. Electrospun chitosan based nanofibres for removal of phenols from drinking water. *Water SA.* 2018;44(3):377–86.
296. Greiner A, Wendorff JH, von Gunten U. Functional Self-Assembled Nanofibers by Electrospinning. In: *Advances in Polymer Science.* Berlin, Germany: Springer; 2008. 107–71.
297. Théry M, Pépin A, Dressaire E, Chen Y, Bornens M. Cell distribution of stress fibres in response to the geometry of the adhesive environment. *Cell Motil Cytoskeleton.* 2006;63:341–55.
298. Dasgupta S, Hammond WB, Goddard WA. Crystal structures and properties of nylon polymers from theory. *J Am Chem Soc.* 1996;118:12291–301.
299. Essalhi M, Khayet M. Self-sustained webs of polyvinylidene fluoride electrospun nanofibers at different electrospinning times: 1. Desalination by direct contact membrane distillation. *J Memb Sci.* 2013;433:167–79.
300. Feng C, Khulbe KC, Matsuura T, Tabe S, Ismail AF. Preparation and characterization of electro-spun nanofiber membranes and their possible applications in water treatment. *Sep Purif Technol.* 2013;102:118–35.
301. Nthunya LN, Masheane ML, Malinga SP, Nxumalo EN, Barnard TG, Kao M, et al. Greener Approach to Prepare Electrospun Antibacterial  $\beta$ -Cyclodextrin/Cellulose Acetate Nanofibers for Removal of Bacteria from Water. *ACS Sustain Chem Eng.* 2017;5(1):153–60.

302. Chaúque EFC, Dlamini LN, Adelodun A, Greyling C, Ngila JC. Modification of electrospun polyacrylonitrile nanofibers with EDTA for the removal of Cd and Cr ions from water effluents. *Appl Surf Sci.* 2016;369:19–28.
303. Zhao W, Liu B, Chen J. Preparation of amino-modified PAN fibers with triethylenetetramine as aminating reagents and their application in CO<sub>2</sub> adsorption. *J Nanomater.* 2014;2014:1–7.
304. Abu-Saied MA, Abdel-Halim ES, Fouda MMG, Al-Deyab SS. Preparation and characterization of iminated polyacrylonitrile for the removal of methylene blue from aqueous solutions. *Int J Electrochem Sci.* 2013;8:5121–35.
305. Wang M, Jiang T, Lu Y, Liu H, Chen Y. Gold nanoparticles immobilized in hyperbranched polyethylenimine modified polyacrylonitrile fiber as for the reduction of 4-nitrophenol. *J Mater Chem A.* 2013;1(19):5923–33.
306. Wang M-L, Jiang T-T, Lu Y, Liu H-J, Chen Y. Gold nanoparticles immobilized in hyperbranched polyethylenimine modified polyacrylonitrile fiber as highly efficient and recyclable heterogeneous catalysts for the reduction of 4-nitrophenol. *J Mater Chem A.* 2013;1(19):5923–33.
307. Callegari A, Boguniewicz-Zablocka J, Capodaglio A. Experimental application of an advanced separation process for NOM removal from surface drinking water supply. *Separations.* 2017;4:2–15.
308. Zhao R, Wang Y, Li X, Sun B, Wang C. Synthesis of  $\beta$ -cyclodextrin-based electrospun nanofiber membranes for highly efficient adsorption and separation of methylene blue. *ACS Appl Mater Interfaces.* 2015;7(48):26649–57.
309. Nthunya LN, Masheane ML, Malinga SP, Nxumalo EN, Mhlanga SD. Electrospun chitosan-based nanofibres for removal of phenols from drinking water. *Water SA.* 2018;44(3).
310. Adebawale KO, Olu-owolabi BI, Chigbundu EC. Removal of Safranin-O from Aqueous Solution by Adsorption onto Kaolinite Clay. *J Encapsulation Adsorpt Sci.* 2014;4:89–104.

311. Nche NG, Bopda A, Raoul D, Tchuifon T, Ngakou CS, Kuete IT, et al. Removal of Paracetamol from Aqueous Solution by Adsorption onto Activated Carbon Prepared from Rice Husk. *J Chem Pharm Res.* 2017;9(3):56–68.
312. Xin G, Xia Y, Lv Y, Liu L, Yu B. Investigation of mesoporous graphitic carbon nitride as the adsorbent to remove Ni (II) ions. *Water Environ Res.* 2016;88:318–24.
313. Kumar NS, Suguna M, Subbaiah M V, Reddy AS, Kumar NP, Krishnaiah A. Adsorption of Phenolic Compounds from Aqueous Solutions onto Chitosan-Coated Perlite Beads as Biosorbent. *Ind Eng Chem Res.* 2010;49(19):9238–47.
314. Salim MD, Muneke Y. Lead Removal from Aqueous Solution Using Silica Ceramic: Adsorption Kinetics and Equilibrium Studies. *Int J Chem.* 2009;1(1):23–30.
315. Kamel MM, Ibrahim MA, Ismael AM. Adsorption of some heavy metal ions from aqueous solutions by using kaolinite clay. *Assiut Univ Bull Environ Res.* 2004;7(1):101–10.
316. Li J, Meng X, Hu C, Du J. Adsorption of phenol, p -chlorophenol and p -nitrophenol onto functional chitosan. *Bioresour Technol.* 2009;100:1168–73.
317. Moyo M, Mutare E, Chigondo F, Nyamunda BC. Removal of phenol from aqueous solution by adsorption on yeast, *Saccharomyces cerevisiae*. *Int J Res Rev Appl Sci.* 2012;11(3):486–94.
318. Wong YC, Szeto YS, Cheung WH, McKay G. Adsorption of acid dyes on chitosan - Equilibrium isotherm analyses. *Process Biochem.* 2004;39(6):693–702.
319. Xiaohong L, Baowei Z, Kun Z, Xuekui H. Removal of Nitrophenols by Adsorption Using  $\beta$  -Cyclodextrin modified Zeolites. *Chinese J Chem Eng.* 2011;19(6):938–43.
320. Badii K, Ardejani FD, Saberi MA, Limaee NY, Shafaei SZ. Adsorption of Acid blue 25 dye on diatomite in aqueous solutions. *Indian J Chem Technol.*

- 2010;17:7–16.
321. Salim M d, Muneke Y. Lead Removal from Aqueous Solution Using Silica Ceramic: Adsorption Kinetics and Equilibrium Studies. *Int J Chem.* 2009;1(1):23–30.
322. Ho Y, Malarvizhi R, Sulochana N. Equilibrium Isotherm Studies of Methylene Blue Adsorption onto Activated Carbon Prepared from *Delonix regia* Pods. *J Environ Prot Sci.* 2009;3:111–6.
323. Shah I, Adnan R, Ngah WSW, Mohamed N. Iron impregnated activated carbon as an efficient adsorbent for the removal of methylene blue: Regeneration and kinetics studies. *PLoS One.* 2015;10(4):1–23.
324. Abdelwahab O. Adsorption of phenol from aqueous solutions by *Luffa cylindrica* fibers: Kinetics, isotherm and thermodynamic studies. *Egypt J Aquat Res.* 2014;39(4):215–23.
325. Mphahlele K, Onyango MS, Mhlanga SD. Kinetics, equilibrium, and thermodynamics of the sorption of bisphenol A onto N-CNTs-  $\beta$ -cyclodextrin and Fe/N-CNTs-  $\beta$ -cyclodextrin nanocomposites. *J Nanomater.* 2015;2015:1–13.
326. Han L, Xiao T, Tan YZ, Fane AG, Chew JW. Contaminant rejection in the presence of humic acid by membrane distillation for surface water treatment. *J Memb Sci.* 2017;541:291–9.
327. Elimelech M, Phillip WA. The future of seawater desalination: Energy, technology and the environment. *Science (80- ).* 2011;333:712–8.
328. Shariful I, Sharif S Bin, Jia J, Lee L, Habiba U, Ang BC, et al. Adsorption of divalent heavy metal ion by mesoporous-high surface area chitosan / poly ( ethylene oxide ) nanofibrous membrane. *Carbohydr Polym.* 2017;157:57–64.
329. Tian Y, Wu M, Liu R, Li Y, Wang D, Tan J, et al. Electrospun membrane of cellulose acetate for heavy metal ion adsorption in water treatment. *Carbohydr Polym.* 2011;83(2):743–8.
330. Kolbasov A, Sinha-ray S, Yarin AL, Pourdeyhimi B. Heavy metal adsorption

- on solution-blown biopolymer nano fiber membranes. *J Memb Sci.* 2017;530:250–63.
331. Roshanfekar L, Momeni A, Farshi B, Irani M, Mahmoudi M. Removal of Ni<sup>2+</sup> and Cd<sup>2+</sup> ions from aqueous solutions using electrospun PVA / zeolite nanofibrous adsorbent. *Chem Eng J.* 2014;256:119–27.
332. Seraji MM, Soleimankhani S, Abadani HA. Adsorption of Phenol by Super Hydrophobic Phenol- Formaldehyde / Silica Hybrid Aerogel. *J Nanoanalysis.* 2017;4(3):214–22.
333. de Vries CJ, Mokwena LM, Buica A, McKay M. Determination of volatile phenol in Cabernet Sauvignon wines, made from smoke-affected grapes, by using HS-SPME GC-MS. *South African J Enol Vitic.* 2016;37(1):15–22.
334. Wang ML, Jiang TT, Lu Y, Liu HJ, Chen Y. Gold nanoparticles immobilized in hyperbranched polyethylenimine modified polyacrylonitrile fiber as highly efficient and recyclable heterogeneous catalysts for the reduction of 4-nitrophenol. *J Mater Chem A.* 2013;1(19):5923–33.
335. Nthunya LN, Masheane ML, Malinga SP, Nxumalo EN, Mamba BB, Mhlanga SD. Thermally and mechanically stable  $\beta$ -cyclodextrin/cellulose acetate nanofibers synthesized using an environmentally benign procedure. *Int J Smart Nano Mater.* 2017;8(1).
336. Nthunya LN, Derese S, Gutierrez L, Verliefde AR, Mamba BB, Barnard TG, et al. Green synthesis of silver nanoparticles using one-pot and microwave-assisted methods and their subsequent embedment on PVDF nanofibre membranes for growth inhibition of mesophilic and thermophilic bacteria. *New J Chem.* 2019;43:4168–80.
337. Santana CM, Ferrera ZS, Padrón MET, Rodríguez JJS. Methodologies for the extraction of phenolic compounds from environmental samples: New approaches. *Molecules.* 2009;14:298–320.
338. Kayali-Sayadi MN, Rubio-Barroso S, Cuesta-Jimenez MP, Polo-Díez LM. Rapid determination of polycyclic aromatic hydrocarbons in tea infusion samples by high-performance liquid chromatography and fluorimetric detection based on solid-phase extraction. *Analyst.* 1998;123:2145–8.

339. Olujimi OO, Fatoki OS, Odendaal J, Okonkwo OJ. Solid-phase extraction method for the analysis of eleven phenolic pollutants in water samples. *Asian J Chem.* 2011;23(2):657–62.
340. Lagergren S. Zur theorie der sogenannten adsorption gelöster stoffe, *Kungliga Svenska Vetenskapsakademiens. Handl Band,*. 1898;24:1–13.
341. Ho YS, McKay G. Sorption of dye from aqueous solution by peat. *Chem Eng J.* 1998;70:115–24.
342. Liu Y, He J, Yu J, Zeng H. Controlling numbers and sizes of beads in electrospun nanofibers. *Polym Int.* 2008;57(4):632–6.
343. Triantafillopoulos N. *Measurement of Fluid Rheology and Interpretation of Rheograms.* 2nd ed. USA: Katec Scientific, Inc., pp 57-98, 1988; 1988.
344. Flory PJ. *Principles of Polymer Chemistry.* Cornell University Press, New York, pp 87-147, 1953;
345. Hou H, Ge JJ, Zeng J, Li Q, Reneker DH, Greiner A, et al. Electrospun polyacrylonitrile nanofibers containing a high concentration of well-aligned multiwall carbon nanotubes. *Chem Mater.* 2005;17:967–73.
346. McMurry J. *Organic Chemistry.* 7th ed. New York: Thomson Learning, Inc.; 2008. 408–516.
347. von Gunten U, Siraj K, Kitte SA. Adsorption of hexavalent chromium from aqueous solution using adsorption of hexavalent chromium from aqueous solution using chemically activated carbon prepared from locally available waste of bamboo (*Oxytenanthera abyssinica* ). *Environ Chem.* 2014;2014:1–9.
348. Ibrahim WM, Aziz YSA, Hamdy SM, Gad NS. Biodegradation comparative study for biosorption of heavy metals from synthetic wastewater by different types of marine algae. *J Bioremediation Biodegrad.* 2018;9(1):5–11.
349. Gholizadeh A, Kermani M, Gholami M, Farzadkia M. Kinetic and isotherm studies of adsorption and biosorption processes in the removal of phenolic compounds from aqueous solutions: comparative study. *J Environ Heal Sci Eng.* 2013;11(29):1–10.

350. Nthunya LN, Masheane ML, George M, Kime M-B, Mhlanga SD. Removal of Fe and Mn from polluted water sources in Lesotho using modified clays. *J Water Chem Technol*. 2019;41(2):81–6.
351. Yamasaki H, Makihata Y, Fukunaga K. Preparation of crosslinked - cyclodextrin polymer beads and their application as a sorbent for removal of phenol from wastewater. *J Chem Technol Biotechnol*. 2008;83(7):991–7.
352. Agarwal B, Balomajumder C, Thakur PK. Simultaneous co-adsorptive removal of phenol and cyanide from binary solution using granular activated carbon. *Chem Eng J*. 2013;228:655–64.
353. Yan J, Quan G. Equilibrium and kinetic studies of phenol sorption by chitosan coated montmorillonite. *J Chil Chem Soc*. 2009;54(1):73–6.
354. Fierro V, Torné-Fernández V, Montané D, Celzard A. Adsorption of phenol onto activated carbons having different textural and surface properties. *Microporous Mesoporous Mater*. 2008;111:276–84.
355. Kumar NS, Subbaiah MV, Reddy AS, Krishnaiah A. Biosorption of phenolic compounds from aqueous solutions onto chitosan-abrus precatorius blended beads. *J Chem Technol Biotechnol*. 2009;84:972–81.
356. Termoul M, Bestani B, Benderdouche N, Belhakem M, Naffrechoux E. Removal of phenol and 4-chlorophenol from aqueous solutions by Olive Stone-based activated carbon. *Adsorpt Sci Technol*. 2006;24(5):375–88.
357. Nadavala SK, Swayampakula K, Boddu VM, Abburi K. Biosorption of phenol and o-chlorophenol from aqueous solutions on to chitosan-calcium alginate blended beads. *J Hazard Mater*. 2009;162:482–9.
358. Aksu Z, Yener J. A comparative adsorption/biosorption study of mono-chlorinated phenols onto various sorbents. *Waste Manag*. 2001;21:695–702.
359. Gutierrez L, Aubry C, Valladares Linares R, Croue JP. Natural organic matter interactions with polyamide and polysulfone membranes: Formation of conditioning film. *Colloids Surfaces A Physicochem Eng Asp*. 2015;477:1–8.
360. Chen Z, Zeng H, Gong H, Wang H, Li CJ. Palladium-catalyzed reductive

- coupling of phenols with anilines and amines: efficient conversion of phenolic lignin model monomers and analogues to cyclohexylamines. *Chem Sci.* 2015;6:4174–8.
361. Ayoob S, Gupta AK. Fluoride in drinking water : A review on the status and stress effects. *Environ Sci Technol.* 2017;36(6):433–87.
362. Benjamin JG, Nielsen DC, Vigil MF, Mikha MM, Calderon F. Water deficit stress effects on corn (*Zea mays*, L.) Root: Shoot ratio. *Open J Soil Sci.* 2014;4:151–60.
363. Srinivasan V, Lambin EF, Gorelick SM, Thompson BH, Rozelle S. The nature and causes of the global water crisis: Syndromes from a meta-analysis of coupled human-water studies. *Water Resour Res.* 2012;48:1–16.
364. McDonald RI, Green P, Balk D, Fekete BM, Revenga C, Todd M, et al. Urban growth, climate change, and freshwater availability. *PNAS.* 2011;108(15):6312–7.
365. Boubakri A, Hafiane A, Bouguecha SAT. Direct contact membrane distillation: Capability to desalt raw water. *Arab J Chem.* 2017;10:S3475–81.
366. Husnain T, Mi B, Riffat R. A combined Forward Osmosis and Membrane Distillation system for sidestream treatment. *J Water Resour Prot.* 2015;07:1111–20.
367. Xiong X, Li Q, Zhang XC, Wang L, Guo ZX, Yu J. Poly(vinylidene fluoride)/silica nanocomposite membranes by electrospinning. *J Appl Polym Sci.* 2013;129:1089–95.
368. Sethupathy M, Sethuraman V, Manisankar P. Preparation of PVDF/SiO<sub>2</sub> composite nanofiber membrane using electrospinning for polymer electrolyte analysis. *Soft Nanosci Lett.* 2013;03:37–43.
369. Jacob M, Francis B, Varughese KT, Thomas S. The effect of silane coupling agents on the viscoelastic properties of rubber biocomposites. *Macromol Mater Eng.* 2006;291:1119–26.
370. Rein M, Delplanque JP. The role of air entrainment on the outcome of drop impact on a solid surface. *Acta Mech.* 2008;201:105–18.

371. Langley KR, Li EQ, Vakarelski IU, Thoroddsen ST. The air entrapment under a drop impacting on a nano-rough surface. *Soft Matter*. 2018;1–11.
372. Kim YJ, Ahn CH, Lee MB, Choi MS. Characteristics of electrospun PVDF/SiO<sub>2</sub> composite nanofiber membranes as polymer electrolyte. *Mater Chem Phys*. 2011;127:137–42.
373. Nasir M, Subhan A, Prihandoko B, Lestariningsih T. Nanostructure and property of electrospun SiO<sub>2</sub>-cellulose acetate nanofiber composite by electrospinning. *Energy Procedia*. 2017;107:227–31.
374. Huan S, Liu G, Han G, Cheng W, Fu Z, Wu Q, et al. Effect of experimental parameters on morphological, mechanical and hydrophobic properties of electrospun polystyrene fibers. *Materials*. 2015;8:2718–34.
375. Huang L, Bui NN, Manickam SS, McCutcheon JR. Controlling electrospun nanofiber morphology and mechanical properties using humidity. *J Polym Sci Part B Polym Phys*. 2011;49:1734–44.
376. Baker SR, Banerjee S, Bonin K, Guthold M. Determining the mechanical properties of electrospun poly- $\epsilon$ -caprolactone (PCL) nanofibers using AFM and a novel fiber anchoring technique. *Mater Sci Eng C*. 2016;59:203–12.
377. Lee J, Jeong YH, Cho DW. Fabrication of nanofibrous mats with uniform thickness and fiber density. *Macromol Mater Eng*. 2014;299:1052–61.
378. Kanduč M, Netz RR. From hydration repulsion to dry adhesion between asymmetric hydrophilic and hydrophobic surfaces. *Proc Natl Acad Sci*. 2015;112(40):12338–43.
379. Gryta M. Effectiveness of water desalination by membrane distillation process. *Membranes*. 2012;2:415–29.
380. Nthunya LN, Gutierrez L, Derese S, Nxumalo EN, Verliefdde AR, Mamba BB, et al. A Review of Nanoparticle-Enhanced Membrane Distillation Membranes: Membrane Synthesis and Applications in Water Treatment. *J Chem Technol Biotechnol*. 2019;1–59.
381. Eykens L, De Sitter K, Dotremont C, Pinoy L, Van Der Bruggen B. How to optimize the membrane properties for membrane distillation: A review. *Ind*

- Eng Chem Res. 2016;55(35):9333–43.
382. Kang G dong, Cao Y ming. Application and modification of poly(vinylidene fluoride) (PVDF) membranes - A review. *J Memb Sci*. 2014;463:145–65.
383. Eykens L, Hitsov I, De Sitter K, Dotremont C, Pinoy L, Van der Bruggen B. Direct contact and air gap membrane distillation: Differences and similarities between lab and pilot scale. *Desalination*. 2017;422:91–100.
384. Eykens L, Rose K, Dubreuil M, De Sitter K, Dotremont C, Pinoy L, et al. Functionalization of a Hydrophilic Commercial Membrane Using Inorganic-Organic Polymers Coatings for Membrane Distillation. *Appl Sci*. 2017;7:637.
385. Eykens L, Reyns T, De Sitter K, Dotremont C, Pinoy L, Van der Bruggen B. How to select a membrane distillation configuration? Process conditions and membrane influence unraveled. *Desalination*. 2016;399:105–15.
386. Li X, Yu X, Cheng C, Deng L, Wang M, Wang X. Electrospun Superhydrophobic Organic/Inorganic Composite Nanofibrous Membranes for Membrane Distillation. *ACS Appl Mater Interfaces*. 2015;7(39):21919–30.
387. Li K, Hou D, Fu C, Wang K, Wang J. Fabrication of PVDF nanofibrous hydrophobic composite membranes reinforced with fabric substrates via electrospinning for membrane distillation desalination. *J Environ Sci*. 2019;75:277–88.
388. Khayet M, García-Payo MC, García-Fernández L, Contreras-Martínez J. Dual-layered electrospun nanofibrous membranes for membrane distillation. *Desalination*. 2018;426:174–84.
389. Weerasekara NA, Choo KH, Lee CH. Biofouling control: Bacterial quorum quenching versus chlorination in membrane bioreactors. *Water Res*. 2016;103:293–301.
390. Bogler A, Lin S, Bar-zeev E. Biofouling of membrane distillation , forward osmosis and pressure retarded osmosis : Principles , impacts and future directions. *J Memb Sci*. 2017;542:378–98.
391. Ashhab A Al, Sweity A, Bayramoglu B, Herzberg M. Biofouling of reverse osmosis membranes : effects of cleaning on biofilm microbial communities ,

- membrane performance , and adherence of extracellular polymeric substances. *Biofouling*. 2017;7014:1–13.
392. Akar N, Asar B, Dizge N, Koyuncu I. Investigation of characterization and biofouling properties of PES membrane containing selenium and copper nanoparticles. *J Memb Sci*. 2013;437:216–26.
393. Biswas P, Bandyopadhyaya R. Water disinfection using silver nanoparticle impregnated activated carbon: *Escherichia coli* cell-killing in batch and continuous packed column operation over a long duration. *Water Res*. 2016;100:105–15.
394. Zielińska A, Skwarek E, Zaleska A, Gazda M, Hupka J. Preparation of silver nanoparticles with controlled particle size. *Procedia Chem*. 2009;1:1560–6.
395. Guzmán MG, Dille J, Godet S. Synthesis of silver nanoparticles by chemical reduction method and their antibacterial activity. *World Acad Sci Eng Technol*. 2008;2(7):312–9.
396. Bhatte KD, Deshmukh KM, Patil YP, Sawant DN, Fujita S, Arai M, et al. Synthesis of powdered silver nanoparticles using hydrogen in aqueous medium. *Particuology*. 2012;10(1):140–3.
397. Pomogailo AD, Dzhardimalieva GI. Reduction of Metal ions in polymer matrices as a condensation method of nanocomposite synthesis. In: *Nanostructured materials preparation via condensation ways*. Berlin: Springer; 2014. 1–89.
398. Ahmed S, Ahmad M, Swami BL, Ikram S. A review on plants extract mediated synthesis of silver nanoparticles for antimicrobial applications: A green expertise. *J Adv Res*. 2016;7:17–28.
399. Shaik MR, Khan M, Kuniyil M, Al-Warthan A, Alkhatlan HZ, Siddiqui MRH, et al. Plant-extract-assisted green synthesis of silver nanoparticles using *Origanum vulgare* L. Extract and their microbicidal activities. *Sustain*. 2018;10(4):1–14.
400. Vanaja M, Paulkumar K, Gnanajobitha G, Rajeshkumar S, Malarkodi C, Annadurai G. Herbal plant synthesis of antibacterial silver nanoparticles by

- Solanum trilobatum and its characterization. *Int J Met.* 2014;2014:1–8.
401. Logeswari P, Silambarasan S, Abraham J. Synthesis of silver nanoparticles using plants extract and analysis of their antimicrobial property. *J Saudi Chem Soc.* 2015;19(3):311–7.
402. Machrafi H, Lebon G. The role of several heat transfer mechanisms on the enhancement of thermal conductivity in nanofluids. *Contin Mech Thermodyn.* 2016;28:1461–75.
403. Thanh NTK, Maclean N, Mahiddine S. Mechanisms of nucleation and growth of nanoparticles in solution. *Chem Rev.* 2014;114:7610–30.
404. Chen S, Zhang X, Zhao Y, Zhang Q. Effects of reaction temperature on size and optical properties of CdSe nanocrystals. *Bull Mater Sci.* 2011;33(5):547–52.
405. Hasanpoor M, Aliofkhaezrai M, Delavari H. Microwave-assisted Synthesis of Zinc Oxide Nanoparticles. *Procedia Mater Sci.* 2015;11:320–5.
406. Motshekga SC, Pillai SK, Sinha Ray S, Jalama K, Krause RWM. Recent trends in the microwave-assisted synthesis of metal oxide nanoparticles supported on carbon nanotubes and their applications. *J Nanomater.* 2012;2012:1–15.
407. Nguyen NT, Nguyen BH, Ba DT, Pham DG, Van Khai T, Nguyen LT, et al. Microwave-assisted synthesis of silver nanoparticles using chitosan: A novel approach. *Mater Manuf Process.* 2014;29:418–21.
408. Sun L, Li J, Cai J, Zhong L, Ren G, Ma Q. One pot synthesis of gold nanoparticles using chitosan with varying degree of deacetylation and molecular weight. *Carbohydr Polym.* 2017;178:105–14.
409. Zhao X, Su Y, Qi X, Han X. A Facile Method to Prepare Novel Ag<sub>2</sub>O/Ag<sub>2</sub>CO<sub>3</sub> Three-Dimensional Hollow Hierarchical Structures and Their Water Purification Function. *ACS Sustain Chem Eng.* 2017;5(7):6148–58.
410. Wu H, Luo T, Gao ZP, Zhang KQ, Song JY, Xiao JS, et al. Granny Smith apple procyanidin extract upregulates tight junction protein expression and modulates oxidative stress and inflammation in lipopolysaccharide-induced

- Caco-2 cells. *Food Funct.* 2018;9:3321–9.
411. Boyer J, Liu RH. Apple phytochemicals and their health benefits. *Nutr J.* 2004;3(5):1–15.
412. Katayama N. Bird diversity and abundance in organic and conventional apple orchards in northern Japan. *Sci Rep.* 2016;6:1–7.
413. Mkenda P, Mwanauta R, Stevenson PC, Ndakidemi P, Mtei K, Belmain SR. Extracts from field margin weeds provide economically viable and environmentally benign pest control compared to synthetic pesticides. *PLoS One.* 2015;10(11):1–14.
414. Beveridge T. Juice extraction from apples and other fruits and vegetables. *Crit Rev Food Sci Nutr.* 1997;37(5):449–69.
415. Jiang XC, Chen CY, Chen WM, Yu AB. Role of citric acid in the formation of silver nanoplates through a synergistic reduction approach. *Langmuir.* 2010;26:4400–8.
416. Rajam BM, Ramasamy P, Mahalingam U. Monodispersed gold nanoparticles as a probe for the detection of Hg<sup>2+</sup> ions in water. *Acta Chim Slov.* 2017;64:186–92.
417. Eisele TA, Drake SR. The partial compositional characteristics of apple juice from 175 apple varieties. *J Food Compos Anal.* 2005;18:213–21.
418. Blanco D, Quintanilla ME, Mangas JJ, Gutierrez MD. Determination of organic acids in apple juices by capillary liquid chromatography. *J Liq Chromatogr Relat Technol.* 1996;19(16):2615–21.
419. Pal A, Shah S, Devi S. Microwave-assisted synthesis of silver nanoparticles using ethanol as a reducing agent. *Mater Chem Phys.* 2009;114:530–2.
420. Zhuang X, Cheng B, Kang W, Xu X. Electrospun chitosan/gelatin nanofibers containing silver nanoparticles. *Carbohydr Polym.* 2010;82:524–7.
421. Nthunya LN, Masheane ML, Malinga SP, Barnard TG, Nxumalo EN, Mamba BB, et al. UV-assisted reduction of in situ electrospun antibacterial chitosan-based nanofibres for removal of bacteria from water. *RSC Adv.* 2016;6(98).

422. Nthunya LN, Masheane ML, Malinga SP, Nxumalo EN, Barnard TG, Kao M, et al. Greener Approach to Prepare Electrospun Antibacterial  $\beta$ -Cyclodextrin/Cellulose Acetate Nanofibers for Removal of Bacteria from Water. *ACS Sustain Chem Eng*. 2017;5(1).
423. Pruller S, Turni C, Blackall PJ, Beyerbach M, Klein G, Kreienbrock L, et al. Towards a standardized method for broth microdilution susceptibility testing of haemophilus parasuis. *J Clin Microbiol*. 2017;55:264–73.
424. Guzmán M, Dille J, Godet S. Synthesis of silver nanoparticles by chemical reduction method and their antibacterial activity. *Int J Chem*. 2009;2(3):104–11.
425. Gawande MB, Shelke SN, Zboril R, Varma RS. Microwave-assisted chemistry: Synthetic applications for rapid assembly of nanomaterials and organics. *Acc Chem Res*. 2014;47:1338–48.
426. Dudley GB, Richert R, Stiegman AE. On the existence of and mechanism for microwave-specific reaction rate enhancement. *Chem Sci*. 2015;6:2144–52.
427. Balashanmugam P, Kalaichelvan PT. Biosynthesis characterization of silver nanoparticles using *Cassia roxburghii* DC. aqueous extract, and coated on cotton cloth for effective antibacterial activity. *Int J Nanomedicine*. 2015;2015(10):87–97.
428. Kumar B, Smita K, Cumbal L, Debut A. Sacha inchi (*Plukenetia volubilis* L.) shell biomass for synthesis of silver nanocatalyst. *J Saudi Chem Soc*. 2017;1–21.
429. Abdullah YI, Hafizuddin M, Jumali H, Yahaya M, Shanshool M. Facile Formation of  $\beta$  Poly (vinylidene fluoride) Films using the Short Time Annealing Process. *Adv Environ Biol*. 2015;9(20):20–7.
430. Choi SS, Lee YS, Joo CW, Lee SG, Park JK, Han K-S. Electrospun PVDF nanofiber web as polymer electrolyte or separator. *Electrochim Acta*. 2004;50:339–43.
431. Li B, Xu C, Zheng J, Xu C. Silver nanowire dopant enhancing piezoelectricity of electrospun PVDF nanofiber web. *Sensors*. 2014;14:9889–99.

432. Li D, Kaner RB. How nucleation affects the aggregation of nanoparticles. *J Mater Chem*. 2007;17:2279–82.
433. Wagner C, Fournier N, Ruiz VG, Li C, Müllen K, Rohlfing M, et al. Non-additivity of molecule-surface van der Waals potentials from force measurements. *Nat Commun*. 2014;5:1–8.
434. Rosicka D, Sembera J. Changes in the nanoparticle aggregation rate due to the additional effect of electrostatic and magnetic forces on mass transport coefficients. *Nanoscale Res Lett*. 2013;8(20):1–9.
435. Liu Y, Zhang L, Willis BG, Mustain WE. Importance of particle size and distribution in achieving high-activity, high-stability oxygen reduction catalysts. *ACS Catal*. 2015;5:1560–7.
436. Zhang X-F, Liu Z-G, Shen W, Gurunathan S. Silver Nanoparticles: Synthesis, Characterization, Properties, Applications, and Therapeutic Approaches. *Int J Mol Sci*. 2016;17:1534.
437. O'Toole A, Ricker EB, Nuxoll E. Thermal deactivation of *Pseudomonas aeruginosa* biofilms. *Biofouling*. 2015;31(8):665–75.
438. Rodrigo F, Fernandez PS, Rodrigo M, Ocio MJ, Martinez A. Thermal resistance of *Bacillus stearothermophilus* heated at high temperature in different substrates. *J Food Prot*. 1997;60(2):144–7.
439. Taisuke W, Soichi F, Junichi H, Koyama T, Hirokazu O, Yamasaki M. Inactivation of *geobacillus stearothermophilus* spores by high-pressure carbon dioxide treatment. *Appl Environ Microbiol*. 2003;69(12):7124–9.
440. Eickhoff TC. In vitro effects of carbenicillin combined with gentamicin or polymyxin B against *Pseudomonas aeruginosa*. *Appl Microbiol*. 1969;18(3):469–73.
441. Hawwa R, Aikens J, Turner RJ, Santarsiero BD, Mesecar AD. Structural basis for thermostability revealed through the identification and characterization of a highly thermostable phosphotriesterase-like lactonase from *Geobacillus stearothermophilus*. *Arch Biochem Biophys*. 2009;488(2):109–20.

442. Wei F, Zhao X, Li C, Han X. A novel strategy for water disinfection with a AgNPs/gelatin sponge filter. *Environ Sci Pollut Res*. 2018;25(20):19480–7.
443. Zhang Z, Xing D, Liang Q, Yong D, Han X. Size controllable synthesis and antimicrobial activity of poly-N,N'-[(4,5-dihydroxy-1,2-phenylene)bis(methylene)]bisacrylamide microspheres. *RSC Adv*. 2014;4:57891–8.
444. Andrews JM. Determination of minimum inhibitory concentrations. *J Antimicrob Chemother*. 2001;48(1):5–16.
445. Tiraferri A, Kang Y, Giannelis EP, Elimelech M. Superhydrophilic thin-film composite forward osmosis membranes for organic fouling control: Fouling behavior and antifouling mechanisms. *Environ Sci Technol*. 2012;46:11135–44.
446. Li F, Huang J, Xia Q, Lou M, Yang B, Tian Q, et al. Direct contact membrane distillation for the treatment of industrial dyeing wastewater and characteristic pollutants. *Sep Purif Technol*. 2018;195:83–91.
447. Zhang M, Feng S, Wang L, Zheng Y. Lotus effect in wetting and self cleaning. *Biotribology*. 2016;5:31–43.
448. Li X, García-payo MC, Khayet M, Wang M, Wang X. Superhydrophobic polysulfone / polydimethylsiloxane electrospun nanofibrous membranes for water desalination by direct contact membrane distillation. 2017;542(April):308–19.
449. Zheng R, Chen Y, Wang J, Song J, Li XM, He T. Preparation of omniphobic PVDF membrane with hierarchical structure for treating saline oily wastewater using direct contact membrane distillation. *J Memb Sci*. 2018;555:197–205.
450. Das R, Ali E, Hamid SBA, Ramakrishna S, Chowdhury ZZ. Carbon nanotube membranes for water purification: A bright future in water desalination. *Desalination*. 2014;336:97–109.
451. Shahkaramipour N, Tran TN, Ramanan S, Lin H. Membranes with surface-enhanced antifouling properties for water purification. *Membranes*.

- 2017;7(13):1–18.
452. Misdan N, Ismail AF, Hilal N. Recent advances in the development of (bio) fouling resistant thin film composite membranes for desalination. *Desalination*. 2016;380:105–11.
453. Tetana ZN, Mhlanga SD, Bepete G, Coville NJ. The synthesis of nitrogen-doped multiwalled carbon nanotubes using an Fe-Co/CaCO<sub>3</sub> Catalyst. *South African J Chem*. 2012;65:39–49.
454. Singh BP, Choudhary V, Teotia S, Gupta TK, Singh VN, Dhakate SR, et al. Solvent free, efficient, industrially viable, fast dispersion process based amine modified MWCNT reinforced epoxy composites of superior mechanical properties. *Adv Mater Lett*. 2015;6(2):104–13.
455. Antsiferova Y, Sotnikova N, Parfenyuk E. Different effects of the immunomodulatory drug GMDP immobilized onto aminopropyl modified and unmodified mesoporous silica nanoparticles upon peritoneal macrophages of women with endometriosis. *Biomed Res Int*. 2013;2013(1–11).
456. Petcu C, Purcar V, Spătaru C-I, Alexandrescu E, Șomoghi R, Trică B, et al. The influence of new hydrophobic silica nanoparticles on the surface properties of the films obtained from bilayer hybrids. *Nanomaterials*. 2017;7(47):1–10.
457. Pigliacelli C, D'Elcio A, Milani R, Terraneo G, Resnati G, Baldelli Bombelli F, et al. Hydrophobin-stabilized dispersions of PVDF nanoparticles in water. *J Fluor Chem*. 2015;177:62–9.
458. He F, Luo B, Yuan S, Liang B, Choong C, Pehkonen SO. PVDF film tethered with RGD-click-poly(glycidyl methacrylate) brushes by combination of direct surface-initiated ATRP and click chemistry for improved cytocompatibility. *RSC Adv*. 2014;4(1):105–17.
459. Bokobza L, Zhang J. Raman spectroscopic characterization of multiwall carbon nanotubes and of composites. *Express Polym Lett*. 2012;6(7):601–8.
460. Masheane ML, Nthunya LN, Malinga SP, Nxumalo EN, Mamba BB, Mhlanga SD. Synthesis of Fe-Ag/f-MWCNT/PES nanostructured-hybrid membranes

- for removal of Cr(VI) from water. *Sep Purif Technol.* 2017;184:79–87.
461. Xiao S, Shen M, Guo R, Huang Q, Wang S, Shi X. Fabrication of multiwalled carbon nanotube-reinforced electrospun polymer nanofibers containing zero-valent iron nanoparticles for environmental applications. *J Mater Chem.* 2010;20:5700–8.
462. Mhlanga SD, Mondal KC, Carter R, Witcomb MJ, Coville N. The effect of synthesis parameters on the catalytic synthesis of multiwalled carbon nanotubes using Fe-Co/CaCO<sub>3</sub> catalysts. *S Afr J Chem.* 2009;62:67–76.
463. Gao M, Du HW, Yang J, Zhao L, Xu J, Ma ZQ. Variation of passivation behavior induced by sputtered energetic particles and thermal annealing for ITO/SiO<sub>x</sub>/Si system. *Chinese Phys B.* 2017;26(4):045201.
464. Sui T, Song B, Wen YH, Zhang F. Bifunctional hairy silica nanoparticles as high-performance additives for lubricant. *Sci Rep.* 2016;6:1–9.
465. Wang YY, Kusumoto K, Li CJ. XPS Analysis of SiC Films Prepared by Radio Frequency Plasma Sputtering. *Phys Procedia.* 2012;32:95–102.
466. Liu J, Janjua Z, Roe M, Xu F, Turnbull B, Choi K-S, et al. Superhydrophobic/icephobic coatings based on silica nanoparticles modified by self-assembled monolayers. *Nanomaterials.* 2016;6(12):2–10.
467. Sublemontier O, Nicolas C, Aureau D, Patanen M, Kintz H, Liu X, et al. X-ray photoelectron spectroscopy of isolated nanoparticles. *J Phys Chem Lett.* 2014;5:3399–403.
468. Helmlinger J, Sengstock C, Groß-Heitfeld C, Mayer C, Schildhauer TA, Köller M, et al. Silver nanoparticles with different size and shape: Equal cytotoxicity, but different antibacterial effects. *RSC Adv.* 2016;6:18490–501.
469. Li J hua, Zhang D bin, Ni X xing, Zheng H, Zhang Q qing. Excellent hydrophilic and anti-bacterial fouling PVDF membrane based on ag nanoparticle self-assembled PCBMA polymer brush. *Chinese J Polym Sci (English Ed.)* 2017;35(7):809–22.
470. Pan Y, Yu Z, Shi H, Chen Q, Zeng G, Di H, et al. A novel antifouling and antibacterial surface-functionalized PVDF ultrafiltration membrane via

- binding Ag/SiO<sub>2</sub>nanocomposites. *J Chem Technol Biotechnol.* 2016;92(262–257).
471. Idris A, Man Z, Maulud AS, Khan MS. Effects of phase separation behavior on morphology and performance of polycarbonate membranes. *Membranes (Basel).* 2017;7(21):1–18.
472. Seuba J, Deville S, Guizard C, Stevenson AJ. Mechanical properties and failure behavior of unidirectional porous ceramics. *Sci Rep.* 2016;6:1–11.
473. Eykens L, De Sitter K, Stoops L, Dotremont C, Pinoy L, Van der Bruggen B. Development of polyethersulfone phase-inversion membranes for membrane distillation using oleophobic coatings. *J Appl Polym Sci.* 2017;134:1–11.
474. Eykens L, De Sitter K, Dotremont C, Pinoy L, Van der Bruggen B. Characterization and performance evaluation of commercially available hydrophobic membranes for direct contact membrane distillation. *Desalination.* 2016;392:63–73.
475. Eykens L, De Sitter K, Paulussen S, Dubreuil M, Dotremont C, Pinoy L, et al. Atmospheric plasma coatings for membrane distillation. *J Memb Sci.* 2018;554:175–83.
476. Masinga SP, Nxumalo EN, Mamba BB, Mhlanga SD. Microwave-induced synthesis of  $\beta$ -cyclodextrin/N-doped carbon nanotube polyurethane nanocomposites for water purification. *Phys Chem Earth, Parts A/B/C.* 2014;67–69:105–10.
477. Rai M, Yadav A, Gade A. Silver nanoparticles as a new generation of antimicrobials. *Biotechnol Adv.* 2009;27:76–83.
478. Kalinichev AG, Iskrenova-Tchoukova E, Ahn WY, Clark MM, Kirkpatrick RJ. Effects of Ca<sup>2+</sup> on supramolecular aggregation of natural organic matter in aqueous solutions: A comparison of molecular modeling approaches. *Geoderma.* 2011;169:27–32.
479. Ahn WY, Kalinichev AG, Clark MM. Effects of background cations on the fouling of polyethersulfone membranes by natural organic matter:

- Experimental and molecular modeling study. *J Memb Sci.* 2008;309:128–40.
480. Mahlangu TO, Thwala JM, Mamba BB, D'Haese A, Verliefde ARD. Factors governing combined fouling by organic and colloidal foulants in cross-flow nanofiltration. *J Memb Sci.* 2015;491:53–62.
481. Lee N, Amy G, Croué JP, Buisson H. Identification and understanding of fouling in low-pressure membrane (MF/UF) filtration by natural organic matter (NOM). *Water Res.* 2004;38:4511–23.
482. Zhu X, Elimelech M. Colloidal fouling of reverse osmosis membranes: Measurements and fouling mechanisms. *Environ Sci Technol.* 1997;31:3654–62.
483. Owili MA. Assessment of impact of sewage effluents on coastal water quality in Hafnarfjordur, Iceland. Iceland; 2003.
484. Begum S, Kausar A, Ullah H, Siddiq M. Exploitation of carbon nanotubes in high performance polyvinylidene fluoride matrix composite: A review. *Polym Plast Technol Eng.* 2016;55:199–222.
485. Motsa MM, Mamba BB, Verliefde ARD. Forward osmosis membrane performance during simulated wastewater reclamation: Fouling mechanisms and fouling layer properties. *J Water Process Eng.* 2018;23:109–18.
486. Janczuk B, Wojcik W, Zdziennicka A. Determination of the components of the surface tension of some liquids from interfacial liquid-liquid tension measurements. *J Colloid Interface Sci.* 1993;157:384–93.
487. Gutierrez L, Nguyen TH. Interactions between rotavirus and natural organic matter isolates with different physicochemical characteristics. *Langmuir.* 2013;29(47):14460–8.
488. Zarebska A, Nieto DR, Christensen K V., Norddahl B. Ammonia recovery from agricultural wastes by membrane distillation: Fouling characterization and mechanism. *Water Res.* 2014;56:1–10.
489. Kumar B, Shrestha S, Prasad A, Kim J, Won S, Kim H, et al. Bio-inspired hybrid scaffold of zinc oxide-functionalized multi-wall carbon nanotubes reinforced polyurethane nano fibers for bone tissue engineering. *Mater Des.*

- 2017;133:69–81.
490. Kanagaraj P, Nagendran A, Rana D, Matsuura T, Neelakandan S, Karthikkumar T, et al. Influence of N -phthaloyl chitosan on poly ( ether imide ) ultrafiltration membranes and its application in biomolecules and toxic heavy metal ion separation and their antifouling properties. *Appl Surf Sci.* 2015;329:165–73.
491. Subramanian S, Seeram R. New directions in nano fi ltration applications — Are nano fi bers the right materials as membranes in desalination? *2013;308:198–208.*
492. Chen TW, Chang SJ, Niu GCC, Hsu YT, Kuo SM. Alginate-coated chitosan membrane for guided tissue regeneration. *J Appl Polym Sci.* 2006;102:4528–34.
493. Lee KY, Mooney DJ. Alginate: properties and biomedical applications *Kuen. Prog Polym Sci.* 2000;37(1):106–26.
494. Barák I, Muchová K. The role of lipid domains in bacterial cell processes. *Int J Mol Sci.* 2013;14(2):4050–65.
495. Krasowska A, Sigler K. How microorganisms use hydrophobicity and what does this mean for human needs? *Front Cell Infect Microbiol.* 2014;4:1–7.
496. Lyklema J, Norde W, Schraa G, Zehnder AJB, Mark CM. The Role of Bacterial Cell Wall Hydrophobicity in Adhesion. *Appl Environ Microbiol.* 1987;53(8):1893–7.
497. Mahdi M, Shirazi A, Kargari A, Tabatabaei M. Chemical Engineering and Processing: Process Intensification Evaluation of commercial PTFE membranes in desalination by direct contact membrane distillation. *Chem Eng Process Process Intensif.* 2014;76:16–25.
498. Nthunya LN, Khumalo NP, Verliefe AR, Mamba BB, Mhlanga SD. Quantitative analysis of phenols and PAHs in the Nandoni Dam in Limpopo Province, South Africa: A preliminary study for dam water quality management. *Phys Chem Earth, Parts A/B/C.* 2019;1–9.
499. Liao Y, Loh C, Tian M, Wang R, Fane AG. Progress in electrospun

- polymeric nanofibrous membranes for water treatment: Fabrication , modification and applications. *Prog Polym Sci.* 2018;77:69–94.
500. Zarebska A, Amor AC, Ciurkot K, Karring H, Thygesen O, Andersen TP, et al. Fouling mitigation in membrane distillation processes during ammonia stripping from pig manure. *J Memb Sci.* 2015;484:119–32.
501. Mohod C V., Dhote J. Review of heavy metals in drinking water and their effect. *Int J Innov Res Sci Eng Technol.* 2013;2(7):2992–6.
502. Crompton TR. Determination of Metals in Natural and Treated Water. New York, USA: Spon Press; 2002. 1108.
503. Carre A. Polar interactions at liquid/polymer interfaces. *J Adhes Sci Technol.* 2007;21(10):961–81.
504. Razmjou A, Arifin E, Dong G, Mansouri J, Chen V. Superhydrophobic modification of TiO<sub>2</sub>nanocomposite PVDF membranes for applications in membrane distillation. *J Memb Sci.* 2012;415–416:850–63.
505. Boulares-Pender A, Thomas I, Prager A, Schulze A. Surface modification of polyamide and poly(vinylidene fluoride) membranes. *J Appl Polym Sci.* 2013;128(1):322–31.
506. Gumbi NN, Hu M, Mamba BB, Li J, Nxumalo EN. Macrovoid-free PES/SPSf/O-MWCNT ultrafiltration membranes with improved mechanical strength, antifouling and antibacterial properties. *J Memb Sci.* 2018;566:288–300.
507. Teli SB, Molina S, Sotto A, Garc E, Abajo J De. Fouling resistant polysulfone – PANI/ TiO<sub>2</sub> ultra filtration nanocomposite membranes. *Ind Eng Chem Res.* 2013;52:9470–9.
508. Colombo I, Wolf W de, Thompson RS, Farrar DG, Hoke RA, L'Haridon J. Acute and chronic aquatic toxicity of ammonium perfluorooctanoate (APFO) to freshwater organisms. *Ecotoxicol Environ Saf.* 2008;71:749–56.
509. Du X, Zhang Z, Carlson KH, Lee J, Tong T. Membrane fouling and reusability in membrane distillation of shale oil and gas produced water: Effects of membrane surface wettability. *J Memb Sci.* 2018;567:199–208.

510. Mokhtar NM, Lau WJ, Ismail AF, Veerasamy D. Membrane distillation technology for treatment of wastewater from rubber industry in Malaysia. *Procedia CIRP*. 2015;26:792–6.
511. Prasad R. *Solid Waste Management and Safe Drinking Water in Context of Mizoram and other States in India*. India: Educreation Publishing; 2011. 6–11.
512. Cook S, Peacock M, Evans CD, Page SE, Whelan MJ, Gauci V, et al. Quantifying tropical peatland dissolved organic carbon (DOC) using UV-visible spectroscopy. *Water Res*. 2017;115:229–35.
513. Haleyur N, Shahsavari E, Mansur AA, Koshlaf E, Morrison PD, Osborn AM, et al. Comparison of rapid solvent extraction systems for the GC-MS/MS characterization of polycyclic aromatic hydrocarbons in aged, contaminated soil. *MethodsX*. 2016;3:364–70.
514. Lehotay SJ, Hajs J. Application of gas chromatography in food analysis. *Trends Anal Chem*. 2002;21(9):686–97.
515. Shrivastava A, Gupta VB. Methods for the determination of limit of detection and limit of quantitation of the analytical methods. *Chronicles Young Sci*. 2011;2(1):21–5.
516. Hoker J, Obersteiner F, Bönisch H, Engel A. Comparison of GC/time-of-flight MS with GC/quadrupole MS for halocarbon trace gas analysis. *Atmos Meas Tech*. 2015;8:2195–206.
517. Wilson ID. Chromatographic and electrophoretic separations combined with mass spectrometry for metabonomics. In: *The Handbook of Metabonomics and Metabolomics*. United Kingdom: Elsevier B.V.; 2007. 149–69.

## APPENDICES

---

### A1 Introduction

The detailed description of the methods used for analysis of the water salinity, organic and bacterial water contaminants presented in the preliminary results on Chapter 1 (Introduction chapter) is provided in the appendices section.

### A2 Experimental design

#### A2.1 Materials

Calcium carbonate ( $\text{CaCO}_3$ , 99.95%, analytical reagent), magnesium (Mg, 99.99% trace metals basis), sodium chloride ( $\text{NaCl}$ , 99.5% volumetric standard), lanthanum oxide ( $\text{La}_2\text{O}_3$  99.9% AAS grade), hydrochloric acid ( $\text{HCl}$ , 37%, reagent grade) were purchased from Sigma Aldrich (Germany). Polyvinylidene fluoride (PVDF) Durapore® membrane filters with pore size of 0.45  $\mu\text{m}$ , the chloride ( $\text{Cl}^-$ ), nitrate ( $\text{NO}_3^-$ ), sulphate ( $\text{SO}_4^{2-}$ ), phosphate ( $\text{PO}_4^{3-}$ ), fluoride ( $\text{F}^-$ ), iodide ( $\text{I}^-$ ), ammonium ( $\text{NH}_4^+$ ) Spectroquant® cell, reagent test kits, polyvinylidene fluoride (PVDF) Durapore® membrane filters with the pore size of 0.22  $\mu\text{m}$  and diameter of 47 mm were purchased from Merck (South Africa). Potassium hydrogen phthalate (KHP)  $\geq 99.95\%$ , phosphoric acid ( $\text{H}_3\text{PO}_4$ ) (85% w/v in  $\text{H}_2\text{O}$ ), phenol mix analytical standard, HPLC grade (phenol, 2-chlorophenol, 2,6-dichlorophenol, 2,4,5-trichlorophenol, 2,3,6 trichlorophenol, 2,3,4,6-tetrachlorophenol, 4-chloro-3-methylphenol, 2,3-dimethylphenol, 3-methylphenol, 2-nitrophenol, 4-nitrophenol), PAHs mix analytical standard, HPLC grade (fluorene, phenanthrene, naphthalene, acenaphthene, pyrene, benz[a]anthracene, benzo[a]pyrene, fluoranthene, benzo[k] fluoranthene, indeno[1,2,3cd]pyrene and dibenzo[def, mno]chrysene, dichloromethane, acetonitrile, ethyl acetate and methanol (HPLC grade), C18–SD SPE cartridges (4 mm/1 mL) were purchased from Sigma Aldrich (Germany). De-ionised water was prepared in our laboratory using Direct-Q® (Millipore) system supplied by Merck Millipore (South Africa). All reagents were used as received.

The standard and stock solutions were stored in a dark refrigerator at 5°C prior to use. Other materials were used as received.

The study area comprised the water bodies in and around Nandoni Dam, located in Vhembe District, Limpopo Province, South Africa. The geographic coordinates of the sampling points were identified using civilian global positioning system (GPS) with a 5 m horizontal accuracy. The coordinates for each sampling point are summarised in **Table A1**. The geographical view of the sampling points is shown in **Figure A1**.

**Table A1:** The geographical location of the sampling points used in this study (at Nandoni Dam, Vhembe District, Limpopo Province, South Africa and the municipal water treatment plant).

Sampling Point	GPS Coordinates		Description
Dam Inlet	-22.99835° South	30.51354° East	The dam entrance located near the bridge between the dam and Luvuvhu River in Muledane village.
Dam Near-Inlet	-22.99687° South	30.54071° East	The middle entrance located 4.6 km away from the dam exit.
Dam Near-Outlet	-22.98237° South	30.57476° East	The middle exit point located 2.7 km away from the dam exit.
Dam Outlet	-22.97901° South	30.59336° East	The dam exit is 100 m away from the Thohoyandou bridge.
Municipal WTP	-23.255636° South	30.77175° East	This treatment plant sources the water from Nandoni Dam for purification and distribution. The water is collected at the rate of 60 × 10 <sup>6</sup> L/day within the distance of 30.7 km from the dam closer to the outlet

\* The raw and treated water were collected at the treatment plant.



**Figure A1:** An overview of the sampling points located using Google Maps.

## A2.2 On-Site Analysis and sampling

The physicochemical parameters of water, including conductivity, total dissolved solids (TDS), salinity, temperature and pH of the collected water samples were measured in situ using a YSI ProDSS Multi-Parameter Water Quality Meter (YSI Incorporated, Yellow Springs, Ohio, USA) with the sampling probe inserted in the dam water. The water samples collected for laboratory analysis were taken at depth of 1 m from the surface of the water and kept in the cooler box during transportation to the laboratories. The water samples were collected twice in one season with 3 replicates per sampling. It worth noting that the standard deviations emanating from this sampling will possibly be lower than the true standard deviations if sampling was to be done continuously.

### **A2.3 Preparation of standard aqueous solutions**

The 50 mg/L stock solutions of  $\text{CaCl}_2$  and  $\text{MgCl}_2$  were prepared by separately dissolving each of  $\text{CaCO}_3$  and  $\text{Mg}$  in 0.1 M HCl. The 50 mg/L NaCl stock solution was on the other hand prepared by dissolving NaCl in de-ionised water. The working standards were prepared by the serial volume/volume dilutions of the stock solutions. Seven working standards (0.5 mg/L, 1 mg/L, 2 mg/L, 4 mg/L, 8 mg/L, 16 mg/L, 32 mg/L for all metal ions) were used to prepare calibration graphs. The stock solution of  $\text{LaCl}_3\text{-HCl}$  that was used to mask the AAS interferences was prepared by dissolving 58 g of lanthanum oxide ( $\text{La}_2\text{O}_3$ ) in 250 mL of 12 M HCl and diluted to a total volume of 500 mL using de-ionised water.

### **A2.4 Atomic absorption spectroscopy (AAS) analysis of metal ions**

The analysis of metal ions was performed using an atomic absorption spectrometer under the following conditions: gratings - visible for calcium and sodium, and ultraviolet for magnesium; wavelength counters - 211.4 (4227 Å), 285.2 (2852 Å) and 294.4 (5888 Å); sources - calcium hollow cathode lamp, magnesium hollow cathode lamp and sodium vapour discharge lamp; lamp current of 10 mA, 20 mA and 900 mA were used for calcium, sodium and magnesium, respectively. The analysis was undertaken under an air pressure of 28 psi, fuel (acetylene) pressure of 8 psi and sample uptake of 4 mL. The samples were filtered using 0.45  $\mu\text{m}$  filters and 0.4 mL of  $\text{LaCl}_3\text{-HCl}$  was added to each sample prior to analysis. The percentage absorption was recorded for each atomised sample. The percentage absorption was converted to absorbance, which was subsequently used to calculate the concentration of each analyte using the calibration graphs.

### **A2.5 The spectroquant analysis of anions**

The concentrations of all anions ( $\text{Cl}^-$ ,  $\text{NO}_3^-$ ,  $\text{SO}_4^{2-}$ ,  $\text{PO}_4^{3-}$ ,  $\text{F}^-$ ,  $\text{I}^-$ ) under investigation as well as  $\text{NH}_4^+$  were determined using Spectroquant® photometry

which is USEPA approved. The advantages of the technique lie in its simplicity to operate, cost-effectiveness and the ability to analyse a variety of analytes. Spectroquant® is a pre-programmed method that is inclusive of the latest micro-process technology with high quality optical and electronic components. The reagents that are specific to individual analytes are provided as both liquids and powders and have buffering capacity to prevent any change in the pH of the solutions. The spectrometer was optimised to correlate the absorbance of the analyte of interest using the barcode of the test cell of each analyte. To determine the concentration of each analyte, the provided kit reagents were added to the sample with the analyte to produce the characteristic colour that will absorb the UV-Vis light, hence measuring the concentrations of each anion [26,27]. During the analyte measurements, the Spectroquant® photometer indicated if the limit of detection and quantification had been exceeded. The analyte with the concentration that falls within the measuring range was detected. Therefore, the analytes with concentrations higher than the detectable limits were diluted and the dilution factors were used to calculate the concentration of such analyte in the water collected from Nandoni Dam. The calibration graphs were prepared using different concentration ranges of different analytes. For instance, the calibration graph for chlorides analysis, was prepared from a total of seven working standards (0.25 mg/L, 5 mg/L, 25 mg/L, 50 mg/L, 100 mg/L, 200 mg/L, 250 mg/L). The instrument was switched to the absorbance mode where the absorbance of the deionised water and the chlorides at these concentrations were measured. Coefficients of determination greater than 0.99 were observed for all analytes. The limit of the detection (LOD), and the limit of quantification (LOQ) were calculated and were found to correspond to the ones provided in the test kits.

## **A2.6 Analysis of organic compounds**

### **A2.6.1 Total organic carbon and dissolved organic carbon**

Parameters such as total organic carbon (TOC) and the dissolved organic carbon (DOC) were determined. These parameters are a cost-effective qualitative method for determining the presence of organic compounds in water, hence provide an

overview of the presence of organic compounds prior to the determination of specific organic compounds present in water (512). The TOC and DOC were analysed using Teledyne Tekmar Torch TOC analyser. A calibration curve was prepared using potassium hydrogen phthalate and the correlation coefficient of 0.998 was obtained. The analysis was undertaken in two steps: (i) Decomposition of inorganic carbon (IC) using 30% w/v  $\text{H}_3\text{PO}_4$  and purging of the liberated carbon dioxide ( $\text{CO}_2$ ) using nitrogen ( $\text{N}_2$ ) as a carrier gas; (ii) Oxidation of the organic carbon (OC) using a furnace at 750 °C, followed by absorption of moisture and detection of the TOC. The liberated  $\text{CO}_2$  from the organic matter was transferred to the non-dispersive infrared analyser.

#### **A2.6.2 Quantification of phenols and PAHs**

The extraction/concentration of phenols and PAHs present in the water samples was performed by solid-phase extraction (SPE) using  $\text{C}_{18}$  cartridges. The quantification analysis of the phenols and PAHs was performed on gas chromatography-time-of-flight mass spectrometer (GC-TOF MS). Mixed standards used were phenols (phenol, 2-chlorophenol, 2,6-dichlorophenol, 2,4,5-trichlorophenol, 2,3,6 trichlorophenol, 2,3,4,6-tetrachlorophenol, 4-chloro-3-methylphenol, 2,3-dimethylphenol, 3-methylphenol, 2-nitrophenol, 4-nitrophenol), in methanol and PAHs (fluorene, phenanthrene, naphthalene, acenaphthene, pyrene, benz[a] anthracene and benzo[a] pyrene, fluoranthene, benzo[k] fluoranthene, indeno[1,2,3cd] pyrene and dibenzo[def, mno] chrysene) in acetonitrile. The stock solutions of phenols and PAHs were serially diluted to the working standards of a specific concentration for preparation of the calibration graphs. A total of five working standards (0.5  $\mu\text{g/L}$ , 1.0  $\mu\text{g/L}$ , 5.0  $\mu\text{g/L}$ , 10  $\mu\text{g/L}$ , 20  $\mu\text{g/L}$ ) of phenol, 2-chlorophenol, 2,6-dichlorophenol, 2,4,5-trichlorophenol, 2,3,6 trichlorophenol, 2,3,4,6-tetrachlorophenol, 4-chloro-3-methylphenol, 2,3-dimethylphenol, 3-methylphenol, 2-nitrophenol, 4-nitrophenol, were used for preparation of calibration graphs of the phenols. A total of five working standards (0.1 mg/L, 0.5 mg/L, 1 mg/L, 5 mg/L, 10 mg/L) of fluorene, phenanthrene, naphthalene, acenaphthene, pyrene, benz(a) anthracene and benzo(a) pyrene,

fluoranthene, benzo(k) fluoranthene, indeno(1,2,3cd) pyrene and dibenzo(def, mno) chrysene were used for preparation of calibration graphs of PAHs.

### **A2.6.3 Solid-phase extraction (SPE) of phenols and PAHs**

The phenols and PAHs were extracted from the water samples using a SPE manifold with C<sub>18</sub> cartridges. The extraction of the PAHs and the phenols was carried out using the methods described by Kayali-Sayadi *et al.* (1998), Olujimi *et al.* (2011), and Santana *et al.* (2009) (337–339). Briefly, the cartridges were pre-conditioned by passing through 10 mL aliquots of DCM, 5 mL of methanol and 5 mL of de-ionised water ensuring that the solid phase does not dry (337,513). Water samples (300 mL) were passed through the cartridges at the rate of 1.5 mL/min. The cartridges were washed with de-ionised water and air-dried for 30 min. The analytes were eluted into the calibrated vials using 4 mL of DCM, followed by 3 mL of acetonitrile and 1 mL of methanol ensuring complete analytes elution. The SPE recoveries of the phenols ranged from 53% to 98% while that of the PAHs ranged from 97% to 98% as shown in **Table A2**. The eluted samples were dried under nitrogen gas and thereafter, DCM (2 mL) was added and the vials were vortexed for 15 min. The SPE extracts were then injected into the GC-TOF MS equipped with an auto-sampler.

### **A2.6.4 Gas chromatography-mass spectrometry analysis of phenols and PAHs**

Initial methods were developed for the identification and quantification of the PAHs and phenols. A 7890A Agilent GC coupled to a LECO PEGASUS 4D time-of-flight (TOF) mass spectrometer equipped with an Agilent autosampler was used for the analysis of the organic contaminants. The RXi 5Sil-MS; 26 m long with the internal diameter of 0.25 mm and film thickness of 0.25 µm, was used as a primary column. This column was used because of its high sensitivity, high thermal stability and reduced bleeds which prevent oxidation of the column. The temperature programming started at 50 °C for 5 min, then ramped to 290 °C at the rate of 20 °C/min and held for 5 min. The transfer line and the ion source temperature were

set at 320 °C and 250 °C respectively. The electron impact ionisation energy was set to -70 eV with an offset of 300 V making a total detector voltage to be 1600 V. Helium was used as the carrier gas at a flow rate of 3 mL/min. To handle co-elution of the mixed standards, accurate determination of the mass spectrum and calculation of the abundance of chromatographic peaks corresponding to individual compounds, a ChromaTOF (LECO software) was used to process the GC-MS data based on a TOF mass analyser. The molecular structures and weights of the PAHs and phenols are presented in **Figure A2**. The ChromaTOF software automatically deconvolutes the co-eluted peaks from the sample and compare the deconvoluted spectra against the given integrated library, thus making the technique more suitable for analysis of the complex extracts compared to quadrupole instruments (514).

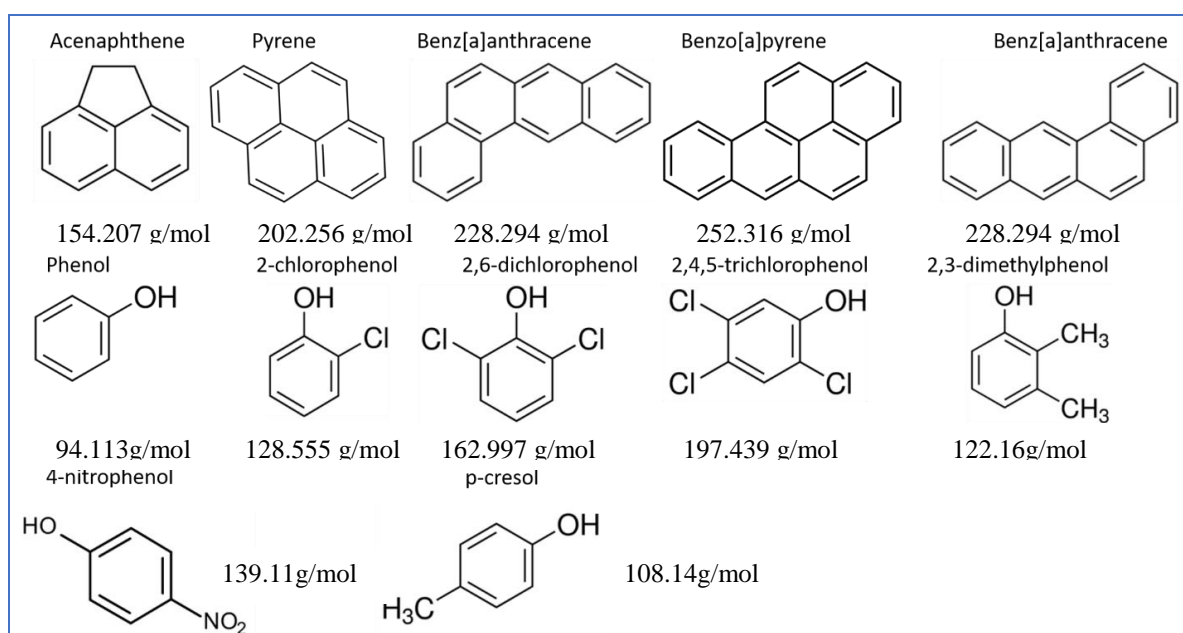


**Figure A2:** Molecular structures and weights of the analysed PAHs and phenols in water.

Identification of the PAHs and phenols was based on the accurate mass measurement. To do this, the GC and MS methods were developed to enable automatic identification of the compounds analysed. At the end of the analysis, the

ChromaTOF software generates the peak table that contains the information about the target compound. In order to quantify the concentrations of the phenols and PAHs present in the water samples, the calibration plots integrated in the method development were used. The peak areas of the phenols and PAHs present in the water samples were subsequently used to determine their respective concentrations (**Figure A3**). The calibration plots of the PAHs and phenols were used to calculate the limit of determination (LOD) and limit of quantification (LOQ). An example of the calibration plots for PAHs (Acenaphthene) and phenol (unsubstituted phenol) are presented on **Figure A3**. The LOD and LOQ were calculated based on the standard deviation of the response and the slope of the calibration plots. The calculations were expressed as follows (515):

$$LOD = \frac{3s}{b}$$

$$LOQ = \frac{10s}{b}$$

Where:

*s* is the standard deviation of the lowest concentration

*b* is the slope of the calibration plot.

The equations of the linear plots for the phenols and PAHs are presented in **Table A2**. The slope of each plot and the standard deviation of the minimum concentrations of the analytes are also recorded in **Table A2**. Moreover, the calibration plots were used to quantify the concentration of the phenols and PAHs present in the water samples. The peak areas of the phenols and PAHs present in the water samples were subsequently used to determine their respective concentrations.

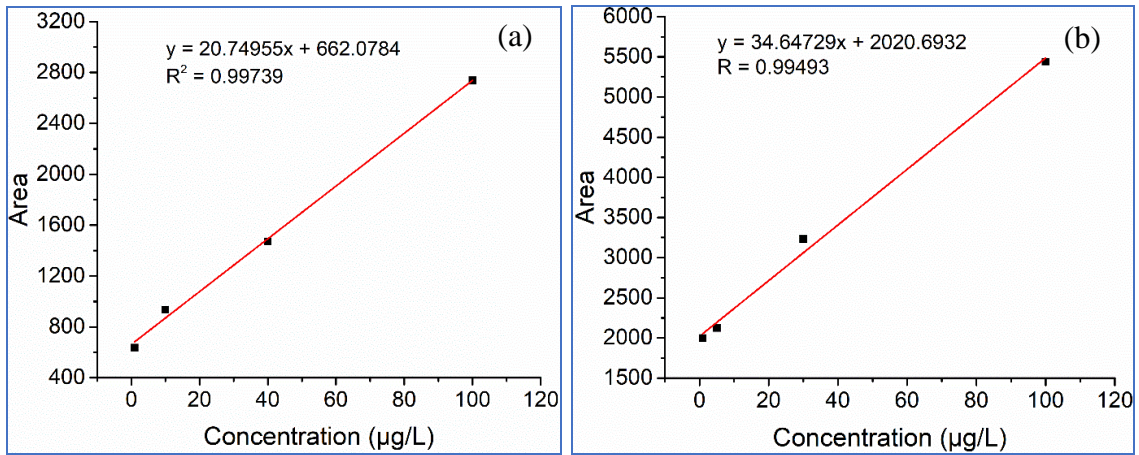


**Figure A3:** An example of organic compounds calibration plots (a) Acenaphthene (b) phenol.

**Table A2:** MDLs and recoveries of the PAHs and phenolic compounds.

Sample	Linear conc. (n=4)	MDL ( $\mu\text{g/L}$ )	SD of MDL ( $\mu\text{g/L}$ )	SPE Rec. (%)	Calibration plot	R <sup>2</sup>
Phenol	0.5 – 100	0.901	0.047	62.41	$y = 34.647x + 2020.7$	0.9949
2-Chlorophenol	1 – 100	2.674	0.054	98.69	$y = 56.61x + 1826.4$	0.9992
2,6-Dichlorophenol	1 – 100	3.499	0.039	74.86	$y = 48.51x + 30071.6$	0.9994
2,4,5-Trichlorophenol	1 – 100	3.684	0.058	86.97	$y = 44.76x + 43606.2$	0.9985
2,4-Dimethylphenol	1 – 100	6.147	0.266	80.13	$y = 176.25x + 78314.3$	0.9991
4-Nitrophenol	1 – 100	9.761	0.018	57.64	$y = 21.69x + 9653.8$	0.9989
p-Cresol	0.5 – 100	1.834	0.115	53.32	$y = 162.58x + 78196.1$	0.9983
Naphthalene	1 – 100	17.697	0.059	97.81	$y = 60.528x + 337.10$	0.9961
Pyrene	1 – 100	2.439	0.292	98.24	$y = 113.81x + 135.52$	0.9966
Acenaphthene	1 – 100	1.843	0.040	98.46	$y = 20.75x + 662.08$	0.9974
Benz(a)anthracene	1 – 100	3.498	0.062	97.68	$y = 8.061x - 0.4681$	0.9983
Benzo(a)pyrene	1 – 100	14.024	0.684	98.14	$y = 62.223x - 37.167$	0.9990

MDL= minimum detectable limit, SD = standard deviation, SPE = solid-phase extraction, Rec = recovery

To handle co-elution of the mixed standards as well as accurate determination of the mass spectrum and calculate the abundance of chromatographic peaks corresponding to individual compound, ChromaTOF (LECO software) was used to process the GC-MS data based on a Time-of-Flight (TOF) mass analyser. Time-of-Flight automatically deconvolute the co-eluted peaks from the sample and compare the deconvoluted spectra against the given integrated library, thus making the technique more suitable for analysis of the complex extracts compared to quadrupole instruments (514). The chromatograms and the MS spectra of some representative PAHs and phenols are presented on **Figure A4-A9**. Other

advantages of GC-TOF-MS include; short flight times, instantaneous acquisition of total mass spectrum from  $m/z$  4 to 1 024, rapid accumulation of several thousands of mass spectra, use of small quantities of samples, lower detection limits, high mass resolution, sensitivity and finally, the excellent reproducibility and better signal-to-noise ratio compared to other separation techniques (514,516,517).

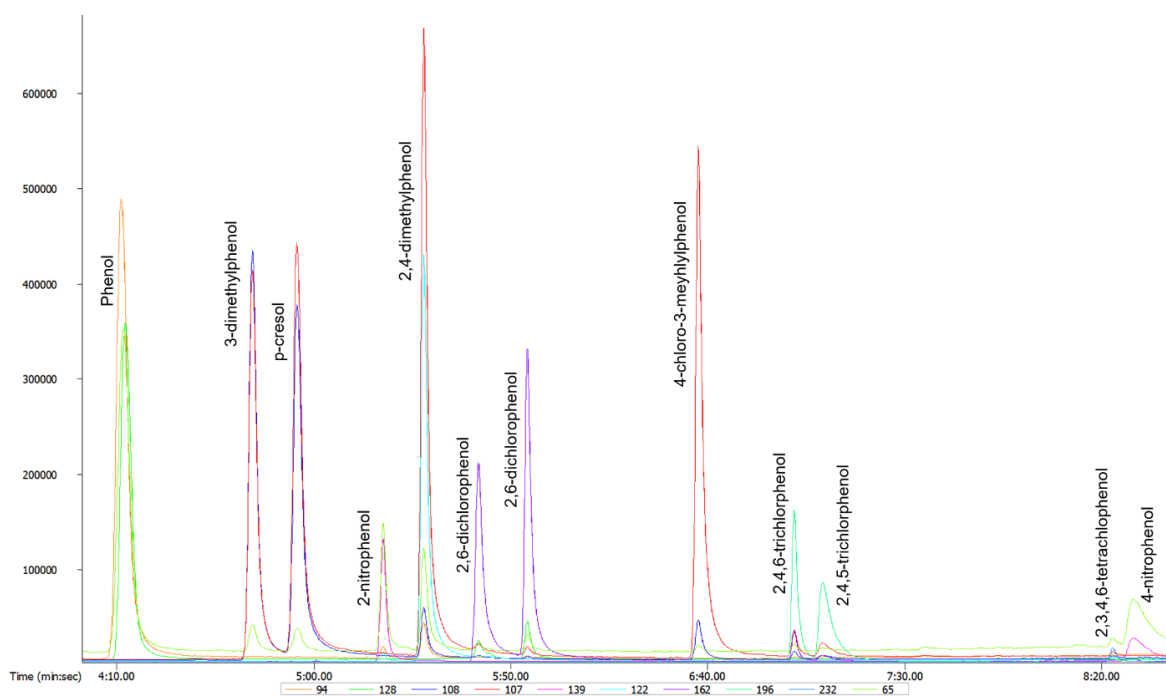


**Figure A4:** Chromatograms of the phenols.

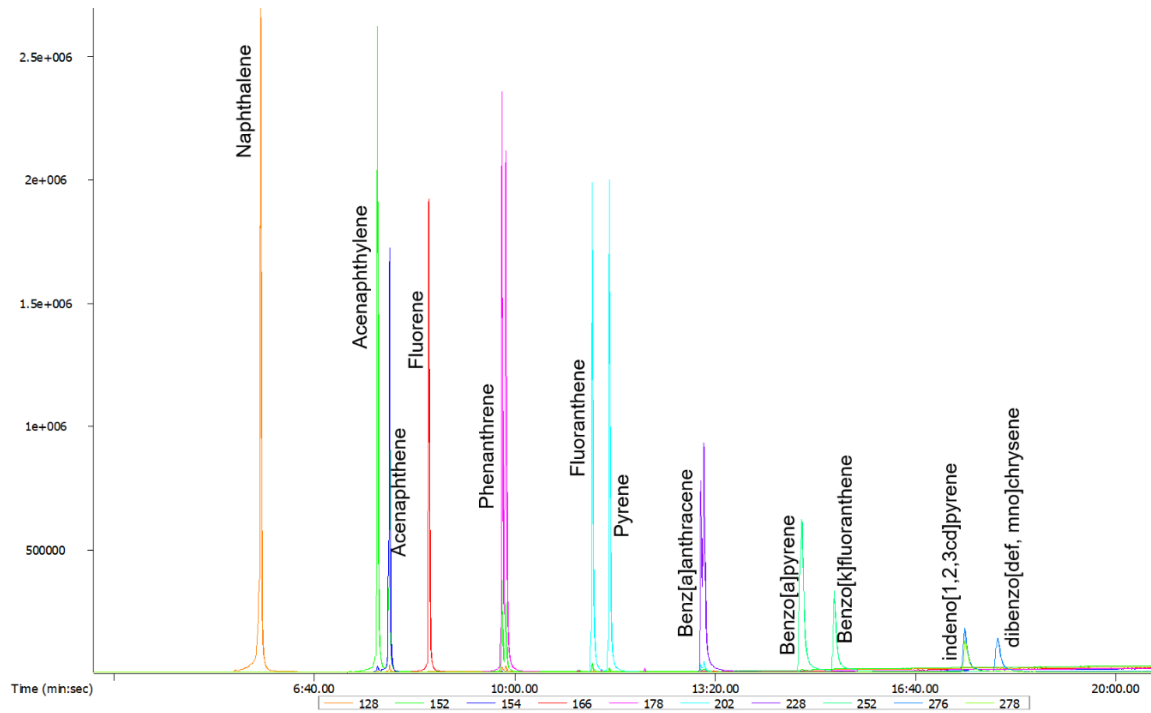


**Figure A5:** Chromatograms of the PAHs.

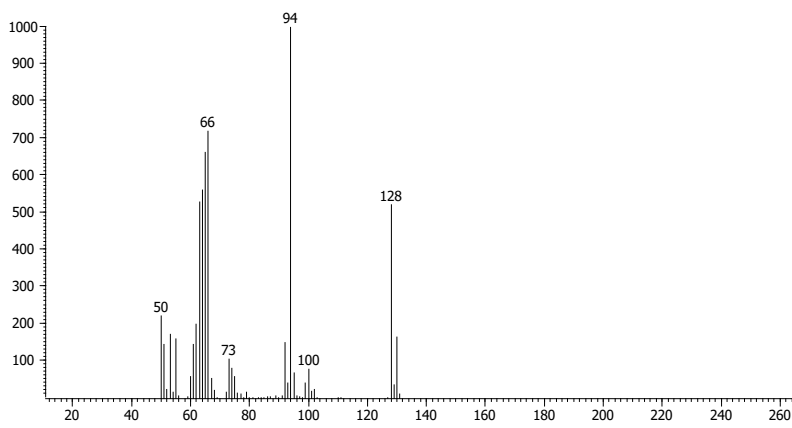


**Figure A6:** Mass spectrum of phenol.

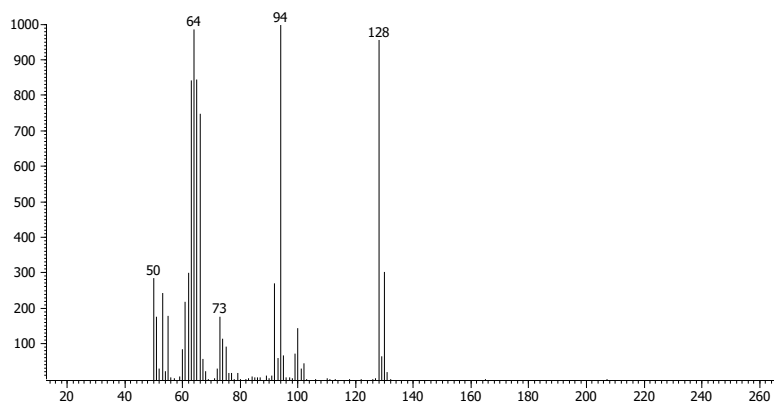


**Figure A7:** Mass spectrum of 2-chlorophenol.

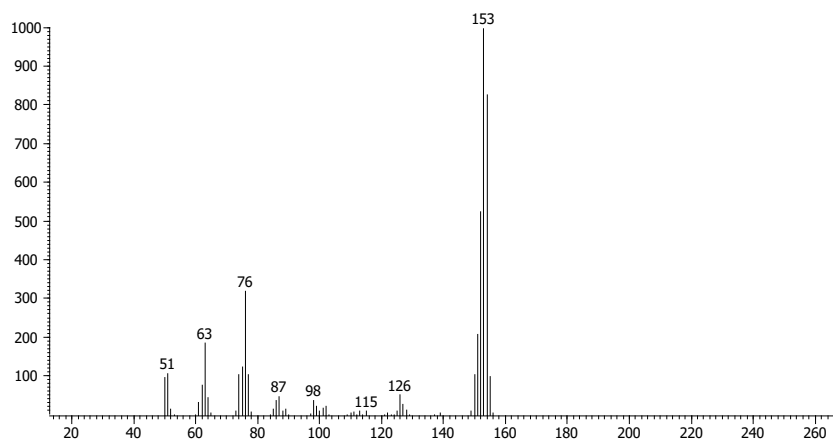


**Figure A8:** Mass spectrum of acenaphthene.

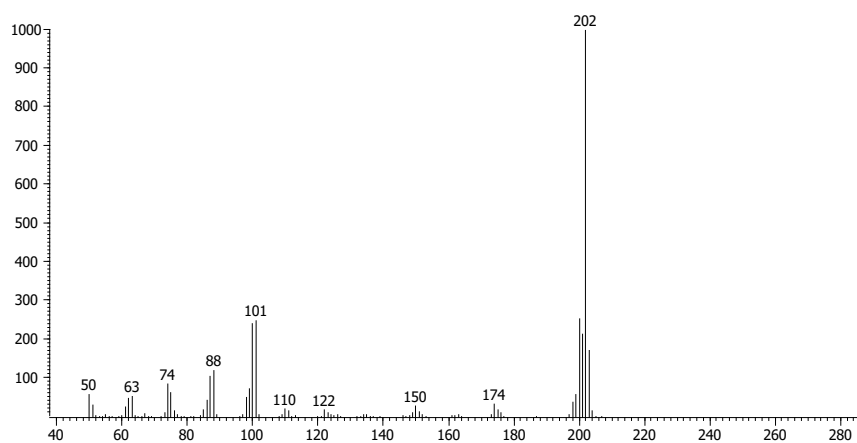


**Figure A9:** Mass spectrum of pyrene.

### A.2.7 Statistical analysis

Two statistical analysis methods were used to determine the variance of the water salinity using SPSS. One-way analysis of variance (ANOVA) was carried out to evaluate the variation of water quality parameters. The physicochemical variables in this analysis are: electrical conductivity (EC), total dissolved solids (TDS), salinity, chlorides ( $\text{Cl}^-$ ), nitrate ( $\text{NO}_3^-$ ), phosphates ( $\text{PO}_4^{3-}$ ), sulphates ( $\text{SO}_4^{2-}$ ), fluoride ( $\text{F}^-$ ), iodide (I), ammonium ( $\text{NH}_4^+$ ), sodium ( $\text{Na}^+$ ), magnesium ( $\text{Mg}^{2+}$ ), calcium ( $\text{Ca}^{2+}$ ), hydrogen carbonate ( $\text{HCO}_3^-$ ). The organic parameters and compounds include TOC, DOC, phenols (phenol, 2-chlorophenol, 2,6-dichlorophenol, 2,4,5-trichlorophenol, 2,4-dimethylphenol, 4-nitrophenol p-cresol) and PAHs (naphthalene, pyrene, acenaphthene, benzo(a) anthracene and benzo(a) pyrene). The formulated null hypothesis was that the mean values of the physicochemical indicators were the same over all seasons of the year while the alternative hypothesis was that the mean values were significantly different. Additionally, the student's t-test was used to determine whether water quality parameters of the particular site demonstrated that the water was brackish or not. The null hypothesis was that the water in Nandoni Dam was brackish (that is the concentration in the range of 500–5000 mg/L). The statistical test for student's ( $t$ ) was given by the **Equation A1** to compare each parameter of a particular site with a defined standard:

$$t = \frac{\bar{x} - \mu}{s/\sqrt{n}} \quad (\text{A.1})$$

where  $\bar{x}$  is the mean value of the examined parameter,  $s$  is the standard deviation and  $n$  is the sample size at 95% confidence level.

## A3 Results and Discussion

### A3.1 Statistical analysis results of the parameters that contribute to water salinity

The F-values above 0.05 (presented in **Table A3**) indicated that there is a significant difference in concentrations of ions contributing to water salinity during all seasons of the year except chloride, nitrate and sodium ions. The p-values of the salinity and magnesium concentrations showed that the water in Nandoni Dam was brackish except the rest of the other parameters that determine if the water is brackish or not.

**Table A3:** Hypothetical test of the variation of the water parameters that contribute to water salinity and the student's t-test results.

Parameters	Mean	Sum of Squares	df	Mean Square	F	Sig.	t	p-value
Conductivity ( $\mu\text{S/cm}$ )	1308	18203	3	6067	0.032	0.992	3.685	0.001
TDS (mg/L)	1153	5759	3	1919	0.067	0.977	-4.019	0.001
Salinity (mg/L)	490.2	83333	3	27777	1.271	0.311	-0.38	0.707
Chloride (mg/L)	62.29	11361	3	3787	9.866	0.000	-74.53	0.000
Nitrate (mg/L)	10.27	441.9	3	147.3	3.327	0.040	6.299	0.000
Phosphate (mg/L)	1.728	4.063	3	1.354	1.967	0.151	8.948	0.000
Sulphate (mg/L)	0.625	0.495	3	0.165	1.507	0.243	-134.4	0.000
Fluoride (mg/L)	0.971	0.001	3	0.000	0.063	0.979	-119.9	0.000
Iodide (mg/L)	1.778	4.394	3	1.465	1.967	0.151	9.237	0.000
Ammonium (mg/L)	3.998	2.000	3	0.667	0.290	0.832	12.74	0.000
Sodium (mg/L)	34.15	4763	3	1588	8.557	0.001	7.441	0.000
Magnesium (mg/L)	4.855	27.17	3	9.059	0.483	0.698	-0.165	0.870
Calcium (mg/L)	18.17	80.64	3	26.87	0.809	0.504	-10.18	0.000
Hydrogen carbonate (mg/L)	29.972	218.136	3	72.712	0.787	0.515	-36.21	0.000

The most likely causes of salinity in the Nandoni Dam are presented in **Figure A10**. Such causes include the erosion of salt-bearing rocks, infiltration of the saline water from aquifers by natural and anthropogenic activities, sewage discharge and the landfill leachates that contain dissolved salts [40–43]. The contribution of the sewage discharge to the surface water salinity is less significant compared to

other sources. However, it affects the quality of the water by introducing high levels of pathogens and other contaminants, thus making the water sources unfit for domestic use [44–46]. The erosion of the salt-bearing rocks is common in the Luvuvhu River and its tributaries, which is the main source of water supply for the Nandoni Dam. Source waters in the Vhembe District such as underground water and open wells are characterised by high levels of dissolved salts, which are assumed to find their way into the Nandoni Dam through small streams and tributaries that flow into the Luvuvhu River. Thus, these factors could contribute to the various levels of water salinity during different seasons of the year. The findings reported from a study conducted in Northern Cape in South Africa indicated the presence of  $\text{Cl}^{-1}$  and  $\text{Na}^{+}$  ions in the river water as well as the alluvial aquifers at concentrations of 320–14588 mg/L and 143–4933 mg/L [47]. The main identified possible sources of the high levels of these ions were seawater intrusion, dissolution of evaporites, concentrations by evaporation, deep aquifer brines, dissolution of minerals from the aquifer geology as well as salts from anthropogenic activities (i.e., mining). Although this work was focused on the determination of the water salinity, it was found that the quality of the water from Nandoni Dam was generally poor. The presence of ammonium in the concentration ranges of 1.32–5.96 mg/L exceeding 1.00 mg/L [48], which is the permissible WHO limit, demonstrates that the water is not only unfavourable for drinking but also toxic for both aquatic life and human use. While other anions were below the permissible limits of different organisations such as WHO, USEPA, and the South African National Standards for Drinking Water (SANS 241), the nitrates were found to be generally higher than the SANS 241 set standard of 6.00 mg/L [49].

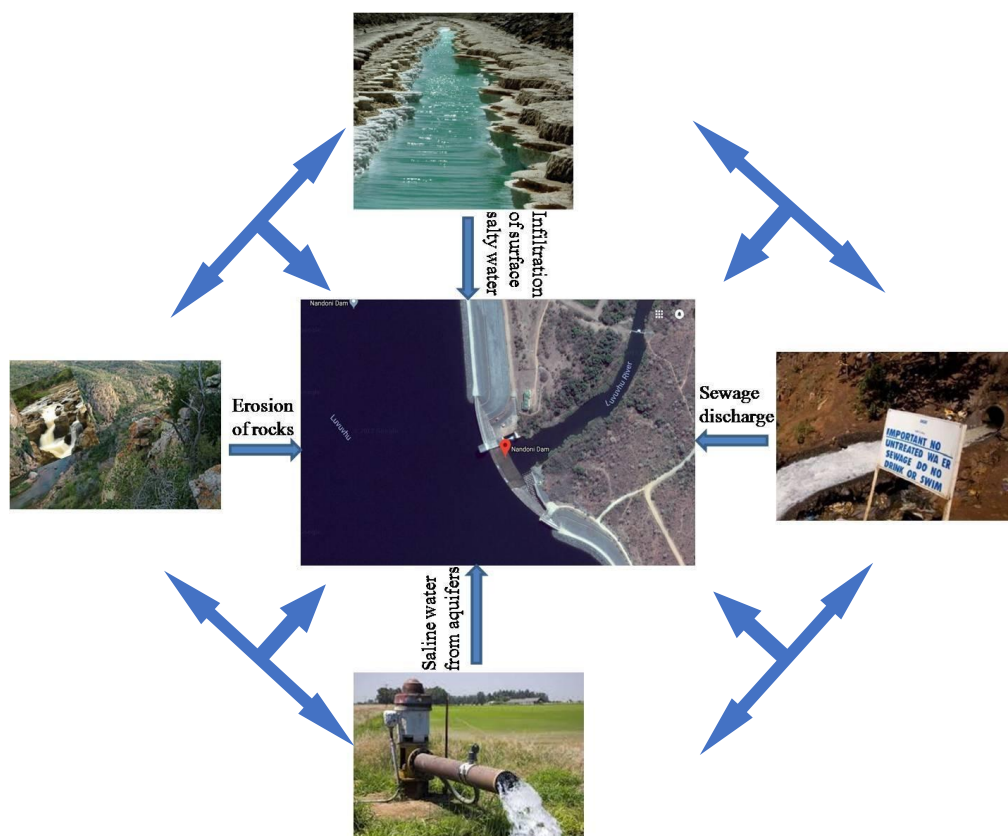


**Figure A10:** Possible sources of water salinity in the Nandoni Dam.

### A3.2 Qualitative analysis of phenols and PAHs

The phenols, PAHs and other organic contaminants present in water samples were detected at different retention times of the GC-TOF MS (**Table A4**). Phenol, 2-chlorophenol, 2,6-dichlorophenol, 2,4,5-trichlorophenol, 2,4-dimethylphenol, 4-nitrophenol and p-cresol were detected at the retention times of 247 s, 250 s, 353 s, 428 s, 326 s, 509 s, and 294 s respectively (**Table A4**). The following PAHs, namely naphthalene, pyrene, acenaphthene, benzo(a)anthracene and benzo[a]pyrene on a separate analysis were detected at the retention times of 321 s, 694 s, 435 s, 784 s, and 887 s respectively (**Table A4**).

The mass-to-charge ratios ( $m/z$ ) of the fragments that correspond to the charged ions of the respective phenols and the PAHs were used to confirm their presence

in water. The  $mz = 94, 128, 162, 196, 122, 139$  and  $108$  with relative abundances of more than 90% are equivalent to the fragmented ions of phenol, 2-chlorophenol, 2,6-dichlorophenol, 2,4,5-trichlorophenol, 2,4-dimethylphenol, 4-nitrophenol and p-cresol in the analysis of phenols (**Table A4**). The  $mz = 128, 202, 153, 228$  and  $252$  with the relative abundance of 99.9% are equivalent to the charged fragmented ions of naphthalene, pyrene, acenaphthene, benzo(a) anthracene and benzo[a] pyrene in the analysis of PAHs (**Table A4**). Phenol, 2-chlorophenol, 2,6-dichlorophenol, 2,4,5-trichlorophenol, 2,4-dimethylphenol, 4-nitrophenol, p-cresol, naphthalene, pyrene, acenaphthene, benzo(a) anthracene and benzo[a] pyrene were quantified using their respective standard solutions after their successful qualitative analysis. The limit of detection (LOD) and limit of quantification (LOQ) of the phenols and PAHs were calculated from the calibration graphs of their respective standards. The quantitative analyses are then discussed in the subsequent sections.

**Table A4:** GC-TOF MS analysis of phenols and PAHs.

Sample	$t_R$ /s	wt (g/mol)	$m/z$	$R^2$	LOD / $\mu\text{g/L}$	LOQ / $\mu\text{g/L}$
Phenol	247	94.11	94	0.9949	0.0041	0.0140
2-Chlorophenol	250	128.6	128	0.9992	0.0029	0.0095
2,6-Dichlorophenol	353	162.9	162	0.9994	0.0024	0.0080
2,4,5-Trichlorophenol	428	197.4	196	0.9985	0.0039	0.0129
2,4-Dimethylphenol	326	122.2	122	0.9991	0.0045	0.0151
4-Nitrophenol	509	139.1	139	0.9989	0.0025	0.0083
p-Cresol	294	108.1	108	0.9983	0.0021	0.0071
Naphthalene	321	128.2	128	0.9961	0.0029	0.0100
Pyrene	694	202.3	202	0.9966	0.0077	0.0257
Acenaphthene	435	154.1	153	0.9974	0.0058	0.0193
Benz(a)anthracene	784	228.3	228	0.9983	0.0230	0.0770
Benzo(a)pyrene	887	252.3	252	0.9990	0.0330	0.1099

$t_R$  = retention time (s) , LOD = limit of detection, LOQ = limit of quantification.

### A3.3 Statistical analysis results of organic compounds in the Nandoni Dam

The p-values of the test statistics on TOC, DOC, phenol, 2-chlorophenol, 2,6-dichlorophenol, 2,4,5-trichlorophenol, 2,4-dimethylphenol, p-cresol, naphthalene, pyrene, acenaphthene, benzo(a) anthracene and benzo[a] pyrene were found to be greater than 0.05 indicating that the null hypothesis is accepted while that of 4-nitrophenol was 0.001 leading to the rejection of the null hypothesis (**Table A5**). This means that the concentrations of TOC, DOC, phenols, 2-chlorophenols, 2,6-dichlorophenol, 2,4,5-trichlorophenols, 2,4-dimethylphenol, p-cresol, naphthalene, pyrene, acenaphthene, benzo(a) anthracene and benzo[a] pyrene were statistically different within four seasons of the year while that of 4-nitrophenol was not significantly different.

**Table A5:** Hypothesis test results of the mean concentration of the organic contaminants measured in four seasons of the year using the one-way ANOVA test.

Phenols		Sum	of	Mean	F	Sig.
		Squares	df	Square		
Phenol	Between Groups	0.450	3	0.150	2.004	0.146
	Within Groups	1.498	20	0.075		
	Total	1.948	23			
2-Chlorophenol	Between Groups	0.007	3	0.002	0.248	0.862
	Within Groups	0.177	20	0.009		
	Total	0.184	23			
2,6-Dichlorophenol	Between Groups	0.016	3	0.005	0.422	0.739
	Within Groups	0.248	20	0.012		
	Total	0.264	23			
2,4,5-Trichlorophenol	Between Groups	0.128	3	0.043	0.977	0.423
	Within Groups	0.872	20	0.044		
	Total	1.000	23			
2,3-Dimethylphenol	Between Groups	0.004	3	0.001	0.731	0.546
	Within Groups	0.040	20	0.002		
	Total	0.045	23			
4-Nitrophenol	Between Groups	0.000	3	0.000	7.584	0.001
	Within Groups	0.000	20	0.000		
	Total	0.000	23			
p-Cresol	Between Groups	0.146	3	0.049	1.141	0.357
	Within Groups	0.853	20	0.043		
	Total	0.999	23			
Acenaphthene	Between Groups	0.000	3	0.000	0.726	0.548
	Within Groups	0.001	20	0.000		
	Total	0.001	23			
Benz(a)nthracene	Between Groups	0.000	3	0.000	0.219	0.882
	Within Groups	0.000	20	0.000		
	Total	0.000	23			
Benzo(a)pyrene	Between Groups	0.000	3	0.000	0.335	0.800
	Within Groups	0.001	20	0.000		
	Total	0.001	23			
Naphthalene	Between Groups	0.000	3	0.000	0.080	0.970
	Within Groups	0.005	20	0.000		
	Total	0.005	23			
Pyrene	Between Groups	0.000	3	0.000	0.392	0.760
	Within Groups	0.007	20	0.000		
	Total	0.008	23			
TOC	Between Groups	0.188	3	0.063	0.160	0.922
	Within Groups	7.856	20	0.393		
	Total	8.044	23			
DOC	Between Groups	0.305	3	0.102	0.829	0.493
	Within Groups	2.448	20	0.122		
	Total	2.753	23			

### A3.4 Synoptic sources of phenols and PAHs in Nandoni Dam

**Figure A11** presents the possible activities in Vhembe District Municipality that introduce several water contaminants which include phenols and PAHs into Nandoni Dam. These activities include leachates from the landfills, pesticides, herbicides, and insecticides used for agricultural purposes and incomplete combustions from burning of the trees, grass and tires. Incomplete combustion results to the formation of the PAHs while the phenols originate from the agricultural activities. The landfills were characterised by households wastes that included detergents and plastics. Other sources of the phenols and PAHs occur naturally as described previously. These phenols and PAHs containing compounds originating from these activities find their ways into nearby streams during rainfall events. The streams connect to the tributaries, which subsequently join the Luvuvhu River (the main water source of Nandoni Dam). The mentioned activities including landfilling and agricultural activities are common practices in Thohoyandou in the Vhembe District. The leachates from these practices find their way into small streams and tributaries that flow directly into the Nandoni Dam or enter the dam indirectly through Luvuvhu River. Unmanaged waste disposals were also observed in the villages of Ha-Mutoti and Ha-Budeli and Ha-Mphego which are a few kilometres away from Luvuvhu river. During community service delivery protests, wood and tyres are burnt while blocking the main roads. The products are discharged into the streams and tributaries that flow directly Nandoni Dam during the rain seasons, hence the observed concentration of unwanted organics in the dam.



**Figure A11:** Possible sources of phenols and PAHs that find their way into Nandoni Dam.

## CURRICULUM VITAE

---



### CONTACT INFORMATION

---

**Name** : Lebea Nathnael Nthunya

**Date of Birth** : 13/03/1987

**Address** : Futhong Hanthoba, Mapoteng 250, Berea, Lesotho

**Cell phone #** : +266 5356 4888 or +27 78 205 1177

**Email** : [nthunylebea@gmail.com](mailto:nthunylebea@gmail.com)

### EDUCATION BACKGROUND

---

<b>Year</b>	<b>Learning Institution</b>	<b>Award</b>
2016/2019	UNISA - Universiteit Gent	Joint PhD
2014/2015	University of Johannesburg	MSc Applied Chemistry
2008/2013	National University of Lesotho	BSc Chemical Technology
2006/2007	Dahon High School	COSC O-Level
2003/2005	Koeneng Secondary School	Junior Certificate

**AWARDS**

<b>Year</b>	<b>Institution</b>	<b>Awards</b>
2016	SACI Conference (Royal Society of Chemistry)	Best PhD Presenter Award
2015	SACI Conference (Royal Society of Chemistry)	Best MSc Presenter Award
2015	University of Johannesburg	Faculty Merit Bursary
2007	Dahon High School	Debating and Leadership
2005	Koeneng High School	Mathematics contest

**PUBLICATIONS (CO)AUTHORED**

**Lebea N. Nthunya**, Monaheng L. Masheane, Soraya P. Malinga, Edward E. Nxumalo, Barnard Tobias, Mahalio Kao, Zikhona N. Tetana, and Sabelo D. Mhlanga. A greener approach to prepare electrospun  $\beta$ -cyclodextrin/cellulose acetate nanofibres for removal of bacteria from water. *ACS Sustainable Chemistry and Engineering*. **2017**; 5(1), 153–160.

**Lebea N. Nthunya**, Sebatatso Maifadi, Bhekie B. Mamba, Arne R. Verliefdede and Sabelo D. Mhlanga. Spectroscopic Determination of Water Salinity in Brackish Surface Water in Nandoni Dam, at Vhembe District, Limpopo Province, South Africa. *Water*. 2018; 10(990), 1-13 377–386.

**Lebea N. Nthunya**, Monaheng L. Masheane, Soraya P. Malinga, Edward E. Nxumalo, and Sabelo D. Mhlanga. Electrospun chitosan-based nanofibres for removal of phenols from drinking water. *Water SA*. **2018**; 44(3), 377–386.

Monaheng L. Masheane, **Lebea N. Nthunya**, Soraya P. Malinga, Edward N. Nxumalo, Bhekie B. Mamba, and Sabelo D. Mhlanga. Synthesis of Fe-Ag/f-MWCNT/PES nanostructured-hybrid membranes for removal of Cr(VI) from water. *Separation and Purification Technology*. **2017**; 184, 79 – 87.

**Lebea N. Nthunya**, Monaheng L. Masheane, Soraya P. Malinga, Edward E. Nxumalo, Bhekie B. Mamba, and Sabelo D. Mhlanga. Determination of toxic metals in drinking water sources in the Chief Albert Luthuli Local Municipality in Mpumalanga, South Africa. *Physics and Chemistry of the Earth, Parts A/B/C*. **2017**; 100, 94 – 100.

**Nthunya L.N.**, Masheane M.L., Malinga, S.P., Nxumalo, E.N., and Mhlanga S.D. Environmentally benign chitosan-based nanofibres for potential use in water treatment. *Cogent Chemistry*. **2017**; 3(1), 1357865.

**Lebea N. Nthunya**, Monaheng L. Masheane, Soraya P. Malinga, Tobias Barnard, Edward E. Nxumalo, Bhekie Mamba, and Sabelo D. Mhlanga. UV-assisted reduction of in-situ electrospun antibacterial chitosan-based nanofibres for removal of bacteria from water. *RSC Advances*. **2016**; 6, 95936–95943.

**Lebea Nthunya**, Monaheng Masheane, Soraya Malinga, Edward Nxumalo, Bhekie Mamba, and Sabelo D. Mhlanga. Thermally and mechanically stable  $\beta$ -cyclodextrin/cellulose acetate nanofibers synthesized using a greener method. *International Journal of Smart and Nano Materials*. **2017**; 8(1) 1 – 19.

Monaheng Masheane, **Lebea Nthunya**, Mukuna Mubiayi, Timothy Thamae, and Sabelo Mhlanga. Physico-chemical characteristics of some Lesotho's clays and their assessment for suitability in ceramics production. *Particulate Science and Technology*. **2018**; 36(1), 117 – 122.

Monaheng L. Masheane, **Lebea N. Nthunya**, Soraya P. Malinga, Edward N. Nxumalo, and Sabelo D. Mhlanga. Chitosan-based nanocomposites for de-nitrification of water. *Physics and Chemistry of the Earth Parts A/B/C*. **2016**; 100, 212 – 224.

Monaheng Masheane, **Lebea Nthunya**, Soraya Malinga, Edward Nxumalo, Tobias Barnard, and Sabelo Mhlanga. Antimicrobial properties of chitosan-alumina/f-MWCNT nanocomposites. *Journal of Nanotechnology*. **2016**; 2016, 1-8.

Monaheng L. Masheane, **Lebea N. Nthunya**, Soraya P. Malinga, Edward N. Nxumalo, and Sabelo D. Mhlanga. Chitosan-based nanocomposite beads for drinking water production. *IOP Conference Series; Materials Science and Engineering*. **2017**; 195,

Diseko Boikanyo, Monaheng L Masheane, **Lebea N Nthunya**, Shivani B Mishra, Sabelo D Mhlanga. *Carbon-supported photocatalysts for organic dye photodegradation*, in New Polymer Nanocomposites for Environmental Remediation. Elsevier B.V. New York. **2018**; 99-138

Nomcebo P Khumalo, **Lebea N Nthunya**, Els De Canck, Sebastiaan Derese, Arne R Verliefe, Alex T Kuvarega, Bhekie B Mamba, Sabelo D Mhlanga, Derrick S Dlamini. Congo red dye removal by direct membrane distillation using PVDF/PTFE membrane. *Separation and Purification Technology*. **2019**; 211, 578-586.

Nomcebo Khumalo, **Lebea Nthunya**, Sebastiaan Derese, Machawe Motsa, Arne Verliefe, Alex Kuvarega, Bhekie B Mamba, Sabelo Mhlanga, Derrick S Dlamini. Water recovery from hydrolysed

human urine samples via direct contact membrane distillation using PVDF/PTFE membrane. *Separation and Purification Technology*. **2019**; 211, 211, 610-617.

**Lebea N. Nthunya**, Mosotho George, Monaheng L. Masheane, Méschac-Bill Kime, Sabelo D. Mhlanga. Removal of Fe and Mn From Polluted Water Sources in Lesotho Using Modified Clays. *Journal of Water Chemistry and Technology*. **2019**; 41, 81-86.

Nikiwe Kunjuzwa, **Lebea N Nthunya**, Edward N Nxumalo, Sabelo D Mhlanga. *The use of nanomaterials in the synthesis of nanofibre membranes and their applications in water treatment*, in *Advanced Nanomaterials for Membrane Synthesis and its Applications*. Elsevier B.V. Amsterdam. **2019**; 101-126.

**Lebea N Nthunya**, Sebastiaan Derese, Leonardo Gutierrez, Arne R Verliefdde, Bhekie B Mamba, Tobias G Barnard, Sabelo D Mhlanga. Green synthesis of silver nanoparticles using one-pot and microwave-assisted methods and their subsequent embedment on PVDF nanofibre membranes for growth inhibition of mesophilic and thermophilic bacteria. *New Journal of Chemistry*. **2019**; 1-14.

**Lebea N. Nthunya**, Nomcebo P. Khumalo, Arne R. Verliefdde, Bhekie B. Mamba, Sabelo D. Mhlanga. Quantitative analysis of phenols and PAHs in the Nandoni Dam in Limpopo Province, South Africa: a preliminary study for dam water quality management. *Physics and Chemistry of the Earth*. **2019**; DOI: 10.1016/j.pce.2019.02.003 (in press).

**Lebea N. Nthunya**, Leonardo Gutierrezb, Sebastiaan Derese, Edward N. Nxumalo, Arne R. Verliefdde, Bhekie B. Mamba, Sabelo D. Mhlanga. A Review of Nanoparticle-Enhanced Membrane Distillation Membranes: Membrane Synthesis and Applications in Water Treatment. *Journal of Chemical Technology and Biotechnology*. **2019**; 94, 2757-2771.

**Lebea N. Nthunya**, Leonardo Gutierrezb, Nomcebo Khumalo, Sebastiaan Derese, Bhekie B. Mamba, Sabelo D. Mhlanga. Superhydrophobic PVDF nanofibre membranes coated with an organic fouling resistant hydrophilic active layer for direct-contact membrane distillation. *Colloids and Surfaces A; Physicochemical and Engineering Aspects*. **2019**; 575, 363-372.

**Lebea N. Nthunya**, Leonardo Gutierrez, Arne R. Verliefdde, Sabelo D. Mhlanga. Enhanced Flux in direct contact membrane distillation using superhydrophobic PVDF nanofibre membranes embedded with organically modified SiO<sub>2</sub> nanoparticles. *Journal of Chemical Technology and Biotechnology*. **2019**; 94, 2826-2837.

**Lebea N. Nthunya**, Leonardo Gutierrez, Sebastiaan Derese, Arne R. Verliefdde, Sabelo D. Mhlanga. Adsorption of phenolic compounds by polyacrylonitrile nanofibre membranes: A pretreatment for the removal of hydrophobic bearing compounds from water. *Journal of Environmental Chemical Engineering*. **2019**; 7, 103254.

**Lebea N. Nthunya**, Leonardo Gutierrez, Linsey Lapeire, Kim Verbeken, Noor Zaouri, Edward N Nxumalo, Bhekie B. Mamba, Arne R. Verliefe, Sabelo D. Mhlanga. Fouling-resistant PVDF nanofibre membranes for the desalination of brackish water in membrane distillation. *Separation and Purification Technology*. **2019**; 228, 115793.

